UNIVERSITÀ
DEGLI STUDI
DI PADOVA

Sede Amministrativa: Università degli Studi di Padova

Dipartimento di Ingegneria Industriale

SCUOLA DI DOTTORATO DI RICERCA IN INGEGNERIA INDUSTRIALE
INDIRIZZO: INGEGNERIA DELL'ENERGIA
CICLO XXVI

TWO-PHASE HEAT TRANSFER INSIDE MINICHANNELS: FUNDAMENTALS AND APPLICATIONS IN REFRIGERATION AND SOLAR TECHNOLOGY

Direttore della Scuola: Prof. Paolo Colombo
Coordinatore d'indirizzo: Prof.ssa Luisa Rossetto
Supervisore: Prof. Davide Del Col

Dottorando: Matteo Bortolato

ABSTRACT

This thesis reports the results of many experimental tests conducted to gain a deeper insight on the two-phase heat transfer inside minichannels and to characterize the thermal performance of two refrigerants with low environmental impact: propane (R290) and R1234ze(E). Furthermore, some considerations on the application of the minichannel technology in refrigeration applications and solar concentrators are presented.

As pressure drops greatly affect the heat transfer in two-phase flow, the experimental investigation on frictional pressure gradient during adiabatic flow of R134a, R1234ze(E) and propane (R290) at different mass velocities and at saturation temperatures between 30°C and 50°C has been conducted in two single copper minichannels with a circular cross section and hydraulic diameters of 0.96 mm and 2 mm. The experimental points are compared with several models available in the open literature.

Heat transfer coefficients have been experimentally measured during the condensation at 40°C and during the vaporization at 31°C of R1234ze(E) and propane at different mass velocities inside a single circular cross section minichannel with an internal diameter of 0.96 mm. During the test runs, the refrigerant exchanges heat with a secondary fluid, that is distilled water, so the local heat flux is not constant along the measuring section and its accurate calculation becomes the main issue. An assessment of several predicting correlations has been presented for predicting the heat transfer coefficient both in condensation and in vaporization.

The condensation process inside minichannels depends on the relative importance of shear stress, gravity and surface tension, especially in presence of corners in the cross section shape. Nevertheless, few studies concern the effect of inclination. In this work, the effect of the channel orientation has been experimentally analyzed and discussed during the condensation of R134a and R32 at 40°C saturation temperature inside a single square cross section minichannel with a hydraulic diameter equal to 1.23 mm. Several configurations of the test section from vertical upward flow to vertical downward flow have been examined.

When considering the application of the minichannel technology in refrigeration, a general methodology to evaluate the potential heat transfer performance of refrigerants during in-tube condensation is a powerful tool to optimize the performance and the design of heat exchangers. The Performance Evaluation Criteria (PEC) named Penalty Factor for condensation (PF) and Total Temperature Penalization on the refrigerant side (TTP) are applied to rank several refrigerants starting from an experimental database collected in a single circular minichannel with internal diameter of 0.96 mm at the Two-Phase Heat Transfer Lab at the University of Padova.

In electronics, the minichannel technology has proved to be reliable and effective in removing high heat fluxes through small heat transfer areas. This feature has suggested to use minichannel-based receivers for solar concentration systems.

In this work, a parabolic trough linear solar concentrator is described and tested using two different minichannel-based receivers: a concentrating hybrid photovoltaic thermal (CPVT) receiver for the cogeneration of electrical energy and heat and a thermal receiver with a selective coating for the generation of heat in the medium temperature range. An optical modeling has been developed for the two cases in order to assess the optical efficiency and the flux distribution on the receiver. Tests with both the receivers have been performed using water in single-phase flow as working fluid in order to get a preliminary characterization of the whole system. The performance of the thermal receiver at medium temperature (up to 150°C) when two-phase heat transfer is realized inside the channels has been evaluated through a numerical model.

RIASSUNTO

In questa tesi sono presentati i risultati di numerose prove sperimentali che mirano a migliorare la conoscenza dello scambio termico bifase all'interno di minicanali e a caratterizzare le prestazioni di due fluidi a basso impatto ambientale come il propano e il refrigerante R1234ze(E). Inoltre, sono contenute alcune considerazioni relative all'applicazione della tecnologia dei minicanali nella refrigerazione e nei concentratori solari.

Dal momento che le perdite di carico influenzano notevolmente lo scambio termico in regime bifase, è stata condotta un'analisi sperimentale sul gradiente di pressione per attrito in condizioni adiabatiche di deflusso con R134a, R1234ze(E) e propano all'interno di due minicanali non lisci in rame, a sezione circolare e con diametri rispettivamente di 0.96 mm e 2.0 mm a diverse portate specifiche di massa e a in un intervallo di temperature di saturazione tra 30°C e 50°C. I punti sperimentali sono stati confrontati con i valori calcolati mediante alcuni modelli disponibili in letteratura.

Sono stati misurati i coefficienti di scambio termico in condensazione a 40°C e in vaporizzazione a 31°C, utilizzando in test successivi R1234ze(E) e propano all'interno di un singolo minicanale non liscio a sezione circolare e con diametro interno di 0.96 mm. Durante le prove sperimentali, il refrigerante in esame scambia calore con un fluido secondario, che nella fattispecie è acqua distillata, pertanto il flusso termico locale non è costante e il suo calcolo accurato rappresenta l'aspetto principale della tecnica sperimentale. È stata valutata la precisione predittiva di alcuni modelli disponibili in letteratura per il calcolo dei coefficienti di scambio termico in condensazione e vaporizzazione in base ai dati sperimentali raccolti.

Le forze che entrano in gioco durante un processo di condensazione all'interno dei minicanali sono dovute allo sforzo tangenziale all'interfaccia delle due fasi, all'accelerazione di gravità e alla tensione superficiale, specie se la sezione del canale presenta degli angoli. Pochissimi studi in letteratura riguardano l'effetto dell'inclinazione. In questo lavoro, è stato analizzato l'effetto dell'orientazione del canale durante la condensazione di R134a ed R32 all'interno di un minicanale a sezione quadrata con un diametro idraulico di 1.23 mm e ad una temperatura di saturazione di 40°C. Sono state esaminate diverse configurazioni della sezione di prova, dal deflusso verticale ascendente al deflusso verticale discendente.

Quando si esamina l'applicazione della tecnologia dei minicanali nell'ambito della refrigerazione, avere a disposizione una metodologia per valutare le prestazioni potenziali di scambio termico di un refrigerante durante la condensazione all'interno di un tubo diventa uno strumento molto utile per ottimizzare le prestazioni dell'intero sistema e la progettazione degli scambiatori di calore. I Criteri di Valutazione delle Prestazioni (PEC) indicati come Fattore di Penalizzazione per la condensazione (PF) e Penalizzazione Totale in termini di Temperatura nel lato refrigerante (TTP) vengono applicati in questa tesi per classificare i refrigeranti che sono stati testati in un minicanale circolare con diametro interno di 0.96 mm nel Laboratorio di Scambio Termico Bifase presso l'Università degli Studi di Padova.

Nell'industria elettronica, la tecnologia dei minicanali ha dimostrato di essere efficiente ed affidabile nell'asportare elevati flussi termici attraverso aree di scambio molto ridotte. Questa caratteristica ha suggerito la realizzazione di ricevitori a minicanali per concentratori solari. In questo lavoro, un concentratore parabolico a fuoco lineare è descritto e testato utilizzando due ricevitori: un ricevitore fotovoltaico termico per la cogenerazione di energia elettrica e calore ed un ricevitore termico con vernice selettiva per la produzione di energia termica a media temperatura. Per ognuno dei due dispositivi,

è stato sviluppato un modello ottico per valutare l’efficienza ottica di concentrazione e la distribuzione del flusso concentrato sul ricevitore. Le prove sperimentali per entrambi i ricevitori sono state condotte utilizzando come fluido operativo acqua in deflusso bifase per avere una caratterizzazione preliminare dell’intero sidtema. Le prestazioni a media temperatura del ricevitore termico considerando uno scambio termico bifase in vaporizzazione all’interno dei minicanali sono state valutate in modo attraverso un modello numerico.

Contents

1 INTRODUCTION

In literature, there is no univocal criterion to distinguish the minichannel geometry from the microchannel geometry. In the present work, the term “minichannels” indicates the channels with an hydraulic diameter less than 3 mm so it is associated to a merely geometrical definition.
Heat transfer inside minichannels has gained an increasing interest both in the scientific community and in industry as its peculiar characteristics lead to the realization of compact, lightweight and efficient heat exchangers for a huge variety of applications such as air conditioning, refrigeration, electronic cooling, fuel cell cooling and aerospace industry. While single-phase flow in minichannel has been established to behave similar to the macroscale flow, many issues related to the two-phase heat transfer inside minichannels need further investigation. Furthermore, the awareness of the serious environmental problems, the climate changes and the worrisome scenarios for the future have lead to the promulgations of regulations, directives, laws and recommendations aiming at replacing the commonly used refrigerants with natural fluids or new refrigerants with lower global warming potential and compatible with a sustainable development. Among these refrigerants, the hydrocarbons show good material compatibility and excellent thermodynamic properties, but they have not be much considered so far because of the flammability and the very low ignition concentration. The minichannel heat exchangers with refrigerant flowing in two-phase regime allow a great reduction of the charge and represent a good opportunity to use these natural fluid. More recently, halogenated olefins (HFOs) have been introduced as low global warming potential refrigerants and those with fluorinated propene isomers, in particular R1234yf and R1234ze(E), have been emerged as possible alternatives to replace the commonly used R134a refrigerant in many applications. In literature, a very few number of experimental data regarding both hydrocarbons and halogenated olefins are available so far, hence the predictive accuracy of the correlations for pressure drop and heat transfer coefficient in condensation and flow boiling that have been validated against common refrigerants should be assessed for these fluids with low environmental impact.
In condensation, all the researchers agree that the heat transfer coefficient increases with decreasing channel hydraulic diameter. In minichannels, the condensation heat transfer results from the relative influences of several forces associated to the interfacial shear stress, the gravity acceleration and the surface tension. The action of these forces may depend on operating conditions and channel orientation. When the condensation inside minichannels is shear stress dominated the heat transfer coefficient increases with vapor quality and mass velocity, just like in macrochannels. But at low mass velocities, the shear stress is not the dominant force and further research is required to a deeper understanding of the characteristics of the condensation heat transfer. In particular, in these working conditions, the shape of the cross section and the channel orientation may play an important role. In fact, in presence of non-circular cross section, the liquid is pulled to the corners leading a thinner film on the flat sides and therefore a lower thermal resistance in these parts of the channel. Furthermore, some studies performed in macrochannels showed that the heat transfer coefficient can be strongly affected by the distribution of the liquid and the vapor phases when varying the channel inclination. On the other side, the effect of the channel inclination during condensation in minichannels has been very poorly investigated.
The flow boiling inside minichannels has proved to be a very promising mechanism to remove high heat fluxes through small heat transfer surfaces. This feature suggests the application of the minichannel technology for the active cooling systems in densely

packed photovoltaic concentrators, where a lower thermal resistance is strictly recommended to avoid damages of the cells due to excess temperature. In some cases, as the linear solar concentrator, the implementation of a minichannel-based active cooling system enables the heat recovery at temperature up to 100°C if triple junction solar cells are employed. Nevertheless, some issue connected to the flow boiling inside small channels should be better studied such as the flow instabilities, the development of reliable models for the prediction of heat transfer coefficients and critical heat flux. The design of such hybrid receivers for solar concentrators has to be meticulously conducted to avoid maldistribution of the fluid. In conclusion, the forced convection boiling in minichannels is in general one of the most promising cooling systems but it requires further research.

The analysis of the two-phase heat transfer in minichannels cannot prescind from the investigation on the two-phase pressure drops. In particular, the frictional pressure drop affects the temperature profile of the refrigerant in a heat exchanger and thus, with respect to the ideal case, the heat transfer driving potential diminishes.

2 EXPERIMENTAL ANALYSIS ON TWO-PHASE FRICTIONAL PRESSURE DROP INSIDE MINICHANNELS

2.1 Abstract

Pressure drops greatly influence the heat transfer both in condensation and in vaporization. Experimental analysis and reliable correlations for the calculation of pressure drops are necessary to characterize the thermal performance of a refrigerant and to optimize the design of heat exchangers. Experimental investigation on two-phase frictional pressure drops during the adiabatic flow of three different refrigerants inside two horizontal copper minichannels are presented. The minichannels have a circular cross section and are provided with stainless steel pressure port carefully realized without perturbing the geometry, the fluid flow and thus the experimental measurements. The first minichannel has an hydraulic diameter equal to 0.96 mm and an average roughness of the inner surface *Ra* equal to 1.3 µm; the pressure ports are realized at a distance of 0.22 m. The second channel has a internal diameter of 2.0 mm, the average roughness of the inner wall *Ra* is 1.7 µm; in this case, the distance between the pressure port is 0.44 m.

The tested refrigerants includes R134a, R1234ze(E) and propane. R134a is commonly employed in refrigeration and air conditioning and widely studied in literature: many correlation for the prediction of two-phase frictional pressure drops have been validated against databases that include this refrigerant. R1234ze(E) is a halogenated olefin with a low global warming potential that is regarded as an environmentally friendly alternative for R134a in refrigeration and electronic cooling applications. It is a quite new fluid and no data of pressure drops during two-phase adiabatic flow inside minichannels are available in the open literature. Propane is a natural refrigerant with interesting thermodynamic and thermophysical properties but its use is limited because of the high flammability. Nevertheless, in minichannel heat exchangers this problem can be overcome because the total charge amount can be considerably reduced without affecting the thermal efficiency. Up to now, few studies on the frictional pressure drop during two-phase flow of propane in minichannels have been presented in the open literature.

For all the considered refrigerants, two-phase frictional pressure drop have been measured in the 0.96 mm circular cross section minichannel at mass velocities between 800 kg m^{-2} s^{-1} and 200 kg m^{-2} s^{-1} and at 40°C saturation temperature. Furthermore, in the same minichannel, at 400 kg m^{-2} s^{-1} mass velocity, experimental points are collected at 50°C saturation temperature for R134a and at 30°C saturation temperature for R1234ze(E).

Finally, test runs have been performed with R134a inside the 2.0 mm circular minichannel at 40°C saturation temperature at 500 kg m^{-2} s^{-1}, 400 kg m^{-2} s^{-1}, 300 kg m^{-2} s^{-1} and 200 kg m^{-2} s^{-1} and at 50°C saturation temperature at 400 kg m^{-2} s^{-1}.

The experimental data collected for each fluid have been compared against four models available in the open literature: the correlations by Friedel [1] and by Muller-Steinhagen and Heck [2] which have been developed specifically for macrochannels and the model by Zhang and Webb [3] and by Del Col *et al.* [4]. which were proposed for minichannels. These models are easy to implement and many researcher found that they can predict quite well experimental frictional pressure drop data related to minichannels.

This chapter includes the description of the test rig and the test sections, the explanation of the experimental technique, the error analysis and the results discussion with the comparisons of data against the selected models.

2.2 Introduction

Pressure drops have a strong effect on the two-phase heat transfer inside tube for three reasons. First, under saturation conditions, the pressure losses along a channel lead to a temperature drop, which increases the irreversibility of the heat transfer due to higher required driving temperature difference. The saturation temperature drop is higher when operating at low working pressure, hence an accurate pressure drop calculation is recommended in the condenser of a Rankine cycle and in the evaporator of a refrigeration cycle. In this last case, let the compressor power and the inlet temperature of the hot fluid remain constant: the saturation temperature drop reduces the heat flux exchanged in the evaporator.
The second and the third issue concern the two-phase heat transfer during a condensation process. The second issue is related to the higher energy consumption on the interface between the liquid phase and the vapor phase. When the shear stress becomes predominant as compared to the gravity forces and the surface tension, the liquid film becomes turbulent and gets thinner due to the liquid entrainment in the vapor core. The thinner the liquid film, the lower the thermal resistance and thus higher heat transfer coefficient is expected. The energy consumption on the liquid-vapor interface leads also to the third issue: higher shear stress implies higher velocity gradient and thus higher temperature gradient in the thermal boundary layer. While the first issue, associated to the saturation temperature drop, penalizes the total heat transfer rate, the other issues are associated with enhanced condensation heat transfer coefficient.
In any case, it is crucial to have reliable pressure drop prediction methods for the modeling and design optimization of the heat exchanger with refrigerants flowing in two-phase regime.
Two-phase total pressure drop is the sum of four components (equation (2-I)) which are in order the frictional term, the momentum term due to change in vapor fraction along the channel, the static term related to the gravity forces and the local term due to abrupt geometry variation in the tube.

$$\Delta p_{total} = \Delta p_{frictional} + \Delta p_{momentum} + \Delta p_{static} + \Delta p_{local} \quad \textbf{(2-I)}$$

With adiabatic flow inside horizontal channels without any geometry variation, the total two-phase pressure drop is expressed by only by the frictional term, as the variation of vapor quality due to the pressure losses in an isenthalpic process can be reasonably neglected in practice. The goal of the present chapter is the investigation on frictional pressure losses inside horizontal minichannels during two-phase flow of different refrigerants and new test sections has been realized for this purpose. Two circular minichannels obtained from a 8 mm thick copper rod have been used for the present analysis: the first has an inner diameter equal to 0.96 mm and an average inner surface roughness *Ra* equal to 1.3 μm while the second has a 2.0 mm internal diameter and an average wall roughness *Ra* of 1.7 μm. The peculiarity of these minichannels regards the pressure ports, which have been soldered directly on the copper rod without perturbing the channel geometry, the refrigerant flow and the experimental measurements. Pressure drop investigations have been performed during adiabatic two-phase flow of R134a, R1234ze(E) and propane at different mass velocities and saturation temperatures. R134a is a widely used refrigerant and many research works focused on its thermal characterization in minichannels. Hence, R134a has been chosen among the tested fluids

in order to compare the data obtained in the new test sections against the values calculated using several models available in the open literature and validated against this hydrofluorocarbon. On the other hand, very few data in the open literature concern the investigation of frictional pressure drop inside tubes for R1234ze(E) and propane.
As the interest on the use if these two refrigerants is growing because of their low global warming potential, the data presented in this work assume a great importance for the characterization of their thermal performance.
Zhang and Webb [3] performed single-phase and two-phase pressure drop measurements during adiabatic flow of R134a, R22 and R404A in a multiport extruded tube with an hydraulic diameter equal to 2.13 mm and in two single copper channels having internal diameter of 3.25 mm and 6.25 mm. During the tests, the mass velocity varied between 200 kg m^{-2} s^{-1} and 1000 kg m^{-2} s^{-1} while the saturation temperature range was between 20°C and 65°C.
Garimella *et al.* [5] measured the pressure drop of R134a in six noncircular channels with hydraulic diameter from 0.42 mm to 0.84 mm and different cross section shape: square, rectangular, triangular, barrel-shaped, W-shaped and N-shaped. The saturation temperature for all the test runs was around 52.3°C and the mass fluxes were between 150 kg m^{-2} s^{-1} and 750 kg m^{-2} s^{-1}. Considering the experimental points at vapor qualities lower than 0.25, a model for two-phase pressure drop in the intermittent flow regime of condensing R134a has been developed.
In another work by Garimella and coworkers [6], pressure drop experimental investigation with refrigerant R134a has been done in three extruded multiport tubes with parallel circular channels and in two single circular tubes ranging in hydraulic diameter from 0.5 mm and 4.91 mm at mass velocities between 150 kg m^{-2} s^{-1} and 750 kg m^{-2} s^{-1} and at a saturation temperature of 52.3°C. The collected database was employed to develop a multiple flow-regime model for pressure drop during the condensation of R134a.
Cavallini *et al.* [7]. measured pressure drop during adiabatic flow of R134a, R236fa and R410A at 40°C saturation temperature inside a multiport minichannel having square cross section with an hydraulic diameter of 1.4 mm. The average roughness of the internal wall *Ra* was 0.08 μm. During the tests, mass velocity varied from 200 kg m^{-2} s^{-1} to 1400 kg m^{-2} s^{-1}. The three refrigerants were chosen because they present a wide range of reduced pressure at test conditions. In fact, at 40°C, the reduced pressure of R236fa is around 0.1; it is 0.25 for R134a and 0.5 for R410A.
In the work by Revellin and Thome [8], 2210 experimental two-phase frictional pressure drop data were taken in two glass minichannels during the adiabatic flow of R134a and R245fa for a wide range of test conditions. The hydraulic diameters were equal to 0.509 mm and 0.790 mm, the mass flux ranged within 210 kg m^{-2} s^{-1} and 2094 kg m^{-2} s^{-1} and saturation temperatures of 26°C, 30°C and 35°C were considered. The authors proved that, similarly to the classic Moody diagram in single-phase flow, when plotting the two-phase friction factor versus the two-phase Reynolds number, three zones can be distinguishes: the laminar zone, the transition zone and the turbulent zone.
Pressure drop experimental data for R1234ze(E) are reported only for macrochannels.
Hossain *et al.* [9] performed an experimental study on condensation heat transfer and pressure drop for R1234ze(E), R32 and R410A in a horizontal smooth copper macrochannel with an inner diameter of 4.35 mm. The mass velocity ranged from 150 kg m^{-2} s^{-1} to 400 kg m^{-2} s^{-1} and the saturation temperature was between 35°C and 45°C. From the comparison among the considered refrigerants, the average pressure gradient of R1234ze(E) resulted to be the highest because this halogenated olefin is a low pressure and high viscosity refrigerant as compared to the other fluids tested in this work.

Grauso *et al.* [10] reported experimental results for heat transfer coefficients and pressure drops during evaporation of R1234ze(E) and R134a inside a 6 mm internal diameter channel. Moreover, flow patterns have been investigated using a high speed camera arranged on a glass tube located at the exit of the test section. The mass velocity has been varied from 146 kg m^{-2} s^{-1} to 520 kg m^{-2} s^{-1} and the saturation temperature from -2.9°C to 12.1°C. The frictional pressure drops of R1234ze(E) resulted to be higher than those obtained for R134a. An assessment of predicting methods both for flow boiling heat transfer coefficients and frictional pressure drops has also been presented.
With respect to propane, very few studies on two-phase pressure drop are available in the open literature.
A rectangular channel with a hydraulic diameter equal to 0.148 mm has been tested with four refrigerants: R134a, R410A, propane and ammonia by Field and Hrnjak [11]. The authors reported the two-phase frictional pressure drop at mass velocity spanning between 300 kg m^{-2} s^{-1} and 700 kg m^{-2} s^{-1} at a saturation temperature around 25°C.
Choi *et al.* [12] examined the two-phase flow boiling pressure drop and heat transfer for propane in horizontal minichannels with inner diameters of 1.5 mm and 3.0 mm. The pressure drops were obtained for mass fluxes ranging between 50 kg m^{-2} s^{-1} and 400 kg m^{-2} s^{-1} and saturation temperatures of 10°C, 5°C and 0°C. They also developed new correlations for pressure drop and boiling heat transfer coefficients.
Maqbool *et al.* [13] investigated the frictional pressure drop during two-phase flow of propane inside a vertical circular minichannel with an internal diameter equal to 1.7 mm and a rough inner surface. Experiments have been carried out at saturation temperatures of 23°C, 33°C and 43°C while the mass flux ranged between 100 kg m^{-2} s^{-1} and 500 kg m^{-2} s^{-1}. The results showed that the two-phase frictional pressure drops increased with mass velocity, vapor qualities and with the decrease of the saturation temperature.

2.3 Experimental apparatus

The pressure drop test section is located in the test facility schematized in Figure 2.1. It includes a primary refrigerant loop which underwent several washing cycles to remove all possible contaminants before filling it with the tested refrigerant. A washing cycle consists of creating a vacuum followed by pressurization with nitrogen and new vacuum. In the primary loop, after exiting the test section, the refrigerant is subcooled in a post-condenser. In the auxiliary loop of the post-condenser, brine flows at a temperature of 5°C, which is kept constant by a dedicated thermal bath. The refrigerant is then dried up before entering an independently controlled gear micropump magnetically coupled to a variable speed electric motor. The micropump is used to set the mass flow rate measured by a Coriolis effect mass flow meter. Hence, the tested fluid passes through a mechanical filter and then it can be sent directly to the test section or to the evaporator. The refrigerant passes through the evaporator and enters the test section as superheated vapor to get experimental data in the vapor quality range 0.5-1 while it enters as subcooled liquid to collect points at vapor quality below 0.5. The evaporator consists of a tube-in-tube heat exchanger where the tested fluid is heated and vaporized using hot water flowing in a closed auxiliary loop with PID-controlled electrical heaters used to set the inlet temperature.
The test section for frictional pressure drop measurements in two-phase adiabatic regime is placed in horizontal and includes two sectors: an inlet condition setter where the desired thermodynamic inlet conditions of the refrigerant are achieved before entering the actual measuring section. The inlet condition setter is connected to the rest of the test rig and to the measuring section through stainless steel tubes. On the capillary stainless steel

tube at the intake of the inlet condition setter, a pressure port and a temperature sensor pocket are located: the state variables there measured give the thermodynamic state of the refrigerant at the inlet of the test section.
The inlet condition setter is a mini shell-and-tube counter-current heat exchanger and its purpose is to achieve the desired saturated thermodynamic state of the refrigerant at the inlet of the measuring section by setting the inlet temperature and the mass flow rate of a secondary flow of distilled water. The secondary fluid is supplied by a dedicated thermal bath through an hydraulic loop provided with a flow regulating valve and a Coriolis effect mass flow meter. The water outlet temperature in the inlet condition setter is measured by a thermocouple and the water temperature difference between inlet and outlet is measured by a copper constantan triple-junction thermopile. Static mixers have been positioned upstream of the water temperature sensors and therefore the measured temperatures can be considered as the mean effective temperatures. The refrigerant vapor quality at the inlet of the measuring section is obtained from the energy balance in the inlet condition setter.
The measuring section is made from a 8 mm copper rod with a circular internal bore and it connected to the rest of the test rig through adiabatic stainless steel capillary tubes. Furthermore, it includes two pressure ports directly soldered on the copper channel. The design of the stainless steel pressure ports has been carefully realized in order to avoid any geometry change in the cross section of the minichannel and any variation of the refrigerant flow. Thus, the copper channel was predrilled with holes of 0.5 mm for the pressure ports accommodation. To avoid melted material from obstructing the flow passage and to reduce oxidation of the tube, soldering was performed at constant nitrogen flow within the minichannel and on the external side. Furthermore, the two pressure ports have been located at a distance equal to 50 times the hydraulic diameter from the inlet and the outlet of the minichannel, in order to be out of the developing flow length. Other details on the realization of the measuring section can be found in [14]. The distance between the pressure ports represent the actual length of the measuring sector.
The pressure port close to the inlet of the measuring section is connected to a digital strain gauge relative pressure transducer, whereas a differential pressure transducer is employed to measure pressure drop along the measuring section. Two thermocouples are placed upstream and downstream of the measuring section, on the external surface of the stainless steel capillary tubes and the recorded values are checked against the gauged pressure to verify the agreement with the saturation temperature.
Two different measuring sections have been employed during the test campaign: in the first one, the internal diameter is equal to 0.96 mm, the inner surface roughness *Ra* is equal to 1.3 µm and the distance between the pressure ports is 220 mm. The second measuring section has an internal diameter of 2 mm, the inner surface roughness *Ra* is 1.7 µm and the pressure ports have been realized at a distance equal to 440 mm. The roughness measurement has been performed following the EN ISO 4287 standard [15] with the digital surface roughness machine ZEISS-TSK Surfcom 1400A.
The entire test section has been insulated to the external environment in order to minimize the heat losses.
All the temperatures are detected using T-type thermocouples. In every test run, when the apparatus is working in steady state conditions, measurements of thermo-fluid-dynamic parameters are recorded for 50 s with a time step of 1 s. Each recording is averaged and then reduced by calculating the fluid properties with NIST Refprop Version 9.0 [16].

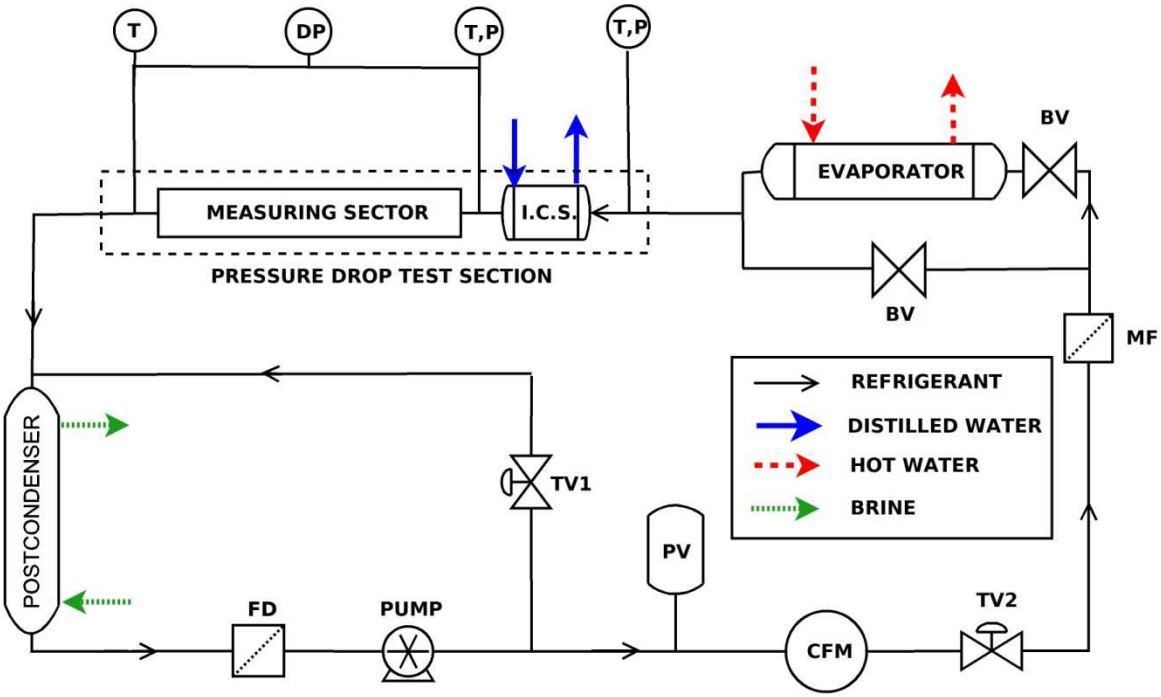

Figure 2.1. Experimental test rig: I.C.S. (inlet condition setter); FD (filter drier); PV (pressure vessel); CFM (Coriolis-effect mass flow meter); TV (throttling valve); MF (mechanical filter); BV (ball valve); P (relative pressure transducer); DP (differential pressure transducer); T (thermocouple).

2.4 Data reduction and experimental uncertainty

The pressure drop along the test section is directly measured. The results will be presented in terms of pressure drop gradient, that is to say that the measured pressure drop is divided by the length of the minichannel between the pressure ports. The uncertainty of the measured length of the test section has been neglected. For each experimental point, the thermodynamic vapor quality is calculated using equation (2-II)

$$x = \frac{h_{in,MS} - h_L}{h_{LV}} \qquad \textbf{(2-II)}$$

where h_L and h_{LV} are respectively the specific enthalpy of saturated liquid and the latent heat of vaporization at the mean pressure in the measuring section and $h_{in,MS}$ is the specific enthalpy of the refrigerant at the inlet of the measuring section and it results from the energy balance in the inlet condition setter, according to Equation (2-III):

$$h_{in,MS} = h_{in,ICS} - \frac{\dot{m}_{wat}\, c_{p,wat}\, \Delta t_{wat,ICS}}{\dot{m}_{ref}} \qquad \textbf{(2-III)}$$

The specific enthalpy of the refrigerant entering the inlet condition setter $h_{in,ICS}$ is calculated from the local measurements of temperature and pressure; the isobaric specific heat $c_{p,wat}$ is referred to the mean water temperature inside the inlet condition setter.
It has been estimated that, considering a perfectly adiabatic flow and the present working conditions, the pressure drop along the measuring section leads to a maximum variation

of the vapor quality lower than 0.02. Thus, vapor quality can be reasonably considered as a constant.
When performing test runs with vapor quality lower than 0.5, the refrigerant enters the inlet condition setter with a subcooling of 17°C - 35°C, therefore in the little tube-and-shell heat exchanger a partial vaporization occurs. On the other hand, to get experimental points with vapor quality higher than 0.5, the fluid enters the inlet condition setter with a superheating of 5°C - 20°C and a partial condensation occurs. As a consequence of the present experimental technique, the difference between the mean water temperature in the inlet condition setter and the saturation temperature at the inlet of the measuring section ranges from -15°C to +15°C.
The experimental uncertainty of a measured parameter θ, as the frictional pressure drop, is made up of two terms (equation (2-IV)): the Type A uncertainty that arises from repeated observations and the Type B uncertainty that results from calibration of instruments and manufacturers' specifications.

$$u_C = \sqrt{u_A(\theta)^2 + u_B(\theta)^2} \quad \textbf{(2-IV)}$$

Type B experimental uncertainties of the measured parameters are reported in Table 2-a, considering a level of confidence equal to 95.45% if not otherwise specified. In the present work, each experimental measurement is taken as the mean value of n = 50 readings with a step time of 1 s. In the case of a measured parameter, Type A uncertainty is given according to the ISO Guide to the Expression of Uncertainty in Measurement [17] as the experimental standard deviation of the mean:

$$u_A(\theta) = \frac{s(\theta)}{\sqrt{n}} \quad \textbf{(2-V)}$$

where n is the number of readings and s is the standard deviation of the measured parameter.
The vapor quality is not directly measured instead. When a searched parameter ξ is not directly measured but it can be expressed as a function F of uncorrelated measured input quantities θ_1, θ_2, …, θ_N, its combined standard uncertainty is determined from equation (2-VI).

$$u_C(\xi) = \sqrt{\sum_{i=1}^{N} \left(\frac{\partial F}{\partial \theta_i}\right)^2 u_C(\theta_i)^2} \quad \textbf{(2-VI)}$$

According to equations (2-II) and (2-III), the standard combined uncertainty of the vapor quality is :

$$u_C(x) = \sqrt{\left(\frac{\partial x}{\partial \dot{m}_{wat}}\right)^2 u_C(\dot{m}_{wat})^2 + \left(\frac{\partial x}{\partial \dot{m}_{ref}}\right)^2 u_C\left(\dot{m}_{ref}\right)^2 + \left(\frac{\partial x}{\partial \Delta t_{wat,ICS}}\right)^2 u_C\left(\Delta t_{wat,ICS}\right)^2} \quad \textbf{(2-VII)}$$

The uncertainties associated to the specific enthalpy at the inlet of test section $h_{in,ICS}$, the specific enthalpy of the saturated liquid h_L and of the latent heat of vaporization h_{LV} at the

mean pressure in the measuring section can be neglected as a consequence of the overall uncertainties of temperature and pressure transducers. The expanded uncertainty on pressure drop and vapor quality are obtained by multiplying the related combined standard uncertainty u_C by a coverage factor equal to 2, which correspond to a level of confidence of about 95.45%.

Table 2-a. Type B uncertainty of measured parameters.

Temperature	± 0.05 °C
Temperature difference (with thermopile)	± 0.03 °C
Water mass flow rate	± 0.2 % at 10 kg h^{-1}
Refrigerant mass flow rate	± 0.2 % at 2 kg h^{-1}
Absolute pressure	± 5 kPa (level of confidence: 99.7%)
Pressure difference (greater than 1 kPa)	± 0.12 kPa (level of confidence: 99.7%)
Pressure difference (below 1 kPa)	± 0.1% (level con confidence 99.7%)

2.5 Calibration procedure and preliminary tests

The accuracy of the experimental measurements of frictional pressure drop during two-phase flow under adiabatic conditions has been assured by the calibration of the thermal sensors and the pressure transducers and by some preliminary tests.
Before the installation on the test section, each T-type thermocouple has been calibrated by using a water filled Dewar vessel where two high precision four wire thermistors are arranged The thermistors are connected to a Hart Scientific Super Thermometer II forming a measure chain with a global accuracy of ±0.002 °C (as from the check against the water triple point). A correction function for each thermocouple has been defined by comparing the temperature measured by the considered thermocouple against the reference temperature gauged by the thermistors and repeating the test at different values of the water temperature.
The triple junctions thermopile has been checked using two Dewar vessels and considering the disagreement between its reading and the temperature difference measured between the two vessels by the high precision thermistors. The calibration test of the thermopile has been repeated several times, varying the temperature difference between the fluids in the two Dewar vessels.
After the calibration, the Type B experimental uncertainty of the thermocouples is ±0.05 °C and that of the thermopile is ±0.02 °C. with a level of confidence of 95.45%.
The thermocouples and the thermopile have been installed in the test section without perturbing their physical, electrical and thermal properties.
The calibration of the relative pressure transducers has been done by connecting them with a pressure calibrator and comparing the static pressure reading of the calibrator against the readings obtained by the measure chain composed by the pressure transducer and the acquisition data system. The disagreement was found within the experimental range of the instruments. With respect to the differential pressure transducer with a full scale of 100 kPa, the calibration has been performed by connecting the high pressure port to the calibrator and the low pressure port to the ambient air. The ambient air pressure was gauged by a mercury barometer. Even in this case, the difference between the readings of the calibrator and those of the measure chain formed by the differential pressure transducer and the acquisition system was within the experimental uncertainty of the instrument. The calibrator has a full scale value of 20 bar and an accuracy of ±0.025%

of the reading between 3% and 100% of full scale and within ±0.15 mbar below 3% of full scale.
The teat apparatus has also been checked by comparing the temperature reading of the thermocouple at the inlet of the measuring section during two-phase flow and the saturation temperature calculated by the pressure measurement at practically the same position. The disagreement between the two values resulted lower than 0.2°C and it is ascribable to the uncertainty of the two instruments.
Since the present experimental technique requires to assure the accuracy of the energy balance in the inlet condition setter and the adiabaticy of the measuring section, prior to any two-phase pressure drop measurements, some tests have been performed to evaluate the heat losses in the test section. Before filling the test rig with refrigerant, the heat losses of the inlet condition setter towards the external environment have been assessed making a vacuum on the refrigerant side and sending water in the shell at an average temperature of 25°C, 40°C and 55°C. Independently of the water mean temperature, the reading of the thermopile has found to be within ± 0.03°C and the heat dissipation rate has been found to be repeatably around 0.5 W in the test range of the water mass flow rate. Hence, the measured heat losses in the inlet condition setter could result from the experimental uncertainty of the thermopile and can be neglected.
Moreover, the energy balance in inlet condition setter was checked by comparing the water side heat transfer rate to the one determined on the refrigerant side during condensation from superheated vapor to subcooled liquid and during vaporization from subcooled liquid to superheated vapor. The overall thermal balance was found to be within 3%.
Since the minimum heat flow rate exchanged inside the inlet condition setter is around 4 W, some additional preliminary tests under single-phase flow have been performed to assess the energy balance at low heat flow rates. It has been noted that under 15 W, the disagreement between the heat flow rate on the water side and the heat flow rate on the refrigerant side is within 0.5 W. This can be probably due to the experimental uncertainties of the measured parameters. Nevertheless, at the lowest refrigerant mass flow rate considered during the test runs, such disagreement can cause a variation of the vapor quality within ±0.02, that is within the experimental uncertainty.
Finally, in the temperature and mass velocity ranges of the present pressure drop test runs, heat losses between the measuring section and the external environment have been examined in both the tested minichannels during single-phase flow of the refrigerant. It was found that this dissipation affects the vapor quality within ±0.007, so can be reasonably neglected.
Furthermore, in order to validate the data acquisition and to gain a critical insight into the test section hydraulic performance, the friction factor has been experimentally determined from pressure drop, temperature and mass flow measurements during adiabatic single-phase flow of each tested refrigerant in the both of the circular minichannels under investigation, according to equation (2-VIII).

$$f = \frac{\rho \, d_h \, \Delta p}{2 \, G^2 \, L_{MS}} \qquad \textbf{(2-VIII)}$$

In Figure 2.2, plots of the friction factor against the Reynolds number obtained during single-phase flow of all the tested refrigerants are presented for both the circular minichannel with 0.96 mm internal diameter and the circular minichannel with 2.0 mm internal diameter.

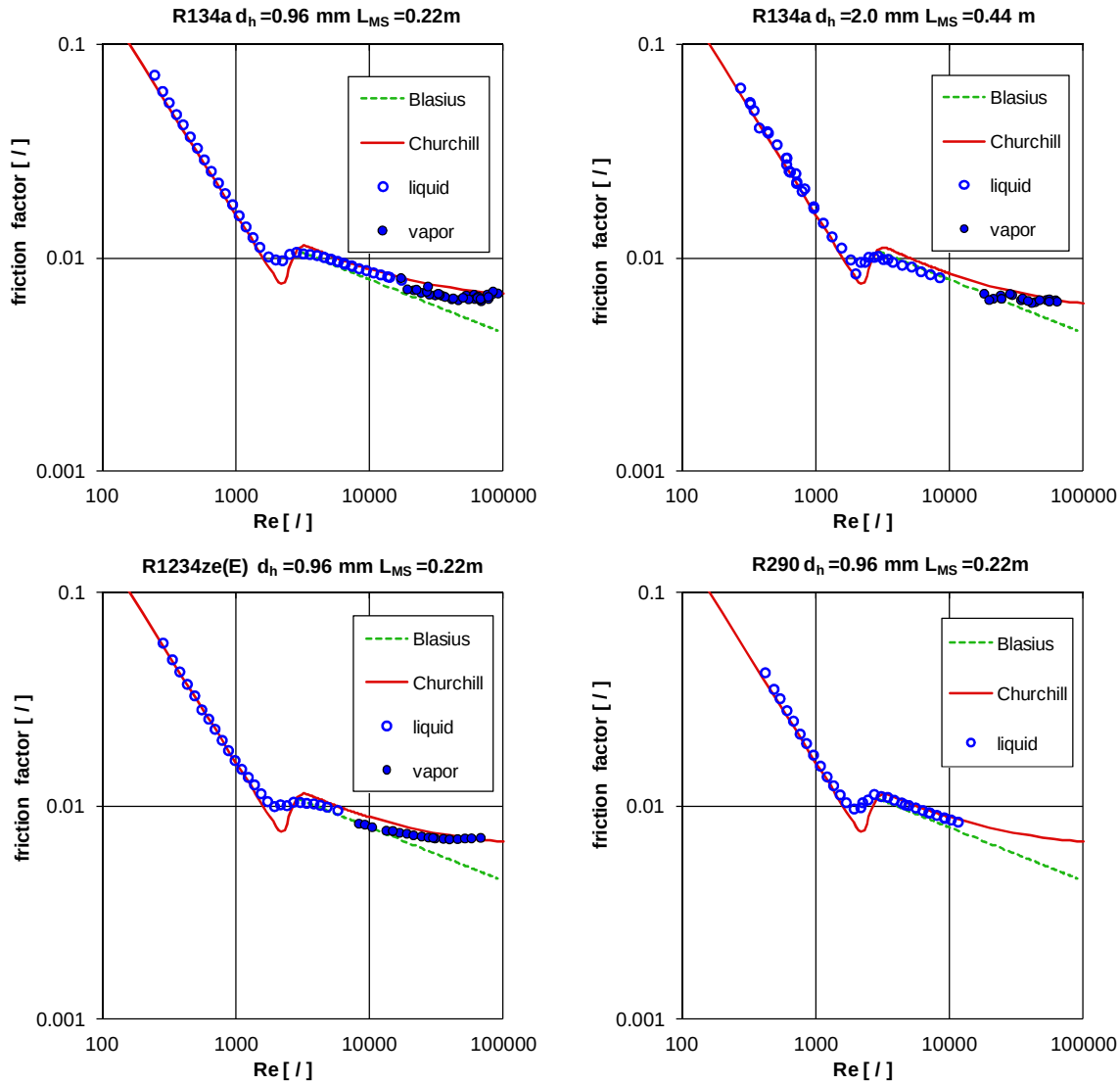

Figure 2.2. Experimental and predicted friction factor versus Reynolds number (Re) during single-phase flow. Top: Left) R134a inside the circular minichannel with 0.96 mm internal diameter; Right) R134a inside the circular minichannel with 2.0 mm internal diameter; Bottom: Left) R1234ze(E) inside the circular minichannel with 0.96 mm internal diameter; Right) Propane (R290) inside the circular minichannel with 0.96 mm internal diameter

In each plot, different symbols are used to distinguish the experimental friction factor obtained during liquid only flow and during vapor only flow. The collected experimental data are compared against the Churchill [18] correlation, which accounts for the minichannel roughness and the agreement comes out to be very good. The relative roughness of the tube ε/d_h in the correlation by Churchill [18] is considered equal to $2Ra/d_h$. Blasius [19] equation for turbulent flow is also plotted: it refers to smooth tubes thus it remains below the experimental points.

2.6 Experimental results and discussion

Frictional pressure drop experimental measurements have been performed during two-phase flow of R134a, R1234ze(E) and propane under adiabatic conditions at different saturation temperatures and mass velocities inside two circular minichannels having internal diameters of 0.96 mm and 2.0 mm, respectively. The experimental conditions

adopted during pressure drop tests for each tested refrigerant have been summed up in Table 2-b.
It may be interesting to mention that at vapor quality around 0.5, the experimental data taken following the two methods (condensation from superheated vapor in the inlet condition setter or vaporization from subcooled liquid) are in good agreement in all the presented data sets, whatever the tested minichannel, the fluid, the mass velocity and the saturation temperature.

Table 2-b. Pressure drop test conditions matrix.

Refrigerant	d_h	Ra	L_{MS}	t_{sat}	G[kg m^{-2} s^{-1}]
R134a	0.96 mm	1.3 μm	0.22 m	40°C	800, 600, 500, 400, 300, 200
				50°C	400
	2.0 mm	1.7 μm	0.44 m	40°C	500, 400, 300, 200
				50°C	400
R1234ze(E)	0.96 mm	1.3 μm	0.22 m	30°C	400
				40°C	800, 600, 400, 200
Propane	0.96 mm	1.3 μm	0.22 m	40°C	800, 600, 400, 200

The experimental data collected for every single fluid have been compared against four two-phase frictional pressure drop models available in the open literature and listed below in chronological order.
The first model has been proposed by Friedel [1] incorporating the most important parameters of the two-phase flow as well as the theoretical boundaries of single-phase liquid and gas-vapor flow and critical pressure conditions in pure fluids. The model has been developed starting from a huge database of 25000 experimental points collected during the two-phase adiabatic flow of several pure fluid and two component mixtures in straight tubes with circular, rectangular and annular cross sections. Horizontal flow, vertical upward flow and vertical downflow points were included in the database. The smallest tube hydraulic diameter in Friedel's database is equal to 1 mm, but most of the data have been taken in macrochannels.
The second model considered for the comparison against the experimental data is by Muller-Steinhagen and Heck [2]. It was developed using a database of 9300 measurements of frictional pressure drop for many fluids in horizontal flow, vertical upflow and vertical downflow. The range of the considered hydraulic diameters is from 4 mm to 392 mm. The proposed correlation is very simple: in fact, it is a combination of the single-phase liquid and vapor pressure drops and differently from the Friedel model, no two-phase multiplier is defined.
The third correlation has been advanced by Zhang and Webb [3] considering a database of two-phase pressure drop measured for R134a, R22 and R404A flowing in channels with hydraulic diameters from 0.96 mm to 6.20 mm. They found that the Friedel correlation was not able to predict the experimental data accurately so they proposed a modified Friedel correlation to evaluate specifically the refrigerant two-phase pressure drop in minichannels. In particular, they suggested to replace the dimensionless group of density and viscosity with the reduced pressure and to neglect the Froude number and the Weber number.
Finally, the present pressure drop data have been checked against the model by Del Col *et al.* [4]. It is an updating of the Cavallini *et al.* [20] correlation, which in turn is based on the Friedel model and accounts for mass velocity, vapor quality, fluid properties, reduced pressure, hydraulic diameter, entrainment ratio and surface roughness. Del Col and

coworkers [4] observed that the Cavallini *et al.* [20] correlation tends to overestimate the experimental data at low liquid-only Reynolds number, with an error increasing as this dimensionless number decreases. This could be explained considering that the model by Cavallini *et al.* [20] assumes that the wall roughness has an uniform effect on the friction drop, whatever the flow characteristics.
From the theory, one would expect that the effect of the inner surface roughness on the frictional pressure drop would also depend on the working conditions: in particular it would be smaller at lower mass velocity and higher liquid phase viscosity, that is to say at lower liquid-only Reynolds number. Estimation of the liquid film thickness as provided in [4], shows that at low mass fluxes, the liquid film may completely flood the peaks of the inner surface of the channel, making the effect of the wall roughness absolutely negligible.
Thus, Del Col *et al.* [4] proposed a correlation that links the effect of the inner surface roughness on the liquid only friction factor to the mass velocity and to the properties of the refrigerant. The model has been validated against experimental pressure gradient data collected by the authors in minichannels with circular, square and irregular cross sections and with a hydraulic diameter ranging from 0.762 mm to 2 mm during the adiabatic two-phase flow of R134a, R32, R1234yf and R245fa at saturation temperature between 26°C and 50°C. Furthermore, the new correlation has been also checked against the experimental pressure gradient data for R134a by Garimella *et al.* [5] and by Zhang [21] and against the experimental points collected using carbon dioxide by Jeong *et al.* [22], Park and Hrnjak [23] [24], Kim *et al.* [25] and Ducoulombier *et al.* [26].
It is worth noting that only the model by Del Col *et al.* [4] accounts for the effect of the internal roughness of the channel.
The absolute mean deviation $|e_R|$, the average deviation e_R and the standard deviation σ_N are reported for each model to assess the predictive accuracy.
For the sake of comparison and analysis, the thermodynamic and thermophysical properties of the saturated refrigerant R134a, R1234ze(E) and propane are calculated using NIST Refprop Version 9.0 [16] and reported in Table 2-c at the corresponding operating conditions.

Table 2-c. Properties of saturated R134a, R1234ze(E) and propane from NIST Refprop Version 9.0 [16].

Refrigerant	t_{sat} [°C]	p_{sat} [bar]	p_r [/]	ρ_L [kg m^{-3}]	ρ_V [kg m^{-3}]	μ_L [μPa s]	μ_V [μPa s]	σ [mN m^{-1}]
R134a	40	10.166	0.25	1146.7	50.085	161.45	12.373	6.1268
	50	13.179	0.32	1102.3	66.272	141.77	12.917	4.8906
R1234ze(E)	30	5.7848	0.16	1146.3	30.564	188.00	12.458	8.2099
	40	7.6663	0.21	1111.3	40.687	167.00	12.930	6.9567
Propane	40	13.394	0.315	467.46	30.165	82.844	8.8918	5.2128

2.6.1 Frictional pressure drop of R134a and comparison against correlations

The investigation on the frictional pressure drop during two-phase adiabatic flow of R134a has been performed in two different minichannels in order to consider the effect of the hydraulic diameter.
In the circular minichannel with an inner diameter equal to 0.96 mm and with an average roughness *Ra* equal to 1.3 μm, the tests are performed at mass velocities ranging from 800 kg m^{-2} s^{-1} to 200 kg m^{-2} s^{-1} at 40°C saturation temperature. Furthermore, in order to

study the effect of the reduced pressure on the frictional pressure losses, at 400 kg m^{-2} s^{-1} the test runs have been done at 40°C and 50°C saturation temperatures. The experimental results are presented in order, in terms of pressure gradient against vapor quality in Figure 2.3.

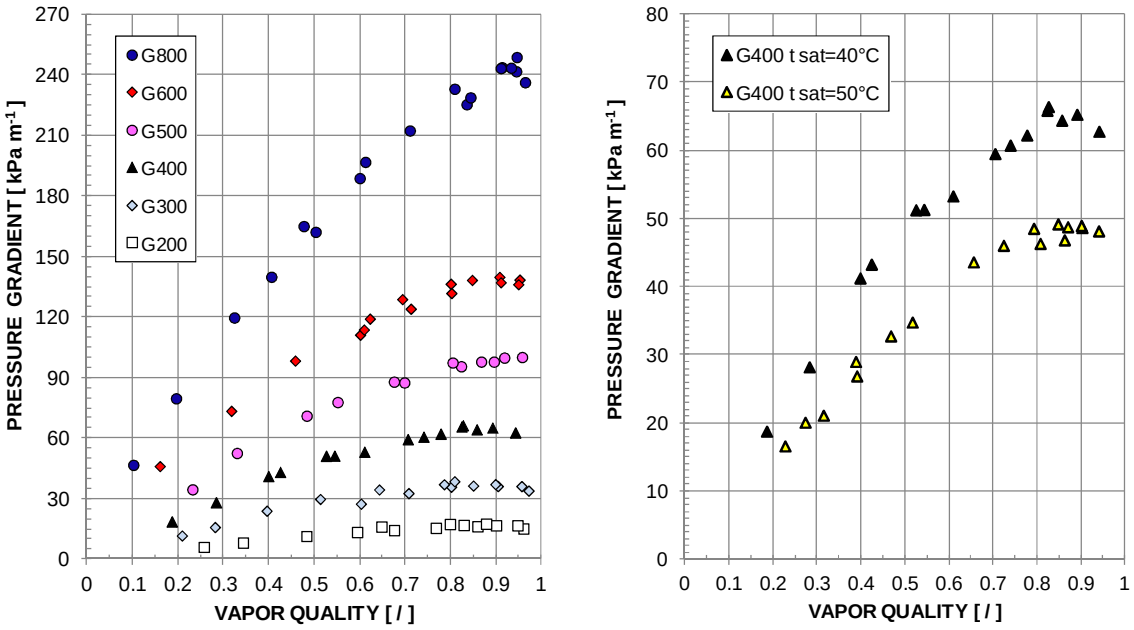

Figure 2.3. Left) Experimental frictional pressure gradient versus vapor quality during two-phase adiabatic flow of R134a inside a circular minichannel with an inner diameter equal to 0.96 mm at 40°C saturation temperature and at different mass velocities *G* [kg m^{-2} s^{-1}].
Right) Experimental frictional pressure gradient versus vapor quality during two-phase adiabatic flow of R134a inside a circular minichannel with an inner diameter equal to 0.96 mm at *G* = 400 kg m^{-2} s^{-1} and at saturation temperature of 40°C and 50°C.

Moreover, in the circular minichannel with an inner diameter of 2 mm and an average roughness of the wall surface *Ra* equal to 1.7 μm, the pressure gradient has been studied at 40°C saturation temperature and at mass velocities of 500 kg m^{-2} s^{-1}, 400 kg m^{-2} s^{-1}, 300 kg m^{-2} s^{-1} and 200 kg m^{-2} s^{-1}. At 400 kg m^{-2} s^{-1} mass velocity, tests have been also run at a saturation temperature equal to 50°C. The experimental pressure gradient are plotted against vapor quality in
Figure 2.4.
At the same mass velocity, in the same minichannel, the pressure gradient decreases with increasing saturation temperature and thus with increasing reduced pressure.
On the other hand, at the same reduced pressure and mass velocity, the pressure losses strongly decreases with increasing hydraulic diameter.
The expanded experimental uncertainties for measured parameters are reported in Table 2-dTable 2-e at all the test conditions. The experimental uncertainty of the frictional pressure gradient in percentage terms increases with decreasing mass velocity and with increasing hydraulic diameter, because of the lower measured value. The experimental uncertainty on the vapor quality increases with decreasing mass velocity and it is slightly lower when performing tests in the circular minichannel with 2.0 mm inner diameter.

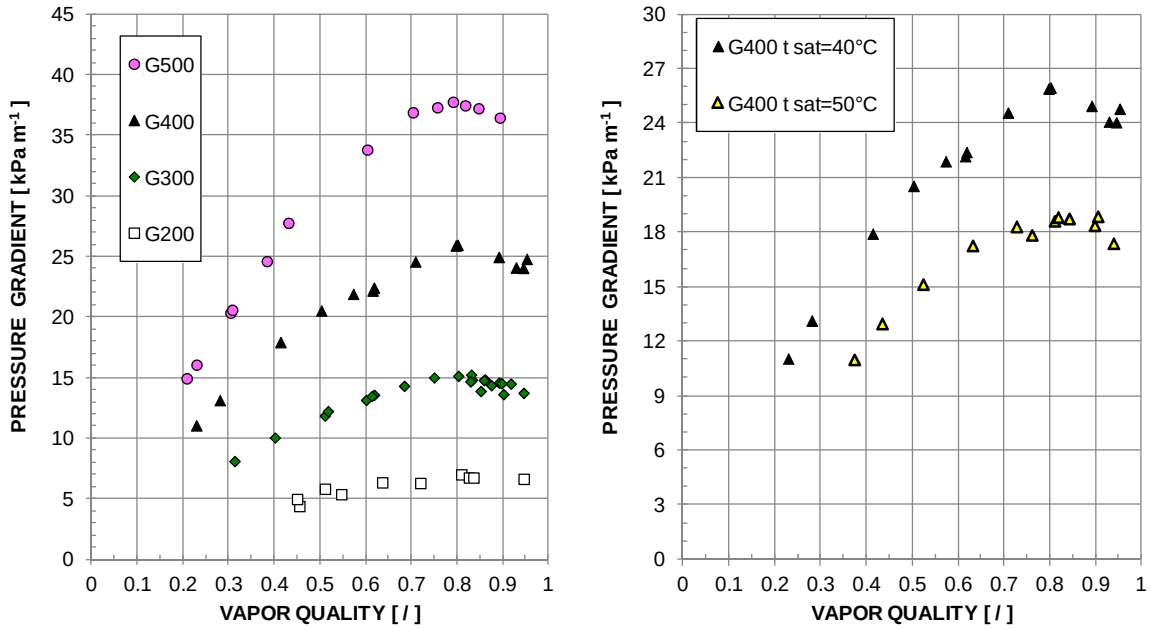

Figure 2.4. Left) Experimental frictional pressure gradient versus vapor quality during two-phase adiabatic flow of R134a inside a circular minichannel with an inner diameter equal to 2.0 mm at 40°C saturation temperature and at different mass velocities *G* [kg m^{-2} s^{-1}].
Right) Experimental frictional pressure gradient versus vapor quality during two-phase adiabatic flow of R134a inside a circular minichannel with an inner diameter of 2.0 mm at *G* = 400 kg m^{-2} s^{-1} and at saturation temperature of 40°C and 50°C.

Table 2-d. Experimental expanded uncertainty of vapor quality and two-phase pressure gradient during adiabatic flow of R134a inside the considered circular minichannels.

Hydraulic diameter	Mass velocity [kg m^{-2} s^{-1}]	Saturation temperature [°C]	Pressure gradient experimental uncertainty	Vapor quality experimental uncertainty [/]
0.96 mm	800	40	< 1.0 kPa m^{-1}	0.01
	600	40	< 0.6 kPa m^{-1}	0.01
	500	40	< 0.5 kPa m^{-1}	0.01
	400	40	< 0.5 kPa m^{-1}	0.02
	400	50	< 0.4 kPa m^{-1}	0.02
	300	40	< 0.4 kPa m^{-1}	0.02
	200	40	< 0.3 kPa m^{-1}	0.03
2.0 mm	500	40	< 0.4 kPa m^{-1}	0.01
	400	40	< 0.4 kPa m^{-1}	0.01
	400	50	< 0.4 kPa m^{-1}	0.01
	300	40	< 0.4 kPa m^{-1}	0.01
	200	40	< 0.3 kPa m^{-1}	0.01

The comparison between the experimental data and the values calculated using the considered models available in the open literature has been performed considering separately the points collected in the two measuring sections in order to assess the predictive accuracy of the correlation when varying the hydraulic diameter. On the whole, 106 experimental points have been collected in the 0.96 mm circular minichannel and 71 points have been obtained during tests in the 2.0 mm circular minichannel.

The calculated trends and the calculated values for the pressure gradient using the correlation by Friedel [1] are depicted with the experimental points obtained in the 0.96 mm minichannel in Figure 2.5. The model predicts 88.7% of the data within ± 20% band, and in particular it tends to underestimate the data at mass velocities between 500 kg m^{-2} s^{-1} and 800 kg m^{-2} s^{-1} and to overrate the points at 200 kg m^{-2} s^{-1}. The standard deviation is equal to 14%, the absolute mean deviation is 12.4% and the average deviation is -6.0%.
When considering the minichannel with 2.0 mm internal diameter (Figure 2.6), the Friedel correlation seems to work slightly better: even if the data at 500 kg m^{-2} s^{-1} and 400 kg m^{-2} s^{-1} are underpredicted, 93% of the data are predicted within ± 20% band .(σ_N = 11.5%*;* $|e_R|$ = 9.8%*;* e_R = -1.7%).
As shown in Figure 2.7 and Figure 2.8, the correlation by Muller-Steinhagen and Heck [2] underestimates most of the experimental points, exhibiting the same predicting performance, whatever the hydraulic diameter of the minichannel. In particular, in the 0.96 mm inner diameter channel, it predicts 72.6% of the data within ± 20% band and 93.4% within ± 30% band (σ_N = 10.0%*;* $|e_R|$ = 14.5%*;* e_R = -13.7%).
As regard the comparison with the experimental data obtained for the 2.0 mm diameter tube, the correlation by Muller-Steinhagen and Heck [2] catches 64.8% of the data within ± 20% band and 84.5% of points in ± 30% band (σ_N = 12.5%*;* $|e_R|$ = 14.8%*;* e_R = -13.5%).
The two-phase frictional pressure drop model by Zhang and Webb [3] underrates the most of the experimental data and present the highest average deviations (Figure 2.9 and Figure 2.10). In particular, in the minichannel with the hydraulic diameter equal to 0.96 mm, only 53.8% of the data are predicted within ± 20% band and 78.3% of the points are predicted within ± 30% band (σ_N = 11.3%*;* $|e_R|$ = 20.7%*;* e_R = -20.3%). On the other hand, with respect to the minichannel with the hydraulic diameter equal to 2.0 mm, the model predicts 56.3% of the data within ± 20% band and 87.3%within ± 30% band and gives a standard deviation of 10.9%, an absolute mean deviation of 17.4% and an average deviation of -17.0%.
Finally, the R134a experimental pressure gradient points are compared against the correlation by Del Col *et al*. [4]: the agreement is satisfactory, in fact all the data collected in the two minichannels are predicted within ± 20% band (Figure 2.11 and Figure 2.12). Nevertheless, the model tends to slightly undervalue the data at 800 kg m^{-2} s^{-1} and 600 kg m^{-2} s^{-1} in the 0.96 mm channel and the data at 500 kg m^{-2} s^{-1} and 400 kg m^{-2} s^{-1} in the 2.0 mm tube. In the smaller diameter minichannel, the model gives a standard deviation of 9.2%, an absolute mean deviation of 9.4% and an average deviation of -6.9%. In the bigger minichannel, the standard deviation is equal to 7.4%, the absolute mean deviation is 6.4% and the average deviation is -1.7%.
The saturation temperature does not affect the predictive accuracy of the models. The considered correlations predict very well the maximum of the pressure gradient in the 0.96 mm but they are not able to catch the trend in the 2.0 mm minichannel.

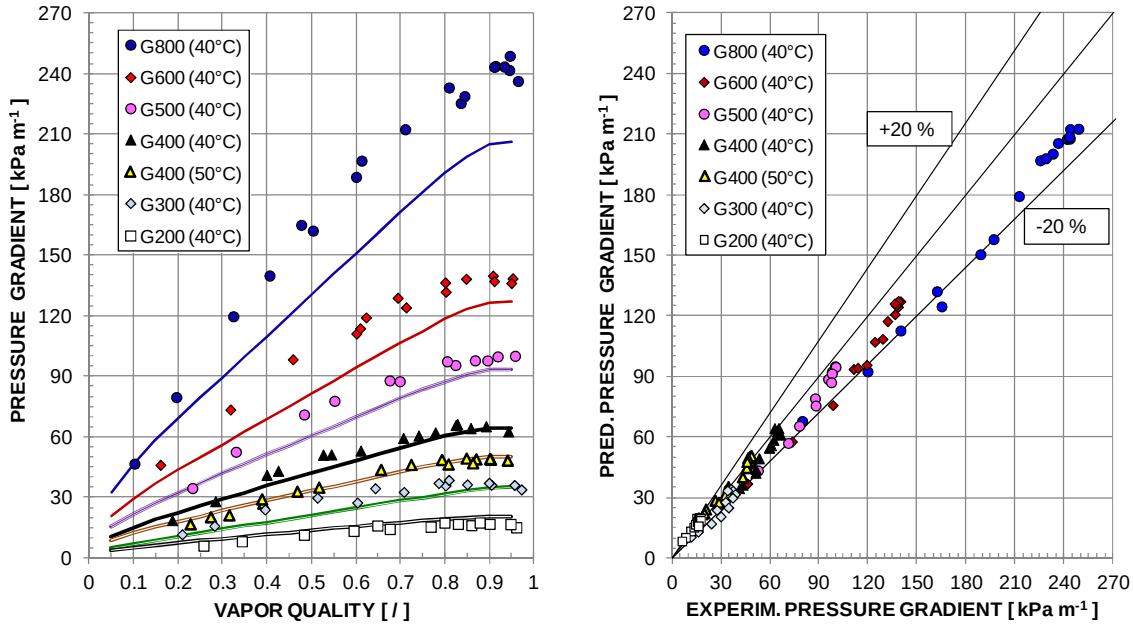

Figure 2.5. Two-phase frictional pressure gradient data during adiabatic flow of R134a inside the circular minichannel with an inner diameter of 0.96 mm at different mass velocities *G* [kg m^{-2} s^{-1}] and saturation temperatures compared against the model by Friedel [1]. Left) Experimental pressure gradient and calculated trends (solid lines) by Friedel model [1]. Right) Comparison between measured frictional pressure gradient and calculated values using the Friedel model [1].

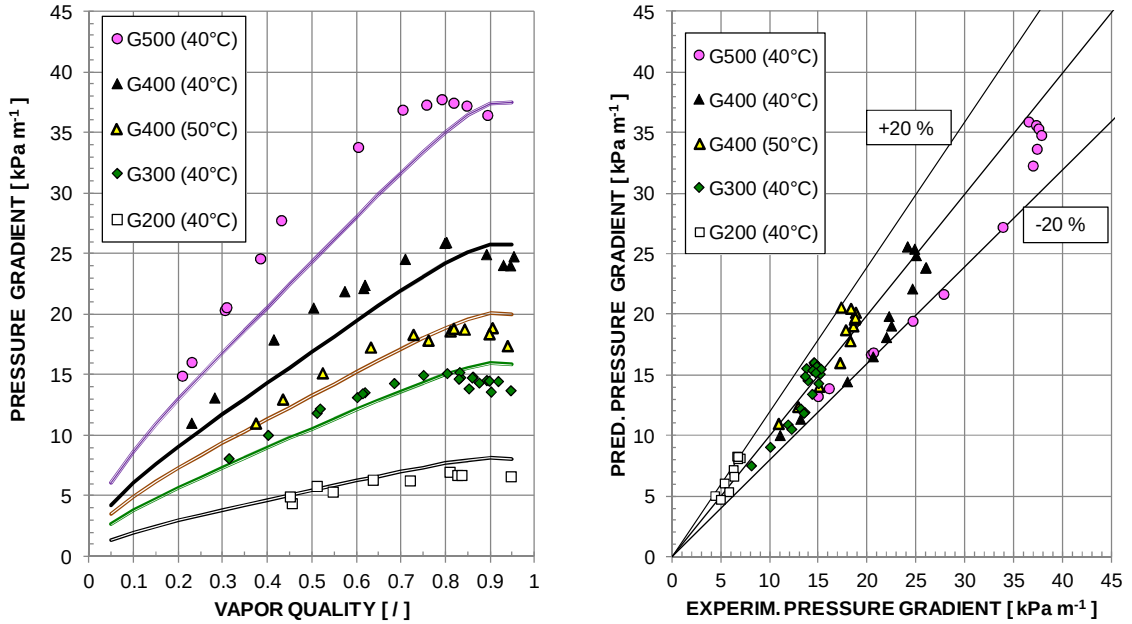

Figure 2.6. Two-phase frictional pressure gradient data during adiabatic flow of R134a inside the circular minichannel with an inner diameter of 2.0 mm at different mass velocities *G* [kg m^{-2} s^{-1}] and saturation temperatures compared against the model by Friedel [1]. Left) Experimental pressure gradient and calculated trends (solid lines) by Friedel model [1]. Right) Comparison between measured frictional pressure gradient and calculated values using the Friedel model [1].

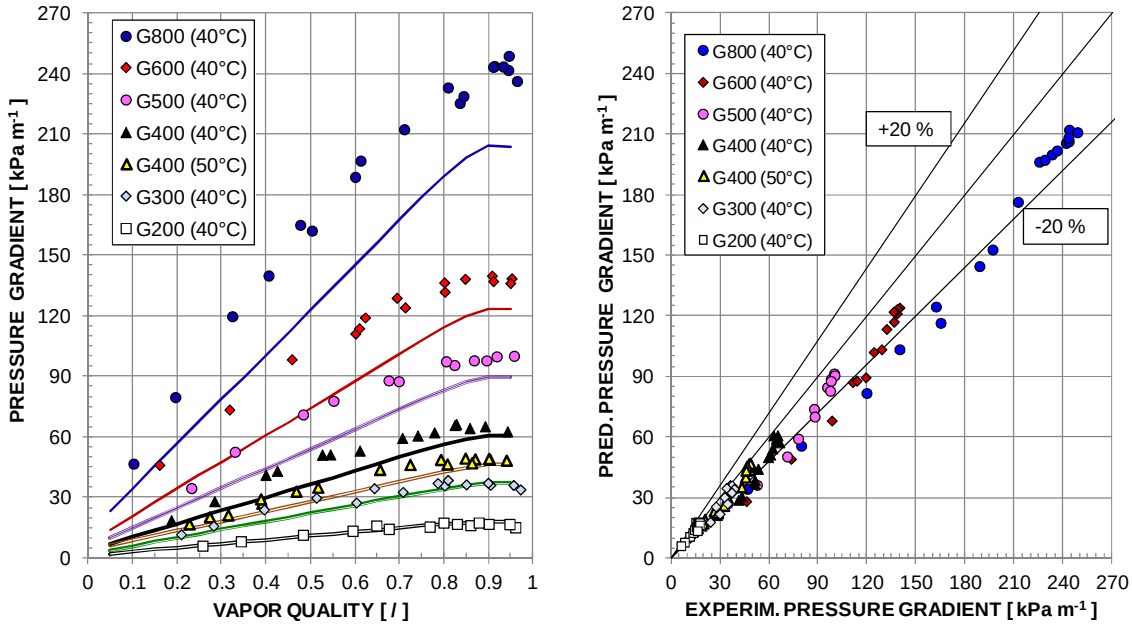

Figure 2.7. Two-phase frictional pressure gradient data during adiabatic flow of R134a inside the circular minichannel with an inner diameter of 0.96 mm at different mass velocities *G* [kg m^{-2} s^{-1}] and saturation temperatures compared against the model by Muller-Steinhagen and Heck correlation [2]. Left) Experimental pressure gradient and calculated trends (solid lines) by Muller-Steinhagen and Heck model [2]. Right) Comparison between measured frictional pressure gradient and calculated values using the Muller-Steinhagen and Heck model [2].

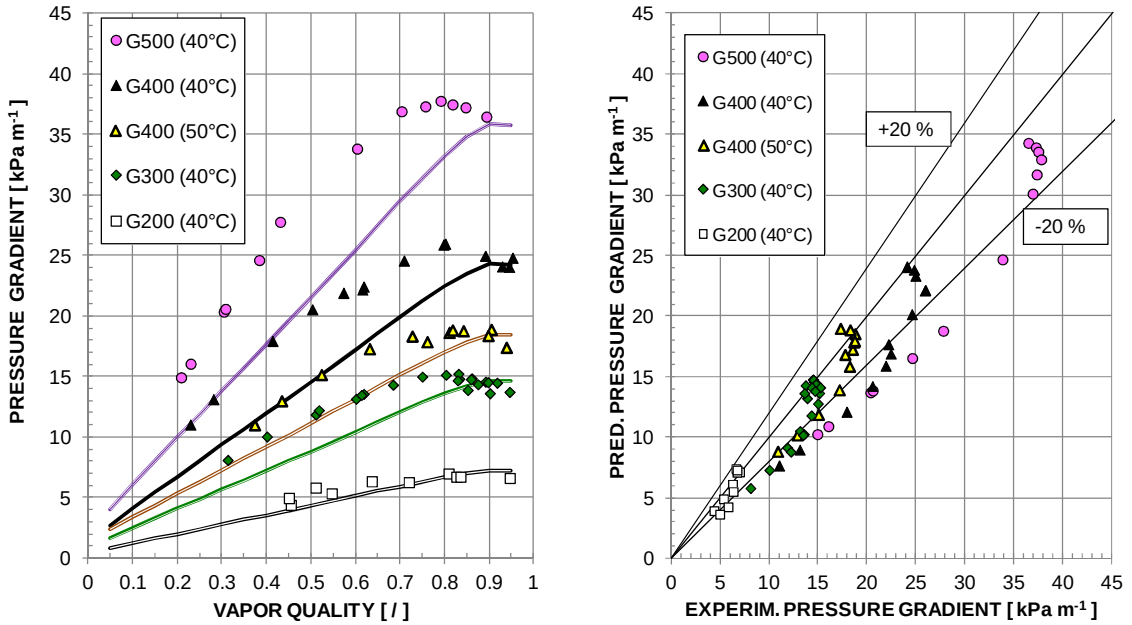

Figure 2.8. Two-phase frictional pressure gradient data during adiabatic flow of R134a inside the circular minichannel with an inner diameter of 2.0 mm at different mass velocities *G* [kg m^{-2} s^{-1}] and saturation temperatures compared against the model by Muller-Steinhagen and Heck correlation [2]. Left) Experimental pressure gradient and calculated trends (solid lines) by Muller-Steinhagen and Heck model [2]. Right) Comparison between measured frictional pressure gradient and calculated values using the Muller-Steinhagen and Heck model [2].

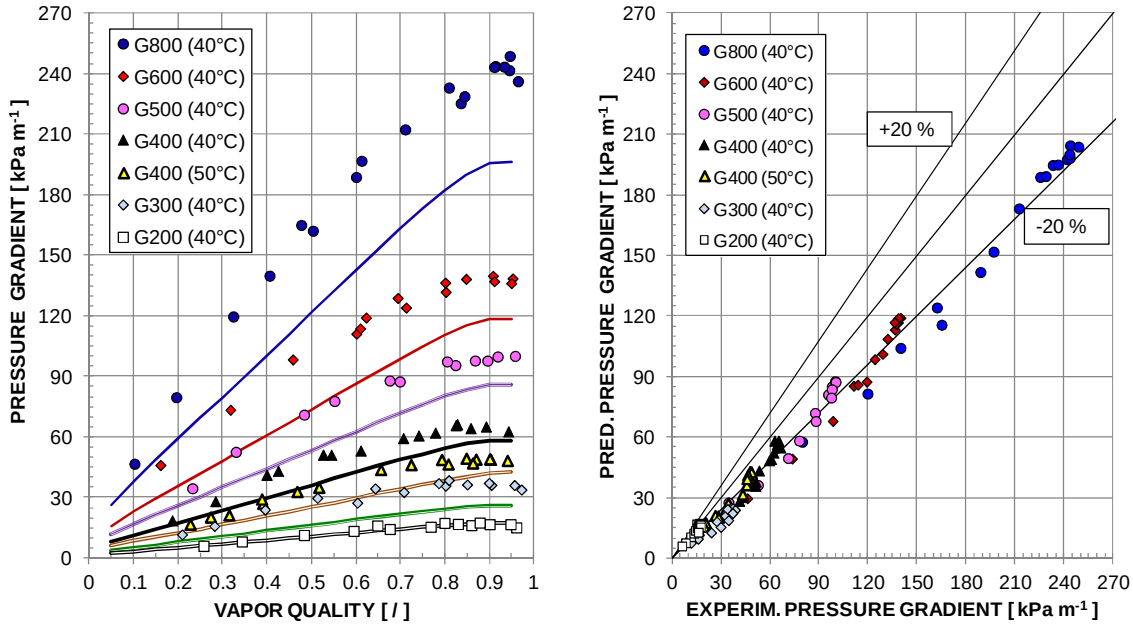

Figure 2.9. Two-phase frictional pressure gradient data during adiabatic flow of R134a inside the circular minichannel with an inner diameter of 0.96 mm at different mass velocities *G* [kg m^{-2} s^{-1}] and saturation temperatures compared against the model by Zhang and Webb [3]. Left) Experimental pressure gradient and calculated trends (solid lines) by Zhang and Webb correlation [3]. Right) Comparison between measured frictional pressure gradient and calculated values using the Zhang and Webb model [3].

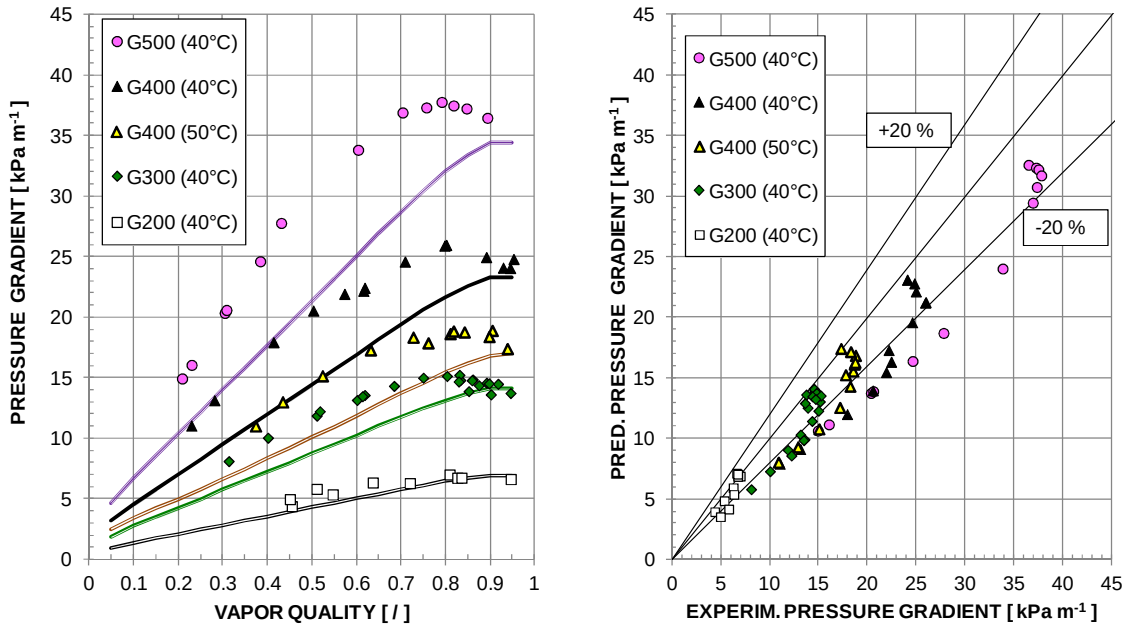

Figure 2.10. Two-phase frictional pressure gradient data during adiabatic flow of R134a inside the circular minichannel with an inner diameter of 2.0 mm at different mass velocities *G* [kg m^{-2} s^{-1}] and saturation temperatures compared against the model by Zhang and Webb [3]. Left) Experimental pressure gradient and calculated trends (solid lines) by Zhang and Webb correlation [3]. Right) Comparison between measured frictional pressure gradient and calculated values using the Zhang and Webb model [3].

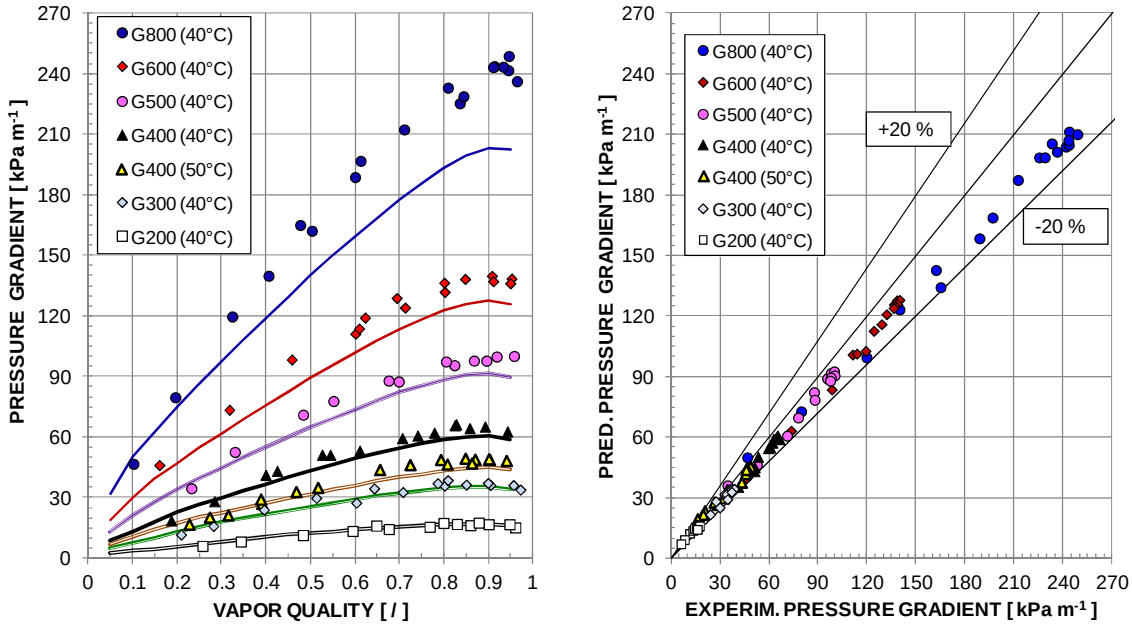

Figure 2.11. Two-phase frictional pressure gradient data during adiabatic flow of R134a inside the circular minichannel with an inner diameter of 0.96 mm at different mass velocities G [kg m^{-2} s^{-1}] and saturation temperatures compared against the model by Del Col *et al.* [4]. Left) Experimental pressure gradient and calculated trends (solid lines) by Del Col *et al.* correlation [4]. Right) Comparison between measured frictional pressure gradient and calculated values using the Del Col *et al.* model [4].

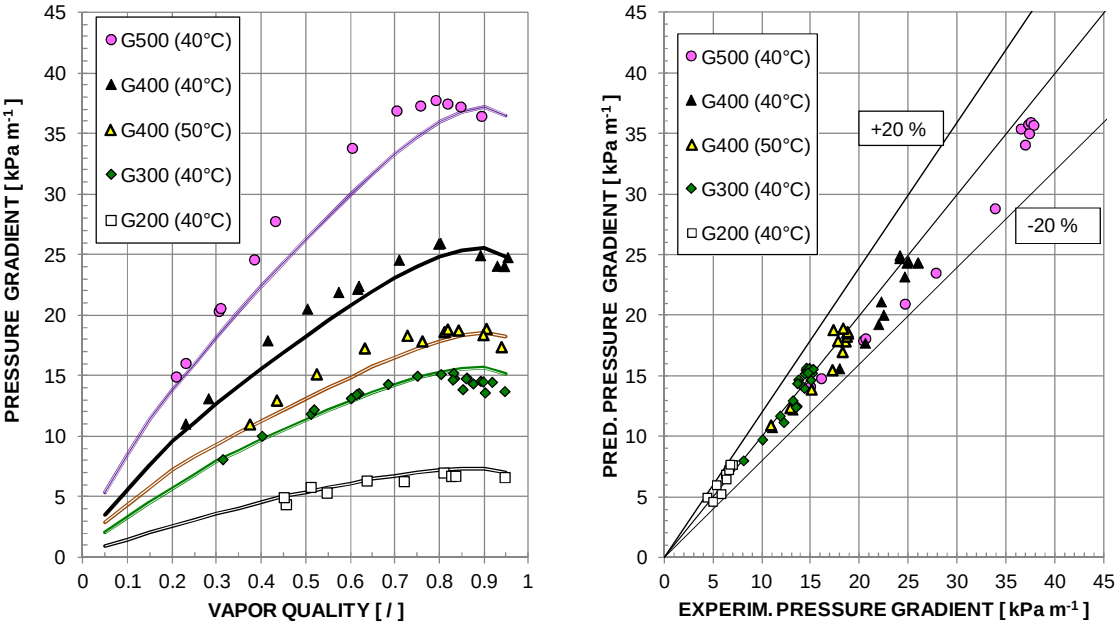

Figure 2.12. Two-phase frictional pressure gradient data during adiabatic flow of R134a inside the circular minichannel with an inner diameter of 2.0 mm at different mass velocities G [kg m^{-2} s^{-1}] and saturation temperatures compared against the model by Del Col *et al.* [4]. Left) Experimental pressure gradient and calculated trends (solid lines) by Del Col *et al.* correlation [4]. Right) Comparison between measured frictional pressure gradient and calculated values using the Del Col *et al.* model [4].

2.6.2 Frictional pressure drop of R1234ze(E) and comparison against correlations

Two-phase frictional pressure drop tests have been carried out during adiabatic flow of R1234ze(E) inside the 0.96 mm circular cross section minichannel at mass velocities ranging from 200 kg m^{-2} s^{-1} to 800 kg m^{-2} s^{-1} at saturation temperature between 39°C and 41°C. Furthermore, in order to investigate the effect of saturation temperature, pressure drop have been measured in the same test section at 400 kg m^{-2} s^{-1} at around 30°C and 40°C.

In Figure 2.13, the experimental pressure drop gradient measured at 40°C saturation temperature is plotted against vapor quality at different mass velocities.

In Figure 2.14, the comparison between the pressure gradient measured inside the circular minichannel at 400 kg m^{-2} s^{-1} mass velocity and at different saturation temperatures of 30°C and 40°C is shown. The pressure gradient decreases with increasing reduced pressure, all other working conditions being equal.

On the whole, 67 experimental points have been collected during the tests performed with R1234ze(E).

The expanded experimental uncertainties for measured parameters are reported in Table 2-e at all the test conditions: at lower mass velocities, the experimental uncertainty of the pressure gradient is higher in percentage terms. Similarly, the experimental uncertainty of the vapor quality increases with decreasing mass velocity. Finally, the saturation temperature does not affect the experimental uncertainty of the considered parameters.

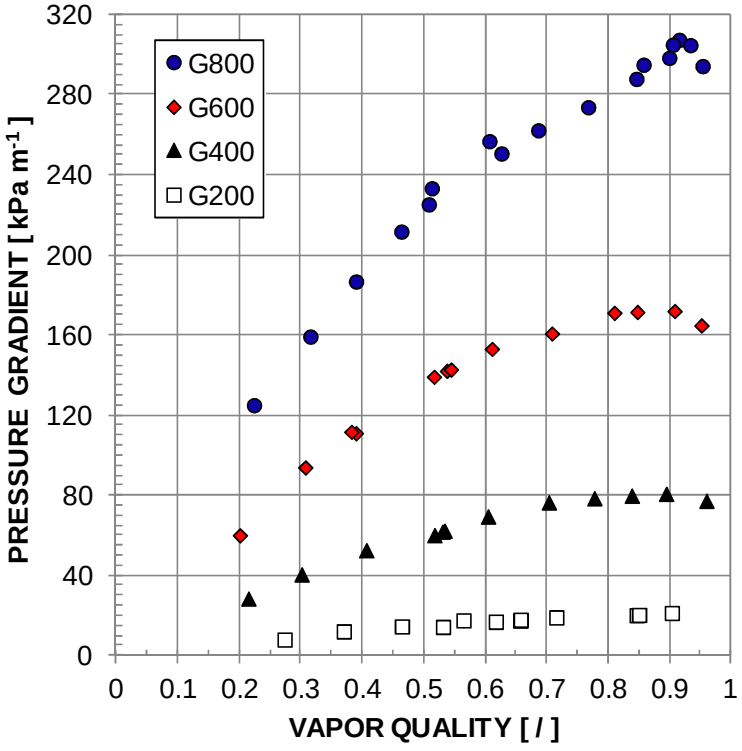

Figure 2.13. Experimental frictional pressure gradient versus vapor quality during two-phase adiabatic flow of R1234ze(E) inside a circular minichannel with an inner diameter equal to 0.96 mm at 40°C saturation temperature and at different mass velocity *G* [kg m^{-2} s^{-1}].

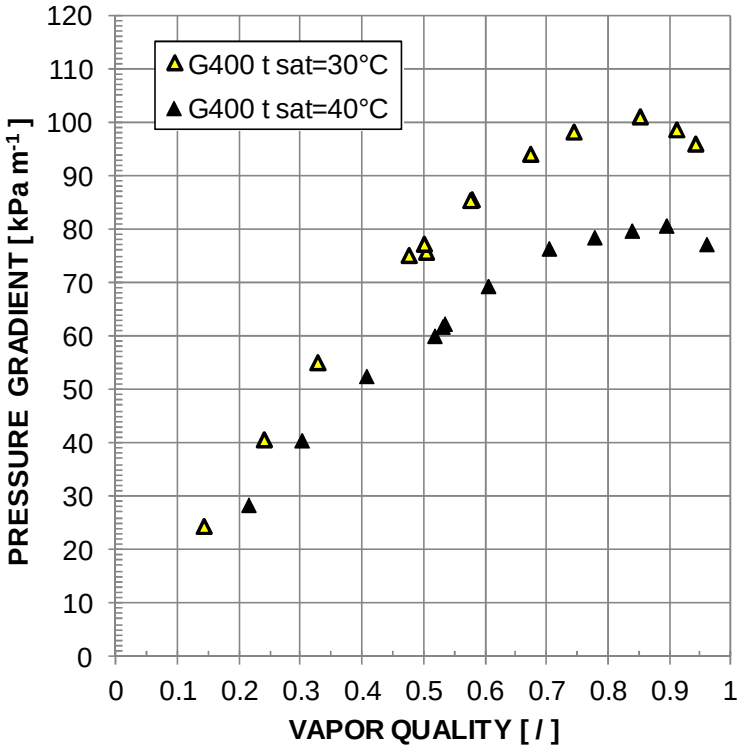

Figure 2.14. Experimental frictional pressure gradient versus vapor quality during two-phase adiabatic flow of R1234ze(E) inside a circular minichannel with an inner diameter equal to 0.96 mm at G = 400 kg m^{-2} s^{-1} and at saturation temperature of 30°C and 40°C.

Table 2-e. Experimental expanded uncertainty of vapor quality and two-phase pressure gradient during adiabatic flow of R1234ze(E) inside the 0.96 mm circular minichannel.

Mass velocity [kg m^{-2} s^{-1}]	Saturation temperature [°C]	Pressure gradient experimental uncertainty	Vapor quality experimental uncertainty [/]
800	40	< 1.3 kPa m^{-1}	0.01
600	40	< 1.1 kPa m^{-1}	0.01
400	30	< 0.7 kPa m^{-1}	0.01
400	40	< 0.7 kPa m^{-1}	0.01
200	40	< 0.3 kPa m^{-1}	0.03

The frictional pressure drop gradient predicted using the Friedel correlation [1] is plotted against the experimental data for R1234ze(E) in Figure 2.15. The model does not catch well the experimental trend as indicated by the standard deviation σ_N equal to 15.5%. Furthermore, it underestimates the data at 800 kg m^{-2} s^{-1} , 600 kg m^{-2} s^{-1} and 400 kg m^{-2} s^{-1}, in particular at vapor quality below 0.5 while it overestimates the data at 200 kg m^{-2} s^{-1} in the entire range of quality. The saturation temperature has no effect on the predictive accuracy. Overall, 71.6% of the experimental points are predicted within the ± 20% band and 98.5% of the data lie within ±30% band; the absolute mean deviation $|e_R|$ is 16.5% and the average deviation e_R is -10.1%.

In Figure 2.16, the experimental data are compared to the values calculated using the model by Muller-Steinhagen and Heck [2]. This model underpredicts all the data except those at 200 kg m^{-2} s^{-1} and vapor quality higher than 0.80. The higher underestimation is found at the higher mass velocity and at low vapor qualities. The standard deviation σ_N amounts to 12%. The absolute mean deviation is 18.3% and the average deviation is -

17.5%: only 55.2% of the experimental points for R1234ze(E) lie within the ±20% band while the ±30% band includes 83.6% of the pressure gradient data. No effect of the saturation temperature on the predictive performance has been noticed.
The R1234ze(E) data are compared against the model by Zhang and Webb [3] in Figure 2.17: this correlation undervalues the pressure gradient at mass velocities down to 400 kg m^{-2} s^{-1}: the higher percentage deviations are found at vapor quality lower than 0.5. On the other hand, the Zhang and Webb model tends to overrate the pressure drop at 200 kg m^{-2} s^{-1}. The deviations at 400 kg m^{-2} s^{-1} do not depend on the operating saturation temperature. On the whole, 73.1% of the data are predicted within ±20% while 98.5% of the points are included within the ±30% band.(σ_N = 11.6%; $|e_R|$ = 14.2%; e_R = -11.6%).
Finally, the comparison against the model by Del Col *et al.* [4] is reported in Figure 2.18. The model best predicts the data and best reproduces the experimental trend but it underestimates the data at 800 kg m^{-2} s^{-1}. On the other hand, the data at 600 kg m^{-2} s^{-1} and 400 kg m^{-2} s^{-1} are slightly undervalued while the points at 200 kg m^{-2} s^{-1} are a little underrated. Nevertheless, all the data are within the ± 20% band (σ_N = 7.7% $|e_R|$ = 8.6% and e_R = -6.1%). The model works well at different reduced pressure values.

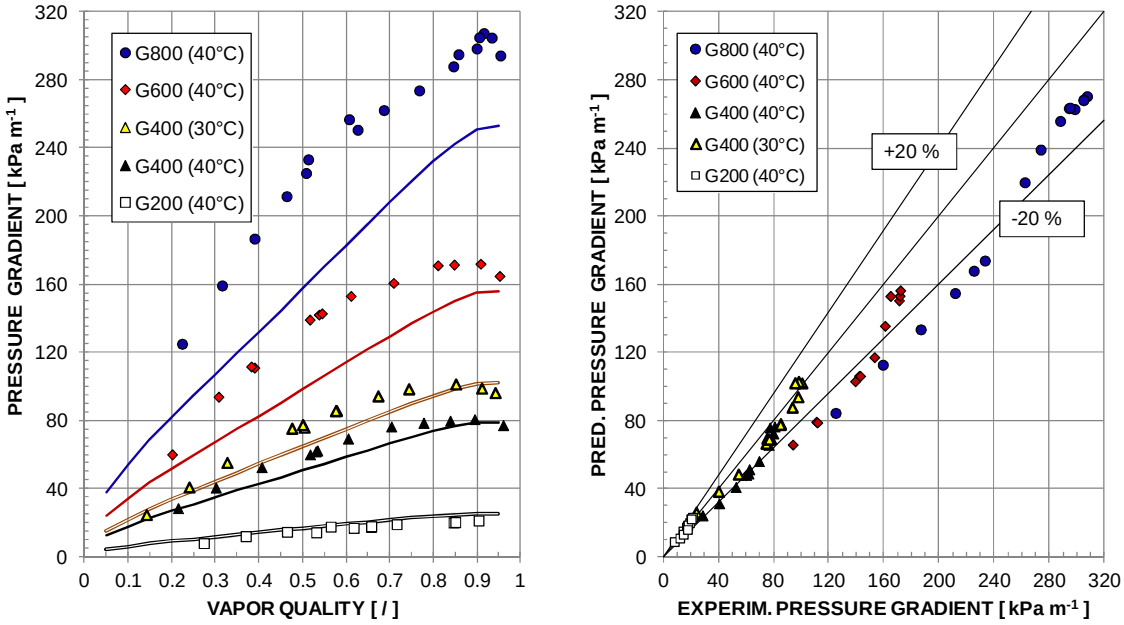

Figure 2.15. Two-phase frictional pressure gradient data during adiabatic flow of R1234ze(E) inside the circular minichannel with an inner diameter of 0.96 mm at different mass velocities *G* [kg m^{-2} s^{-1}] and saturation temperatures compared against the model by Friedel [1]. Left) Experimental pressure gradient and calculated trends (solid lines) by Friedel model [1]. Right) Comparison between measured frictional pressure gradient and calculated values using the Friedel model [1].

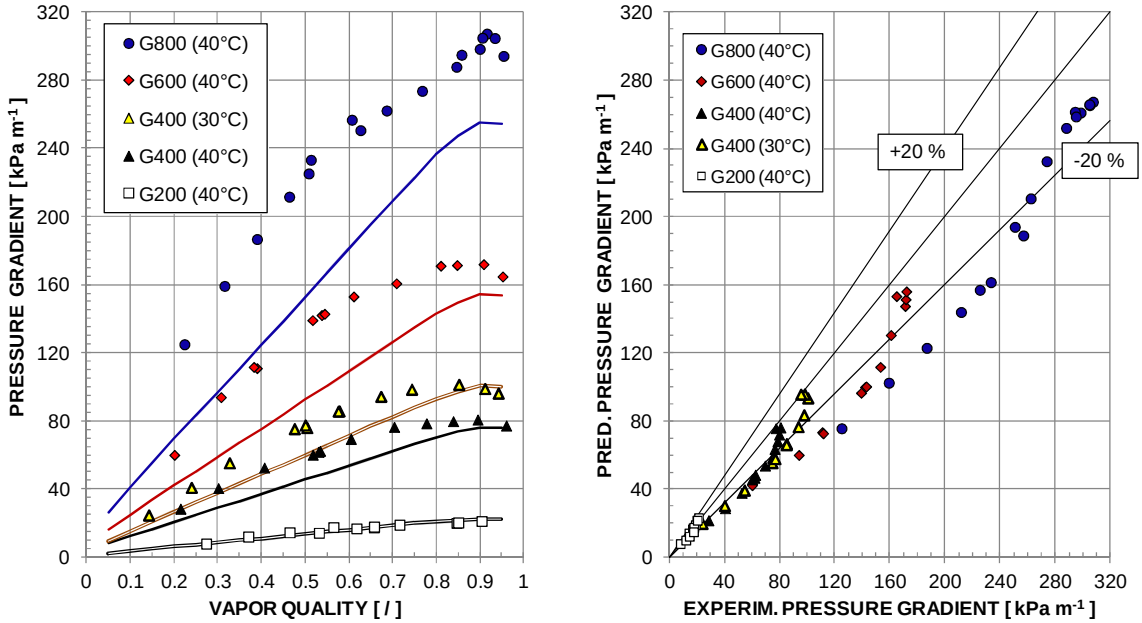

Figure 2.16. Two-phase frictional pressure gradient data during adiabatic flow of R1234ze(E) inside the circular minichannel with an inner diameter of 0.96 mm at different mass velocities *G* [kg m^{-2} s^{-1}] and saturation temperatures compared against the model by Muller-Steinhagen and Heck correlation [2]. Left) Experimental pressure gradient and calculated trends (solid lines) by Muller-Steinhagen and Heck model [2]. Right) Comparison between measured frictional pressure gradient and calculated values using the Muller-Steinhagen and Heck model [2].

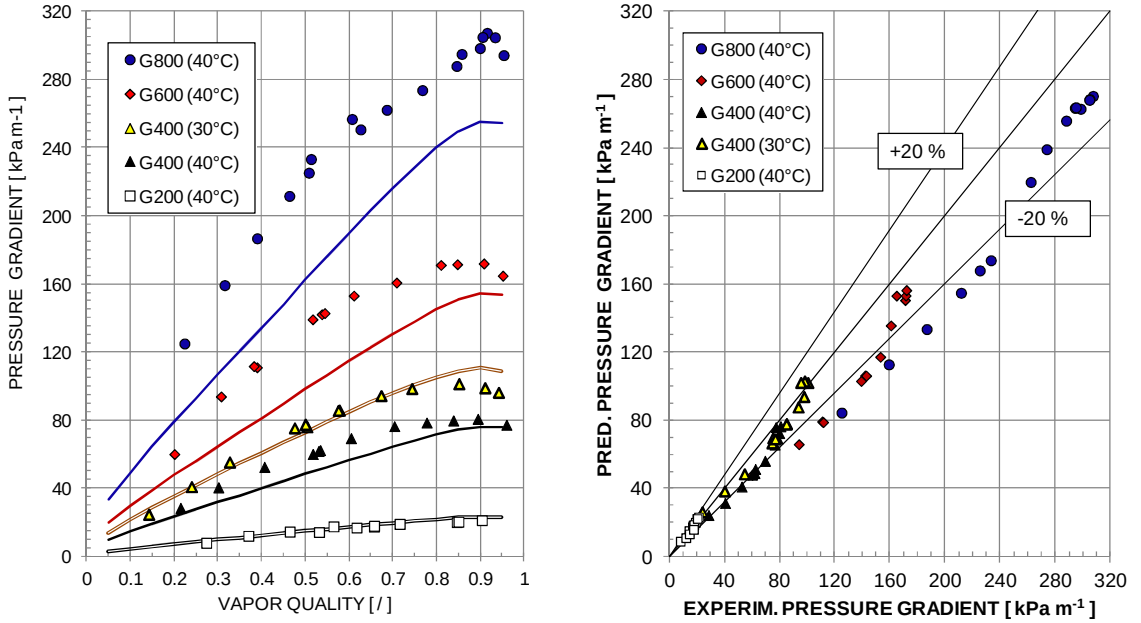

Figure 2.17. Two-phase frictional pressure gradient data during adiabatic flow of R1234ze(E) inside the circular minichannel with an inner diameter of 0.96 mm at different mass velocities *G* [kg m^{-2} s^{-1}] and saturation temperatures compared against the model by Zhang and Webb [3]. Left) Experimental pressure gradient and calculated trends (solid lines) by Zhang and Webb correlation [3]. Right) Comparison between measured frictional pressure gradient and calculated values using the Zhang and Webb model [3].

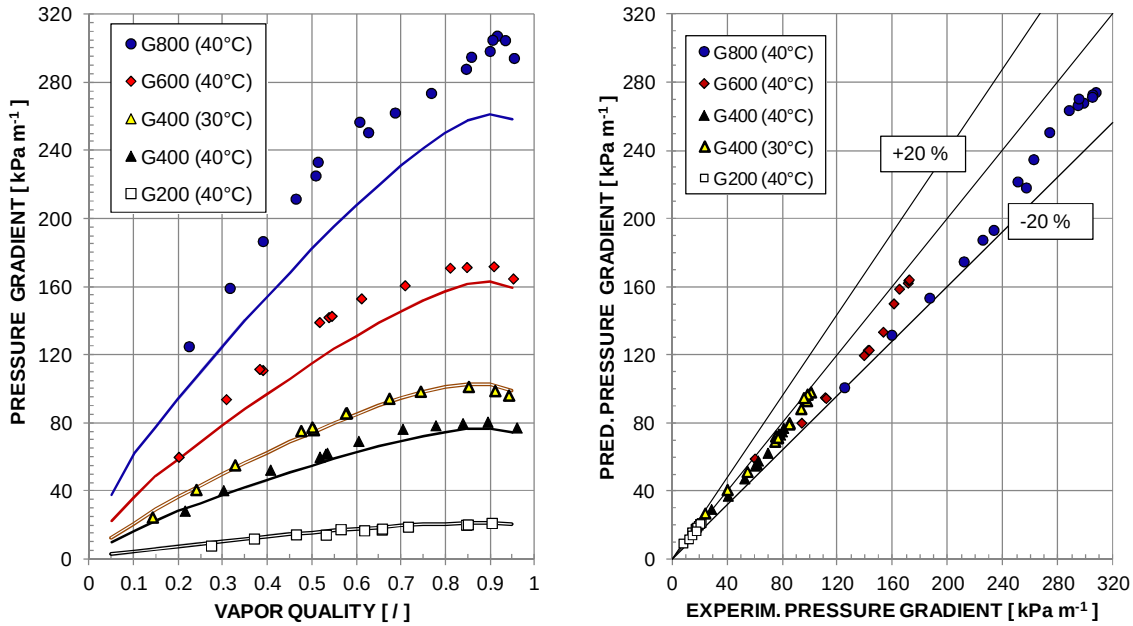

Figure 2.18. Two-phase frictional pressure gradient data during adiabatic flow of R1234ze(E) inside the circular minichannel with an inner diameter of 0.96 mm at different mass velocities *G* [kg m^{-2} s^{-1}] and saturation temperatures compared against the model by Del Col *et al.* [4]. Left) Experimental pressure gradient and calculated trends (solid lines) by Del Col *et al.* correlation [4]. Right) Comparison between measured frictional pressure gradient and calculated values using the Del Col *et al.* model [4].

2.6.3 Frictional pressure drop of propane and comparison against correlations

Two-phase frictional pressure drop tests have been performed during adiabatic flow of propane at a mean saturation temperature between 39.5°C and 42°C inside the circular cross section minichannel with an inner diameter equal to 0.96 and mm and an average roughness equal to 1.3 μm, at mass velocities between 200 kg m^{-2} s^{-1} and 800 kg m^{-2} s^{-1}.
The experimental pressure gradient is plotted against vapor quality in Figure 2.19.
Differently from what has been observed with the other tested refrigerants, at high mass velocities of 600 kg m^{-2} s^{-1} and 800 kg m^{-2} s^{-1}, at vapor quality between 0.5 and 0.6, the pressure gradient trend for propane shows an inflection point and the slope becomes steeper at high vapor qualities. This may be due to the strong liquid entrainment in these particular working conditions. The liquid entrainment appears during shear dominated flow regime, where the shear stress strips liquid drops away from the liquid-vapor interface. Since the entrained liquid in the gas core virtually increases the vapor phase density, its effect is similar to the increase in reduced pressure. Furthermore, Hewitt and Hall-Taylor [27] showed that as the liquid film gets thinner, the liquid-vapor interface roughness decreases. As a consequence, in a tube with a given gas flow rate, the pressure gradient is decreased when the liquid entrainment increases.
The expanded experimental uncertainties for measured parameters are reported in Table 2-f, at all the test conditions. The experimental uncertainty of the pressure gradient in percentage terms and the experimental uncertainty of the vapor quality slightly increase with decreasing mass velocity.

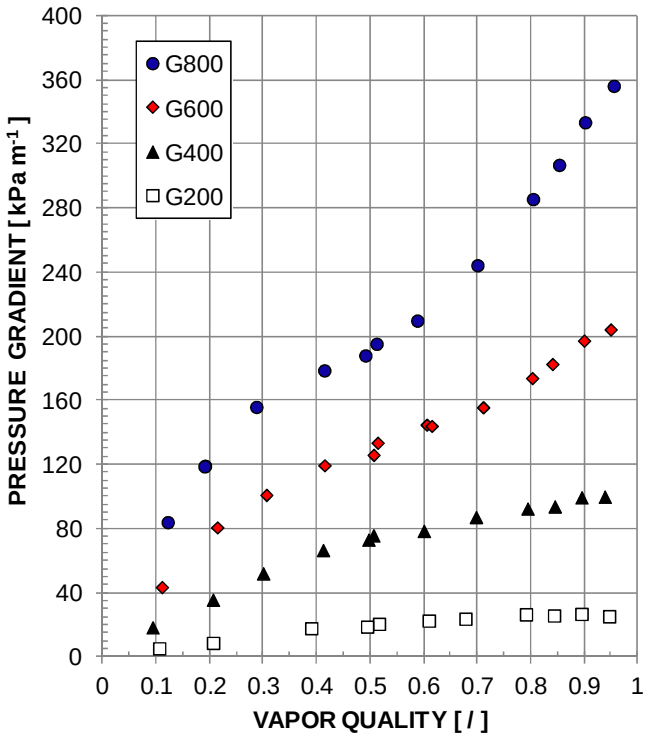

Figure 2.19. Experimental frictional pressure gradient versus vapor quality during two-phase adiabatic flow of propane inside a circular minichannel with an inner diameter equal to 0.96 mm at 40°C saturation temperature and at different mass velocity *G* [kg m^{-2} s^{-1}].

Table 2-f. Experimental expanded uncertainty of vapor quality and two-phase pressure gradient during adiabatic flow of propane inside the 0.96 mm circular minichannel.

Mass velocity [kg m^{-2} s^{-1}]	Saturation temperature [°C]	Pressure gradient experimental uncertainty	Vapor quality experimental uncertainty (-)
800	40	< 1.0 kPa m^{-1}	< 0.01
600	40	< 1.2 kPa m^{-1}	< 0.01
400	40	< 1.0 kPa m^{-1}	< 0.01
200	40	< 0.4 kPa m^{-1}	< 0.02

As regard the comparison of the 49 experimental pressure gradient data for propane against the correlations chosen form literature, the Friedel model [1] gives satisfactory predictions (Figure 2.20). Almost all the data (93,9%) are predicted with a percentage deviations below 20% in absolute value. The few exceptions concern points collected at 200 kg m^{-2} s^{-1} and at vapor qualities lower than 0.2. The model slightly underestimates the data at 800 kg m^{-2} s^{-1}, 600 kg m^{-2} s^{-1} and 400 kg m^{-2} s^{-1}, while it slightly overrates the experimental points at 200 kg m^{-2} s^{-1}. On the whole, the standard deviation amounts to 12.1%, the absolute mean deviation is 9.6% and the average deviation is -4.0%.
The correlation by Muller-Steinhagen and Heck [2] catches 71.4% of the experimental point within ±20% band and 98% within ±30% band. Observing the calculated trend (Figure 2.21), the model tends to underpredict the data in the entire working condition range, giving the highest deviations at low vapor qualities (σ_N = 10.5%, $|e_R|$ = 12.7% , e_R = - 12.0%).

The calculated trends and predictions obtained by Zhang and Webb correlation [3] for two-phase pressure drop on small diameter channels are plotted against the experimental data in Figure 2.22. This model predicts 69.4% of the data within ±20% band and 85.7% of the experimental points within ±30% band. It altogether underestimates the present data for all the investigated mass velocities, giving the highest deviations at low vapor qualities (σ_N = 10.0%, $|e_R|$ = 16.7% , e_R = - 16.5%).
The correlation by Del Col *et al.* [4] best predicts the experimental database (
Figure 2.23). Deviations between experimental values and predictions are altogether very low (within ± 20% band). The standard deviation σ_N is 8.2%, the absolute mean deviation $|e_R|$ is equal to 9.1% and the average deviation e_R is -6.7%. The highest deviations are found at vapor quality lower than 0.3. The pressure drop gradient at 800 kg m^{-2} s^{-1} is slightly underestimated.
Finally, at 800 kg m^{-2} s^{-1} and 600 kg m^{-2} s^{-1} mass velocities, the predicted trends of all the models do not exhibit any change of slope.

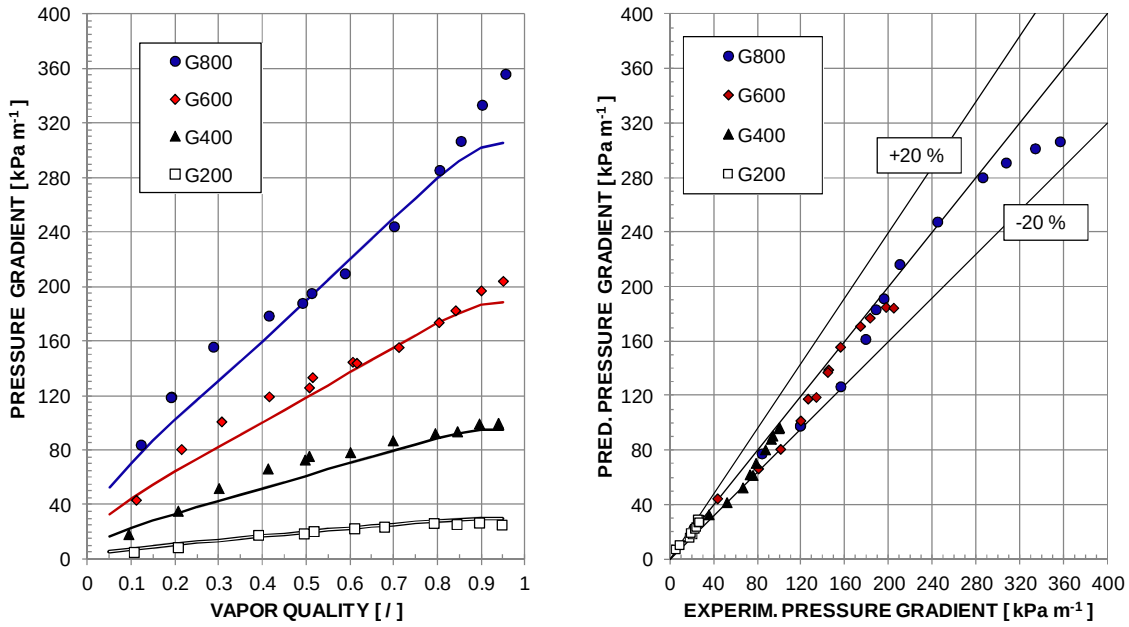

Figure 2.20. Two-phase frictional pressure gradient data during adiabatic flow of propane inside the circular minichannel with an inner diameter of 0.96 mm at 40°C saturation temperature and at different mass velocities *G* [kg m^{-2} s^{-1}] compared against the model by Friedel [1]. Left) Experimental pressure gradient and calculated trends (solid lines) by Friedel model [1]. Right) Comparison between measured frictional pressure gradient and calculated values using the Friedel model [1].

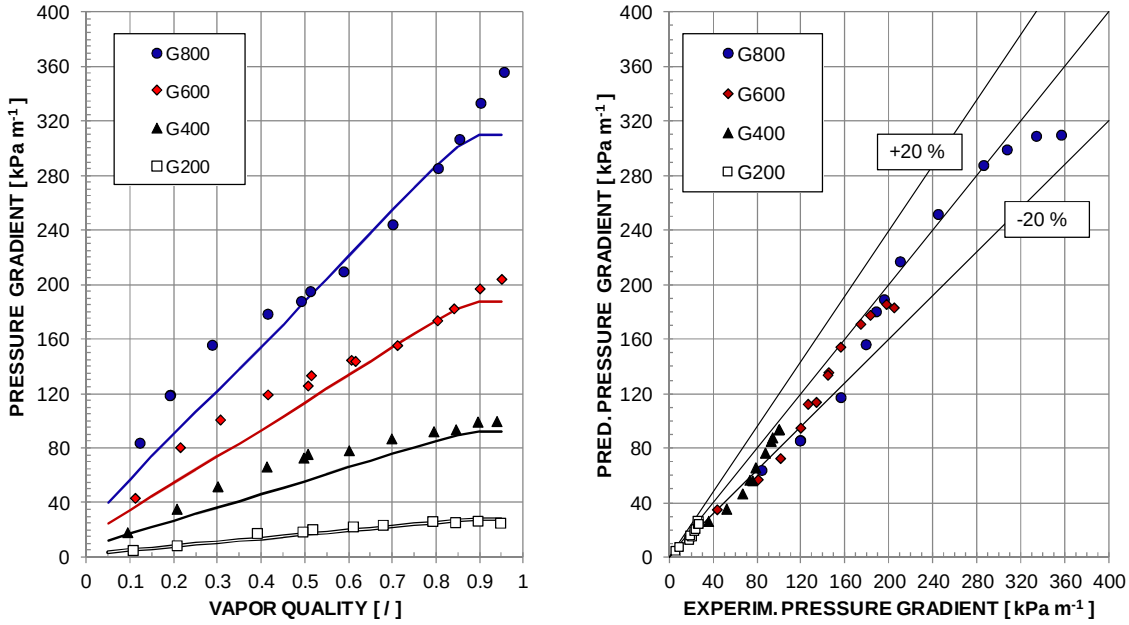

Figure 2.21. Two-phase frictional pressure gradient data during adiabatic flow of propane inside the circular minichannel with an inner diameter of 0.96 mm at 40°C saturation temperature and at different mass velocities *G* [kg m^{-2} s^{-1}] compared against the model by Muller-Steinhagen and Heck correlation [2]. Left) Experimental pressure gradient and calculated trends (solid lines) by Muller-Steinhagen and Heck model [2]. Right) Comparison between measured frictional pressure gradient and calculated values using the Muller-Steinhagen and Heck model [2].

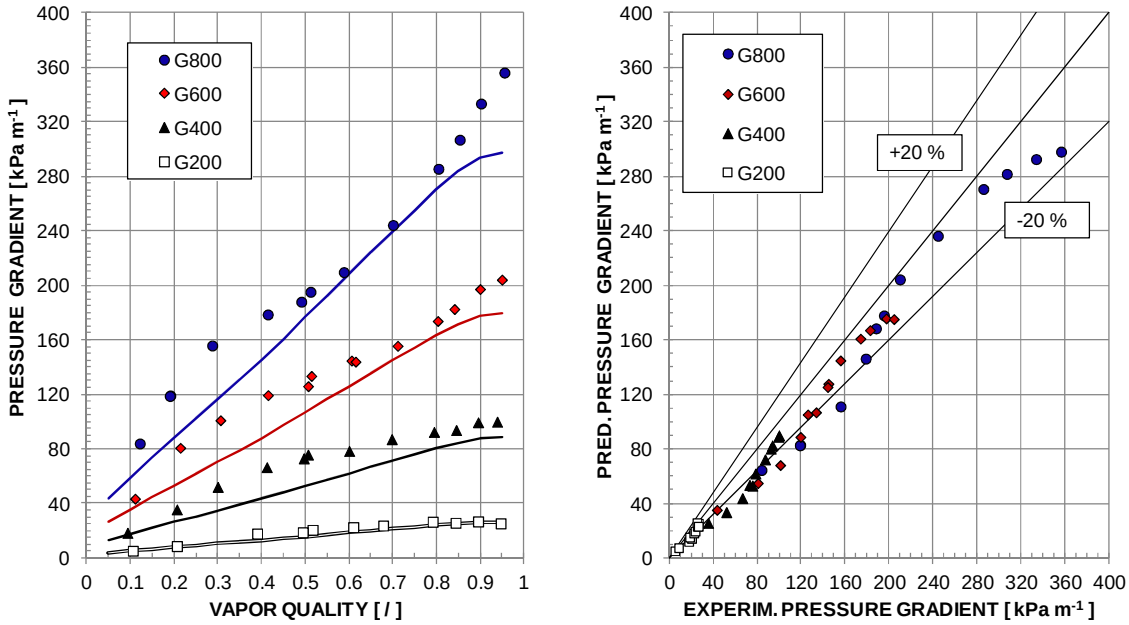

Figure 2.22. Two-phase frictional pressure gradient data during adiabatic flow of propane inside the circular minichannel with an inner diameter of 0.96 mm at 40°C saturation temperature and at different mass velocities *G* [kg m^{-2} s^{-1}] compared against the model by Zhang and Webb [3]. Left) Experimental pressure gradient and calculated trends (solid lines) by Zhang and Webb correlation [3]. Right) Comparison between measured frictional pressure gradient and calculated values using the Zhang and Webb model [3].

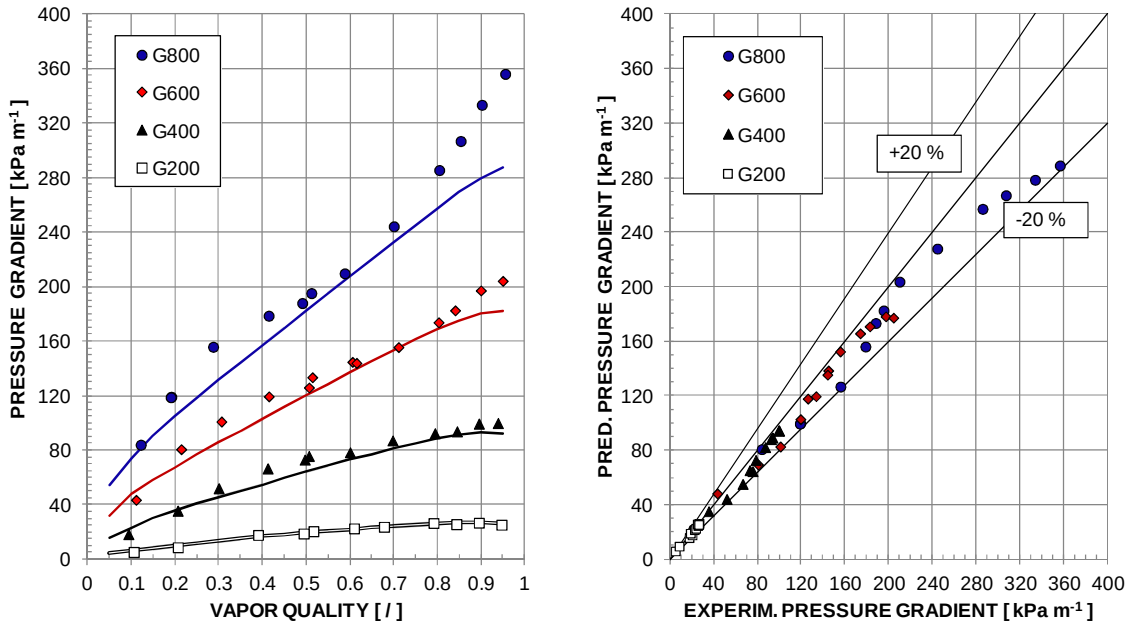

Figure 2.23. Two-phase frictional pressure gradient data during adiabatic flow of propane inside the circular minichannel with an inner diameter of 0.96 mm at 40°C saturation temperature different mass velocities *G* [kg m^{-2} s^{-1}] compared against the model by Del Col *et al.* [4]. Left) Experimental pressure gradient and calculated trends (solid lines) by Del Col *et al.* correlation [4]. Right) Comparison between measured frictional pressure gradient and calculated values using the Del Col *et al.* model [4].

2.6.4 Comparison among the investigated refrigerants

Considering the circular minichannel with internal diameter of 0.96 mm, the results show that, at the same hydraulic diameter, mass velocity and saturation temperature, the two-phase frictional pressure drop for R134a are always the lowest. On the other hand, at 200 kg m^{-2} s^{-1} and 400 kg m^{-2} s^{-1} the pressure gradient for propane is clearly the highest (Figure 2.24 left). This is probably due to the low vapor density of propane, as compared to the other tested refrigerants.

Differently from what has been observed with R134a and R1234ze(E), at high mass velocities of 600 kg m^{-2} s^{-1} and 800 kg m^{-2} s^{-1}, at vapor quality between 0.5 and 0.6, the pressure gradient trend for propane shows an inflection point and the slope becomes steeper at high vapor qualities. This may be a consequence of the strong liquid entrainment due to the low liquid density of propane in these particular working conditions.

Hence, when comparing the experimental points obtained for the considered fluids at 800 kg m^{-2} s^{-1} and 40°C inside the minichannel with internal diameter of 0.96 mm, it is found that the data for propane are lower than those for R1234ze(E) up to 0.85 vapor quality (Figure 2.24 right).

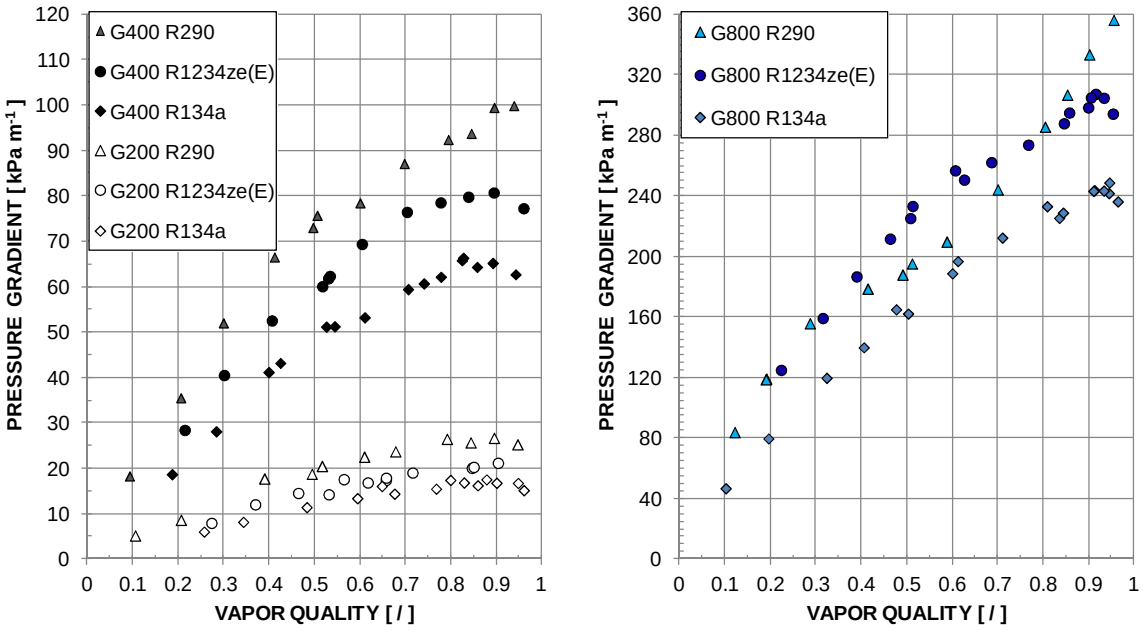

Figure 2.24. Comparison between the experimental data collected during adiabatic flow of the three tested refrigerants in the circular minichannel with internal diameter of 0.96 mm at 40°C saturation temperature at different mass velocity *G* [kg m^{-2} s^{-1}]. Left) 200 kg m^{-2} s^{-1} and 400 kg m^{-2} s^{-1} mass velocities. Right) 800 kg m^{-2} s^{-1} mass velocity.

3 CONDENSATION AND FLOW BOILING OF LOW GLOBAL WARMING POTENTIAL REFRIGERANTS INSIDE A HORIZONTAL SINGLE CIRCULAR MINICHANNEL

3.1 Abstract

Measurements of the local heat transfer coefficient during condensation at 40°C saturation temperature of and during flow boiling at 31°C saturation temperature inside a single minichannel are reported in the present chapter. The test section is horizontally arranged and consists of a circular tube having an internal diameter equal to 0.96 mm and a rough inner surface. During the tests, the heat is transferred between the refrigerant and a secondary fluid, that is cold distilled water. As a consequence, the local heat flux results as a variable parameter depending on the testing conditions and its accurate measurement becomes the main issue. While in condensation the local heat flux is calculated only from the slope of the water temperature gradient, during flow boiling tests, it is also calculated using a method based on the estimation of the water heat transfer coefficient in single-phase regime. Finally, the local heat transfer coefficient is obtained from the ratio of the local heat flux and the wall to saturation temperature difference. In agreement with the increased attention in anthropogenic global warming, the tested refrigerants are attractive alternatives to develop environmentally friendly thermo-fluid-dynamic equipments: the propane (R290), which is a natural hydrocarbon and the R1234ze(E) refrigerant, which is a halogenated olefin and seems to be suitable to substitute R134a in refrigeration and electronic cooling applications. Furthermore, very few studies of two-phase heat transfer data for the both of these refrigerants are available in the open literature.
The condensation tests are carried at mass velocity ranging between 100 kg m^{-2} s^{-1} and 1000 kg m^{-2} s^{-1} for R290 and between 100 kg m^{-2} s^{-1} and 800 kg m^{-2} s^{-1} for R1234ze(E). On the other hand, the flow boiling tests are performed at mass velocities between 100 kg m^{-2} s^{-1} and 600 kg m^{-2} s^{-1} for R290 and between 100 kg m^{-2} s^{-1} and 500 kg m^{-2} s^{-1} for R1234ze(E). The experimental uncertainty of the collected data is defined through an accurate error analysis.
The experimental condensation heat transfer coefficients are compared against those calculated using three correlations: the first by Cavallini *et al.* [28], the second by Moser *et al.* [29] with the pressure drop correlation by Zhang and Webb [3] and the third by Shah [30].
The results obtained during flow boiling tests are reported with the aim of investigate the effect of heat flux, vapor quality and mass velocity on heat transfer coefficient. The experimental database presented in this work has been compared against some models available in the open literature. This chapter includes the description of the test rig and the test section, the explanation of the experimental technique for and the results discussion first for the condensation tests and then for the flow boiling tests.

3.2 Introduction

Nowadays, there is an increasing interest in refrigerant possessing low global warming potential (GWP) because of a higher attention to environmental problems and climatic changes and a growing number of regulations and laws promulgated by the main international organizations. The Montreal Protocol on Substances that Deplete the Ozone Layer [31] and its subsequent amendments imposed a ban on the use of CFCs refrigerants

and the progressive phase-out of the HCFCs refrigerants. These restrictions led to the choice of hydrofluorocarbons (HCFs) as refrigerants in most applications. Afterwards, the Kyoto Protocol [32] placed these substances among the six categories of greenhouse gases because of their large values of global warming potential and called for their phase-out. Furthermore, the European Parliament and the Council has faced the climate change issue by redacting the mobile air conditioning (MAC) Directive 2006/40/EC [33] and the Regulation 842/2006 [34]. The former states that the use of the fluorinated gases (F-gases) with a global warming potential higher than 150 is forbidden in all new vehicles from 1 January 2011 and for all vehicles from January 2017. The latter establishes regulations for the containment, use, recovery and destruction of certain fluorinated greenhouse gases. Finally, in 2012, the European Commission proposed to cut F-gases emission by two third by 2030 [35].

The search for alternatives primarily focuses on the use of natural refrigerants in heat pump and air conditioning equipment or in industrial processes, because the direct effect on the anthropogenic emissions due to atmospheric emissions is almost completely avoided. In particular, hydrocarbons show good material compatibility and desirable thermodynamic and transport properties, which can reduce the indirect effect on anthropogenic global warming. Because of flammability and very low ignition concentration, charge minimization is a major design objective for the equipment when using hydrocarbons as refrigerants. From previous experience, it appears that the estimated charge of unitary air conditioners is expected to be mainly trapped in the heat exchangers. In particular, Harms *et al.* [36] estimated the charge in three unitary air conditioners from 9 kW up to 26 kW and using R22 and R407C; they found that the computed charge in the condenser may vary from 30% up to 70% of the total amount, while the charge in the evaporator is lower (around 20%). Similar results have been obtained by Corberán and Martínez [37] for a water-to-water propane heat pump using plate heat exchangers: 50% of the total charge is expected to be found in the condenser, while about 20% should be trapped in the evaporator.

In this regard, minichannel technology appears to be a very good opportunity to minimize the charge without energy performance loss. Cavallini *et al.* [38] presented the experimental performance of a 100 kW heat pump using propane. Shell-and-tube heat exchangers using minichannels and providing low charge have been installed in the unit along with conventional brazed plate heat exchangers. It is shown that a 100 kW heat pump without a liquid receiver could be run with around 3 kg of propane using a plate condenser; but when using the minichannel condenser, around 0.8 kg reduction can be obtained with a negligible performance loss.

Among natural refrigerants, propane is usually regarded as a long term alternative refrigerant and its employment in the refrigeration applications delineates an interesting opportunity as the physical properties are close to those of R22. Nevertheless, in the open literature, a very limited number of experimental data of propane in small diameter channels is available so far.

Lee and Son [39] presented an experimental comparison of pressure drop and heat transfer coefficient during condensation at 40°C of isobutene (R600a), propane (R290), R134a and R22 inside a horizontal tube-in-tube heat exchanger with inner diameters ranging from 5.8 mm to 10.07 mm. In the investigated mass flux range (35.5 kg m^{-2} s^{-1} - 210.4 kg m^{-2} s^{-1}), the authors found that the average condensation heat transfer coefficient and the pressure drops of the hydrocarbons were higher than those of the halogenated refrigerants.

Shao *et al.* [40] developed a distributed-parameter model of serpentine minichannel condensers; the Cavallini *et al.* [41] correlation has been selected to calculate the

refrigerant condensation heat transfer coefficient. The model was experimentally validated with a serpentine minichannel condenser using propane as working fluid; the predictions on the heat capacity and the pressure drop fall into ±10% error band.
Fernando *et al.* [42] studied heat transfer during propane condensation inside a minichannel aluminum heat exchanger vertically mounted. The condenser was constructed of 36 multiport tubes; each multiport tube contained six rectangular parallel channels having a 1.42 mm hydraulic diameter. Experiments were performed at constant condensation temperatures of 30°C, 40°C and 50°C and mass flux ranging between 20 kg m^{-2} $s^{-1}$and 50 kg m^{-2} s^{-1}. The authors showed that the experimental heat transfer coefficients were higher than those predicted by available correlations.
In the same test section, Fernando and coworkers [43] also investigated the evaporation process with propane flowing upward inside minichannels heated by a temperature controlled glycol solution flowing downward on the shell side at a fixed mass flow rate. Tests were conducted for a range of mass velocities between 13 and 66 kg m^{-2} s^{-1}, heat flux between 2 kW m^{-2} and 9 kW m^{-2} and saturation temperature from -15°C to 10°C. The experimental heat transfer coefficients were compared against several correlations from the literature and resulted to be higher than those predicted by many models.
Choi *et al.* [12] examined the two-phase flow boiling pressure drop and heat transfer for propane in horizontal minichannels with inner diameters of 1.5 mm and 3.0 mm. The pressure drop and local heat transfer coefficients were obtained for heat fluxes ranging between 5 and 20 kW m^{-2}, mass fluxes ranging between 50 kg m^{-2} s^{-1} and 400 kg m^{-2} $s^{-1}$and saturation temperatures of 10 °C, 5°C and 0°C. They also developed new correlations for pressure drop and boiling heat transfer coefficients.
Maqbool *et al.* [13] investigated the flow boiling of propane under electrically imposed heat flux inside a vertical circular minichannel with an internal diameter equal to 1.7 mm and a rough inner surface. Experiments have been carried out at saturation temperatures of 23°C, 33 °C and 43°C while the heat flux is varied from 5 to 280 kW ,$^{-2}$ and the mass flux ranged between 100 kg m^{-2} s^{-1} and 500 kg m^{-2} s^{-1}. The heat transfer coefficients increased with heat flux and saturation temperature, while the effect of mass flux and vapor quality resulted to be negligible. The experimental database has been compared against available correlations from literature. The same authors [44] presented a study on the dryout characteristics of propane in single vertical circular minichannels with internal diameters of 1.224 mm and 1.70 mm and a uniformly heated length of 245 mm. With regard to the test conditions, the mass flux varied from 100 kg m^{-2} s^{-1} to 500 kg m^{-2} s^{-1} , the heat flux from 5 kW m^{-2} to 276 kW m^{-2} at saturation temperatures of 23°C, 33 °C and 43°C. The experimental dryout heat flux increased with increasing mass flux and decreasing vapor quality, while the effect of saturation temperature was negligible. It was found that the heat flux was higher for the larger internal diameter at the same mass flux. The collected data has been compared against correlations from the literature.

More recently, halogenated olefins (HFOs) have been investigated as low GWP refrigerants and those with fluorinated propene isomers have emerged as possible solutions. In particular, R1234yf, which has a 100-year horizon global warming potential of 4 has been regarded as the R134a replacement refrigerant in future mobile air conditioning systems while R1234ze(E), which has a 100-years horizon global warming potential of 6 seems to be suitable to substitute R134a in refrigeration and electronic cooling applications.
Some works available in the open literature concern the study and the definition of the thermodynamic properties of the HFOs and their possible applications while only few data on two-phase heat transfer have been published so far.

To the present author's knowledge, the work by Park *et al.* [45] is the only one that reports experimental data on condensation for R1234ze(E) in minichannels. The tests therein described were performed in a vertical aluminum multiport tube with rectangular channels having a hydraulic diameter of 1.45 mm and the experimental data were compared versus the data for R134a and R236fa obtained in the same test section. A wide range of test conditions has been covered, with mass velocity ranging between 50 kg m^{-2} $s^{-1}$and 260 kg m^{-2} $s^{-1}$and saturation temperature from 25°C to 70°C. They found that the heat flux and the inlet conditions of the refrigerant negligibly affect the heat transfer during condensation. Moreover, the authors pointed out that at 150 kg m^{-2} s^{-1} mass velocity and at 40°C saturation temperature, the heat transfer coefficients of R1234ze(E) were 15-25% lower than those for R134a and 5% lower than those for R236fa. Finally, the authors proposed a new correlation for the prediction of the heat transfer coefficient in a vertical multi-minichannel tube which has been validated against the collected database.
Hossain *et al.* [9] performed an experimental study on condensation heat transfer and pressure drop for R1234ze(E), R32 and R410A in a horizontal smooth copper macrochannel with an inner diameter of 4.35 mm. The mass velocity ranged from 150 kg m^{-2} s^{-1} to 400 kg m^{-2} s^{-1} and the saturation temperature was between 35°C and 45°C. The experimental results obtained both in condensation tests and in pressure drop investigation were compared against models available in the open literature. From the comparison among the considered refrigerants, it was found that the condensation heat transfer coefficient of R1234ze(E) is intermediate among the values of the tested fluids. With regard to the pressure drop, the average pressure gradient of R1234ze(E) resulted the highest because R1234ze(E) is a low pressure and high viscosity refrigerant as compared to the other fluids tested in this work.
In the same test section, Hossain and coworkers [46] measured and compared the quasi local heat transfer coefficients during flow boiling of R1234ze(E), R32, R410A and a mixture of R1234ze(E) and R32 (55/45 % mass) inside a water heated double heat exchanger. Experimental data were reported at mass velocity between 150 kg m^{-2} s^{-1} and 445 kg m^{-2} s^{-1} and at saturation temperature equal to 5°C and 10°C over the entire range of vapor quality. It was found that the heat transfer coefficient increases with the heat flux for the pure fluids and the R410A mixture, while the effect of heat flux is not clear for the mixture of R1234ze(E) and R32. Furthermore, the heat transfer coefficient slightly increases with the saturation temperature for all the tested refrigerants and mixtures. With regard to the comparisons, it was shown that at about 0.5 vapor quality and at 300 kg m^{-2} s^{-1} mass velocity, the heat transfer coefficients of R1234ze(E) were lower than those of the R1234ze(E)/R32 mixture, R410A and R32 by 11%, 56% and 83% respectively.
Grauso *et al.* [10] reported experimental results for heat transfer coefficients and pressure drops during evaporation of R1234ze(E) and R134a inside a 6 mm internal diameter channel. Moreover, flow patterns have been investigated using a high speed camera arranged on a glass tube located at the exit of the test section. In the test runs operating conditions, R1234ze(E) is generally preferred than R1234yf to substitute R134a: in particular, the mass velocity has been varied from 146 kg m^{-2} s^{-1} to 520 kg m^{-2} s^{-1}, the saturation temperature from -2.9°C to 12.1°C and the heat flux from 5 kW m^{-2} to 20.4 kW m^{-2}. Local heat transfer coefficients of the two refrigerants resulted very similar in the test conditions, showing the same trends with vapor quality, mass flux and heat flux. The most important differences were found to be the earlier dry-out inception for the halogenated olefin and the higher heat transfer coefficients of R134a at vapor quality below 0.2. On the other hand, the frictional pressure drops of R1234ze(E) resulted to be higher than those obtained for R134a. An assessment of predicting methods both for flow boiling heat transfer coefficients and frictional pressure drops is also presented.

In the work by Tibiriçà *et al.* [47],the flow boiling heat transfer of R1234ze(E) inside two stainless steel circular minichannels with internal diameter of 1.0 mm and 2.2 mm has been investigated. In test runs, the mass velocity ranged between 50 kg m^{-2} s^{-1} and 1500 kg m^{-2} s^{-1} and the imposed heat flux ranged from 10 kW m^{-2} to 300 kW m^{-2} at exit saturation temperature of 25°C, 31°C and 35°C. Their results included the heat transfer coefficient under saturated conditions, the critical heat flux and the flow pattern map, moreover a comparison with an experimental database obtained using R134a in the same test section has been performed. In particular, the values of heat transfer coefficient of R1234ze(E) increased with mass velocity and they were slightly lower than those referred to R134a. The critical heat flux for R1234ze(E) increased with mass velocity and it was independent on subcooling; it was actually slightly lower as compared to the one of R134a. The authors concluded that the two fluids have similar thermal performance.
Vakili-Farahani *et al.* [48] performed upward flow boiling tests considering R245fa and R1234ze(E) refrigerants inside a flat aluminum extruded multiport with 7 parallel minichannels having a hydraulic diameter equal to 1.45 mm. During the tests, the heat was transferred from water flowing at a constant mass flow rate in a jacket encircling the flat tube to the evaporating refrigerant, so the local heat flux is not uniform. The water temperature profile and the heat flux distribution on the water side have been computed by a numerical method from the preliminary determination of the water Nusselt numbers and the energy balance. The local heat flux distribution on the refrigerant side has been then calculated accounting for the heat losses to the external ambient and the heat conduction along the tube wall. The local heat transfer coefficient during flow boiling has been finally obtained as the ratio of heat flux and saturation to wall temperature difference, where the refrigerant saturation temperature was derived taking into account the pressure drop. A large variety of test conditions is considered, with saturation temperature varying between 30 °C and 70 °C and mass velocity ranging between 50 and 400 kg m^{-2} s^{-1}. The heat transfer coefficient increased with increasing heat flux, mass velocity and saturation temperature, while the effect of the vapor quality was dependent on the occurrence of either annular flow regime or intermittence dryout condition. The comparison of the collected database against the models available in the open literature showed that the three zone model for slug flows worked well in the presented test conditions.

3.3 Experimental apparatus

3.3.1 General description of the test facility

The test sections for pressure drop investigation (see chapter 2) and for two-phase heat transfer analysis are accommodated in the same test rig presented in chapter 2. For the sake of clarity, a description of the test facility is reported also in this section in order to better present the operative conditions during condensation and flow boiling test runs.
As reported in Figure 3.1 the test facility includes a primary refrigerant loop which underwent several washing cycles to remove all possible contaminants before filling it with the fluid under consideration. A washing cycle consists of creating a vacuum followed by pressurization with nitrogen and new vacuum. In the primary loop, after exiting the test section, the refrigerant is subcooled in a post condenser and dried up before entering an independently controlled oil-free gear micro pump which is used to set the mass flow rate measured by a Coriolis effect mass flow meter. Hence, the tested fluid passes through a mechanical filter and enters a tube-in-tube heat exchanger where the

primary fluid can be either heated up or superheated using hot water flowing in a closed auxiliary loop equipped with PID-controlled electrical heaters to fix the inlet temperature.

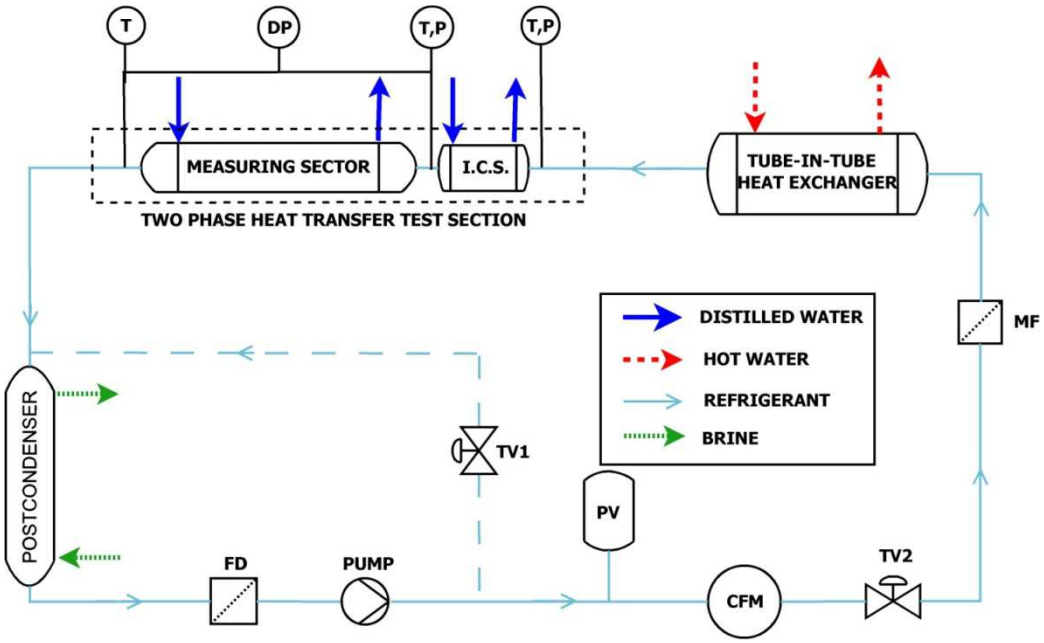

Figure 3.1. Experimental test rig: I.C.S. (inlet condition setter); FD (filter drier); PV (pressure vessel); CFM (Coriolis-effect mass flow meter); TV (throttling valve); MF (mechanical filter); P(relative pressure transducer); DP (differential pressure transducer); T (thermocouple)

When operating in condensation mode, the refrigerant enters the test section as superheated vapor, while when performing flow boiling tests the refrigerant in only slightly heated up in the tube-in-tube heat exchanger, nevertheless it enters the test section as subcooled liquid. The test section for two-phase heat transfer investigation is placed in horizontal and includes two counter flow heat exchangers where heat is exchanged between the working refrigerant and a secondary fluid, that is distilled water. In detail, the first heat exchanger works as an inlet condition setter as the desired thermodynamic conditions of the refrigerant at the inlet of the next heat exchanger are here achieved. In condensation mode, the first part of the test section acts as desuperheater and sometimes as pre-condenser with the refrigerant exiting with a vapor quality lower than 1. In flow boiling experiments, the inlet conditions setter is used to achieve the desired subcooling of the refrigerant before entering the second part of the test section. The second heat exchanger has been designed in order to measure accurately the local heat transfer coefficient and it is referred as measuring section. At the inlet of each part of the test section, the pressure is gauged by means of two digital strain gauges relative pressure transducers, whereas a differential pressure transducer is employed to measure pressure drop along the measuring section. All the pressure transducers are connected to the pressure ports of the test section by pressure lines on whose external surface wire electrical heaters are applied.
Two thermal baths are employed: the first serves brine at 5°C to the auxiliary loop of the post condenser, while the second controls the temperature of the distilled water which is used as secondary fluid for the heat transfer in the two heat exchangers of the test section. Thus, the distilled water flows in two different loops served by the same thermal bath. Each loop is provided with a flow regulating valve, which allows to set the water mass

flow rate measured by a Coriolis-effect mass flow meter. When necessary the inlet water temperature in the inlet condition setter and the measuring section can be maintained at different values by using electrical heaters installed downstream of the thermal bath in each loop. In every test run, when the apparatus is working in steady state conditions, measurements of thermo-fluid-dynamic parameters are recorded for 50 s with a time step of 1 s. Each recording is averaged and then reduced by calculating the fluid properties with NIST Refprop Version 9.0 [16].The test section and the experimental technique are described below.

3.3.2 Test section for heat transfer coefficient measurements

The two-phase heat transfer test section (Figure 3.2) is connected to the rest of the test rig by stainless steel tubes. The test section consists of two parts that work as counter-current heat exchangers: the inlet condition setter which is 55 mm long and the measuring section, that is 227.5 mm long. They both are made from a 8 mm external diameter copper rod having a 0.96 mm internal bore and an arithmetic mean roughness of the inner surface (*Ra*) of 1.3 µm. The uncertainty associated to the diameter is determined from an enlarged image of the minichannel obtained by a microscope and it is equal to ± 0.02 mm including dimensional and geometric tolerances. At the intake of the inlet condition setter, on the outer surface of the stainless steel connection tube, a pressure port was realized and a T-type thermocouple was placed, so the thermodynamic state of the entering refrigerant in single-phase flow regime is determined by means of pressure and temperature measurements. The measuring section is thermally separated from the inlet condition setter and from the rest of the test rig through two stainless steel adiabatic sector, having an inner diameter of 0.762 mm and an arithmetic mean roughness of the inner surface (*Ra*) of 2 µm. Because of the low thermal conductivity, the adiabatic sectors can be use for the measurement of the refrigerant temperature at the inlet of the measuring section and of the refrigerant saturation temperature drop along the measuring section by means of a T-type thermocouple (located 12 mm far from the inlet) and a three junctions thermopile soldered on the outer surface of the stainless steel segments. Moreover, the adiabatic sectors are the accommodations of the pressure ports, which are placed 23 mm far from the measuring section ends and connected to the relative and differential pressure transducers. The presence of both temperature and pressure transducers at the inlet of the measuring section allows a check of the saturation temperature during two-phase heat transfer tests.
The roughness measurement has been performed following the EN ISO 4287 standard [15] with the digital surface roughness machine ZEISS-TSK Surfcom 1400A.

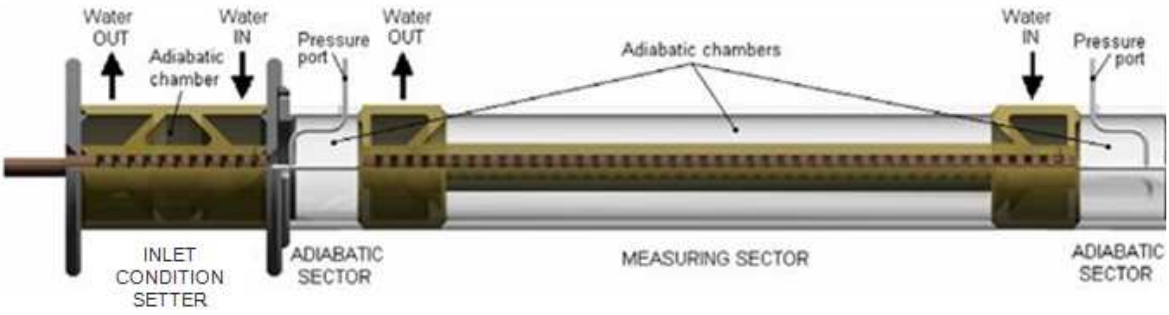

Figure 3.2. Circular minichannel test section for two-phase heat transfer experimental analysis.

The external surface of each part of the test section was machined in order to obtain the complex geometry of the distilled water external channel schematically reported in Figure 3.3, which refers to a segment of the measuring section.

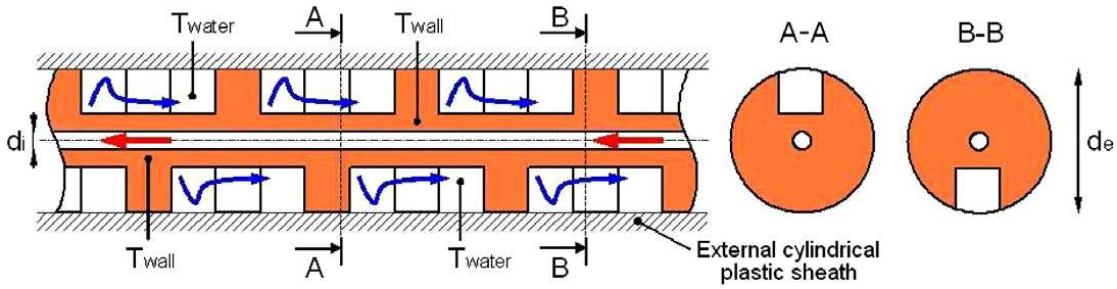

Figure 3.3. Detailed sketch of the test section showing geometry and temperature instrumentation of the water channel along the measuring section.

The inlet and outlet water temperatures are measured by thermocouples at the ends of each part of the test section, while the water temperature differences across both parts are measured by multi-junction copper-constantan thermopiles. Moreover, in the measuring section, the local water temperature profile is calculated from the measurements of fifteen thermocouples placed in the secondary fluid channel. The local wall temperatures are gauged by thirteen thermocouples embedded into 0.6 mm diameter cylindrical holes in the wall thickness, which were realized 0.5 mm far from the internal tube surface along the measuring section (Figure 3.3.4). The accommodation of the wall thermocouples is made in such a way as the thermocouple wires do not cross the coolant path, therefore the error of the temperature measurements due to axial conduction along the thermocouple wire and the spurious electromotive force build up for the presence of high temperature gradients is minimized.

Figure 3.3.4. Enlarged image of the cross section of the fin sample showing the accommodation of a wall thermocouple.

Finally, the water channel is externally closed by plastic sheath. The tortuous path geometry enables good water mixing for precise local coolant temperature measurements, which is essential to obtain a reliable water temperature profile. Furthermore, in such a geometry, the external heat transfer resistance is not the dominant one in the heat transfer process and this point leads to a low uncertainty of heat transfer coefficient. After the

construction, the test section was accurately insulated to minimize heat dissipation. More details on the test section design and building are given in [49].

3.3.3 Calibration and preliminary tests

The pressure transducers are calibrated using a pressure calibrator, as described in Chapter 2. All the temperatures are detected using T-type thermocouples which have been calibrated as well as the thermopiles following the technique illustrated in Del Col *et al.* [50]. During the periodical calibration, water circulates under adiabatic conditions at a temperature close to that of the surrounding ambient in the channel along the measuring section where two high precision four wire thermistors are arranged at the inlet and at the outlet respecively. The thermistors are connected to a Hart Scientific Super Thermometer II forming a measure chain with a global accuracy of ±0.002 °C (as from the check against the water triple point). A correction function for each thermocouple is defined by comparing the temperature measure by the considered thermocouple against the reference temperature gauged by the thermistors. The thermopile are checked considering the disagreement between their readings and a temperature difference of 0 °C. After the calibration, the water and wall thermocouple and thermopiles readings are within ± 0.02 °C as compared to the reference temperature, allowing to state conservatively a Type B experimental uncertainty of the measured temperatures of ±0.05 °C and of the measured temperature difference of ±0.02 °C.
In Figure 3.5, the wall and water thermocouples' readings are reported against the thermistors' reading before and after a periodical calibration. The periodical calibration is repeated at the beginning of every test campaign and the correction on the thermocouples' readings is done only if the disagreements with the reference temperature are not within ±0.05 °C.

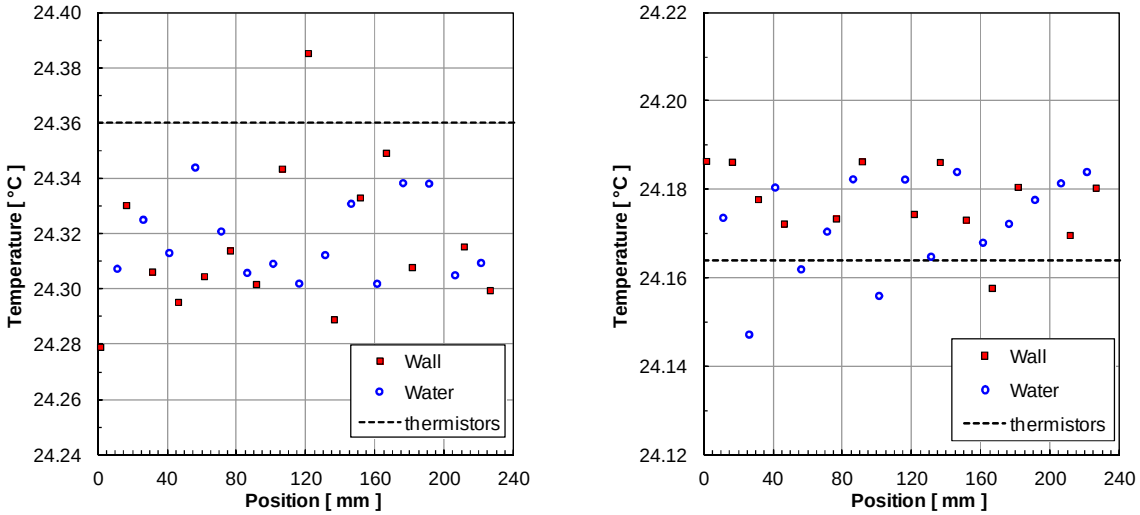

Figure 3.5. Water and wall temperature in the measuring section against the thermistors reading: a) before on-site calibration; b) after on-site calibration.

In addition to the on-site calibration of thermocouples, thermopiles and pressure transducers, some preparatory tests have been conducted in order to assure the accuracy and the repeatability of the measurements. First, the refrigerant temperature at the inlet of the measuring section is detected by the thermocouple during two-phase adiabatic flow at an inlet vapor quality in the range from 0.75 to 0.9 and it has been checked against the saturation temperature derived from the measurement of local pressure. In the test range

of saturation temperature between 30 °C and 40°C, for all the tested fluids, the disagreement is found to be lower than 0.25 °C, which is within the experimental uncertainty range of the two instruments. When the wire heaters placed on the pressure lines are working, no relevant effects are noticed on the check of temperature and pressure under saturated conditions.
Secondly, the energy balance in the test section is controlled by comparing water side heat transfer rate to refrigerant side heat transfer rate when the refrigerant enters the test section as superheated vapor and exits as subcooled liquid. The agreement is found to be within 3.3% for all the considered refrigerants under examination. Finally, as reported in previous works in the same section [51], preliminary tests on the influence of the ambient temperature on the measurements have been performed. The heat losses towards the ambient air were found to be negligible over the entire range of test conditions.

3.4 Condensation tests

3.4.1 Data reduction

During the present condensation tests, the refrigerant enters with 10 °C – 20° C superheating, so the thermodynamic state at the intake of first part of the test section is determined from local pressure and temperature measurements. The inlet condition setter works as a desuperheater and pre-condenser, as in the condensation tests for R290 and R1234ze(E) the refrigerant enters the measuring section under saturated condition, at a vapor quality within 0.75 and 0.9. In Matkovic *et al.* [51], it has been shown that the heat transfer coefficient obtained during condensation in the present test section does not depend on the refrigerant conditions. In other words, it has been stated that the present test apparatus provides exactly the same value of the heat transfer coefficient at the same refrigerant conditions, no matter at which position this coefficient is measured at along the channel. The vapor quality at the inlet of the measuring section is calculated from the energy balance in the inlet condition setter, according to equation (3-I).

$$x_{in,MS} = \frac{1}{h_{LV}} \left[\left(h_{in,ICS} - \frac{\dot{m}_{wat,ICS}}{\dot{m}_{ref}} c_{p,wat}\, \Delta t_{wat,ICS} \right) - h_L \right] \qquad \textbf{(3-I)}$$

Three parameters are used for the determination of the local heat transfer coefficient: in fact, it is defined as the ratio of the local heat flux and the difference between the local saturation temperature and the local wall temperature, as reported in equation (3-II) where *z* is the axial position along the minichannel.

$$\mathrm{HTC}\,(z) = \frac{q'(z)}{t_{sat}(z) - t_{wall}(z)} \qquad \textbf{(3-II)}$$

These parameters can be determined from the measurements of refrigerant, wall and water temperature along the measuring section (see Figure 3.6). As the local wall temperature is directly measured at a certain axial position, the corresponding value of heat flux and saturation temperature should be defined. The local heat flux is calculated from the water temperature profile in the measuring section (equation (3-III)).

$$q'(z) = -\dot{m}_{wat,MS}\, c_{p,wat} \frac{1}{\pi\, d_h} \frac{\mathrm{d}t_{wat}(z)}{\mathrm{dz}} \qquad \textbf{(3-III)}$$

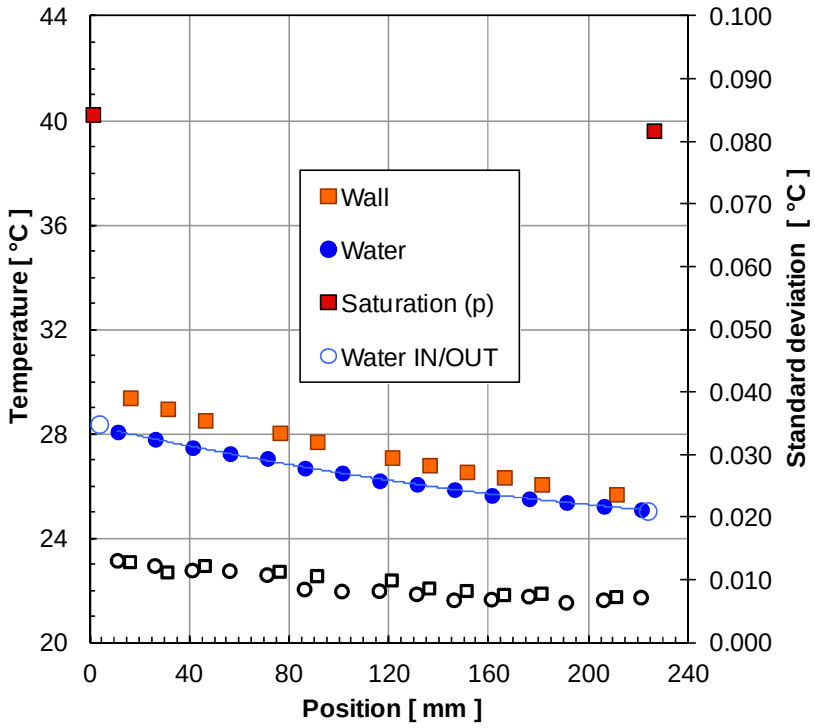

Figure 3.6. Refrigerant, wall and water temperature measurements during condensation of R1234ze(E) at 40°C saturation temperature and 400 kg m^{-2} s^{-1} mass velocity along the measuring section. The empty points represent the standard deviations of wall and water measurements.

In order to obtain the local heat flux, a proper interpolating function of the measured water temperatures along the measuring section is required. First, the number of the water temperatures detected in the actual measuring section to be considered in data reduction is decided. As condensation is the process under investigation, the last employed temperature datum on the water side is the first one at which the thermodynamic vapor quality becomes negative. By considering the conservation of energy in the measuring section, the coolant temperature change is directly associated to the corresponding enthalpy variation of the refrigerant, so the thermodynamic vapor quality correspondent to the *j-th* thermocouple placed in the water flows can be calculated according to equation (3-IV)

$$x_j = x_{in,MS} - \frac{\dot{m}_{wat,MS}}{\dot{m}_{ref}\, h_{LV}} c_{p,wat} \left(t_{wat,out} - t_{wat,j}\right) \qquad \textbf{(3-IV)}$$

Afterwards, three possible interpolating equations are considered in the following order of preference to minimize the uncertainty of heat transfer coefficients: a second order polynomial, an exponential equation with three parameters and a third order polynomial: in fact, the greater the number of parameters, the higher the experimental uncertainty. The exponential function is expressed as:

$$t_{wat}(z) = a_0 + a_1\, e^{-\frac{z}{a_2}} \qquad \textbf{(3-V)}$$

The equation parameters are calculated by means of the least square method. Given the observed water temperature trends during condensation, a higher number of parameters is not required for the present interpolations.
In statistics, the coefficients of determination *R* square (R^2) and adjusted R square (R_{adj}^2) are utilized to assess the fitting procedure (Rawlings *et al.* [52]). Unlike R^2, R_{adj}^2 increases with the number of parameters of the fitting equation only if the new term improves significantly the model. Thus, let y_1 and y_2 be two functions that are one after the other in the aforementioned order of preference: in the present data reduction, by convention, y_1 would be the chosen fitting if the following condition is satisfied:

$$\left|R_{adj}^2(y_1) - R_{adj}^2(y_2)\right| \leq 0.0035 \qquad \textbf{(3-VI)}$$

Besides, the fitting function emerging from the previous statistical criterion has to satisfy a second criterion based on the experimental uncertainty. Specifically, the calculated values of the water temperatures have to be within the expanded experimental uncertainty of the corresponding thermocouple readings and, in addition, at least 68% of the calculated values has be within ± 0.03°C of the corresponding measured values. If this checking test fails, the next fitting equation in the order of preference will be considered and verified. Finally, in order to assure the accuracy and repeatability of the results, the heat transfer coefficients has to result insensitive to the method of interpolation, that is to say that the variation in heat transfer coefficients using the fitting equation that meets the conditions of the statistical and uncertainty criteria and the next admissible equation in the order of preference should be within the experimental uncertainty. If the third order polynomial interpolates the data in the best way, the sensitivity analysis is performed by comparison with the fourth order polynomial fitting.
Once the interpolating equation for the water temperature is established, the local heat flux can be defined along the channel. Actually, from the measurements of the local wall temperatures along the measuring section, it is possible to calculate the contribution of the axial conduction in the copper wall from an energy balance and to correct the value of the heat flux calculated from equation (3-III). This correction term has found to be higher than 5% only at the inlet of the measuring section when working at low mass velocities. Given the fitting function of the water temperatures, the vapor quality can be calculated at any axial coordinate *z* along the tube (equation (3-VII))

$$x(z) = x_{in,MS} - \frac{\dot{m}_{wat,MS}}{\dot{m}_{ref}\, h_{LV}} c_{p,wat} \left(t_{wat,out} - t_{wat}(z)\right) \qquad \textbf{(3-VII)}$$

The saturation temperature is obtained from the values of the pressure measured in the adiabatic segments only at the inlet and outlet of each part of the measuring section. Along the measuring section, the saturation temperature is obtained from the calculation of the local pressure, taking into account the two-phase flow regime condition and the geometry of the test section between the pressure ports upstream and downstream of the measuring section (see Figure 3.7). Thus, the evaluation of the local pressure of the refrigerant is iterative and includes the following terms: the frictional pressure drop in the stainless steel adiabatic sectors, the frictional pressure drop in the copper measuring

section, the pressure variations due to the cross section geometry changes and the pressure recovery due to momentum variation during condensation.

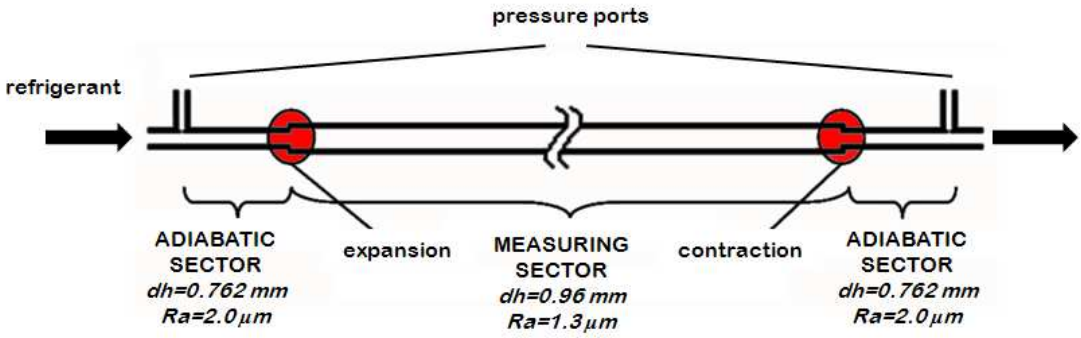

Figure 3.7.Geometry of the test section between the pressure ports located upstream and downstream the measuring section. The abrupt geometry changes between the stainless steel segments and the copper minichannel are highlighted in circles.

The Del Col *et al.* [4] model is taken for frictional pressure drop evaluation, while the pressure variation due to momentum is expressed as reported in Cavallini *et al.* [20], the Paliwoda equation [53] is employed for the evaluation of the pressure drops for abrupt geometry changes under two-phase flow condition and formulae reported in Idelchik [54] are adopted to calculate the pressure drop across a sudden contraction if subcooled refrigerant exits the test section. The resulting pressure gradient is finally multiplied by a corrective factor in order to match the pressure measurement at the outlet of the measuring section.

3.4.2 Uncertainty analysis

In the condensation test runs, each measured quantity (temperature, pressure, mass flow rate) is read and recorded 50 times with a time step of 1 s. All the readings are independent observations of the quantity under the same condition of measurement, thus the mean value is the best expected value of that measured quantity and the standard deviation of the mean represents its Type A standard uncertainty u_A, according to the ISO Guide to the Expression of Uncertainty in Measurement [17]. The Type B standard uncertainty u_B for each measured quantity, on the other hand, derives from calibration certificates or manufacturers' specifications. With reference to the instrument employed during the tests carried out in at the Two-Phase Heat Transfer Lab at the University of Padova, the Type B experimental uncertainties of the measured parameters with a level of confidence of 95.45% where not differently specified are reported in Table 3-a.
The combined standard uncertainty u_C of a measured parameter θ result from the Type A and Type B components according to equation (3-VIII).

$$u_C = \sqrt{u_A(\theta)^2 + u_B(\theta)^2} \qquad \textbf{(3-VIII)}$$

When a searched parameter ξ is not directly measured but it can be expressed as a function F of uncorrelated measured input quantities $\theta_1, \theta_2, \ldots, \theta_N$, as in the case of heat transfer coefficient or thermodynamic vapor quality, its combined standard uncertainty is determined from equation (3-IX).

$$u_C(\xi) = \sqrt{\sum_{i=1}^{N} \left(\frac{\partial F}{\partial \theta_i}\right)^2 u_C(\theta_i)^2} \quad \textbf{(3-IX)}$$

Table 3-a. Type B uncertainty of measured parameters.

Temperature	± 0.05 °C
Temperature difference (with thermopile)	± 0.03 °C
Water flow rate in inlet condition setter	± 0.2 % at 10 kg h^{-1}
Water flow rate in measuring section	± 0.14 % at 10 kg h^{-1}
Refrigerant flow rate	± 0.2 % at 2 kg h^{-1}
Absolute pressure	± 5 kPa (level of confidence: 99.7%)
Pressure difference (greater than 1 kPa)	± 0.12 kPa (level of confidence: 99.7%)
Pressure difference (below 1 kPa)	± 0.1% (level con confidence 99.7%)

According to equation (3-II) and equation (3-III), the function describing the local condensation heat transfer coefficient is:

$$\mathrm{HTC}(z) = F\left(t_{sat}, t_{wall}, \dot{m}_{wat,MS}, \frac{\mathbf{d}t_{wat}}{\mathbf{d}z}, d_h\right) \quad \textbf{(3-X)}$$

In the present technique, because of the geometry of the water channel, the dominant thermal resistance during the condensing process is on the refrigerant side and the saturation to wall temperature difference remains above 10° C. This aspect is favourable to the reduction of the experimental uncertainty associated to the determination of the heat transfer coefficient. As mentioned above, while the local wall temperature is directly measured, the local saturation temperature is estimated by an iterative procedure which implements several models in order to account for the pressure drop due to friction, abrupt geometry changes and momentum variation. Consequently, in this work, it has been considered appropriate to calculate the experimental combined uncertainty for the local saturation temperature from a linear combination of the experimental combined uncertainty of the inlet and outlet saturation temperature, derived from the pressure measurements. The uncertainty of a saturation temperature derived by a pressure measurement is determined by the difference between the value of saturation temperature at the measured pressure *p* and the value of saturation temperature at a pressure equal to $p+u_C(p)$ (equations (3-XI) and (3-XII)).

$$u_C\left(t_{sat,in\,MS}\right) = t_{sat,in\,MS}\left(p_{in,MS}\right) - t_{sat,in\,MS}\left(p_{in,MS} + u_C\left(p_{in,MS}\right)\right) \quad \textbf{(3-XI)}$$

$$u_C\left(t_{sat,out\,MS}\right) = t_{sat,out\,MS}\left(p_{out,MS}\right) - t_{sat,out\,MS}\left(p_{out,MS} + u_C\left(p_{out,MS}\right)\right) \quad \textbf{(3-XII)}$$

Equation (3-XIII) sets out the expression assumed for the uncertainty of local saturation temperature:

$$u_C(t_{sat}(z)) = \sqrt{\left(1 - \frac{z}{L_{MS}}\right)^2 \left(u_C\left(t_{sat,in\,MS}\right)\right)^2 + \left(\frac{z}{L_{MS}}\right)^2 \left(u_C\left(t_{sat,out\,MS}\right)\right)^2} \quad \textbf{(3-XIII)}$$

The other main uncertainty terms are associated to the water mass flow rate, the hydraulic diameter and water temperature gradient. In turn, the water temperature gradient depends on the operating conditions, mainly mass flux and vapor quality, yielding higher uncertainty at lower mass flux. The procedure that has been implemented for determining the uncertainty related to the water temperature gradient is the weighted least square *(WLS)* regression method (Press *et al.* [55]).
As described in section 3.4.1, for each test run a function of the axial position z has been determined to fit the water temperature along the measuring section. The fitting function has been chosen among a second order polynomial, an exponential function or a third order polynomial. Whatever the fitting function *y(z)*, its *M+1* coefficients a_0, …, a_M are defined in order to minimize the merit figure χ^2.
Let *i* varies from 1 to *nTC*, that is the number of water thermocouples considered for the data reduction as described in section 3.4.1 and let $t_{wat,i}$ be the measured values read by the *i-th* water thermocouple located at an axial coordinate z_i. Hence, $y(z_i)$ is the calculated water temperature at the axial position z_i using the fitting function and the merit figure χ^2 is defined as:

$$\chi^2 = \sum_{i=1}^{nTC} \left[\frac{t_{wat,i} - y(z_i)}{u_C(t_{wat,i})} \right]^2 \quad \textbf{(3-XIV)}$$

The minimum of the merit figure occurs where its derivatives with respect to all parameters of the fitting function a_0, …, a_M are equal to zero. This condition yields the following matrix equation:

$$\left(\mathbf{A^T} \cdot \mathbf{A}\right) \cdot \mathbf{a} = \mathbf{A^T} \cdot \mathbf{b} \quad \textbf{(3-XV)}$$

where **A** is a *nTC* x *(M+1)* matrix whose elements are obtained as reported in equation (3-XVI);

$$A_{ij} = \left(\frac{\frac{\partial y}{\partial a_{j-1}}}{u_C(t_{wat,i})} \right) \quad \textbf{(3-XVI)}$$

b is a vector of *nTC* constant terms defined as the ratio between the water temperature measured at the *i-th* location and the correspondent uncertainty:

$$b_i = \left(\frac{t_{wat,i}}{u_C(t_{wat,i})} \right) \quad \textbf{(3-XVII)}$$

and finally **a** is the vector of the *(M+1)* coefficients of the fitting equation. The covariance matrix **C**, defined according to equation (3-XVIII), is closely related to the standard uncertainty of the parameters a_0, …, a_M: the diagonal elements C_{jj} are the square uncertainties of the fitted parameters a_0, …, a_M, while the off-diagonal elements C_{jk} are the covariances between the estimated coefficients a_j and a_k, dubbed cov(a_j, a_k).

$$\mathbf{C} = \left(\mathbf{A}^{\mathbf{T}} \cdot \mathbf{A}\right)^{-\mathbf{1}} \quad \textbf{(3-XVIII)}$$

The elements of the covariance matrix **C** are useful to calculate the uncertainty related to the water temperature gradient by applying the law of propagation of uncertainty for correlated input quantities (equation (3-XIX)). In this calculation, the coefficient a_0 is not present, as it is a constant term in the water temperature fitting function *y(z)*.

$$u_C\left(\frac{\mathbf{d}t_{wat}}{\mathbf{d}z}\right) = \sqrt{\sum_{i=1}^{M}\left(\frac{\partial\left(\frac{\mathbf{d}y(z)}{\mathbf{d}z}\right)}{\partial a_i}\right)^2 \left(u(a_i)\right)^2 + 2\sum_{i=1}^{M-1}\sum_{j=i+1}^{M}\left(\frac{\partial\left(\frac{\mathrm{d}y(z)}{\mathrm{d}z}\right)}{\partial a_i}\right)\left(\frac{\partial\left(\frac{\mathrm{d}y(z)}{\mathrm{d}z}\right)}{\partial a_j}\right)\mathrm{cov}(a_i, a_j)} \quad \textbf{(3-XIX)}$$

As reported in Del Col *et al.* [50], the effect of the uncertainty in the thermocouple location has also been investigated and it was found to be negligible as compared to the uncertainty due to the temperature readings. As it was done for the heat transfer coefficient, the experimental uncertainty is also specified for the vapor quality, which is described along the test section by the following function:

$$x(z) = F\left(x_{in}, \dot{m}_{wat,MS}, c_{p,wat}, t_{wat,out\ MS}, t_{wat}(z), \dot{m}_{ref}, h_{LV}\right) \quad \textbf{(3-XX)}$$

The uncertainty of the latent heat of condensation as well as the uncertainty of the water isobaric specific heat are neglected. The uncertainty of the water temperature at the axial location z is calculated applying the law of propagation of uncertainty for correlated input, according to the chosen fitting function.
The expanded uncertainty for a given quantity is obtained considering a coverage factor equal to 2 and thus a level of confidence of 95.45%.

3.4.3 Experimental results and comparison against correlations of propane

The local heat transfer coefficient has been measured during condensation of propane (R290). The experiments have been performed over the entire range of vapor quality at mass velocity ranging from 100 kg m^{-2} s^{-1} up to 1000 kg m^{-2} s^{-1} and saturation temperature between 40°C and 41°C, correspondent to a saturation pressure between 1369 kPa and 1401 kPa. The refrigerant enters the test section as superheated vapor at a temperature ranging between 50°C and 60°C. The complete set of the experimental heat transfer coefficients measured during condensation is plotted in Figure 3.8 versus vapor quality with the corresponding error bands. Each point in the diagram is associated to a wall temperature reading. The first and the last temperature readings in the wall may be affected to axial boundary effect, therefore they are not considered in the calculation of the heat transfer coefficient. As expected for forced convective condensation inside conventional pipes, the heat transfer coefficient increases with mass velocity and with vapor quality. This fact suggests that in these working conditions, the condensation process inside the single circular minichannel must be dominated by the shear stress.
From these experimental results, propane proves to be very attractive as refrigerant for condensation heat transfer inside minichannels: the heat transfer coefficient is up to 20 kW m^{-2} K^{-1} and the local heat flux is up to 230 kW m^{-2} at 1000 kg m^{-2} s^{-1} mass velocity (see Figure 3.9).

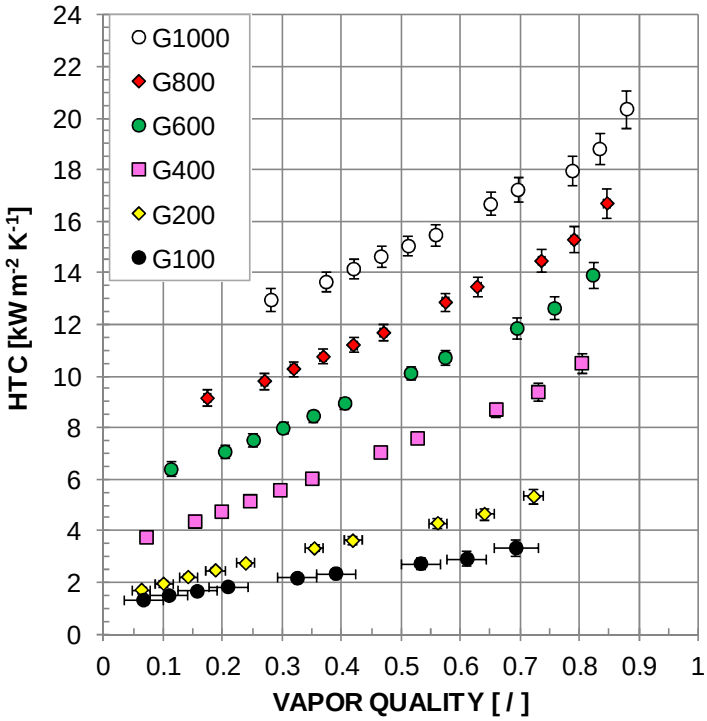

Figure 3.8. Experimental local condensation heat transfer coefficient (HTC) versus vapor quality with the corresponding error bands for propane at 40°C and at mass velocities *G* ranging from 100 kg m^{-2} s^{-1} to 1000 kg m^{-2} s^{-1}.

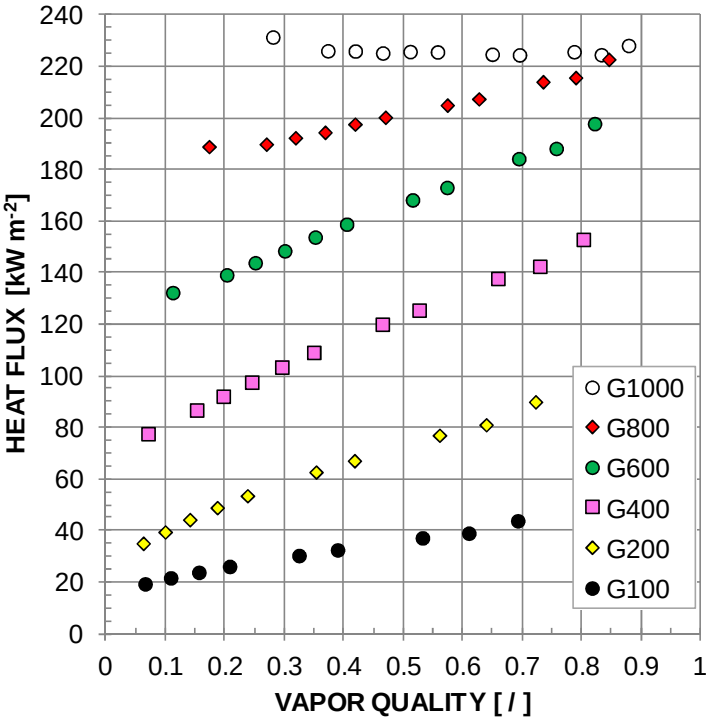

Figure 3.9. Local heat flux versus vapor quality measured during condensation of propane at 40°C and at different mass velocities *G* [kg m^{-2} s^{-1}].

In agreement with the error analysis reported in [51] for the present test section, at high mass velocity the percent expanded uncertainty of heat transfer coefficient is rather

constant in the entire vapor quality range, while at low mass velocities, it has the same trend of the relative uncertainty of heat flux and it is higher at the ends of the measuring section and lower in the centre. As reported in Figure 3.10, at mass velocities, higher than 400 kg m^{-2} s^{-1}, the heat transfer coefficient expanded uncertainty is below ±4%, while at the lowest mass velocity (G = 100 kg m^{-2} s^{-1}) it ranges between ±5% and ±12%.
As regards the vapor quality, the expanded experimental is within ±0.01 at mass velocities higher than 400 kg m^{-2} s^{-1}, whereas it ranges within ±0.02 at G=200 kg m^{-2} $s^{-1}$and within ±0.04 at G=100 kg m^{-2} s^{-1}. For each mass velocity, using the method described in section 3.4.1, the function interpolating the water temperatures along the measuring section resulted to be a second order polynomial.

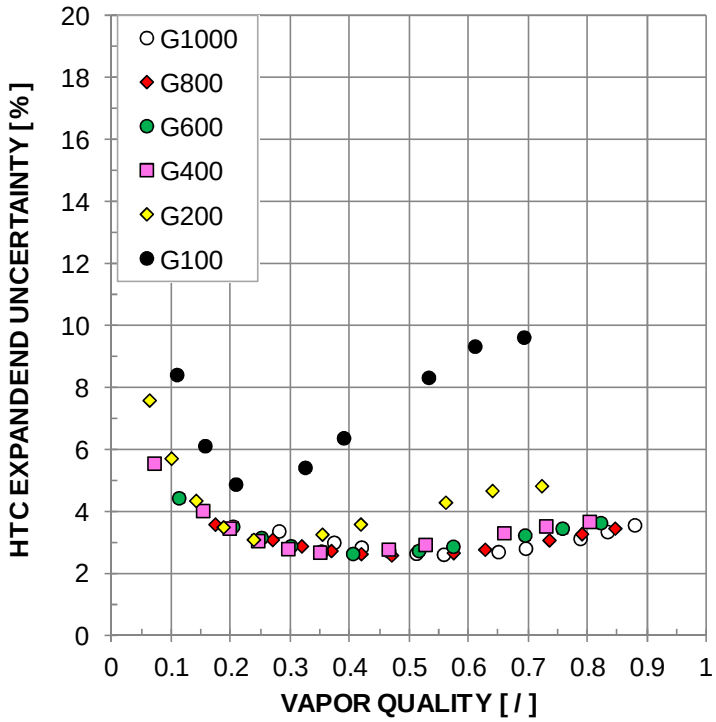

Figure 3.10. Calculated percents (in absolute value) of experimental expanded uncertainty of propane condensation heat transfer coefficients versus vapor quality for all the tested mass velocities *G* [kg m^{-2} s^{-1}].

Experimental results have been compared against three models available in the open literature and developed for condensation heat transfer coefficient predictions.
The first correlation is the one by Cavallini *et al.* [28]., which has been developed for condensation inside smooth channels with hydraulic diameters higher or equal to 3 mm. It was validated against experimental data related to tests performed using HCFCs, HFCs, hydrocarbons, carbon dioxide, ammonia and water. Furthermore, this correlation proved effective in the prediction of condensation heat transfer coefficient in the present test section, as reported in [51], [56] and [57]. It also accounts for the transition from ΔT-independent to ΔT-dependent region, where ΔT is the saturation minus wall temperature difference. All the data points collected for propane at mass velocity higher or equal to 100 kg m^{-2} s^{-1} lay in the ΔT independent region and may be predicted by using a model for annular flow condensation. Figure 3.11 reports the comparison between experimental heat transfer coefficients versus predicted values by using the correlation by Cavallini *et al.*: the propane data are well predicted by this correlation, which is able to catch the

experimental trend. In particular, the average deviation e_R is equal to +7.7% and the standard deviation σ_N results equal to 8.5%.

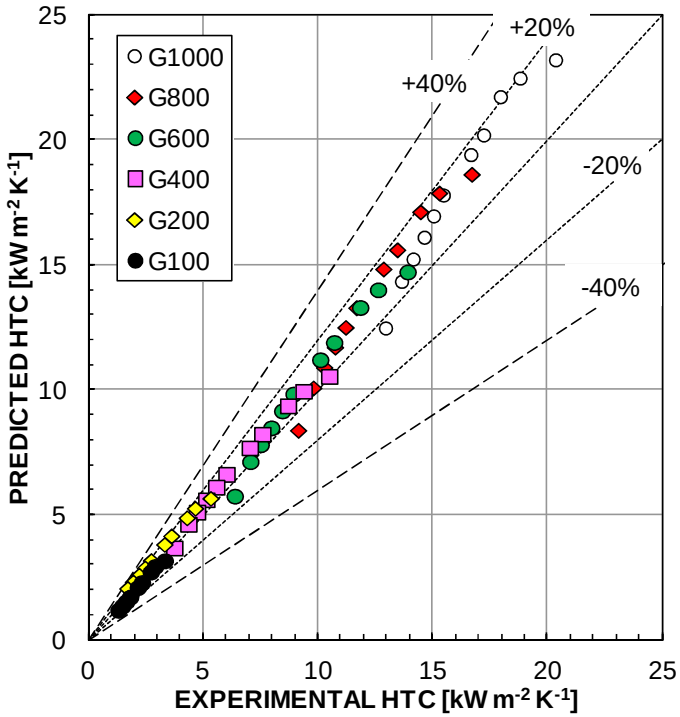

Figure 3.11. Comparison between measurements and calculated heat transfer coefficients (HTC) by Cavallini *et al.* [28] during condensation of propane at 40°C and at different mass velocities *G* [kg m^{-2} s^{-1}].

The second model used in the present comparison is the one by Moser *et al*. [29], which was initially developed for the condensation of halogenated fluids and mixtures inside conventional smooth pipes with internal diameters as small as 3.14 mm and modified by using the Zhang and Webb method [3] for pressure drop calculation inside small diameter channels. This correlation also proved to work well with different fluids in the present test section [51], [56].

The comparison between experimental values and predictions is depicted in Figure 3.12: even if the model by Moser *et al.* extended to the minichannel geometries with the Zhang and Webb pressure drop correlation has never been validated against hydrocarbons, it is able to predict almost all experimental data within ± 20% band, except some points at low vapor quality and low mass velocity. In this case, the average deviation e_R is equal to +5.2% and the standard deviation σ_N results equal to 7.6%.

The third considered correlation is by Shah [30]: it has been developed considering the condensation process inside tubes in a range of hydraulic diameters from 2 mm to 49 mm, in horizontal, vertical and downward inclined orientations. Afterwards, the author has proved that the use of this correlation can be extended to diameters as small as 0.49 mm [58]. Moreover, the Shah correlation has been validated against experimental data of many refrigerants, including CFCs, HCFCs, HFCs, water, organics and hydrocarbons. Among the two regimes identified by Shah in his work, all the present experimental data for propane fall in Regime I.

This model clearly overestimates the heat transfer coefficient of propane in the present test section and for the considered working conditions, as depicted in Figure 3.13; the

average deviation e_R is equal to +31.8% and the standard deviation σ_N results equal to 10.3%.

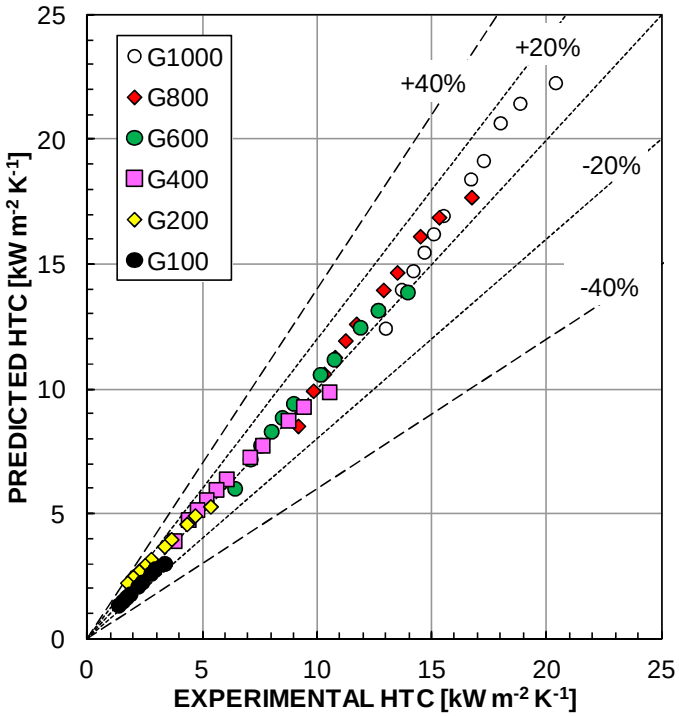

Figure 3.12. Comparison between measurements and calculated heat transfer coefficients (HTC) by Moser *et al.* [29] modified by Zhang and Webb [3] during condensation of propane at 40°C and at different mass velocities *G* [kg m^{-2} s^{-1}].

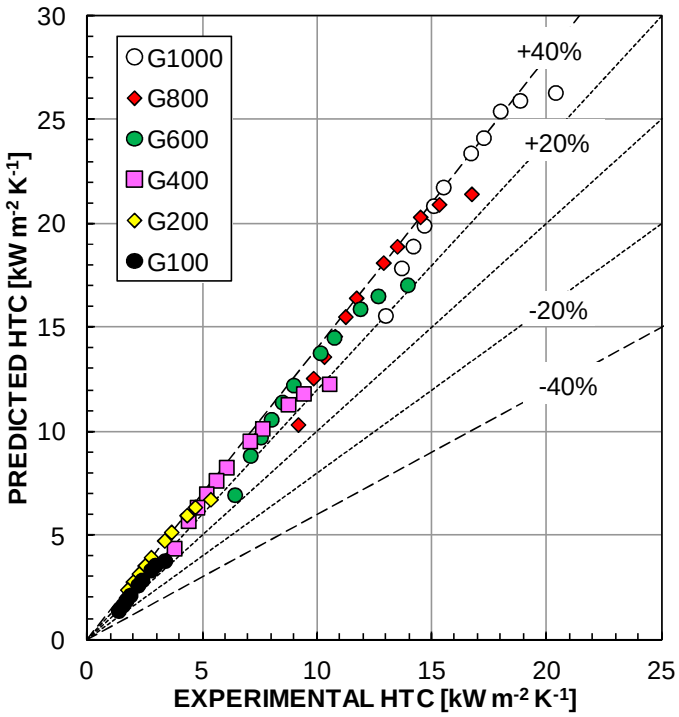

Figure 3.13. Comparison between measurements and calculated heat transfer coefficients (HTC) by Shah [30] during condensation of propane at 40°C and at different mass velocities *G* [kg m^{-2} s^{-1}].

3.4.4 Experimental results and comparison against correlations of R1234ze(E)

The condensation heat transfer test runs for R1234ze(E) are performed with mass velocity ranging from 100 kg m^{-2} s^{-1} to 800 kg m^{-2} s^{-1} at saturation temperature between 39.5°C and 41.5°C, corresponding to a saturation pressure between 756 kPa and 798 kPa. The refrigerant enters the test section as superheated vapor at a temperature ranging between 56°C and 63°C.

The measured experimental condensation heat transfer coefficient is plotted against vapor quality in Figure 3.14 with the relative error bands: the heat transfer coefficient increases with vapor quality and mass velocity above 200 kg m^{-2} s^{-1} suggesting a shear stress dominated heat transfer while it does not vary significantly in the working range between 150 kg m^{-2} s^{-1} and 100 kg m^{-2} s^{-1}. This may indicate that at low mass velocities the shear stress is not the dominating mechanism during condensation, but it can be supposed a major effect of gravity and a different flow regime of the liquid film, from turbulent to laminar. In Figure 3.15, the measured local heat fluxes are reported against the vapor quality.

As shown in Figure 3.16,the expanded experimental uncertainty in percent for heat transfer coefficient is below 6% at 600 kg m^{-2} s^{-1} and at 800 kg m^{-2} s^{-1}, while it is between 10 % and 3% at 400 kg m^{-2} s^{-1}. At lower mass velocity, the expanded experimental uncertainty is lower than 12%.

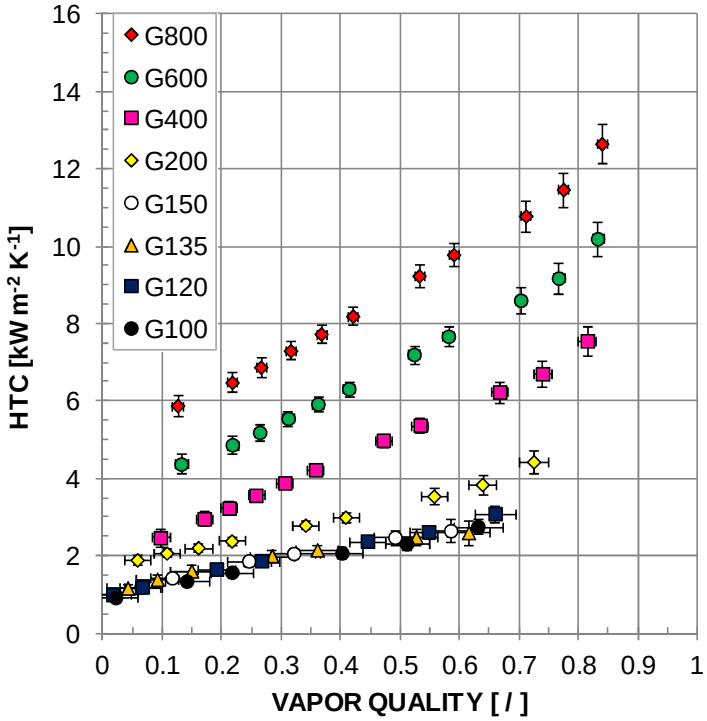

Figure 3.14.Experimental local condensation heat transfer coefficient versus vapor quality with the corresponding error bands for R1234ze(E) at 40°C and at mass velocities *G* ranging from 100 kg m^{-2} s^{-1} to 800 kg m^{-2} s^{-1}.

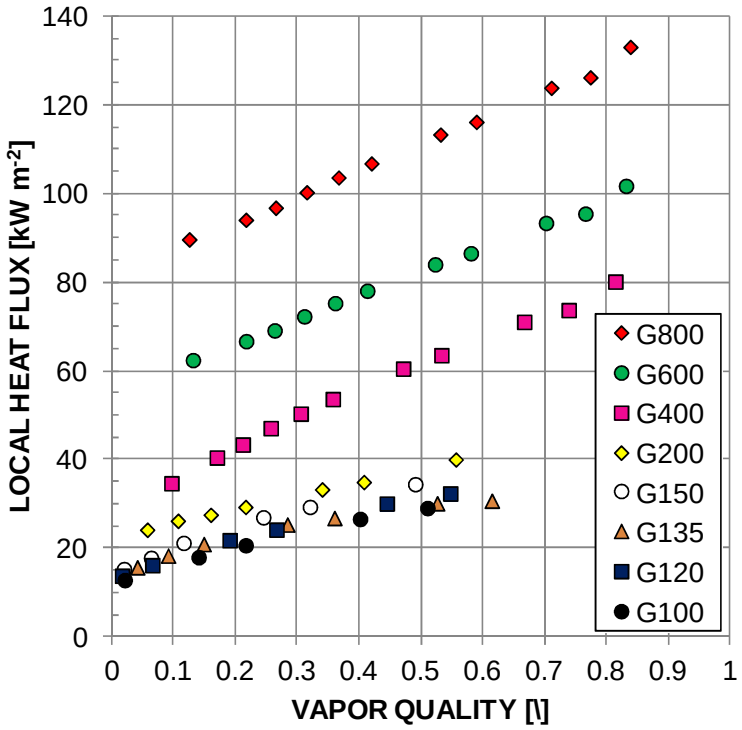

Figure 3.15. Local heat flux versus vapor quality measured during condensation of R1234ze(E) at 40°C and at different mass velocities *G* [kg m^{-2} s^{-1}].

From Figure 3.16, higher values of the percent uncertainty have been found at 150 kg m^{-2} s^{-1} and 135 kg m^{-2} s^{-1} as compared to the values obtained at 120 kg m^{-2} s^{-1} and 100 kg m^{-2} s^{-1}. This can be explained making two considerations. At mass velocity lower than 200 kg m^{-2} s^{-1}, the condensation process is no more dominated by the shear stress and generally a second order polynomial could not catch well the water temperature trend in the entire measuring section. At the outlet of the measuring section, when operating with low mass velocities (120 kg m^{-2} s^{-1} and 100 kg m^{-2} s^{-1}), the refrigerant exits as slightly subcooled liquid and the condensation process finishes inside the measuring section, so no heat transfer coefficient is calculated in this part of the minichannel. Furthermore, as a consequence of the previous observations, the number of water thermocouples employed in the data reduction at 120 kg m^{-2} s^{-1} and 100 kg m^{-2} s^{-1} is lesser that that related to the data sets at 135 kg m^{-2} s^{-1} and 150 kg m^{-2} s^{-1}. Thus, different interpolating functions comes out from the procedure described in 3.4.1: at 150 kg m^{-2} s^{-1} and 135 kg m^{-2} s^{-1} a third order polynomial has been used while at 120 kg m^{-2} s^{-1} and 100 kg m^{-2} s^{-1} a second order polynomial is good enough to satisfy the selection criteria.
The expanded experimental uncertainty for vapor quality is within ± 0.01 at 800 kg m^{-2} s^{-1} and within ± 0.04 at 100 kg m^{-2} s^{-1}.
During the condensation tests with the halogenated olefin R1234ze(E), an investigation on the effect of the water temperature at the inlet of measuring section on the heat transfer coefficient has been performed. At a constant mass velocity of 200 kg m^{-2} s^{-1}, the water temperature has been gradually incremented from 21.2°C to 30°C. These variations of the water temperature imply a change of the wall temperature.
The results (Figure 3.17) show that the difference in heat transfer coefficients calculated with water entering at different temperatures, thus with refrigerant entering at different vapor qualities, is within the experimental uncertainty. Thus, one can conclude that the water inlet condition and the inlet vapor quality have no effect on the calculated heat transfer coefficients. These results reconfirm the remarks on the non-sensitivity of the

heat transfer coefficient to water conditions in the work by Matkovic *et al.* [51] and once again can be regarded as an additional assessment of the experimental technique.

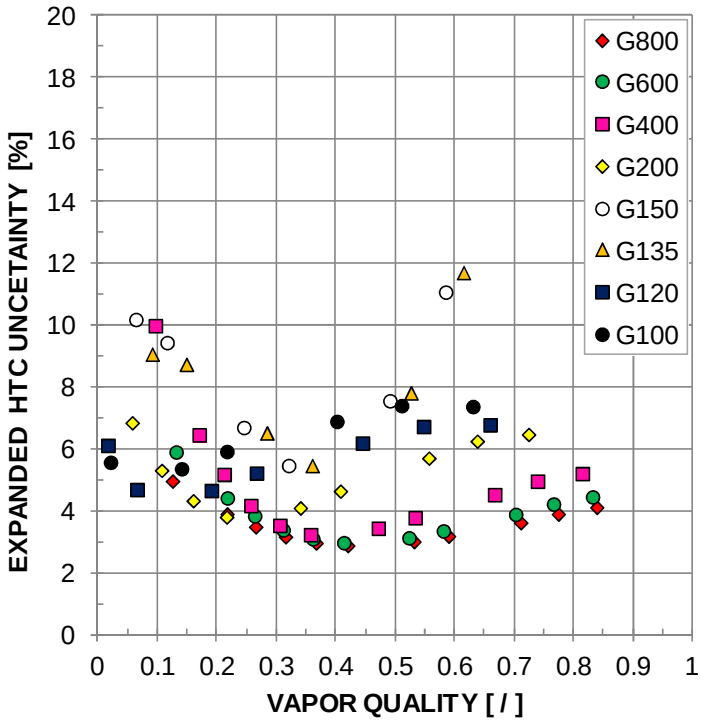

Figure 3.16. Calculated percents in absolute values of experimental expanded uncertainty of R1234ze(E) condensation heat transfer coefficients (HTC) versus vapor quality for all the tested mass velocities *G* [kg m^{-2} s^{-1}].

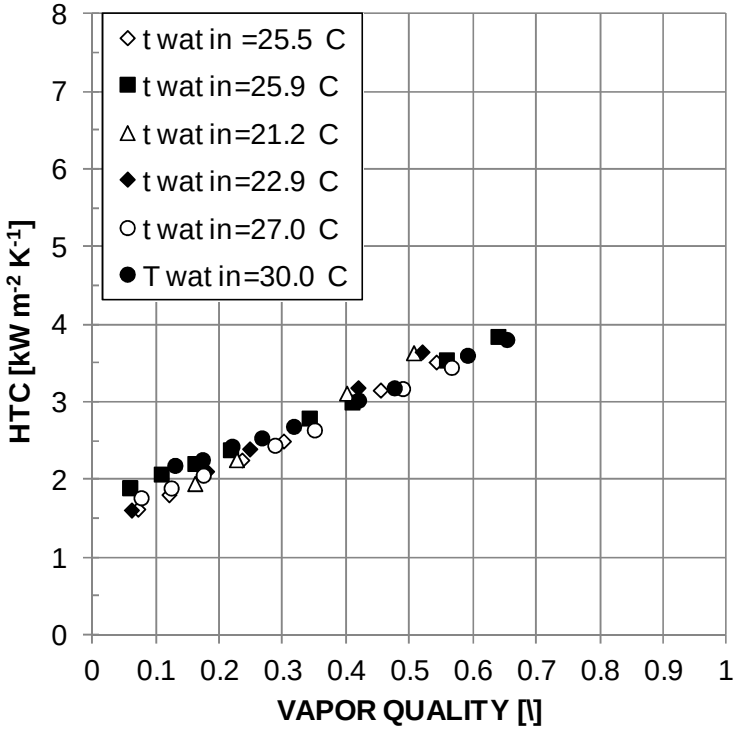

Figure 3.17. Experimental local heat transfer coefficient (HTC) versus vapor quality for R1234ze(E) at 200 kg m^{-2} s^{-1} at 40°C saturation temperature and at different inlet water temperatures ($t_{wat,in}$).

In Figure 3.18, the present database is compared against the model by Cavallini *et al.* [28]. The experimental point at mass velocity higher than 200 kg m^{-2} s^{-1} are included in the ΔT-independent region, while the experimental points related to the following working conditions lie in the ΔT-dependent region:

- 150 kg m^{-2} s^{-1} mass velocity and vapor quality lower than 0.25;
- 135 kg m^{-2} $s^{-1}$and 120 kg m^{-2} s^{-1} mass velocities and vapor quality lower than 0,4;
- 100 kg m^{-2} s^{-1} mass velocity in the entire range of vapor quality.

From the comparison, on the whole, it can be seen that the collected data for R1234ze(E) are well predicted by the model: the average deviation between experiments and predictions e_R is -10.3% and the standard deviation σ_N is 8.5 %. Only some data at vapor quality below 0.1 are not predicted within ±30%, but this is most probably due to the different flow regime that one would expect on such operating conditions in a minichannel as compared to a conventional channel.

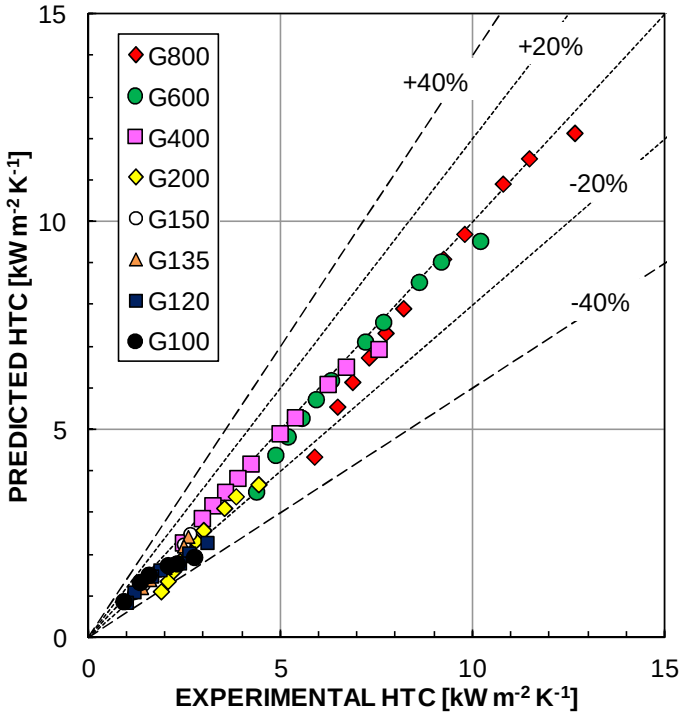

Figure 3.18. Comparison between measurements and calculated heat transfer coefficients (HTC) by Cavallini *et al.* [28] during condensation of R1234ze(E) at 40° and at different mass velocities *G* [kg m^{-2} s^{-1}].

The second comparison is shown in Figure 3.19, where the predicted heat transfer coefficients are calculated using the model by Moser *et al.* [29] applied with the correlation by Zhang and Webb [3] for pressure drop in small diameters channels. This correlation tends to underestimate the heat transfer coefficient and the major percentage deviations are found at low mass velocities probably because here the working conditions are out of the validation range of the model, which is limited to the annular flow regime (e_R = -10.8%, σ_N = 8.7 %.). Finally, the correlation by Shah [30] overestimates the experimental data at mass velocities higher than 400 kg m^{-2} s^{-1} and tends to underestimate the heat transfer coefficients at mass velocities up to 200 kg m^{-2} s^{-1} (Figure 3.20), nevertheless all the collected points lie in the flow regime dubbed Regime I. As a consequence, the average deviation is very low (e_R = 1.45%), but the high standard

deviation (σ_N = 15.3 %.) indicates that this model is not able to catch the trend of the experimental data.

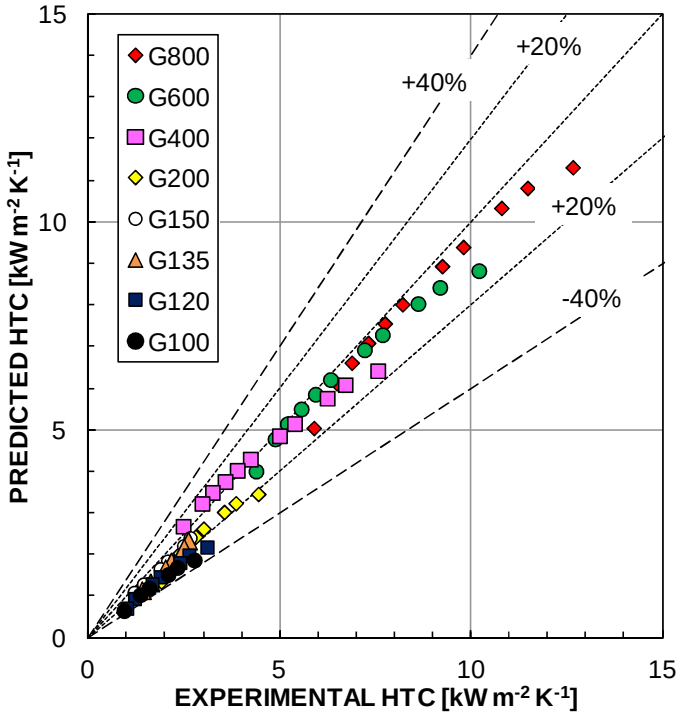

Figure 3.19. Comparison between measurements and calculated heat transfer coefficients (HTC) by by Moser *et al.* [29] modified by Zhang and Webb [3] during condensation of R1234ze(E) at 40° and at different mass velocities *G* [kg m^{-2} s^{-1}].

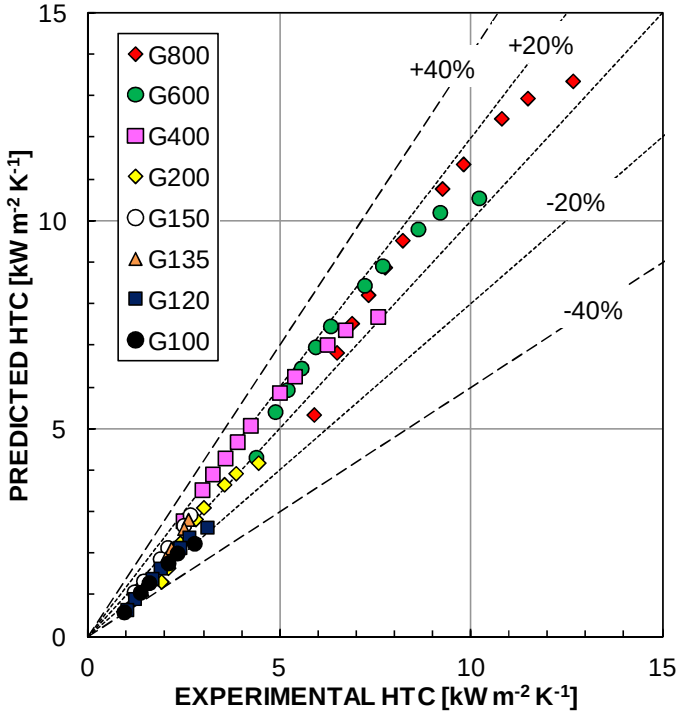

Figure 3.20. Comparison between measurements and calculated heat transfer coefficients (HTC) by Shah [30] during condensation of R1234ze(E) at 40° and at different mass velocities *G* [kg m^{-2} s^{-1}].

3.5 Flow boiling tests

3.5.1 Data reduction

During flow boiling tests, the refrigerant is slightly heated up in the tube-in-tube heat exchanger and in the inlet condition setter, the water mass flow rate and its inlet temperature are set so that the refrigerant enters the measuring section as a liquid with few degrees of subcooling (2°C -5 °C). Thus, the flow boiling process occurs only in the measuring section, where the inlet water temperature is increased until the trigger of the vaporization. For all the tested refrigerants, the saturation temperature is 31°C. At constant mass velocity, inlet temperature and saturation temperature of the working refrigerant, the test runs have been performed first increasing the water temperature at the inlet of the measuring section and then decreasing it. In the first case, the raise of the inlet water temperature leads to an increase of the wall to saturation temperature difference and of the heat flux. This procedure allows to observe if an hysteresis can be found in the boiling curve. If not otherwise specified, all the experimental points reported in this section are taken decreasing the water temperature when all the nucleation sites have been activated.
The peculiarity of the present tests is that, in the measuring section, the refrigerant vaporizes by heat transferring with hot water, thus the heat flux is not imposed.
Two different situations have been observed during the flow boiling of each refrigerant, as reported in the following charts.

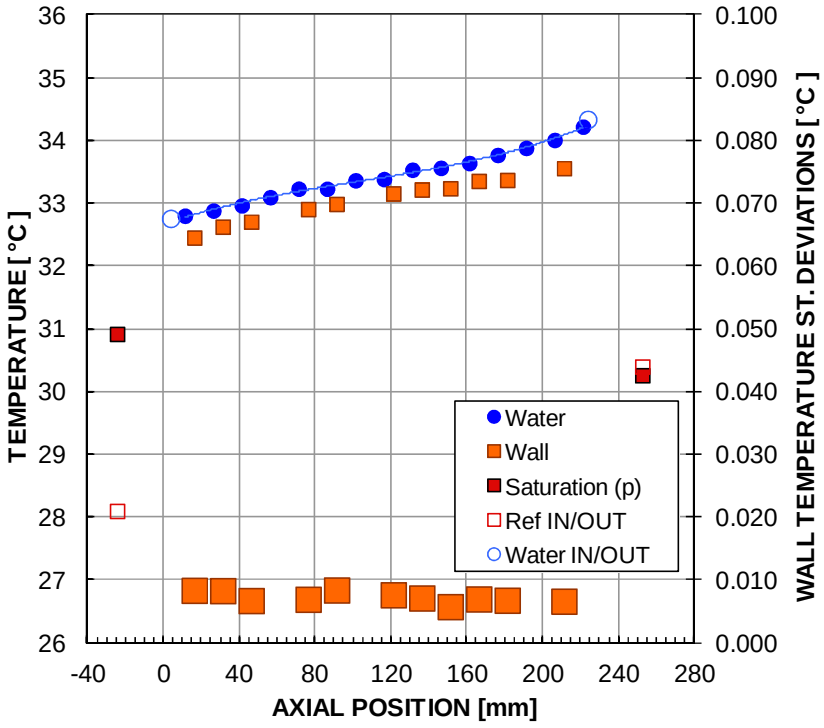

Figure 3.21.Water, wall and saturation temperature during the boiling process of R1234ze(E) at 31°C in the 0.96 mm diameter channel at G = 300 kg m^{-2} s^{-1}. The big square dots represent the standard deviation of the wall temperature measurements.

Figure 3.21 shows the refrigerant, wall and water temperature measurements along the measuring section during flow boiling of the halogenated olefin R1234ze(E) at 31°C and at a mass velocity G of 300 kg m^{-2} s^{-1}.
In this test run, the refrigerant enters the measuring section at a saturation temperature of 31°C with 3°C of subcooling. The saturation temperatures refer to the pressure measured upstream and downstream the measuring section. At the exit, the saturation temperature is decreased due to pressure drop. The water enters from the opposite end of the test tube at 34.3°C and its temperature decreases due to the heat transfer to the boiling refrigerant. As the vaporization proceeds, the wall temperature increases uniformly up to the end of the test section and the refrigerant exits as saturated vapor.
Figure 3.21 also shows the standard deviation of the temperature measurements in the wall: the limited deviations prove that no dryout occurs in the channel according to the consideration of Del Col and Bortolin [59].
In some of the test runs, the refrigerant exits as superheated vapor or saturated vapor with quality close to one. In this case, the heat flux increases with vapor quality in the channel up to a certain point, where the wall starts to dry up and the wall temperature deviates from its trend to approach the water temperature. As an example,
Figure 3.22 depicts the refrigerant, wall and water temperature measurements along the measuring section during flow boiling of propane at G = 400 kg m^{-2} s^{-1}.

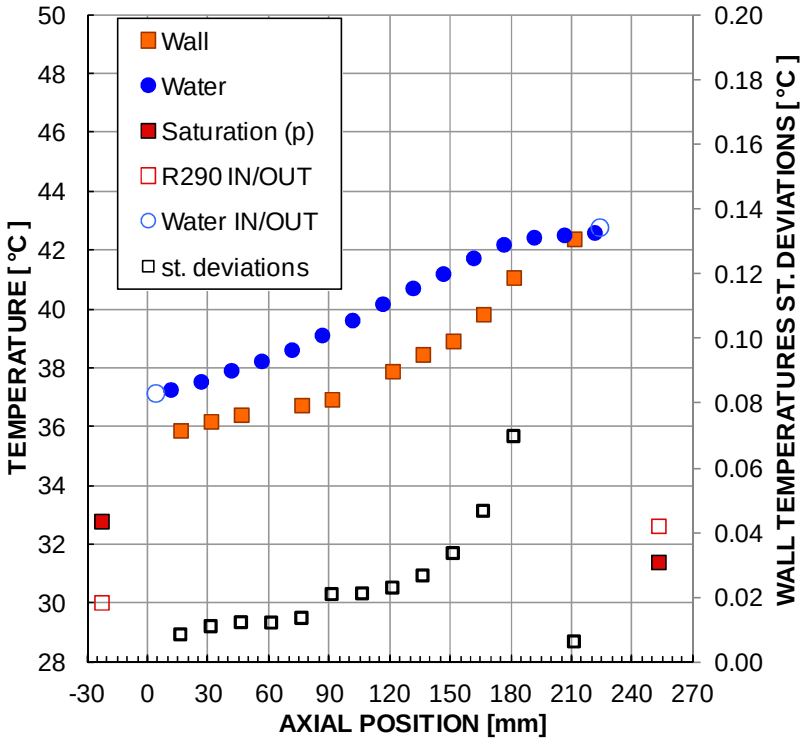

Figure 3.22. Water, wall, refrigerant, saturation temperature and standard deviation of the wall temperature measurements during a flow boiling process of propane in the 0.96 mm diameter channel at 31°C saturation temperature and G=400 kg m^{-2} s^{-1} mass velocity.

The refrigerant enters the measuring section with 2.8 °C subcooling and exits the test section with 1.2 °C superheating while the saturation temperature between the pressure ports decreases 1.4 °C due to pressure drop. The water flow is in countercurrent with an inlet temperature equal to 42.8°C and cools to an outlet temperature of 37.2°C as it transfers heat to the boiling refrigerant. As regards the wall temperature, it increases

uniformly as the vaporization proceeds up to the distance of 180 mm, than a sudden change occurs with a sensible diminishing in the difference between water and wall temperature. In the last part of the channel, this temperature difference approaches zero, revealing an abrupt decrease in the heat transfer coefficient on the refrigerant side. At the same distance, the standard deviation trend of wall temperature readings shows a clear maximum. These trends are related to the dryout of the liquid film on the internal surface of the minichannel and the temperature fluctuation is the symptom of an oscillating drying process of the film at the wall [59]. All the data points reported in the present section refer to boiling conditions before the dryout occurs.
The local heat transfer coefficient (HTC) inside the minichannel is obtained as the ratio of heat flux *q'(z)* to the wall to saturation temperature difference.

$$\mathrm{HTC}\ (z) = \frac{q'(z)}{t_{wall}(z) - t_{sat}(z)} \qquad \textbf{(3-XXI)}$$

As previously mentioned, the wall temperature is measured by means of thermocouples embedded in the copper tube. The local saturation temperature is determined from the calculation of the pressure profile along the channel starting from the pressure measurements at the inlet of the measuring section. In this case, the implemented correlations are the following: the equations by Churchill [18] for the pressure drop related to the subcooled liquid flow at the inlet of the tested minichannel under laminar or turbulent flow condition, the formulae reported in Idelchik [54] for the pressure drop across the inlet expansion, the correlation by Del Col [4] for two-phase frictional pressure drop, the Rohuani and Axelsson [60] model for the void fraction in boiling region to compute the pressure variation due to momentum and the Paliwoda [53] equation for the pressure drop across the outlet contraction under two-phase flow condition. The calculated pressure gradient is corrected by a multiplicative empirical coefficient to match the measured pressure drop along the measuring section.
The local vapor quality calculation takes into account the fact that the refrigerant enters the measuring section as subcooled liquid and requires the calculation of the local water temperature at the axial position *z*, according to equation (3-XXII):

$$x(z) = \frac{\dot{m}_{wat,MS}\ \boldsymbol{c_{p,wat}}\left(t_{wat}(z) - t_{wat,out}\right) - \dot{m}_{ref}\left(h_L - h_{sub,in,MS}\right)}{\dot{m}_{ref}\ h_{LV}} \qquad \textbf{(3-XXII)}$$

The specific enthalpy of the subcooled refrigerant is determined from the inlet pressure and temperature measurements.
In order to obtain the local heat transfer coefficient (equation (3-XXI)) the local heat flux *q'(z)* is also needed. Two different procedures denoted as method 1 and method 2 have been implemented: in the first method the local heat flux is determined from the temperature profile of the water along the measuring section; as in the condensation tests; in the second method the heat flux is obtained from an estimation of the water heat transfer coefficient.
Whichever the method, the local heat flux is corrected accounting for the axial thermal conduction arisen from the wall temperature profile and the heat losses to the surrounding environment, which have been evaluated during a preliminary calibration.

3.5.2 Determination of the local heat flux

3.5.2.1 Method 1

The local heat flux *q'(z)* is indirectly determined from the temperature profile of the coolant in the measuring section, as it is proportional to the derivative of the distilled water temperature with respect to the axial position *z*. This procedure is very similar to that implemented in the condensation test runs.

$$q'(z) = \dot{m}_{wat,MS}\, c_{p,wat} \frac{1}{\pi\, d_h} \frac{\mathrm{d}t_{wat}(z)}{\mathrm{dz}} \qquad \textbf{(3-XXIII)}$$

A polynomial function is used to interpolate the water temperature profile along the channel and the polynomial coefficients are determined using the least square method. Two independent criteria (as reported in Del Col *et al.* [61]) have been adopted for the determination of the fitting polynomial degree of the water temperature along the channel. The first criterion derives from physical considerations. It is based on the assumption that the values of the water temperatures calculated by the fitting equation should be within the experimental uncertainties of the measured quantities and at least 68% of the predicted values should be within ±0.03°C with respect to the experimental values. In the second criterion, a statistical approach is taken into account: the coefficient of determination *R* square (R^2) is adjusted on the basis of residual degree of freedom, leading the definition of the adjusted *R* square (R_{adj}^2) coefficient [52]. In most of the test cases, the two methods have given the same interpolation polynomial function, in any case, the values of heat transfer coefficients have been considered only when the disagreement between the values provided by the two methods is within the expanded experimental uncertainty. The weak point of the method 1 is the inapplicability in cases when dryout occurs. In fact, after the dryout takes place, the wall temperature approaches the water temperature as a consequence of an abrupt decrease of the refrigerant heat transfer coefficient due to the presence of vapor on the internal wall surface. In this situation, the water temperature exhibits a trend that cannot be described properly by a simple fitting equation, making this procedure not reliable.

3.5.2.2 Method 2

Differently from the previous approach, this method is desired to be independent on the choice of the polynomial degree that interpolates the profile of water temperature during the flow boiling tests.
This procedure aims at computing the heat flux by estimating the single-phase convective heat transfer coefficient on the water side. Since the water flows through the complex external path from one groove to the following one, it is very difficult to define the flow regime. In this work, the heat transfer coefficient is correlated to the Reynolds number and the Prandtl number of the water by means of a Dittus-Boelter type relationship. It should be noticed that the tortuous external water path cannot lead to a unique definition of the Reynolds number. The Reynolds number is thus defined with reference to a cross section connecting a groove to the following one along the water path, with an area equal to $6.5 \cdot 10^{-6}$ m^2 and a hydraulic diameter equal to 0.003 m (section A-A or B-B in Figure 3.3). With these premises, at each wall thermocouple position, a Dittus-Boelter correlation has been developed in the form of equation (3-XXIV).

$$\mathrm{Nu} = C\ \mathrm{Re}^{m}\ \mathrm{Pr}^{0.33}\left(\frac{\mu}{\mu_{wall}}\right)^{0.11} \quad \textbf{(3-XXIV)}$$

In order to determine the constants *C* and *m*, condensation test runs have been performed with R1234ze(E) varying the water mass flow rate and the water inlet temperature. The local heat flux as well as the local water temperature have been calculated applying the first method. During these condensation tests, the mass velocity of refrigerant has been kept at values higher than 400 kg m^{-2} s^{-1}, hence the experimental uncertainty on the calculated heat flux is quite low, because a second order polynomial equation was always sufficient to obtain a good fitting of the water temperature according to the selection criteria. The refrigerant used during these condensation tests is irrelevant with respect to the investigation of the heat transfer in forced convection on the water side. The experimental water heat transfer coefficient is determined dividing the local heat flux by the local wall-to-water temperature difference in correspondence to each wall thermocouple position.
The considered Dittus-Boelter type relationship has proved to fit well the experimental data and the parameters *C* and *m* have been found for each wall thermocouple position by linearizing the nonlinear problem according to equation (3-XXV) and applying the least square method.

$$ln\left(\frac{Nu}{\mathrm{Pr}^{0.33}\left(\frac{\mu}{\mu_{wall}}\right)^{0.11}}\right) = \ln(C) + m ln(\mathrm{Re}) \quad \textbf{(3-XXV)}$$

After the equations of water side heat transfer coefficient are determined, the new procedure can be used to evaluate the heat flux during propane and R1234ze(E) flow boiling tests. In fact, in each vaporization test, the water mass flow rate is measured by means of a Coriolis mass flow meter: thus, in conjunction with the water temperature measurements, it is possible to calculate the water thermodynamic properties and the Reynolds number. The Nusselt number and the water side heat transfer coefficient will be computed through the proper Dittus-Boelter type correlation. Hence, the local heat flux on the water side *q'(z)* will be determined by multiplying the water side heat transfer coefficient $\alpha_w(z)$ by the temperature difference between the water and the wall.

$$q'(z) = \mathrm{HTC}_{wat}(z)(t_{wat}(z) - t_{wall}(z)) \quad \textbf{(3-XXVI)}$$

When using this procedure, the water temperature at the axial position *z* can be estimated from a linear interpolation of the two nearest water thermocouples readings with a negligible error. The method 2 can be applied to calculate the quality, the heat transfer coefficient and local heat flux even at the onset of the dryout.

3.5.3 Uncertainty analysis

The uncertainty analysis has been conducted according to the ISO Guide to the Expression of Uncertainty in Measurement [17] using the same method described for condensation tests. As describe in section 3.4.2, in order to find the uncertainty of the heat flux defined with the method 1, the uncertainty related to the polynomial fitting coefficients must be known. On the other side, when applying the method 2, the

calculation of the uncertainty associated with regression parameters *C* and *m* of each correlation corresponding to a wall thermocouple axial position is required and it is obtained as illustrated below.
Equation (3-XXV) expresses a fitting model that linearly depends on the parameters ln*(C)* and *m*, thus the covariance matrix obtained applying the weighted least square regression method is exact. For the sake of simplicity, let equation (3-XXV) be written in the following form:

$$\hat{y} = \ln(C) + m\hat{x} \qquad \textbf{(3-XXVII)}$$

The related covariance matrix **C** (equation (3-XXVIII) is directly associated to the uncertainty of the fitting parameters: in this case, its diagonal terms represent the square uncertainty of *ln(C)* and *m* respectively, while its off diagonal terms correspond to the covariance between the fitting parameters *ln(C)* and *m*.

$$\boldsymbol{C} = \begin{bmatrix} \frac{1}{u^2(\hat{y})} & \frac{x}{u^2(\hat{y})} \\ \frac{x}{u^2(\hat{y})} & \frac{x^2}{u^2(\hat{y})} \end{bmatrix}^{-1} \qquad \textbf{(3-XXVIII)}$$

The uncertainty on the left side of equation (3-XXVII) is determined by the uncertainty in the Nusselt number, which in turn depends on the experimental uncertainty on the heat transfer coefficient on the water side. The experimental uncertainty on the thermo-physical properties of the water are neglected. Now, the relationship between the variance of *ln(C)* and the variance of *C* is easily found from equation (3-XXIX):

$$u^2(F(\theta)) = u^2(\theta)\left(\frac{dF(\theta)}{d\theta}\right)^2 \qquad \textbf{(3-XXIX)}$$

Finally, the relationship between the covariance of *m* and *C* and the covariance of *m* and *ln(C)* can be found applying the law of propagation of errors to equation (3-XXVII) considering two set of parameters. First, if the considered parameters are *m* and *C*, the variance of *y*, that is the square uncertainty of *y* can be expressed as:

$$u^2(\hat{y}) = u^2(m)\hat{x}^2 + u^2(C) * \frac{1}{C^2} + 2\frac{\hat{x}}{C}\mathrm{cov}(m, C) \qquad \textbf{(3-XXX)}$$

On the other hand, if the law of propagation of errors is applying with respect to the parameters *m* and ln*(C)*, the square uncertainty of *y* is

$$u^2(\hat{y}) = u^2(m)\hat{x}^2 + u^2(\ln(C)) + 2\hat{x}\mathrm{cov}(m, \ln(C)) \qquad \textbf{(3-XXXI)}$$

Equating the two expressions and considering equation (3-XXIX), it follows that:

$$\mathrm{cov}(m, C) = \mathrm{cov}(m, \ln(C)) * C \quad \textbf{(3-XXXII)}$$

A checking of this uncertainty analysis has been performed by calculating the estimated covariance matrix from the non linear model derived from equation (3-XXIV) in the form:

$$\hat{y} = C\ \mathrm{Re}^{m} \quad \textbf{(3-XXXIII)}$$

It has been proved that the two procedures give the same variances of *C* and *m* and the same covariance between these two parameters.

3.5.4 Experimental results and comparison against correlations for propane

Flow boiling tests have been performed with propane at mass velocities ranging from 100 kg m^{-2} s^{-1} to 600 kg m^{-2} s^{-1} and at a saturation temperature of 31°C, which corresponds to a saturation pressure of 1106 kPa. The present investigation is not performed by using electrical heating to promote the boiling heat transfer; the heat is transferred to the evaporating fluid by using a secondary circuit as in the case of automotive and domestic air conditioning. In this way, the inlet temperatures and the mass flow rates of the two fluids are imposed while the local heat flux results from the testing conditions (it is a dependent variable).
Two methods have been employed for the determination of the local heat flux: the validation of the experimental technique for the investigation of the flow boiling heat transfer process inside the circular minichannel can be performed comparing the heat transfer coefficients obtained with each method during the same test run. Hence, in Figure 3.23, two sets of data are plotted: they refer to test runs at 300 kg m^{-2} s^{-1} and 400 kg m^{-2} s^{-1}. The error bands for each measured quantity are reported. In both cases, a satisfactory agreement between results of method 1 and method 2 is found. On average, the expanded experimental uncertainty of heat transfer coefficient with a level of confidence of 95% is equal to 8.5% when the local heat flux is calculated with method 1 and it is around 16.4% when the method 2 is employed. Because of the lower uncertainty, the method 1, which is based on the interpolation of the water temperatures to calculate the local heat flux, has been chosen hereinafter to present the experimental data. On the other hand, as a result of the present analysis, the method 2 has been validated and can be reliably use to study the heat transfer process during dryout, as in this case the calculation of the local heat flux is independent of the interpolation of water temperatures. In Table 3-b, the expanded uncertainty of vapor quality and heat transfer coefficient with a level of confidence of 95.45% is reported when using the method 1 in the data reduction for the tests with propane.

Table 3-b. Experimental expanded uncertainty of vapor quality and heat transfer coefficient during the flow boiling tests with propane

Heat transfer coefficient experimental uncertainty (%)	5 % - 16 %
Percent of data within ± 12 % band of uncertainty	90 %
Vapor quality experimental uncertainty (-)	0.01 – 0.02

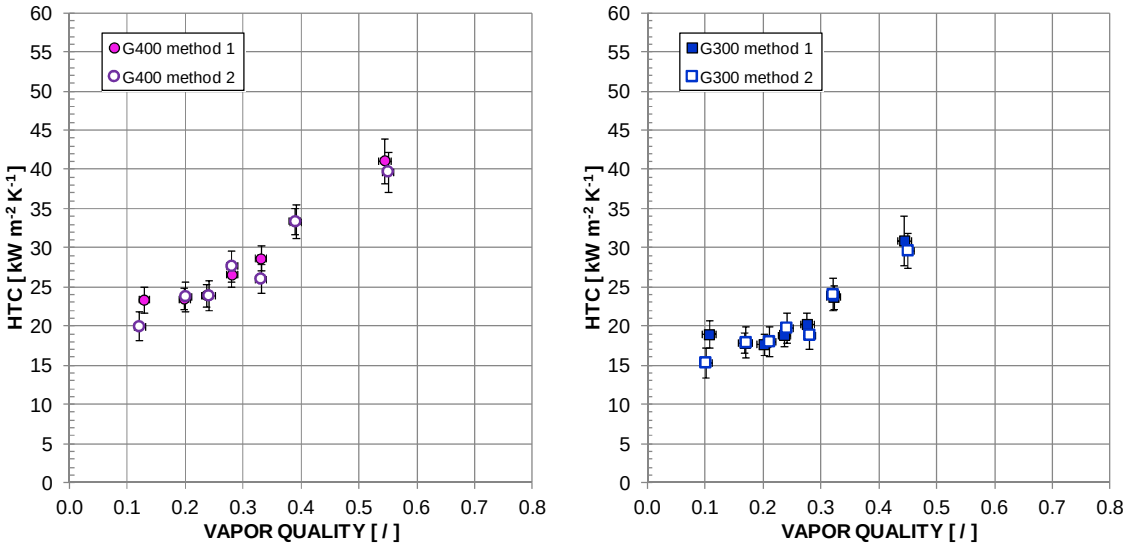

Figure 3.23. Comparison between the heat transfer coefficients (HTC) obtained during the flow boiling of propane using the two methods for heat flux determination. Left: data set at G = 400 kg m^{-2} s^{-1} mass velocity. Right: data set at G = 300 kg m^{-2} s^{-1} mass velocity.

Some results of the tests carried out by increasing and then decreasing the temperature of the water entering the measuring section are reported in the boiling curve in Figure 3.24. The boiling curve refers to a flow boiling trial at 500 kg m^{-2} s^{-1} and to a fixed axial position z = 166 mm. No hysteresis effect of the heat flux variation on the flow boiling heat transfer coefficients has been found.

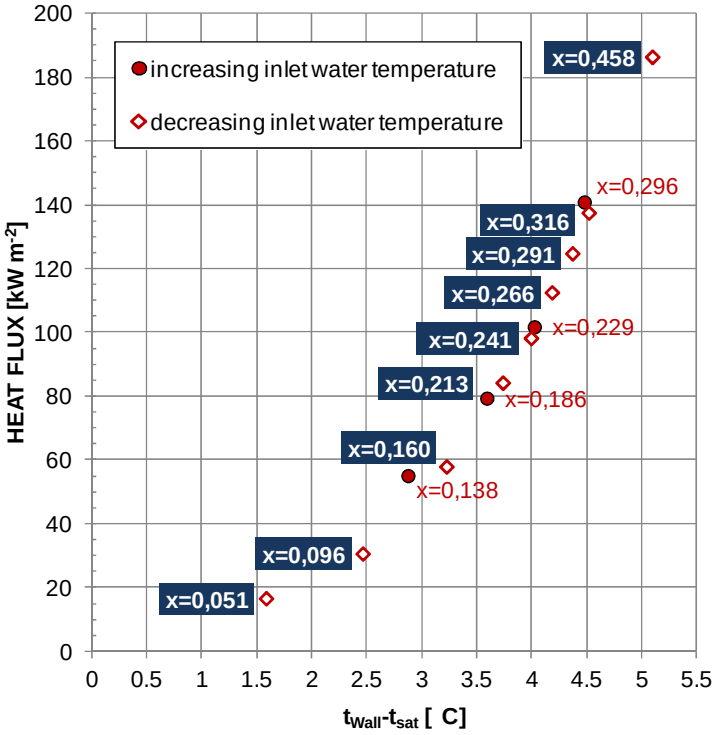

Figure 3.24. Boiling curve for propane: data refer to the temperature measurement at axial position z=166 mm and mass velocity equal to 500 kg m^{-2} s^{-1}.

Figure 3.25 depicts completely the test range conditions: the heat flux is plotted against vapor quality for all the performed tests in the circular minichannel: vapor quality varies from 0.05 to 0.6, while the heat flux is comprised within 10 kW m^{-2} and 315 kW m^{-2}.

Since in measuring section the refrigerant and the water flow in countercurrent, most of the experimental points at low vapor quality correspond to a low heat flux. In fact, at the entrance of the minichannel, the difference between the wall temperature and the saturation temperature and the derivative of the water temperature profile are lower than at the exit.

The same database is graphed as heat transfer coefficient versus heat flux in Figure 3.26, where it is clear to see the dependence of the heat transfer coefficient on the heat flux: the higher the heat flux, the higher the heat transfer coefficient. Moreover, given a heat flux, the corresponding heat transfer coefficients lie within a narrow band, showing that they weakly depend on other parameters, such mass velocity and vapor quality. In addition, it must be considered that the present minichannel has a rough internal surface. The roughness of the surface is known to be important in the nucleation process as it is related with the required superheat to activate the boiling sites. Nevertheless, the role of the surface roughness is not completely understood and agreed in minichannel flow boiling.

In order to get some information on the effect of vapor quality, several series of experimental heat transfer coefficients at a constant value of mass velocity and heat flux are considered and graphed in Figure 3.27 with the relative error bands. The heat transfer coefficient decreases with vapor quality in all the sets of data up to 0.25-0-3. At higher values, the vapor quality seems to have a minor effect on the heat transfer coefficient.

Furthermore, in Figure 3.28, the effect of mass velocity is examined by filtering the data at constant mass velocity and constant vapor quality and by depicting the heat transfer coefficient versus heat flux. From the trends observed at 0.16 and 0.36 vapor quality, it is plain to conclude that mass velocity has a negligible effect on the heat transfer coefficient.

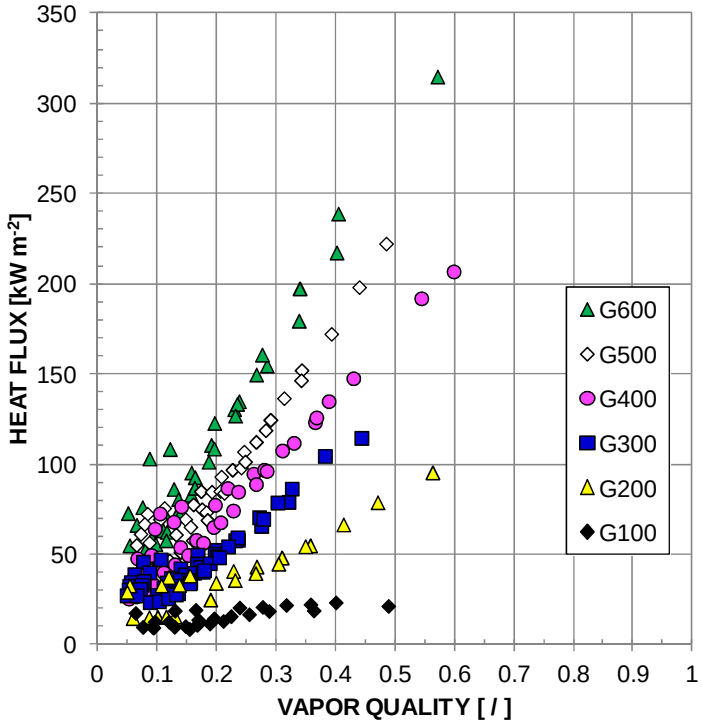

Figure 3.25. Heat flux versus vapor quality for all the flow boiling test runs in the circular minichannel with propane at different mass velocities *G* [kg m^{-2} s^{-1}] and at a saturation temperature of 31°C.

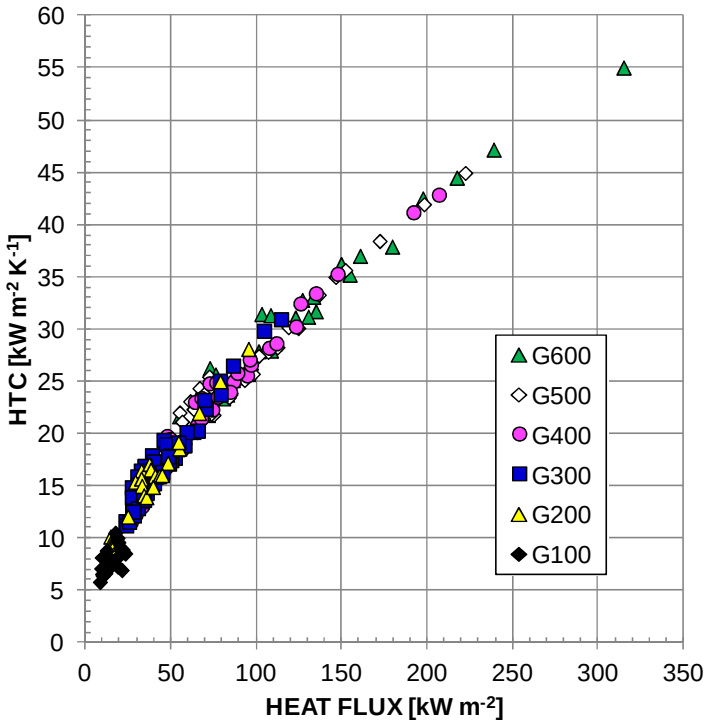

Figure 3.26. Heat transfer coefficient (HTC) versus heat flux for all the flow boiling test runs in the circular minichannel with propane at different mass velocities *G* [kg m^{-2} s^{-1}] and at 31°C saturation temperature.

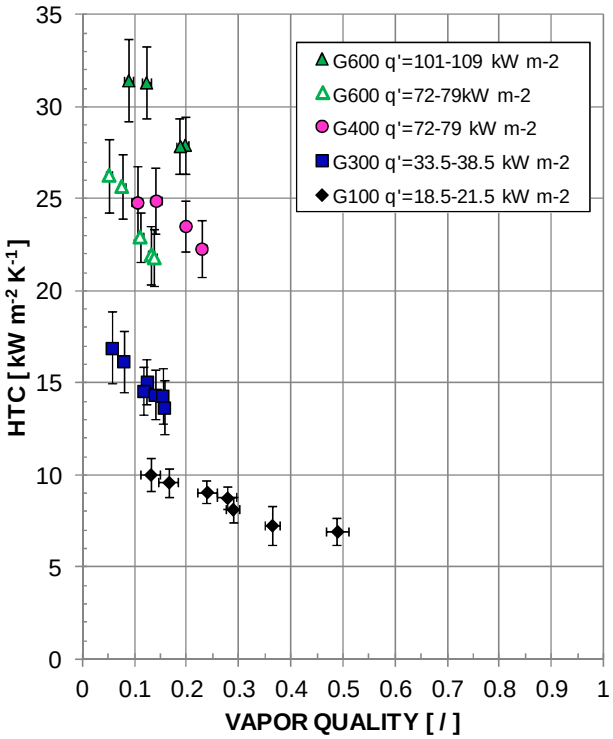

Figure 3.27. Effect of vapor quality on heat transfer coefficient (HTC) during flow boiling test with propane. Each series of experimental data refers to a constant mass velocity *G* [kg m^{-2} s^{-1}] and a constant heat flux *q'* [kW m^{-2}].

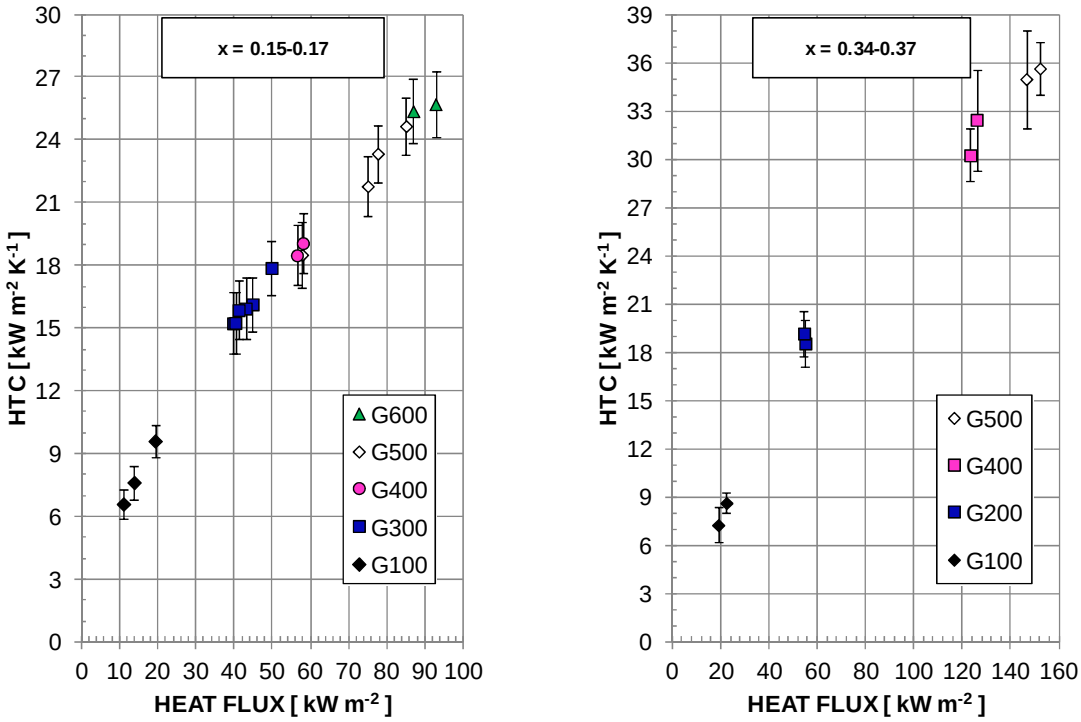

Figure 3.28. Effect of mass velocity *G* [kg m^{-2} s^{-1}] on heat transfer coefficient (HTC) during flow boiling of propane. The two graph are related to different values of vapor quality *x*; left: 0.15-0.17; right: 0.34-0.37.

The experimental database presented for propane has been summed up in Table 3-c with the ranges of some dimensionless parameters and compared against six models available in the open literature: the models by Lazarek and Black [62], by Kew and Cornwell [63], two models by Choi and coworkers [12], [64], the correlation by Sun and Mishima [65] and the model by Bertsch *et al.* [66].

Table 3-c. Parameter ranges of the experimental database collected during propane flow boiling tests.

Data number	243
Working fluid	propane
Hydraulic diameter	0.96 mm
Saturation temperature	31°C
Heat flux	10 - 315 kW m^{-2}
Vapor quality	0.05-0.6
Mass velocity	100 - 600 kg m^{-2} s^{-1}
Bo	$1.18 \cdot 10^{-4}$ - $1.615 \cdot 10^{-3}$
$Re_{LO} = G \cdot d_h / \mu_L$	1049-6382
$We_{LO} = G^2 d_h / (\rho_L \sigma)$	3.16 - 116.84
$Re_{LIQ} = G \cdot (1-x) \cdot d_h / \mu_L$	550-6030
$Re_{VAP} = G \cdot x \cdot d_h / \mu_V$	733-38710
$1000 < Re_{LIQ} < 2000$ or $1000 < Re_{VAP} < 2000$	53 data (21.8%)
$Co = \sigma / [g \cdot (\rho_L - \rho_V) d_h^2]$	1.27 - 1.29

The correlation by Lazerek and Black [62] comes from a study of saturated boiling of R113 in a smooth stainless steels round tube with an inner diameter of 0.315 cm where both an upward and downward flow occurred. It was observed that the saturated boiling

heat transfer was strongly dependent on the heat flux, while vapor quality had a negligible effect. Thus, the authors supposed that the controlling mechanism of the heat transfer was the nucleate boiling and proposed an expression of the Nusselt number as a function of the liquid only Reynolds number and of the boiling number.
The comparison of the experimental data against the predicted values by Lazarek and Black [62] is shown in Figure 3.29.
The model developed for a vertical channel configuration underestimates the experimental heat transfer coefficient. (e_R = -28.6% ; σ_N = 10.5%) and only 55% of the data are captured within ±30% error band.
Kew and Cornwell [63] performed boiling tests with R141b inside circular section stainless steel channels with diameters of 1.39-3.69 mm. They observed that in 3.69 mm and 2.87 mm tubes, the heat transfer coefficient increased with heat flux at low vapor quality, while at higher qualities it was independent of heat flux. In 1.39 mm tube, the heat transfer coefficient fell rapidly with increasing vapor quality at high mass velocities. Thus, they modified the Lazarek and Black [62] equation introducing a vapor quality related term. They concluded that the proposed equation must be refined for small diameter channels, where they supposed that intermittent local dryout occurs.
In Figure 3.30, the predicted heat transfer coefficient values by using Kew and Cornwell [63] equation are plotted against the experimental data, showing no significant improvements as compared to the previous model (e_R = -26.2% ; σ_N = 11.7%): it captures only 64% of the data within ±30%.

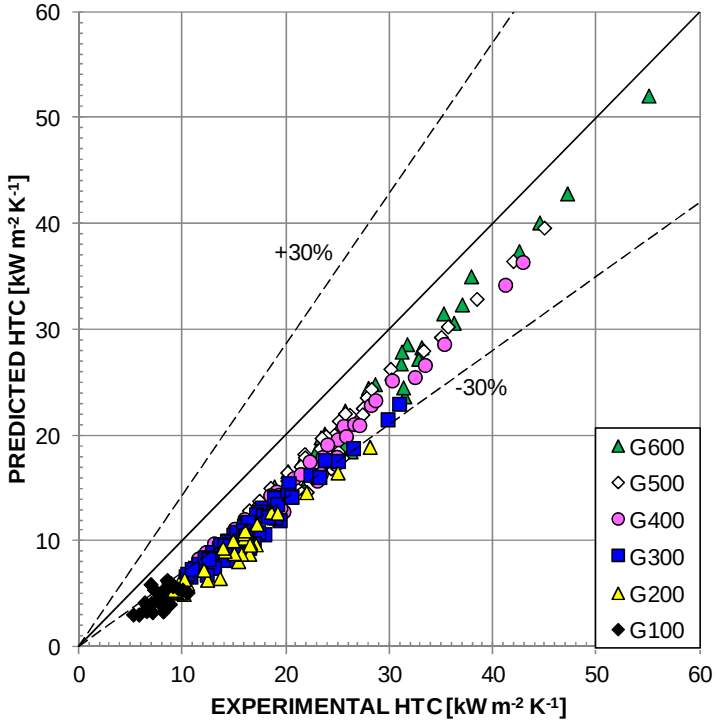

Figure 3.29. Flow boiling experimental data with propane compared against the model by Lazarek and Black [62].

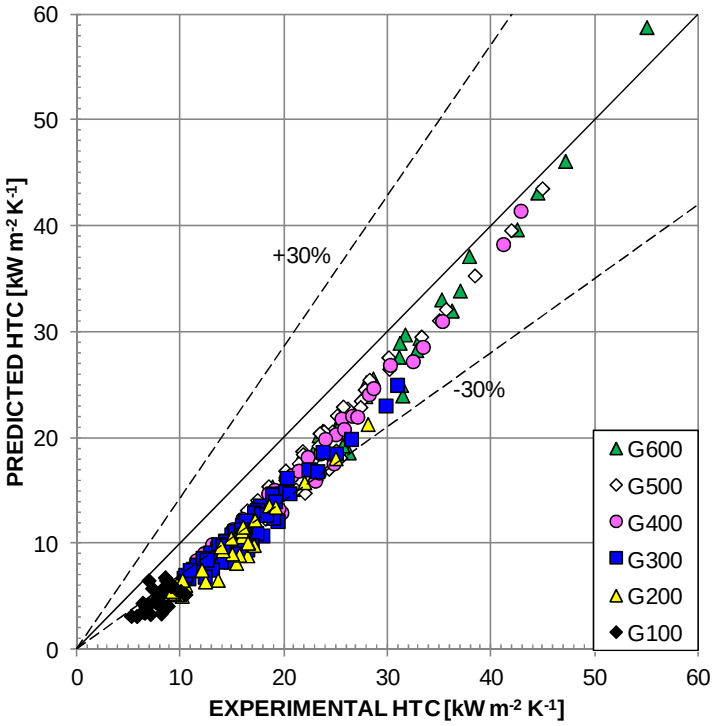

Figure 3.30. Flow boiling experimental data with propane compared against the model by Kew and Cornwell [63].

The model by Choi *et al.* [64] was developed from the convective boiling heat transfer studies using R22, R134a and carbon dioxide at a saturation temperature of 10°C inside horizontal stainless steel smooth minichannels with inner diameters of 1.5 mm and 3 mm. In their work, the mass velocity ranged between 200 kg m^{-2} s^{-1} and 600 kg m^{-2} s^{-1} while the heat flux was between 10 kW m^{-2} and 40 kW m^{-2}. They noticed a strong dependence of heat transfer coefficient on heat flux at low vapor quality, with no effect of vapor quality and mass velocity, whereas at moderate and high quality regions, heat transfer coefficient increased with mass flux and vapor quality. Using their data, the authors submitted a new correlation based on the Chen [67] equation with the following changes. The nucleate boiling heat transfer coefficient is predicted by the Cooper [68] correlation and new expressions are adopted to calculate the enhancement factor and the suppression factor.

The comparison between calculated and experimental vales is depicted in Figure 3.31:the experimental trend is not well predicted, the average deviation is e_R = -4.4% and the standard deviation is very high: σ_N = 19.9%.

In another work [12] ,Choi and coworkers proposed a correlation for flow boiling heat transfer based on experimental tests with propane in horizontal smooth stainless steel channels having inner diameter of 1.5 mm and 3 mm. In their study, the heat flux ranged within 5 kW m^{-2} and 20 kW m^{-2}, so it was considerably lower than the values obtained in this work. The correlation has the same form of the one proposed in [64] but different definitions for enhancement and suppression factors are implemented. On the whole, 190 experimental points collected in the present circular minichannel are within the range of the model by Choi *et al.* [12]. and satisfy the following conditions:

- $Re_L < 1000$ or $Re_L < 2000$
- $Re_G < 1000$ or $Re_G < 2000$

The comparison against the predicted values is reported in Figure 3.32. The model by Choi *et al.* [12] underestimates significantly the experimental heat transfer coefficient, the

average deviation e_R results equal to -47.4% ;while the standard deviation σ_N is 11.6%, indicating that the model doesn't catch the experimental trend.
Sun and Mishima [65] considered a wide heat transfer coefficient database referred to the boiling process in channels with diameter ranging from 0.21 mm to 6.5 mm of several fluids, including 6 halogenated pure fluids, 3 halogenated mixtures, carbon dioxide and water. Assuming that the nucleate boiling were the dominant mechanism, they perceived that the heat transfer coefficient was much more dependent on the Weber number than on the vapor quality so they modified the Lazarek and Black [62] model by introducing the Weber number for liquid phase.
As reported in Figure 3.33, even if the Sun and Mishima [65] correlation underestimates the propane experimental data, it is the best predicting method, giving an average deviation e_R = -13.3% and a standard deviation σ_N = 7.2% and capturing over 99% of the points within ±30% error band.
A clear remark is that a significant underprediction of the experimental heat transfer coefficients obtained during the flow boiling of propane is found in all the considered models. Similar trends were found for database collected in the present circular minichannels with R134a and R1234yf [61]). A possible explanation for such disagreement could be the effect of the internal surface roughness of the minichannel that is not accounted for in the correlations under examination.

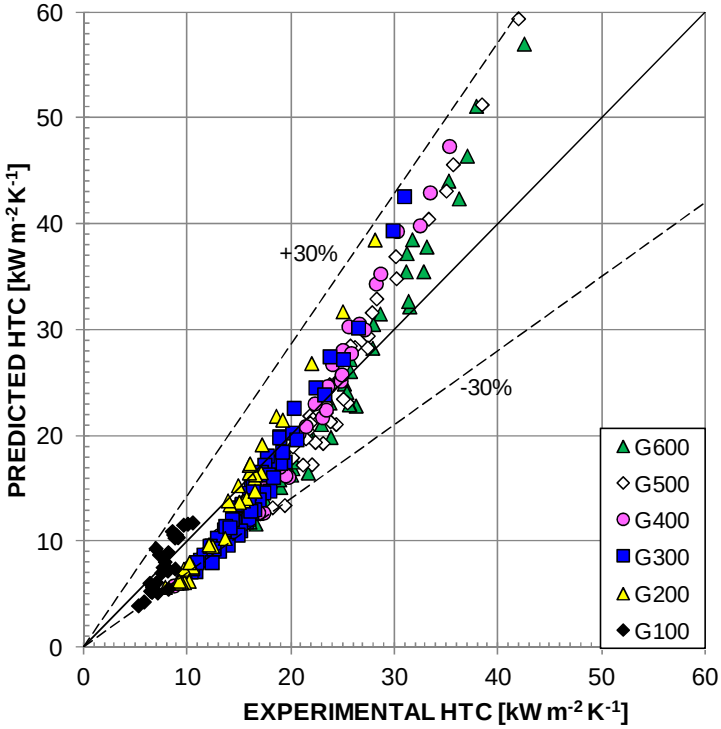

Figure 3.31. Flow boiling experimental data with propane compared against the model by Choi *et al.* [64].

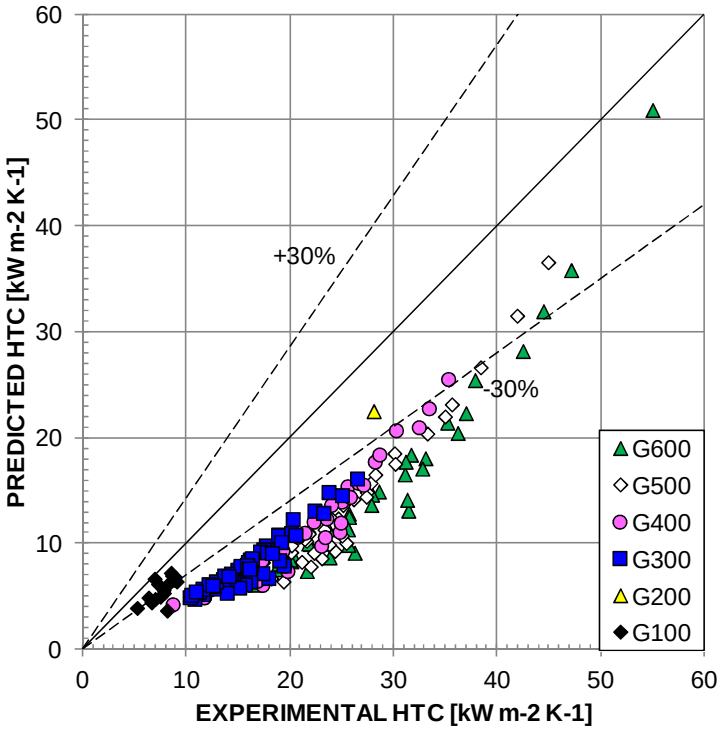

Figure 3.32. Flow boiling experimental data with propane compared against the model by Choi *et al.* [12].

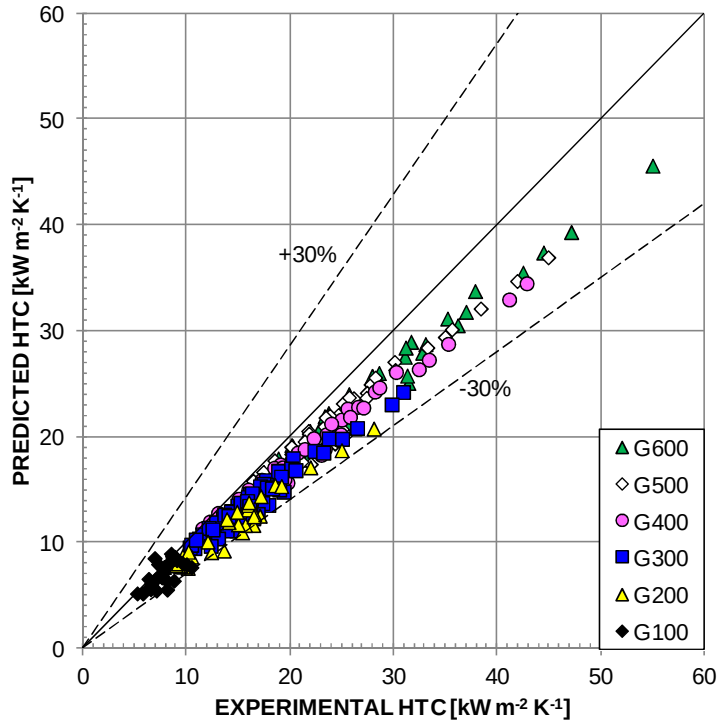

Figure 3.33. Flow boiling experimental data with propane compared against the model by Sun and Mishima [65].

In order to complete the considered models' assessment, the database collected for propane during flow boiling tests inside the circular minichannel is compared against the model by Bertsch *et al.* [66]. They proposed a correlation in the form of the Chen [67]

equation which define the flow boiling heat transfer coefficient as a weighted sum of nucleate boiling and convective heat transfer terms, while accounting for the effect of bubble confinement and the surface roughness in small channels. It comes from a wide database covering saturated flow boiling studies on 12 fluids (CFCs, HCFCs, HFC, FC-77, water, nitrogen) inside channels with diameters from 0.16 mm to 2.92 mm. As of the working condition, in their study the mass velocity ranged between 20 kg m^{-2} s^{-1} and 3000 kg m^{-2} s^{-1}, the heat flux was between 0.4 kW m^{-2} and 115 kW m^{-2} and the saturation temperature was within -194°C and 97°C.
The heat transfer coefficient are strongly underestimated by the Bertsch *et al.* model, as illustrated in Figure 3.34 (e_R = -27.3 % ; σ_N = 7.4%). Probably, the Bertsch *et al.* [66] model should be use for low reduced pressure conditions.

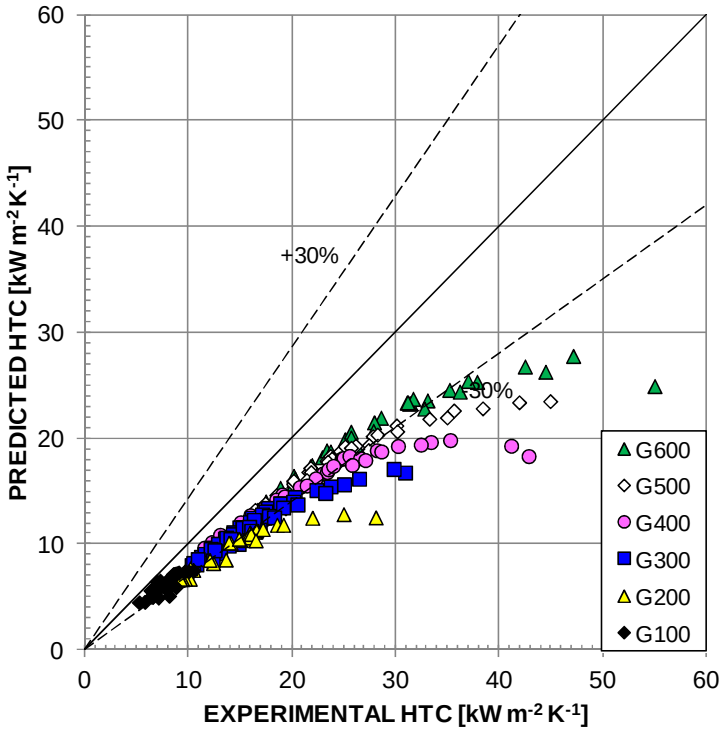

Figure 3.34. Flow boiling experimental data with propane compared against the model by Bertsch *et al.* [66].

3.5.5 Experimental results and comparison against correlations for R1234ze(E)

Flow boiling tests have been performed with R1234ze(E) at mass velocity ranging between 200 kg m^{-2} s^{-1} and 600 kg m^{-2} s^{-1}, around 31 °C saturation temperature, in the 0.96 mm circular channel. During the test runs, refrigerant mass velocity and inlet temperature can be controlled, while the heat flux varies along the measuring section.
In order to assess the methods employed for the determination of the local heat flux the heat transfer coefficient obtained with each procedure is plotted against the vapor quality during the same test run. Two sets of data are plotted in
Figure 3.35, they refer to test runs at 300 kg m^{-2} s^{-1} and 400 kg m^{-2} s^{-1}. The error bands for each measured quantity are reported. As for the flow boiling tests with propane, a satisfactory agreement between the results of method 1 and method 2 is found and once again this point validates the experimental technique here adopted. On average, the expanded experimental uncertainty of heat transfer coefficient with a level of confidence

of 95% is equal to 11% when the local heat flux is calculated with method 1 and it is around 16.5% when the method 2 is employed. Therefore, the method 1, which is based on the interpolation of the water temperatures to calculate the local heat flux, has been chosen hereinafter to present the experimental data. In Table 3-d, the expanded uncertainty of vapor quality and that of heat transfer coefficient with a 95.45% level of confidence are reported when using the method 1 in the data reduction for the tests with R1234ze(E).

Table 3-d. Experimental expanded uncertainty of vapor quality and heat transfer coefficient during flow boiling of R1234ze(E).

Heat transfer coefficient experimental uncertainty (%)	6 % - 18 %
Percent of data within ± 13 % band of uncertainty	80 %
Vapor quality experimental uncertainty (-)	0.02 – 0.05

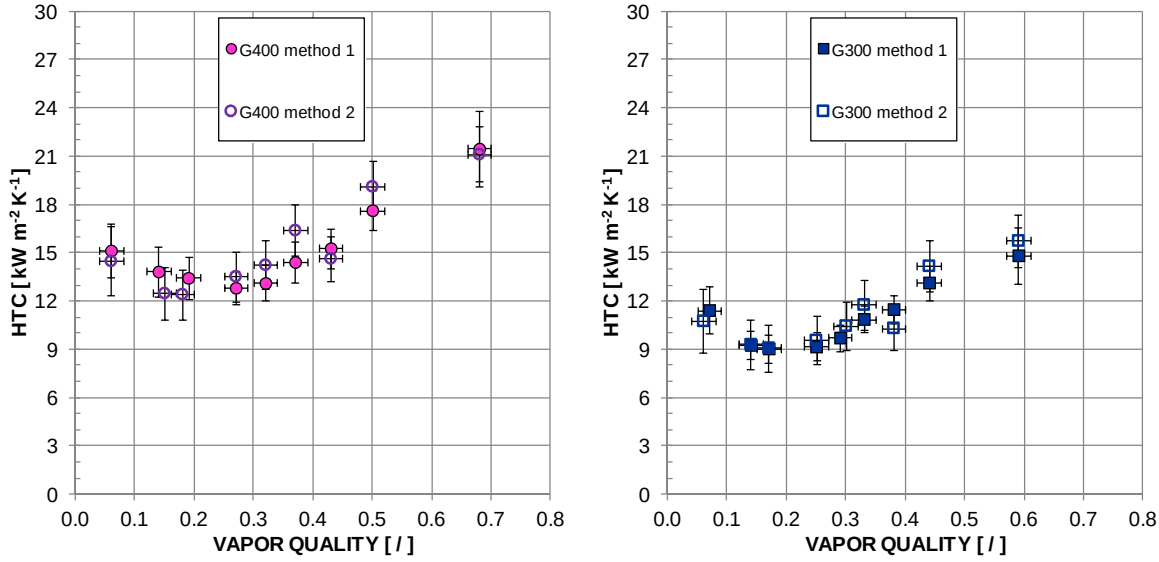

Figure 3.35.Comparison between the heat transfer coefficients (HTC) obtained during the flow boiling of R1234ze(E) at 31°C using the two methods for heat flux determination. Left: data set at *G* = 400 kg m^{-2} s^{-1} mass velocity. Right: data set at *G* = 300 kg m^{-2} s^{-1} mass velocity.

At constant mass velocity and saturation temperature, some test runs have been performed by varying the inlet temperature of the water in order to vary the heat flux, first by increasing the temperature difference between inlet water and saturated refrigerant and then by decreasing it. The related results are presented in form of boiling curve in Figure 3.36, referring to the temperature measurements at a fixed axial position z = 76 mm during flow boiling tests at 400 kg m^{-2} s^{-1} mass velocity. At the same vapor quality and heat flux, the difference between the wall temperature and the saturation temperature is practically identical, showing no hysteresis effect on the heat transfer coefficient.
The experimental conditions during the flow boiling study with R1234ze(E) are depicted in Figure 3.37, where the heat flux is plotted against vapor quality for all the performed tests in the circular minichannel: vapor quality varies from 0.05 to 0.7, while the heat ranges within 10 kW m^{-2} and 165 kW m^{-2}. Since in measuring section the refrigerant and the water flow in countercurrent, most of the experimental points at low vapor quality

display a low heat flux. In fact, at the inlet of the measuring section, the difference between the wall temperature and the saturation temperature and the derivative of the water temperature profile are lower than at the outlet.

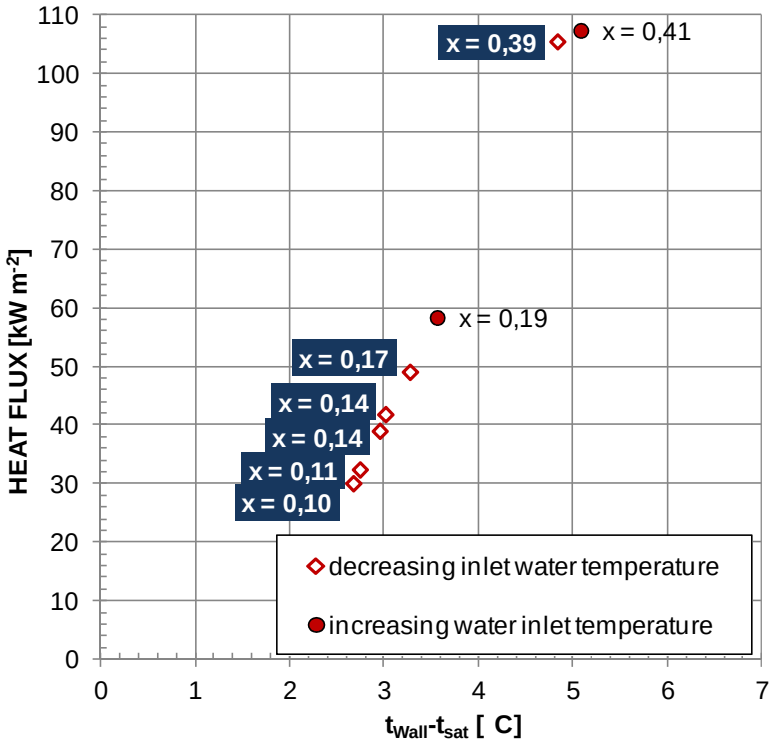

Figure 3.36. Boiling curve for R1234ze(E). Data refer to the temperature measurement at axial position *z*=76 mm and mass velocity equal to 400 kg m^{-2} s^{-1}.

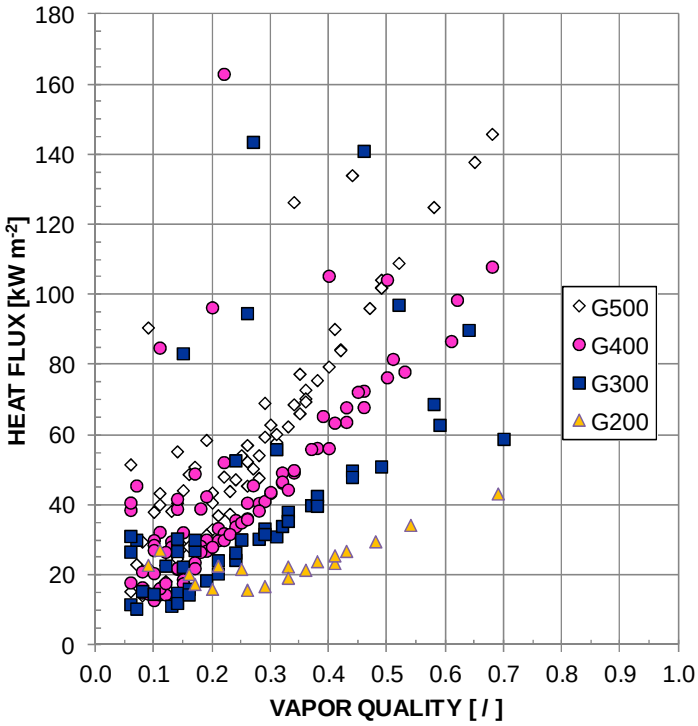

Figure 3.37. Heat flux versus vapor quality for all the flow boiling test runs in the circular minichannel with R1234ze(E) at different mass velocities *G* [kg m^{-2} s^{-1}] and at 31°C saturation temperature.

The same database is graphed as heat transfer coefficient versus heat flux in Figure 3.38: the present data points with R1234ze(E) show a strong dependence of the heat transfer coefficient on the heat flux. Moreover, given a heat flux, the corresponding heat transfer coefficients lie within a band, showing that they may depend on other parameters, such mass velocity, vapor quality and internal roughness, as the investigated minichannel is not smooth. The roughness of the surface is known to be important in the nucleation process as it is related with the required superheat to activate the boiling sites but further research is needed to assess its role in the flow boiling process inside minichannels. From Figure 3.38, one can see that the heat transfer coefficient increases with heat flux. Nevertheless, in order to discuss the effect of vapor quality and mass flux on the heat transfer coefficient, an appropriate and different data processing is required.
Hence, the effect of vapor quality on heat transfer coefficient has been investigated by processing data at almost constant heat flux and mass velocity. In Figure 3.39 some data sets with R1234ze(E) are reported with the corresponding error bands and show that the heat transfer coefficient decreases with vapor quality up to 0.2, then at higher qualities the effect of vapor quality on the heat transfer coefficient is negligible.
Furthermore, in order to study the effect of mass velocity on the flow boiling heat transfer coefficient, the experimental data have been processed at the same vapor quality and grouped in data set at the same mass velocity. As shown in Figure 3.40, at the same heat flux and vapor quality, the heat transfer coefficient variations due to changes in mass velocity are within the expanded experimental uncertainty, so no clear trends are observed.

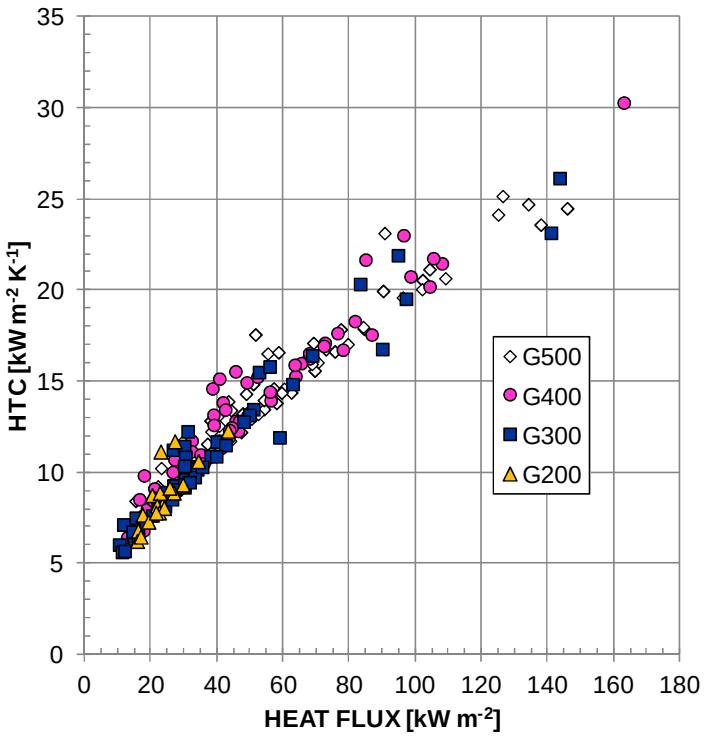

Figure 3.38. Heat transfer coefficient (HTC) versus heat flux for all the flow boiling test runs in the circular minichannel with R1234ze(E) at different mass velocities *G* [kg m^{-2} s^{-1}] and at 31°C saturation temperature.

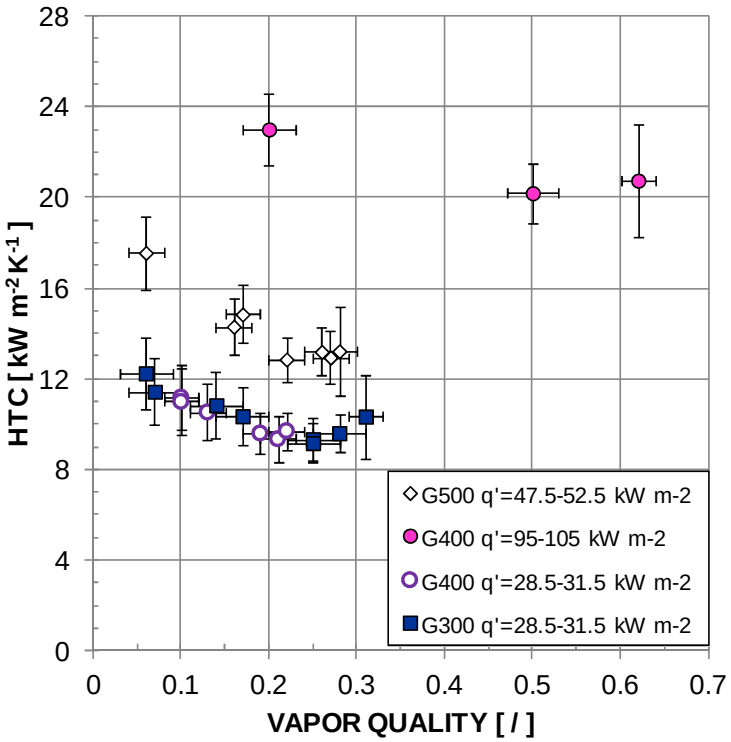

Figure 3.39. Effect of vapor quality on heat transfer coefficient (HTC) during flow boiling test with R1234ze(E). Each series of data refers to a constant mass velocity *G* [kg m^{-2} s^{-1}] and a constant heat flux *q'*[kW m^{-2}]

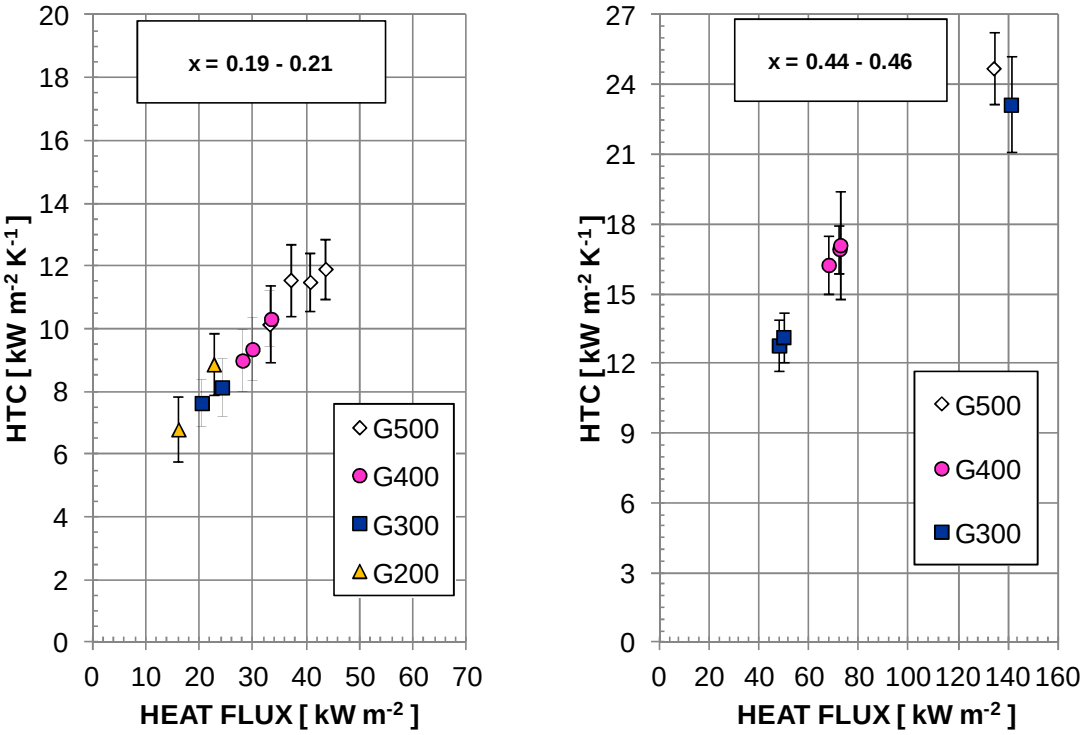

Figure 3.40. Effect of mass velocity *G* [kg m^{-2} s^{-1}] on heat transfer coefficient (HTC) during flow boiling of R1234ze(E). The two graph are related to different values of vapor quality *x*; left: 0.19-0.21; right: 0.44-0.46.

The experimental database presented for R1234ze(E) has been compared against four models available in the open literature: the models by Lazarek and Black [62], by Kew and Cornwell [63], the models by Choi and coworkers [64], the correlation by Sun and Mishima [65] and the model by Bertsch *et al.* [66]. Table 3-e summarizes the test conditions for the flow boiling study with R1234ze(E) together with the range of the dimensionless parameters included in the models: the boiling number *Bo*, the liquid only Reynolds number Re_{LO}, the Weber number for the liquid phase We_{LO} and the confinement number *Co*.

Table 3-e. Parameter ranges of the experimental database collected during flow boiling tests with R1234ze(E).

Data number	221
Working fluid	R1234ze(E)
Hydraulic diameter	0.96 mm
Saturation temperature	31°C
Heat flux	10 - 165 kW m^{-2}
Vapor quality	0.05 - 0.7
Mass velocity	200 - 500 kg m^{-2} s^{-1}
Bo	$1.76 \cdot 10^{-4}$ - $2.95 \cdot 10^{-3}$
$Re_{LO} = G \cdot d_h / \mu_L$	1042 - 2647
$We_{LO} = G^2 \cdot d_h / (\rho_L \cdot \sigma)$	4.22 - 27.07
$Co = \sigma / [g \cdot (\rho_L - \rho_V) \cdot d_h^{\,2}]$	0.89-0.90

Lazarek and Black [62] developed a correlation in which the heat transfer coefficient strongly depends on the heat flux while the vapor quality has no influence, suggesting that the heat transfer process is dominated by the nucleate boiling mechanism. From the comparison of the data collected with R1234ze(E) with the values calculated with the model by Lazarek and Black [62] (Figure 3.41), one can see that all the data are severely underestimated, with an average deviation e_R = -33.3% and standard deviation σ_N = 8.2%
A modified Lazarek and Black equation for has been suggested by Kew and Cornwell [63] to involve an increase in the heat transfer coefficient with vapor quality observed in their flow boiling experiments. Nevertheless, they stated that the proposed equation must be refined for small diameter channels, where they supposed that intermittent local dryout occurs. The model by Kew and Cornwell [63] underpredicts all the experimental data as shown in Figure 3.42: the average deviation e_R is -29.9% and standard deviation σ_N is 10.5%.
Choi *et al.* [64] submitted a new correlation based on the form of the Chen [67] equation. The comparison between predicted and experimental values highlights that the experimental trend is not well predicted (Figure 3.43): the average deviation is e_R = -18.6% and the scattering is very high as proved by the standard deviation σ_N = 22.3%.
Sun and Mishima [65] proposed a modification of the Lazarek and Black correlation including the Weber number for the liquid phase. All the experimental data for R1234ze(E) collected in the present work are underrated by the Sun and Mishima model, as illustrated in Figure 3.44. The average deviation e_R is equal to -25.8% while the standard deviation σ_N is 5.9%.
In conclusion, all the considered models strongly underestimate the heat transfer coefficient during the flow boiling of the halogenated olefin R1234ze(E). Similar trends were found for database collected in the present circular minichannels with R134a and R1234yf [61] and with propane (see 3.5.4). Therefore, the observed predicting inaccuracy

is not related to the properties of the new olefin but can be due to the internal surface roughness of the minichannel that is not accounted for in the correlations under examination.
Bertsch *et al.* [66] presented a correlation in the form of the Chen [67] equation which accounts for the effect of bubble confinement and the surface roughness in small channels. This model has proved to predict well the experimental data obtained in the present circular minichannel during the flow boiling of R245fa [69] but it is not suitable for the calculation of the heat transfer coefficients of R1234ze(E) inside the same minichannel (Figure 3.45). Probably, the Bertsch *et al.* [66] model should be use only for low reduced pressure conditions.

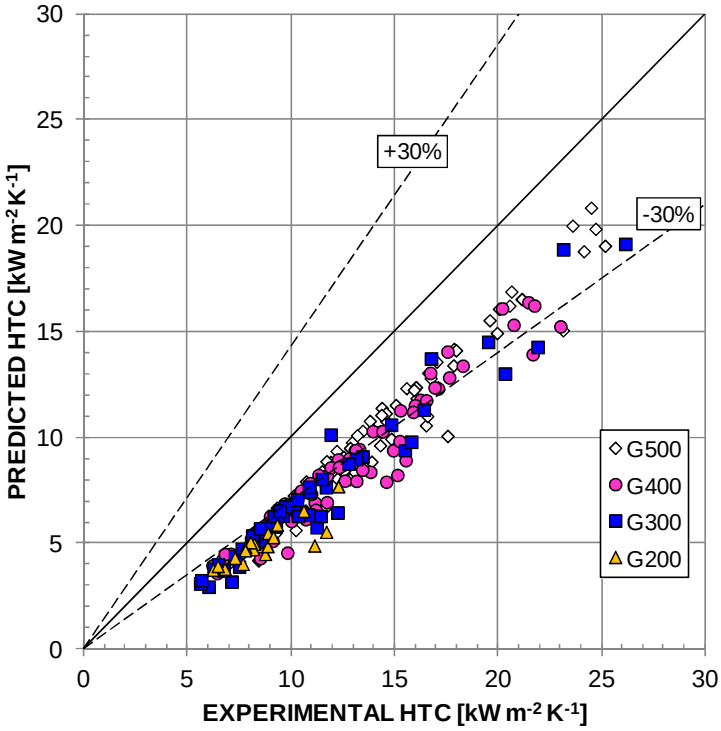

Figure 3.41. Flow boiling experimental data with R1234ze(E) compared with the model by Lazarek and Black [62].

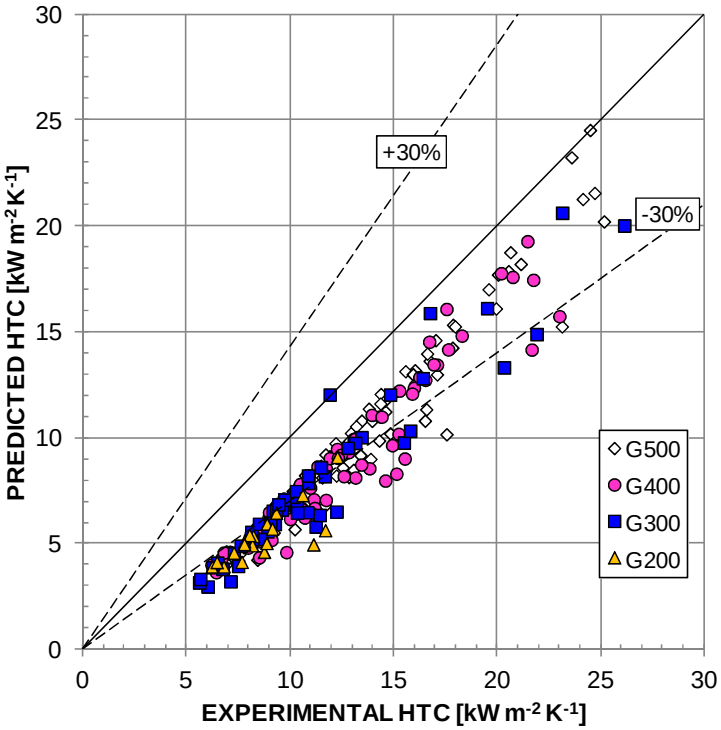

Figure 3.42. Flow boiling experimental data with R1234ze(E) compared with the model by Kew and Cornwell [63].

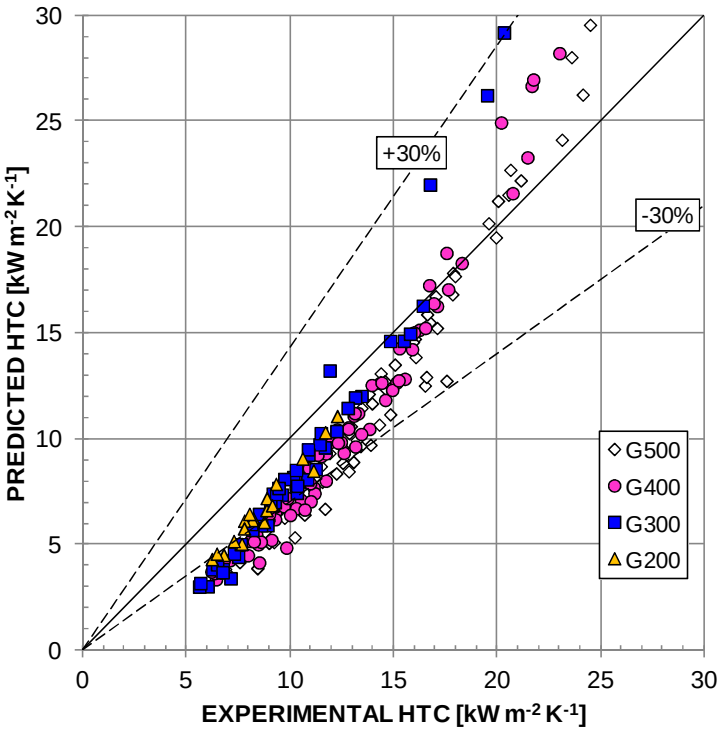

Figure 3.43. Flow boiling experimental data of R1234ze(E) compared with the model by Choi *et al.* [64].

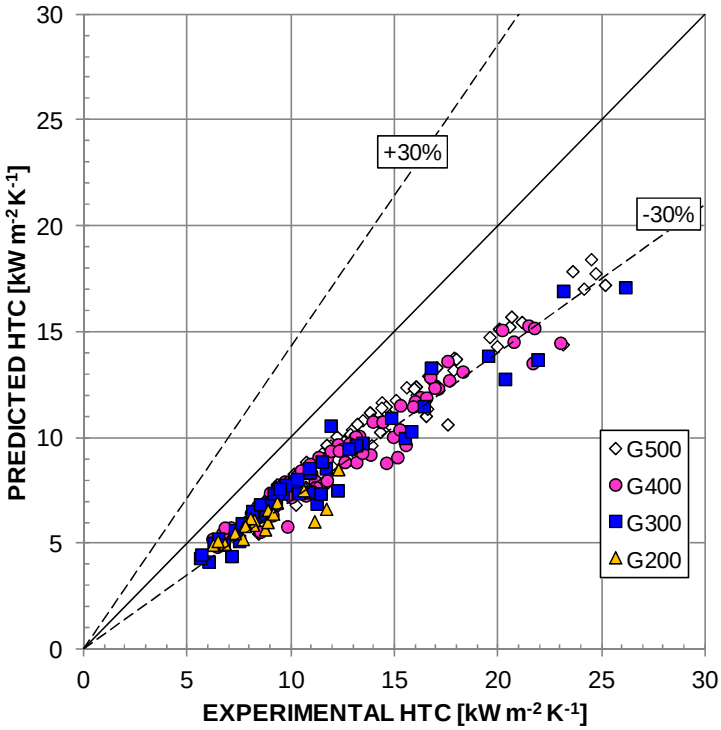

Figure 3.44. Flow boiling experimental data of R1234ze(E) compared with the model by Sun and Mishima [65].

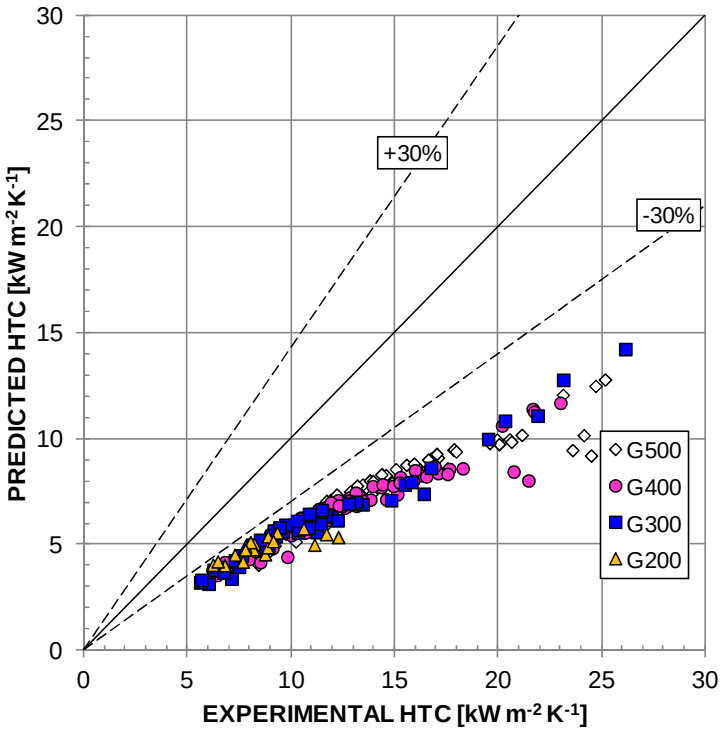

Figure 3.45. Flow boiling experimental data of R1234ze(E) compared with the model by Bertsch *et al.* [66].

4 EFFECT OF CHANNEL INCLINATION DURING CONDENSATION INSIDE A SQUARE CROSS SECTION SINGLE MINICHANNEL

4.1 Abstract

Despite the widespread use, in the literature the studies on the condensation process inside non-circular minichannels are rather limited and the effect of channel orientation during condensation is not much investigated. Some studies have been performed in inclined smooth tubes of larger diameters, where it was shown that the heat transfer coefficient is strongly affected by the liquid and vapor distributions. But minichannels may display a different behavior because of the relative importance of shear stress, gravity and surface tension. The action of these forces may depend on operating conditions and orientation. The relative importance of gravity force, for instance, depends on orientation but also on mass velocity. For some operating conditions, in particular in non circular minichannels, the heat transfer coefficients are also dependent on the effect of surface tension: the liquid is pulled towards the corners leading to a thinner liquid film on the flat sides and therefore to a lower thermal resistance on these parts of the channel. Hence, this effect may enhance the heat transfer in the presence of corners, as compared to the case of circular minichannels, at low mass velocity, when the relative importance of shear stress diminishes.

In the present study, an experimental investigation of condensation of two refrigerants inside a single square cross section minichannel when varying the channel orientation is presented. The minichannel is obtained from a copper rod by electro erosion and has a square cross section with 1.18 mm side length. Each corner has a curvature radius equal to 0.15 mm, which leads to a hydraulic diameter equal to 1.23 mm. The condensation is obtained by using cold distilled water passing through the coolant channel which is realized by digging grooves on the external part of the copper rod. The thermocouples for the measurement of the wall temperature are placed in the copper fins between the grooves of the water path. The coolant channel is externally enclosed by means of a covering sheath made with epoxy resin. Thermocouples are inserted also in the water channel for the measurement of the coolant temperature. The local heat flux is obtained from the coolant temperature profile and the local heat transfer coefficient is determined from the ratio of the local heat flux and the local saturation to wall temperature difference. The test section is installed in a aluminium mechanical structure which allows to set the channel at any orientation from vertical upflow to vertical downflow.

In this chapter, local heat transfer coefficients of R134a are measured in horizontal , in downflow and upflow configurations at inclination angles of 30°, 45°, 60°, 90°. Furthermore, local heat transfer coefficients of R32 are investigated in horizontal and in downflow at inclination angles of 15°, 30°, 45°, 60° and 90°. The inclination angle is computed from the horizontal. Tests have been performed with the refrigerants at 40°C saturation temperature, at mass velocity ranging between 100 kg m^{-2} $s^{-1}$and 390 kg m^{-2} s^{-1}. From the experimental results, the effect of the channel inclination when varying mass velocity and vapor quality is discussed.

Finally, applying the Buckingham theorem, a correlation among dimensionless groups has been develop to predict at which mass velocity the channel inclination starts to become important during in-tube condensation heat transfer.

The description of the test rig and the test section, the illustration of the experimental technique, the discussion of the condensation test results taking into account the effect of the channel orientation and the dimensional analysis for the tilted square minichannel are presented in order in this chapter.

4.2 Introduction

Heat transfer inside minichannels has gained an increasing interest both in the scientific community and in industry as its peculiar characteristics lead to the realization of compact, lightweight and efficient heat exchangers for a huge variety of applications such as air conditioning, refrigeration, electronics and aerospace industry. In the literature, so far, the condensation has been extensively studied inside conventional size channels while there are few studies about the evaluation of heat transfer coefficient in condensation in minichannel geometry, where the determination of the heat flow without perturbing the investigated process is a central issue. In this work, the presence of more than sixty thermocouples in the actual measuring section makes possible the calculation of the local heat flux from the coolant temperature profile and the evaluation of the local heat transfer coefficients from the saturation and wall local temperatures with a good accuracy.
All the researchers agree that the condensation heat transfer coefficient increases with decreasing channel hydraulic diameter, because of the differences in the relative influences of interfacial shear stress, gravity and surface tension in a such geometry. The action of these forces may depend on operating conditions and channel orientation. The gravity seems to play a negligible role in horizontal channels with an inner diameter smaller than 1 mm, at least for high mass velocities [70]. Generally, heat transfer coefficient increases with mass flow and vapor quality but further activity is definitely needed to verify this trend at low mass flows [51].
Moreover, at small scales, the shape of the cross section becomes an outstanding parameter, because of the effect of the surface tension: during condensation inside non circular minichannels, it is supposed to enhance the heat transfer because the liquid phase is pulled towards the corners, making the liquid film thinner and the thermal resistance lower at the flat sides.
Wang and Rose [71] proposed a theoretical study on the effect of minichannel shape in film condensation, taking into account surface tension, shear stress and gravity. In their work, Wang and Rose treated the condensate film by assuming laminar flow while inertia and convection terms were neglected. According to the authors, due to the benefit of the thin liquid film at the flat sides, the heat transfer coefficient in a square channel was expected to be significantly higher than in a circular one in a wide range of operating conditions, but the simulations were not supported by experimental trials. According to their theory, the heat transfer coefficient in a 1 mm diameter square channel should be roughly the same at mass fluxes ranging from 300 kg m^{-2} $s^{-1}$to 1300 kg m^{-2} s^{-1}, in a wide range of vapor quality. But this is contrary to the experimental results, which display a strong dependence of the heat transfer coefficient on the mass flux even in the square minichannel, as shown by Del Col *et al.* [50].
A number of steady-state simulations of condensation of R134a (40°C saturation temperature) at mass fluxes G=100 kg m^{-2} $s^{-1}$and G=800 kg m^{-2} s^{-1}inside a square cross section minichannel has been reported by Da Riva *et al.* [72] and compared with the same simulation in a circular cross section channel with the same hydraulic diameter. The Volume of Fluid (VOF) method is employed to track the vapor-liquid interface and a uniform wall temperature is considered as boundary condition. The results have been validated against experimental data by Del Col *et al.* [50] and showed that the effect of

surface tension did not lead to any difference in the heat transfer coefficient between square and circular cross section at high mass fluxes, while it provided a heat transfer enhancement in the square cross section channel at low mass velocities. The authors concluded that at high mass velocities, the interfacial stress is always the prevailing force so the cross section shape has low influence. Differently from the theory by Wang and Rose [71], Da Riva *et al.* [72] did not limit the treatment of the liquid film under the hypothesis of laminar flow. The importance of considering turbulence in the liquid film during condensation in minichannels has been discussed by Da Riva *et al.* [73].

Shin and Kim [74] tested and compared three circular channels and three rectangular channels with a hydraulic diameter between 0.493 mm and 1.067 mm for mass velocities between 100 kg m^{-2} $s^{-1}$and 600 kg m^{-2} $s^{-1}$and a heat flux ranging from 5 kW m^{-2} to 20 kW m^{-2}. They pointed out that, for a similar hydraulic diameter, heat transfer coefficients during condensation of R134a at 40°C are higher in rectangular channels at lower mass velocities and higher in circular channels at higher mass velocities. No meaningful effect of heat flux was found.

Agarwal *et al.* [75] measured heat transfer coefficients in six non circular horizontal multiport microchannels of different shapes (barrel-shaped, N-shaped, W-shaped, rectangular, square and triangular), with a hydraulic diameter between 0.424 mm and 0.839 mm, during the condensation of R134a at 55°C, over the mass flow range between 150 kg m^{-2} $s^{-1}$and 750 kg m^{-2} s^{-1}. For the geometries with smooth corners or corner angle of about 90°, the use of an annular-film flow based prediction model has been suggested while, for those with sharp corners, it was supposed that the liquid phase is retained at the corners so a mist flow based predicting correlation has been recommended.

Derby *et al.* [76] reported experimental data for the condensation of R134a at temperatures up to 50°C in a square, a triangular and a semi-circular minichannel with the same hydraulic diameter of 1 mm. No cross sectional shape effect has been noticed by the authors, but they thought this fact could be due to the three-sided cooling boundary conditions during the experiments.

Rare references to the effect of channel orientation during condensation are available in the literature; furthermore, to the authors' knowledge, almost all of them concern inclined tubes with larger diameters as compared to those of minichannels (over 3 mm).

Lips and Mayer [77] presented an experimental research on convective condensation of R134a at 40°C saturation temperature in a smooth tube (8.38 mm inner diameter) for the whole inclination angles from vertical downward to vertical upward and for mass velocities ranging from 200 kg m^{-2} s^{-1} to 600 kg m^{-2} s^{-1}. In such cases, the heat transfer coefficient was dependent on the distribution of the two-phases inside the tube, which resulted from the balance between gravitational force, shear stress and surface capillary force. It was highlighted that flow pattern was strongly dependent on the inclination angle only for low mass velocities and low vapor qualities. Under these conditions, the results showed that for an inclination angle of 15° in downward flow, the maximum heat transfer coefficient was achieved. At high mass velocities, the shear stress has been regarded as the dominant force and there was no effect of inclination on the heat transfer.

Both theoretical and experimental results have been submitted by Wang and Du [78] for the condensation of water inside an inclined small diameter tube. They modeled and tested circular tubes with inner diameters ranging from 1.94 mm to 4.98 mm and for low mass fluxes (up to 100 kg m^{-2} s^{-1}) varying the orientation of the channel (horizontal and downward flow at 17°, 34° and 45°). They found that the effect of inclination on the heat transfer coefficient was poor for the smallest tubes and strong for the tubes with bigger inner diameters.

Saffari and Naziri [79] presented a theoretical and numerical analysis of heat transfer during stratified condensation inside inclined tubes. The results have been presented for the condensation of three different refrigerants, R141b, R11 and R134a, inside a channel with an internal diameter equal to 14.3 mm. The inclination angle had a significant effect on condensation heat transfer coefficient and the inclination angle giving the maximum heat transfer coefficient was found in the range between 30°and 50° from the horizontal position in upflow configuration.
An experimental analysis was conducted by Lyulin *et al.* [80] to investigate the heat transfer coefficient during convective condensation of pure ethanol vapor inside a smooth tube with an inner diameter of 4.8 mm and a length of 200 mm. During the tests, mass velocity varied from 0.24 kg m^{-2} s^{-1} to 2.04 kg m^{-2} s^{-1}, the saturation temperature was fixed at 58°C and the inclination of the condenser was varied from 0° to 90° considering only downflow configurations.. The study focused both on the difference between the wall to saturation temperature and the influence of inclination angles. The results showed that the heat transfer coefficient decreased with growth of the wall to saturation temperature difference; the trend of the heat transfer coefficient on inclination had a maximum in the range within 15°and 35° due to the complex gravity drainage mechanism of the condensed liquid.
Da Riva and Del Col [81] simulated the condensation process inside a circular cross section minichannel (0.96 mm inner diameter) assuming horizontal orientation, vertical downflow orientation under normal gravity conditions and finally vertical orientation under zero-gravity conditions. In the simulations, R134a was the working refrigerant at 40°C saturation temperature and two mass velocities (100 kg m^{-2} s^{-1} and 800 kg m^{-2} s^{-1}) have been considered. At 100 kg m^{-2} s^{-1}, much higher heat transfer coefficients were obtained in the horizontal configuration as compared to the vertical one. At 800 kg m^{-2} s^{-1}, all the simulation cases displayed almost identical results and shear stress was found to be the dominant force since the distribution of local condensate thickness and local heat transfer were axisymmetrical.
In the present study, an experimental investigation of condensation inside a single square cross section minichannel when varying the channel orientation is presented. Local heat transfer coefficients are measured in several downflow and upflow configurations and are compared against those obtained in horizontal configuration. The channel is obtained from a copper rod and has a square cross section with 1.18 mm side length. Each corner has a curvature radius equal to 0.15 mm, which leads to a hydraulic diameter equal to 1.23 mm. Tests have been performed with R134a and R32 at 40°C saturation temperature, at mass velocity ranging between 100 kg m^{-2} s^{-1} and 390 kg m^{-2} s^{-1}. From the experimental results, the effect of the channel inclination when varying mass velocity and vapor quality is investigated. Finally, it is put forward a correlation of dimensionless parameters that can be useful to predict at which mass velocity the effect of inclination starts to affect the condensation process.

4.3 Condensation test apparatus

4.3.1 Description of the test rig

A schematic representation of the test rig for the experimental tests during condensation in a square minichannel at different orientations is depicted in Figure 4.1.
After passing through the test section, the working refrigerant is subcooled in the post condenser by using brine at 5°C which flows inside an auxiliary loop served by a thermal bath. The subcooled refrigerant is sent through a filter dryer into an independently

controlled oil-free gear micro pump and a Coriolis-effect mass flow meter which is used to measure the mass flow rate. A mechanical filter is placed upstream the test section to prevent foreign matters from entering. In the tube-in-tube heat exchanger, the refrigerant is vaporized and superheated by using hot water flowing in a closed auxiliary loop where the inlet temperature is kept at a desired value by PID-controlled electrical heaters.
The test section consists of two heat exchangers where the heat is transferred between the refrigerant and a secondary fluid, that is distilled water. From the inlet of the test section, the first sector is a co-current heat exchanger is dubbed inlet condition setter as the desired thermodynamic inlet conditions of the refrigerant are here achieved. During condensation tests, it works as desuperheater and in case as pre-condenser with the refrigerant exiting with a vapor quality close to 1. The second heat exchanger is the actual measuring section as it is provided with all the instrumentation to analyze the two-phase heat transfer process during condensation. In the measuring section, a countercurrent flow arrangement is realized. At the inlet of each part of the test section, the pressure is gauged by means of two digital strain gauges relative pressure transducers, whereas a differential pressure transducer is employed to measure pressure drop along the measuring section. All the pressure transducers are connected to the pressure ports of the test section by pressure lines on whose external surface wire electrical heaters are applied. The distilled water flows in two independent loops served by the same thermal bath. Each loop is provided with a flow regulating valve, which allows to set the water mass flow rate and a Coriolis effect mass flow meter. When necessary, the water entering the inlet condition setter and the measuring section can be maintained at different temperatures through electrical heaters installed downstream of the thermal bath in each distilled water loop. In every test run, when the apparatus is working in steady state conditions, measurements of thermo-fluid-dynamic parameters are recorded for 50 s with a time step of 1 s. Each recording is averaged and then reduced by calculating the fluid properties with NIST Refprop Version 9.0 [16].

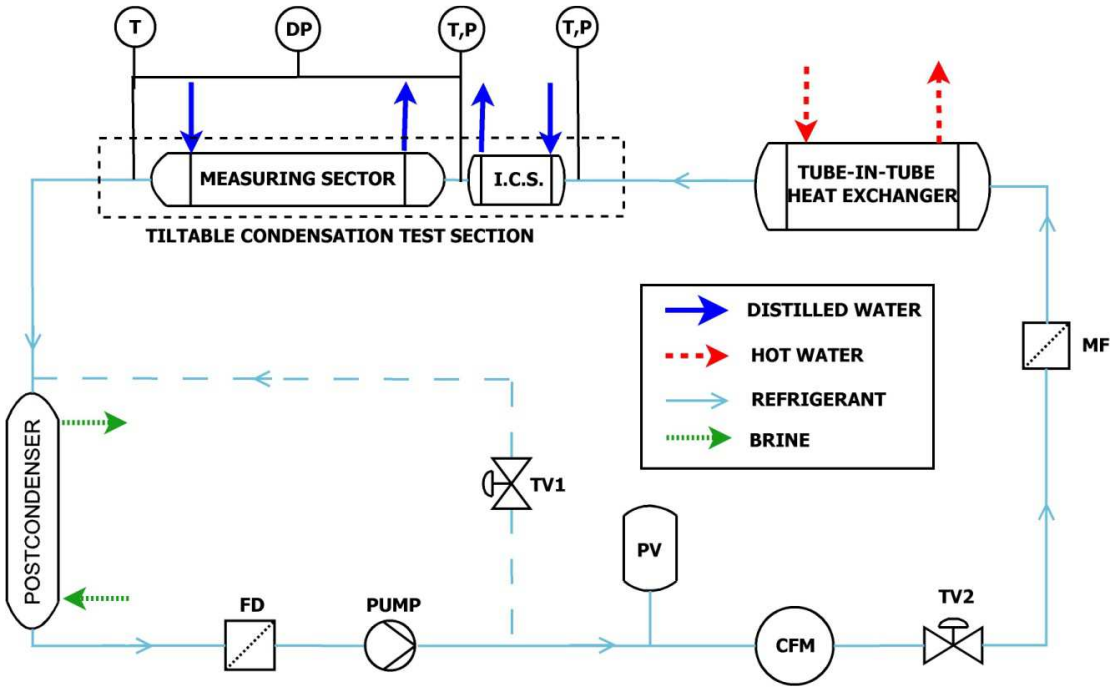

Figure 4.1. Experimental test rig: I.C.S. (inlet condition setter); FD (filter drier); TV (throttling valve); PV (pressure vessel); CFM (Coriolis-effect mass flow meter); MF (mechanical filter); P (relative pressure transducer); DP (differential pressure transducer)

4.3.2 Description of the test section

The geometry of the test section leads to a high precision in the evaluation of condensation heat transfer coefficients. The minichannel is obtained from a copper rod soldered together with stainless steel rods, which are located downstream of the test section, between the inlet condition setter and the measuring section and between the measuring section and the rest of the test rig. They work as adiabatic sectors and provide a good thermal separation as their thermal conductivity is much lower than that of copper. Copper and steel rods have been internally holed by electro-erosion to obtain a square cross section with 1.18 mm side length. Each corner has a curvature radius equal to 0.15 mm, which leads to a hydraulic diameter of 1.23 mm. The measuring section is 224 mm long (Figure 4.2). The internal surface roughness of the copper channel has been measured with a digital surface roughness machine at different positions. The mean roughness *Ra*, as defined by the ISO 4287:1998 standard [15], ranges between 0.80 µm and 1.32 µm, with a mean value equal to 1.02 µm. On the outer tube surface of the adiabatic stainless steel sectors, the temperature of the refrigerant at the inlet and at the outlet of the measuring section can be measured with good accuracy; the pressure taps are also placed in the adiabatic segments and they are connected to digital strain gauge pressure (relative and differential) transducers. The distance between the pressure ports is equal to 249 mm.

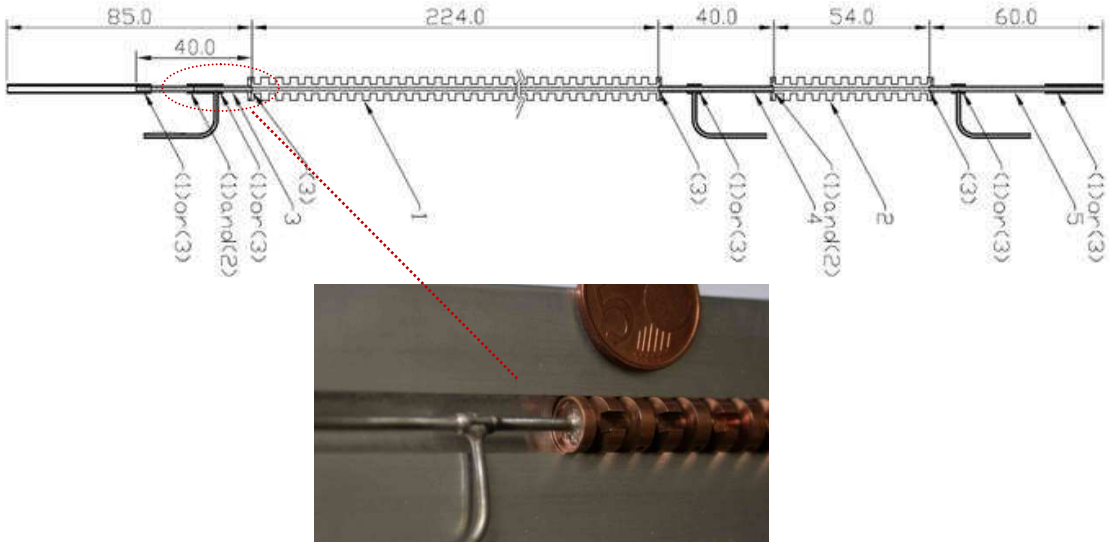

Figure 4.2. Top: design of the test section: 1. Measuring section; 2. Inlet condition setter; 3-4-5. Stainless steels adiabatic sectors; (1). Soldering performed with inertial atmosphere; (2). High precision positioning; (3) Soldering performed prior to the electric discharge machining of the square minichannel. Bottom: pressure port in a stainless steel adiabatic sector and coolant channel inner geometry in the copper rod.

The coolant path consists of grooves in a row obtained by machining the copper rod external wall: this particular coolant channel is externally covered by a film of epoxy resin that has been holed in some places to insert the thermocouples for the measurement of the coolant temperature profile during condensation. This geometry (Figure 4.3) allows the accurate measurement of the quasi-mixing cup temperature of the water. Besides, other thermocouples have been inserted in the copper fins to measure the wall

temperature without passing through the cooling water and so minimizing errors due to thermal conduction along the thermocouples' wires and thus to temperature gradients and spurious EMFs. The wall thermocouples are embedded into 0.6 mm diameter cylindrical holes in the wall thickness, 0.4 mm - 0.5 mm far from the internal tube surface along the measuring section. On the whole, the measuring section has been equipped with more than sixty T-type thermocouples and some more have been placed in the inlet condition setter. Secondly, the large heat transfer area on the water side implies that the dominant thermal resistance and the maximum fluid to wall temperature difference are on the refrigerant side. As a consequence, according to the experimental technique described below, a very good precision in the evaluation of the heat transfer coefficients can be achieved. After the construction, the test section was inserted in a glass cylinder to reduce heat dissipation towards the external environment and then installed in a aluminum mechanical structure which allows to set the channel at any orientation from vertical upflow to vertical downflow (Figure 4.4).

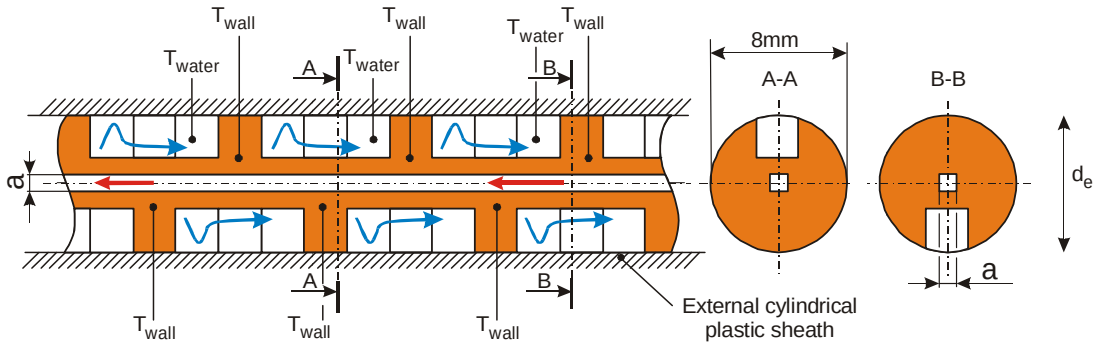

Figure 4.3. Detailed sketch of a portion of the measuring section showing geometry and temperature instrumentation of the coolant channel.

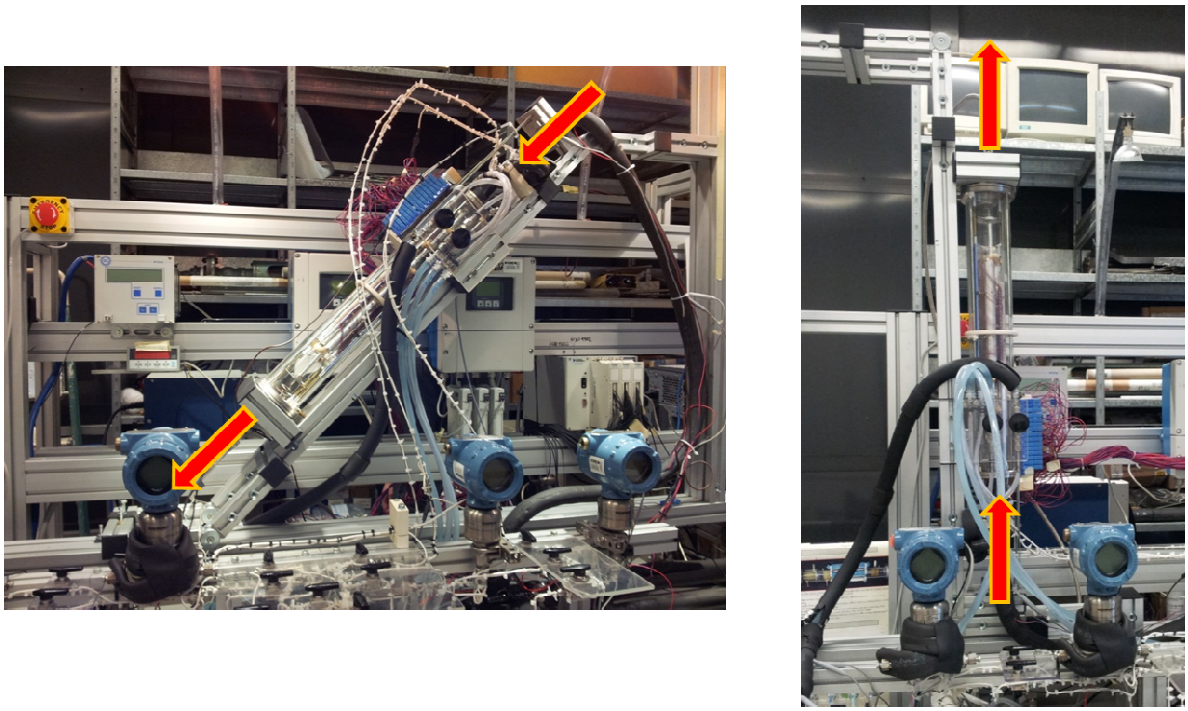

Figure 4.4. Different orientation of the test section to study the effect of inclination in condensation: Left:45° downflow; Right: vertical upflow.

4.4 Experimental technique for condensation tests

4.4.1 Data reduction

During the condensation tests inside the square single minichannel, the temperature of the distilled water flowing in the inlet condition setter remains slightly higher than the saturation temperature. Therefore, the refrigerant exits the inlet condition setter with 4 °C – 6° C superheating and the condensation process begins inside the measuring section. Thus, the thermodynamic state of the refrigerant at the inlet of the measuring section is known from the local pressure and temperature measurements. Nevertheless, some condensation tests have been performed with the refrigerant entering the measuring section as saturated vapor, in order to verify that the condensation heat transfer coefficient does not depend on the inlet refrigerant conditions. In this case, the specific enthalpy of the refrigerant at the inlet of the measuring section is calculated from an energy balance in the inlet condition setter, where desuperheating and partial condensation occur. In each test run, when the experimental apparatus is working in steady state conditions, measurements of temperature, mass flow and pressure (relative and differential) are recorded for 50 s at 1 Hz sampling frequency, averaged and then reduced in a MATLAB [82] environment, calculating fluids properties with NIST Refprop Version 9.0 [16].
The following three parameters are used for the determination of the local heat transfer coefficient HTC: the local heat flux *q'*, the saturation temperature and the wall temperature (equation (4-II)).

$$\mathrm{HTC}\,(z) = \frac{q'(z)}{t_{sat}(z) - t_{wall}(z)} \qquad \textbf{(4-I)}$$

The local heat flux is determined from the derivative of the water temperature profile in the measuring section, therefore the definition of a proper fitting function for the water temperature readings is needed (equation (4-II)).

$$q'(z) = -\dot{m}_{wat,MS}\, c_{p,wat} \frac{1}{\pi\, d_h} \frac{\mathrm{d}t_{wat}(z)}{\mathrm{dz}} \qquad \textbf{(4-II)}$$

First, the number of the water temperatures detected in the actual measuring section to be considered in data reduction is decided. As the condensation process is under investigation, the last employed temperature datum on the water side is the first one at which the thermodynamic vapor quality becomes negative. By considering the conservation of energy in the measuring section, the coolant temperature change is directly associated to the corresponding enthalpy variation of the refrigerant so the thermodynamic vapor quality correspondent to the *j-th* thermocouple placed in the water flows can be calculated according to equation (4-III).

$$x_j = \frac{h_{in,MS} - \frac{\dot{m}_{wat,MS}}{\dot{m}_{ref}} c_{p,wat} \left(t_{wat,out} - t_{wat,j}\right) - h_L}{h_{LV}} \qquad \textbf{(4-III)}$$

After that, a suitable equation to interpolate the selected water temperature measurements along the axial position *z* is established. The equation parameters are calculated by means of the least square method. Four possible interpolating equations are considered in the following order of preference to minimize the uncertainty of heat transfer coefficients: a second order polynomial, an exponential equation with three parameters, a third order

polynomial and a fourth order polynomial. A major number of parameters is not required for the present interpolations. The exponential function is expressed as:

$$t_{water}(z) = a_0 + a_1\, e^{-\frac{z}{a_2}} \qquad \textbf{(4-IV)}$$

Two different criteria are taken into account to find the best fitting equation: the first is based on the use of the coefficients of determination and the second is related to consideration on the experimental uncertainty of the thermocouples' readings.
In statistics, the coefficients of determination *R* square (R^2) and adjusted *R* square (R_{adj}^2) are utilized to assess the goodness of fit (Rawlings *et al.* [52]). Unlike R^2, R_{adj}^2 increases with the number of parameters of the fitting equation only if the new term improves significantly the model. Thus, let y_1 and y_2 be two functions that are one after the other in the aforementioned order of preference: in the present data reduction, by convention, y_1 would be the chosen fitting if the following condition is satisfied:

$$\left|R_{adj}^2(y_1) - R_{adj}^2(y_2)\right| \leq 0.0035 \qquad \textbf{(4-V)}$$

The fitting function emerging from the aforementioned statistical criterion has to satisfy the second criterion based on the experimental uncertainty. Specifically, the calculated values of the water temperatures have to be within the expanded experimental uncertainty of the corresponding thermocouple readings and, in addition, at least 68% of the calculated values has be within ± 0.03°C of the corresponding measured values. If this checking test fails, the next fitting equation in the order of preference will be considered. Finally, in order to assure the accuracy and repeatability of the results, the heat transfer coefficients have to be insensitive to the method of interpolation, that is to say that the variation in heat transfer coefficients using the fitting equation that meets the conditions of the two criteria and the next admissible equation in the order of preference should be within the experimental uncertainty. If the fourth order polynomial interpolates the data in the best way, the sensitivity analysis is performed by comparison with the fifth order polynomial fitting.
Once the interpolating equation for the water temperature is established, the heat local flux can be defined along the channel. Actually, from the direct measurements of the local wall temperatures along the test section, it is possible to calculate the contribution of the axial conduction in the copper wall from an energy balance and to correct the heat flux calculated from equation (4-II).
Given the fitting function of the water temperatures, the vapor quality can be calculated at any axial coordinate *z* along the tube:

$$x(z) = \frac{h_{in,MS} - \dfrac{\dot{m}_{wat,MS}}{\dot{m}_{ref}\, h_{LV}}\, c_{p,wat}\left(t_{wat,out} - t_{wat}(z)\right) - h_L}{h_{LV}} \qquad \textbf{(4-VI)}$$

As the local wall temperature are directly measured at certain axial position, the corresponding value of heat flux and saturation temperature should be defined. The saturation temperature is obtained from the values of the measured pressure in the adiabatic segments only at the inlet and outlet of each part of the test minichannel. As

stated in Del Col *et al.* [50], since the difference between saturation temperature and wall temperature is pretty large for typical test conditions in the present measuring section (7°C – 16°C) and the saturation temperature drop due to pressure drop is small, the local saturation temperature can be obtained from the linear trend between values calculated from pressure measurements the ends of the measuring section without making a significant error in the evaluation of heat transfer coefficients.

4.4.2 Uncertainty analysis

In the present test runs, each measured quantity (temperature, relative pressure, pressure difference, mass flow rate) is read and recorded 50 times with a time step of 1 s. All the readings are independent observations of the quantity under the same condition of measurement, thus the mean value is the best expected value of that measured quantity and the standard deviation of the mean represents its Type A standard uncertainty u_A, according to the ISO Guide to the Expression of Uncertainty in Measurement [17]. The Type B standard uncertainty u_B for each measured quantity, on the other hand, derives from calibration certificates or manufacturers' specification. With reference to the instruments employed during the present tests carried out at the Two-phase Heat Transfer Lab of the University of Padova, the Type B experimental uncertainties of the measured parameters with a level of confidence of 95.45% if not differently specified are reported in Table 4-a. The combined standard uncertainty u_C of a measured parameter θ result from the Type A and Type B components according to equation (4-VII).

$$u_C = \sqrt{u_A(\theta)^2 + u_B(\theta)^2} \tag{4-VII}$$

When a searched parameter ξ is not directly measured but it can be expressed as a function F of uncorrelated input quantities $\theta_1, \theta_2, \ldots, \theta_N$, as in the case of heat transfer coefficient or thermodynamic vapor quality, its combined standard uncertainty is determined from equation (4-VIII).

$$u_C(\xi) = \sqrt{\sum_{i=1}^{N} \left(\frac{\partial F}{\partial \theta_i}\right)^2 u_C(\theta_i)^2} \tag{4-VIII}$$

Table 4-a. Type B uncertainty of measured parameters.

Temperature	± 0.05 °C
Temperature difference (with thermopile)	± 0.03 °C
Water flow rate in inlet condition setter	± 0.2 % at 10 kg h^{-1}
Water flow rate in measuring section	± 0.14 % at 10 kg h^{-1}
Refrigerant flow rate	± 0.2 % at 2 kg h^{-1}
Absolute pressure	± 5 kPa (level of confidence: 99.7%)
Pressure difference (greater than 1 kPa)	± 0.12 kPa (level of confidence: 99.7%)
Pressure difference (below 1 kPa)	± 0.1% (level con confidence 99.7%)

According to equation (4-I) and equation (4-II), the function describing the local condensation heat transfer coefficient is:

$$\mathrm{HTC}(z) = F\left(t_{sat}, t_{wall}, \dot{m}_{wat,MS}, \frac{\mathrm{d}t_{wat}}{\mathrm{dz}}, d_h\right) \quad \textbf{(4-IX)}$$

While the local wall temperature is directly measured, the local saturation temperature is estimated by a linear combination of the values derived from pressures gauged at the ends of the measuring section. Thus, the experimental uncertainty of the local saturation temperature results from a linear interpolation of the experimental uncertainty of the inlet and outlet saturation temperature. The uncertainty of a saturation temperature derived by a pressure measurement is determined by the difference between the value of saturation temperature at the measured pressure p and the value of saturation temperature at a pressure equal to $p+u_C(p)$ (equations (4-X) and (4-XI))

$$u_C\left(t_{sat,in\ MS}\right) = t_{sat,in\ MS}\left(p_{in,MS}\right) - t_{sat,in\ MS}\left(p_{in,MS} + u_C\left(p_{in,MS}\right)\right) \quad \textbf{(4-X)}$$

$$u_C\left(t_{sat,out\ MS}\right) = t_{sat,out\ MS}\left(p_{out,MS}\right) - t_{sat,out\ MS}\left(p_{out,MS} + u_C\left(p_{out,MS}\right)\right) \quad \textbf{(4-XI)}$$

Equation (4-XII) sets out the expression of the uncertainty for local saturation temperature:

$$u_C(t_{sat}(z)) = \sqrt{\left(1 - \frac{z}{L_{MS}}\right)^2 \left(u_C\left(t_{sat,in\ MS}\right)\right)^2 + \left(\frac{z}{L_{MS}}\right)^2 \left(u_C\left(t_{sat,out\ MS}\right)\right)^2} \quad \textbf{(4-XII)}$$

The other main uncertainty terms are associated to the water mass flow rate, the hydraulic diameter and water temperature gradient. In turn, the water temperature gradient depends on the operating conditions, mainly mass flux and vapor quality, yielding higher uncertainty at lower mass flux. The procedure that has been implemented for determining the uncertainty related to the water temperature gradient is the weighted least square *(WLS)* regression method (Press *et al.* [55]).

As described in section 4.4.1, for each test run a function of the axial position z has been determined to fit the water temperature. Whatever the fitting function $y(z)$, its $M+1$ coefficients $a_0, \ldots, a_M$ are defined in order to minimize the merit figure χ^2.

Let i varies from 1 to nTC, that is the number of water thermocouples considered for the data reduction as described in section 4.4.1 and let $t_{wat,i}$ be the measured values read by the *i-th* water thermocouple located at an axial coordinate z_i. Hence, $y(z_i)$ is the water temperature at the axial position z_i calculated using the fitting function and the merit figure χ^2 is defined as:

$$\chi^2 = \sum_{i=1}^{nTC} \left[\frac{t_{wat,i} - y(z_i)}{u_C(t_{wat,i})}\right]^2 \quad \textbf{(4-XIII)}$$

The minimum of the merit figure occurs where its derivatives with respect to all parameters of the fitting function $a_0, \ldots, a_M$ are equal to zero. This condition yields the following matrix equation:

$$\left(\mathbf{A^T} \cdot \mathbf{A}\right) \cdot \mathbf{a} = \mathbf{A^T} \cdot \mathbf{b} \quad \textbf{(4-XIV)}$$

where **A** is a *nTC* x *(M+1)* matrix whose elements are obtain as reported in equation (4-XV)

$$A_{ij} = \left(\frac{\frac{\partial y}{\partial a_{j-1}}}{u_C(t_{wat,i})} \right) \quad \textbf{(4-XV)}$$

b is a vector of *nTC* constant terms defined as the ratio between the water temperature measured at the *i-th* location and the correspondent combined uncertainty:

$$b_i = \left(\frac{t_{wat,i}}{u_C(t_{wat,i})} \right) \quad \textbf{(4-XVI)}$$

and finally **a** is the vector of the (*M+1)* coefficients of the fitting equation. The covariance matrix **C**, defined according to equation (4-XVII), is closely related to the standard uncertainty of the parameters $a_0, \ldots, a_M$: the diagonal elements C_{jj} are the square uncertainties of the fitted parameters $a_0, \ldots, a_M$, while the off-diagonal elements C_{jk} are the covariances between the estimated coefficients a_j and a_k, dubbed cov(a_j, a_k).

$$\mathbf{C} = \left(\mathbf{A^T} \cdot \mathbf{A}\right)^{-1} \quad \textbf{(4-XVII)}$$

The elements of the covariance matrix **C** are useful to calculate the uncertainty related to the temperature gradient by applying the law of propagation of uncertainty for correlated input quantities (equation (3-XIX)). In this calculation, the coefficient a_0 is not present, as it is a constant term in the water temperature fitting function *y(z)*, whatever its form.

$$u_C\left(\frac{\mathrm{d}t_{wat}}{\mathrm{d}z}\right) = \sqrt{\sum_{i=1}^{M} \left(\frac{\partial \left(\frac{\mathrm{d}y(z)}{\mathrm{d}z}\right)}{\partial a_i} \right)^2 \left(u(a_i)\right)^2 + 2 \sum_{i=1}^{M-1} \sum_{j=i+1}^{M} \left(\frac{\partial \left(\frac{\mathrm{d}y(z)}{\mathrm{d}z}\right)}{\partial a_i} \right) \left(\frac{\partial \left(\frac{\mathrm{d}y(z)}{\mathrm{d}z}\right)}{\partial a_j} \right) \mathrm{cov}(a_i, a_j)} \quad \textbf{(4-XVIII)}$$

As reported in Del Col *et al.* [50], the effect of the uncertainty in the thermocouple location has also been investigated and it was found to be negligible as compared to the uncertainty due to the temperature readings. As it was done for the heat transfer coefficient, the experimental uncertainty is also specified for the vapor quality, which is described along the test section by the following function:

$$x(z) = F\left(h_{in,MS}, \dot{m}_{wat,MS}, c_{p,wat}, t_{wat,out\ MS}, t_{wat}(z), \dot{m}_{ref}, h_{LV}\right) \quad \textbf{(4-4-XIX)}$$

The uncertainty of the specific enthalpy at the inlet of the measuring section, of the latent heat of condensation as well as the uncertainty of the water isobaric specific heat are neglected. The uncertainty of the water temperature at the axial location z is calculated

applying the law of propagation of uncertainty for correlated inputs, according to the chosen fitting function.
The expanded uncertainty for a given quantity is obtained considering a coverage factor equal to 2 and thus a level of confidence of 95.45%.

4.5 Calibration and preliminary tests

In order to assure the accuracy of the analysis of the two-phase heat transfer process using the experimental technique above illustrated, several preliminary tests must be performed. Prior to any condensation test, the on-site periodical calibration of the thermocouples, the check of the agreement between temperature and pressure under saturated conditions and the check of the thermal balance in the test section and the measuring section have been carefully carried out.
The thermal balance in the test section and in the measuring section, comparing the water side heat transfer rate to the one on the refrigerant side when superheated vapor enters the test section and subcooled liquid exits is checked: the agreement is found within 2%.
The periodical calibration of the T-type thermocouples along the measuring section have been calibrated following the technique illustrated in Del Col *et al.* [50], by circulating water under adiabatic conditions in the channel where two high precision four wire thermistors are arranged. The thermistors are connected to a Hart Scientific Super Thermometer II forming a measure chain with a global accuracy of ±0.002 °C (as from the check against the water triple point). The goal of the periodical calibration is the definition of a correction function for each thermocouple by comparing the temperature measured by the considered thermocouple against the reference temperature gauged by the thermistors. Actually, the correction on a thermocouple reading is done only if the disagreement with the reference temperature is not within ± 0.05 °C. At first, the water temperature is close to that of the surrounding environment. After the calibration , some verification tests are done at different water temperatures to check if the thermocouples reading are within ± 0.05 °C as compared to the reference temperature. During these verification tests, the water circulates under adiabatic conditions at a temperature within 20°C and 30°C to cover the working condition in the measuring section during the condensation tests. In Figure 4.5, the wall and water thermocouples readings in the measuring section are reported against the thermistors' reading before the periodical calibration and after a verification test.
A similar on site calibration procedure is performed for the thermal sensors of the initial condition setter.
The agreement between the measuring section inlet temperature of the refrigerant, measured by a thermocouple and the saturation temperature obtained from the pressure measurement is checked and it is found to be lower than 0.2°C, that is within the experimental uncertainty of the two instruments.
Finally, the pressure transducers have been checked against a pressure calibrator as described in Chapter 2.
Beside this, as reported in Del Col *et al.* [50] , the accuracy of the measurements performed with the experimental apparatus described above is also assured by:

- an investigation of the influence of the ambient temperature on the measurements to confirm experimentally that the heat dissipation to ambient is negligible;
- measurements of single-phase pressure drops to characterize test channel, verify its dimension and validate the data acquisition system;
- performing single-phase heat transfer tests, which represent a good validation of the experimental technique for condensation tests.

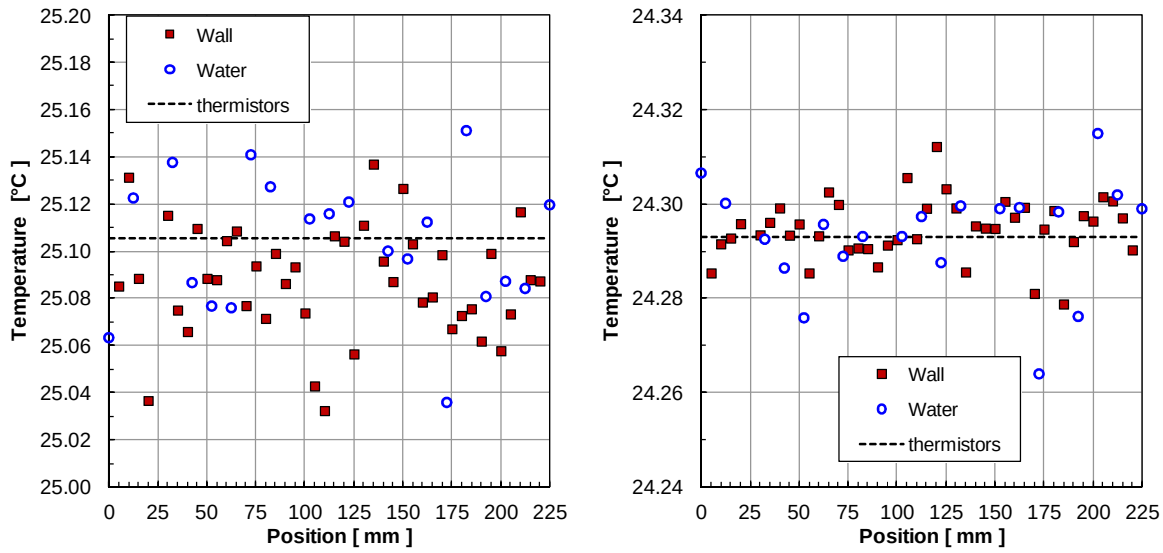

Figure 4.5. Water and wall temperatures along the measuring section against the thermistors reading. Left: before on-site calibration; Right: after on-site calibration.

4.6 Experimental results and discussion

The local heat transfer coefficients have been measured during the condensation of R134a and of R32 at 40°C saturation temperature, varying the mass velocity and the orientation of the test section. In the presented results, the vapor quality ranges between 0.2 and 0.9. The R134a condensation tests are performed at mass velocities within 100 kg m^{-2} s^{-1} and 390 kg m^{-2} s^{-1}, first in horizontal configuration and then considering both downward flow and upward flow conditions at inclination angles of 30°, 45°, 60° and 90°. On the other hand, R32 condensation tests have been done at mass velocities between 100 kg m^{-2} s^{-1} and 390 kg m^{-2} s^{-1}, in horizontal and in downward flow conditions at inclination angles of 15°, 30°, 45°, 60° and 90°. The inclination angle is computed from the horizontal, which corresponds to 0°. In Table 4-b , the expanded experimental uncertainty range of heat transfer coefficient *U*(HTC) is reported for each fluid at any considered mass velocity taking into account all the channel orientations. According to the trends observed in Del Col *et al.* [50], at low mass velocities, the experimental uncertainty is lower in the middle of the measuring section and it is higher at the inlet and the outlet. At high mass velocity the experimental uncertainty of the heat transfer coefficient is within a narrow range along the entire measuring section. Furthermore, it decreases in percent terms when increasing mass velocity. In Table 4-b, the expanded uncertainty of the vapor quality *U(x)* is also included: it decreases when increasing mass velocity.

Table 4-b. Expanded experimental uncertainty of heat transfer coefficient and vapor quality during condensation tests of R134a and R32 inside the square minichannel at different orientations.

Mass velocity [kg m^{-2} s^{-1}]	R134a		R32	
	U (HTC) [%]	*U (x)* [/]	*U* (HTC) [%]	*U (x)* [/]
100	4.0 % - 11.8%	0.035	4.0% - 12.1%	0.022
120	4.0 % - 9.9%	0.029	4.0% - 9.1%	0.018
135	4.0% - 7.1%	0.027	4.0% - 8.9%	0.017
150	4.0 % - 6.1%	0.023	4.0% - 8.8%	0.016
200	4.0- 5.0%	0.016	4.0% - 6.0%	0.01
390	4.0%	0.01	4.0%	0.01

Several tests have been performed to check accuracy and repeatability of the experimental technique. Figure 4.6 shows that two data sets determined in different test runs overlap. The first set of data has been collected with the working refrigerant entering the measuring sector as superheated vapor ($x_{in} > 1$, $\Delta T_{superheat} \approx 5$ K) while the second one refers to a test run with refrigerant entering as saturated vapor ($x_{in} < 1$). Some differences in the first and in the last values of the heat transfer coefficient may be due to boundary effects in the measurements and to the increased uncertainty associated to the local heat flux, as described above. One can conclude that the present test apparatus provides the same HTC at the same refrigerant conditions, no matter at which location this coefficient is measured along the channel and no matter the inclination of the channel.

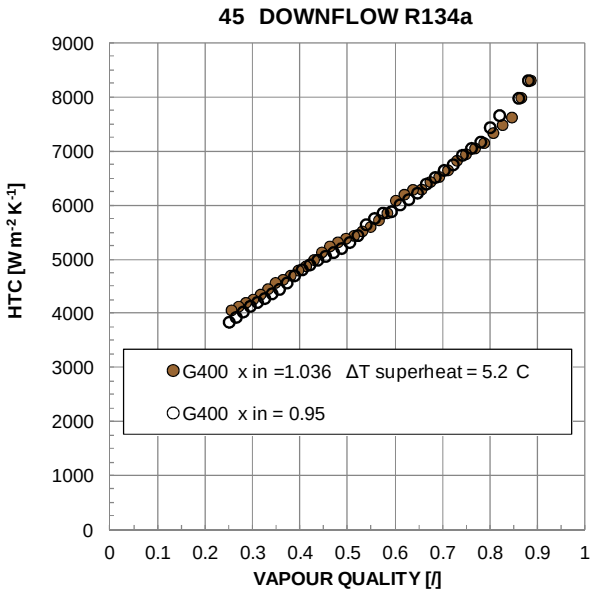

Figure 4.6. Experimental local heat transfer coefficient (HTC) during the condensation of R134a inside the square minichannel at 40°C saturation temperature and at varying inlet refrigerant conditions (superheated vapor or saturated vapor) at G= 400 kg m^{-2} s^{-1} and at 45° downflow.

The effect of mass velocity on condensation heat transfer coefficient has been investigated by plotting the experimental data at a fixed channel orientation and at different mass fluxes. In
Figure 4.7, the heat transfer coefficients of R134a are plotted against vapor quality in horizontal configuration.
The R134a experimental heat transfer coefficients found for the test runs with horizontal channel agree with those calculated for the same conditions in Del Col *et al.* [50] within the experimental uncertainty.
The heat transfer coefficients obtained during condensation of R134a are reported versus vapor quality for all the tested configurations from Figure 4.8 to Figure 4.11. Each one of these figures presents a comparison between the results at a certain channel inclination in downward flow and at the corresponding inclination in upward flow.

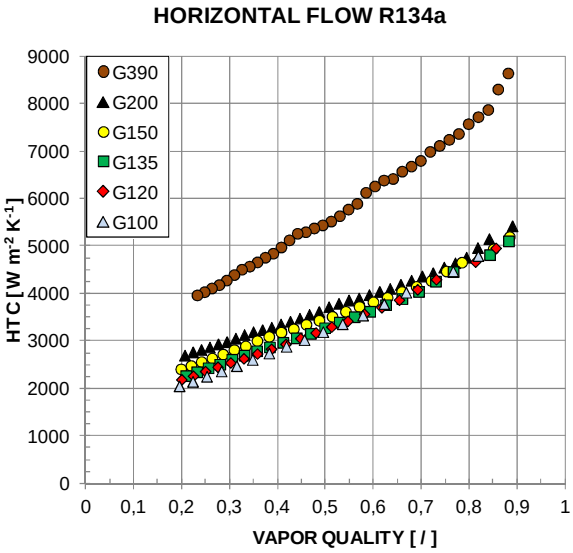

Figure 4.7. Experimental local heat transfer coefficient (HTC) during condensation of R134a inside the square cross section minichannel at different mass fluxes *G* [kg m^{-2} s^{-1}] in horizontal flow.

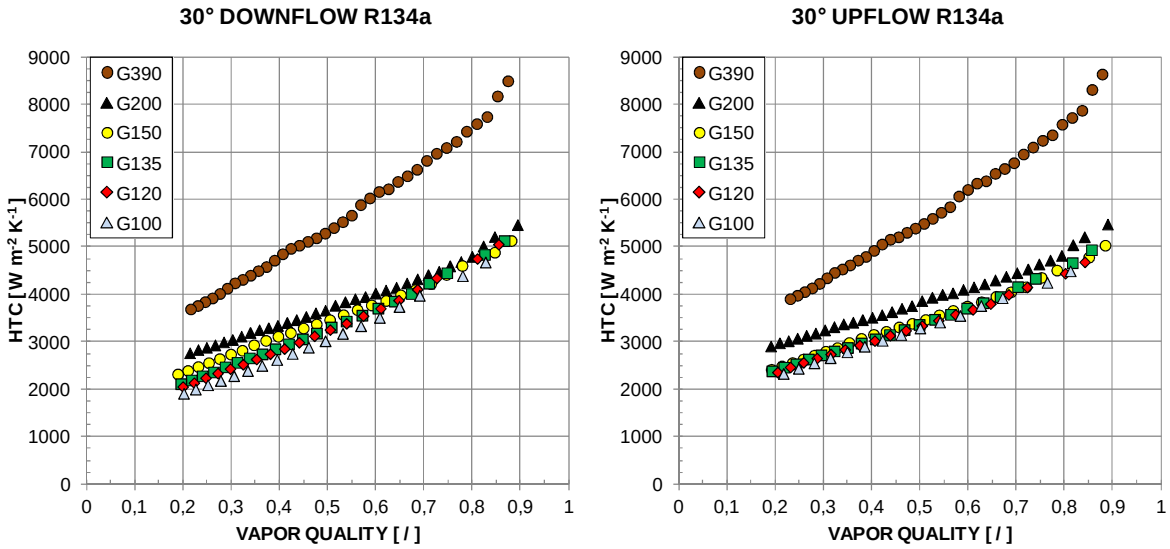

Figure 4.8. Experimental local heat transfer coefficient (HTC) during condensation of R134a inside the square cross section minichannel at different mass fluxes *G* [kg m^{-2} s^{-1}] and channel inclinations. Left: 30° downward flow; Right: 30° upward flow.

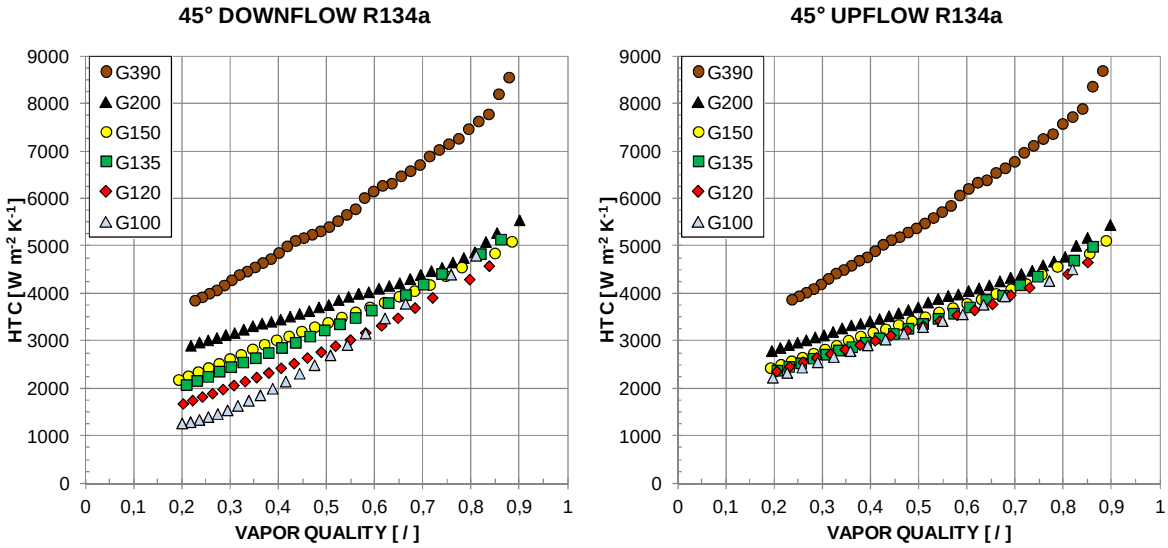

Figure 4.9. Experimental local heat transfer coefficient (HTC) during condensation of R134a inside the square cross section minichannel at different mass fluxes *G* [kg m^{-2} s^{-1}] and channel inclinations. Left: 45° downward flow; Right: 45° upward flow.

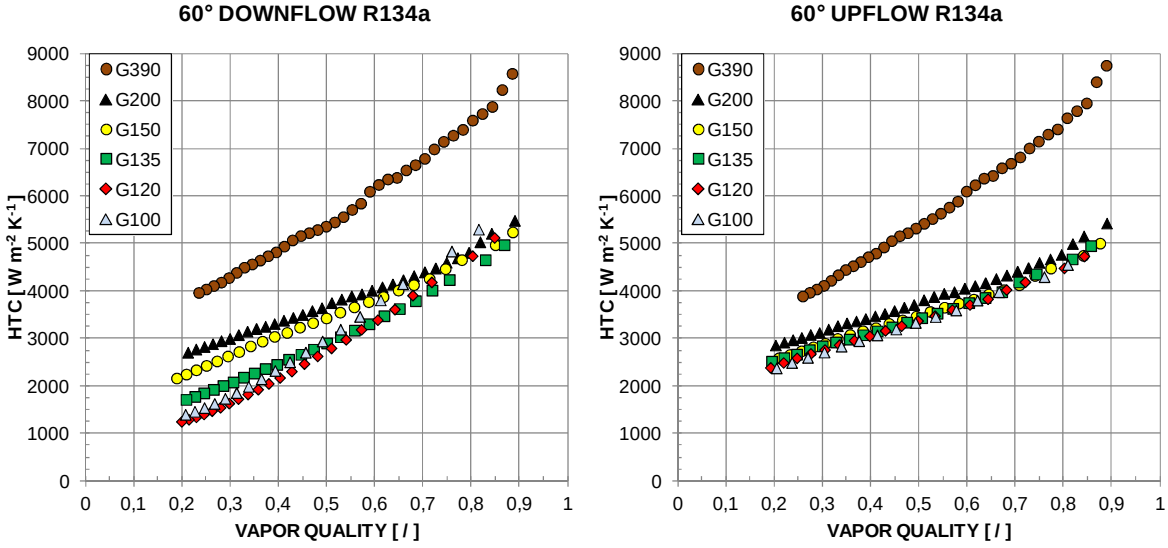

Figure 4.10. Experimental local heat transfer coefficient (HTC) during condensation of R134a inside the square cross section minichannel at different mass fluxes *G* [kg m^{-2} s^{-1}] and channel inclinations. Left: 60° downward flow; Right: 60° upward flow.

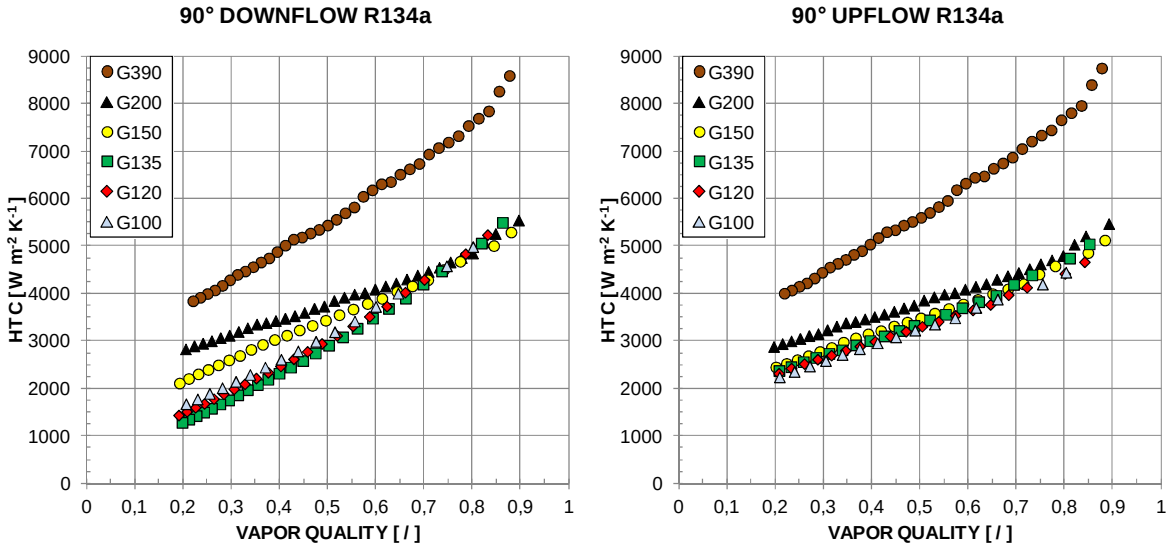

Figure 4.11. Experimental local heat transfer coefficient (HTC) during condensation of R134a inside the square cross section minichannel at different mass fluxes *G* [kg m^{-2} s^{-1}] and channel inclinations. Left: vertical downward flow; Right: vertical upward flow.

The heat transfer coefficients during condensation of R32 inside the minichannel square minichannel are depicted in Figure 4.12, while the experimental results obtained in several downward configurations are shown in Figure 4.13.

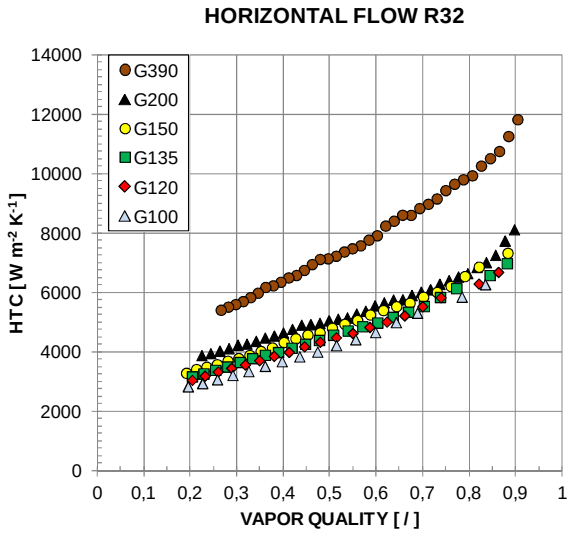

Figure 4.12. Experimental local heat transfer coefficient (HTC) during condensation of R32 inside the square cross section minichannel at different mass fluxes *G* [kg m^{-2} s^{-1}] in horizontal flow.

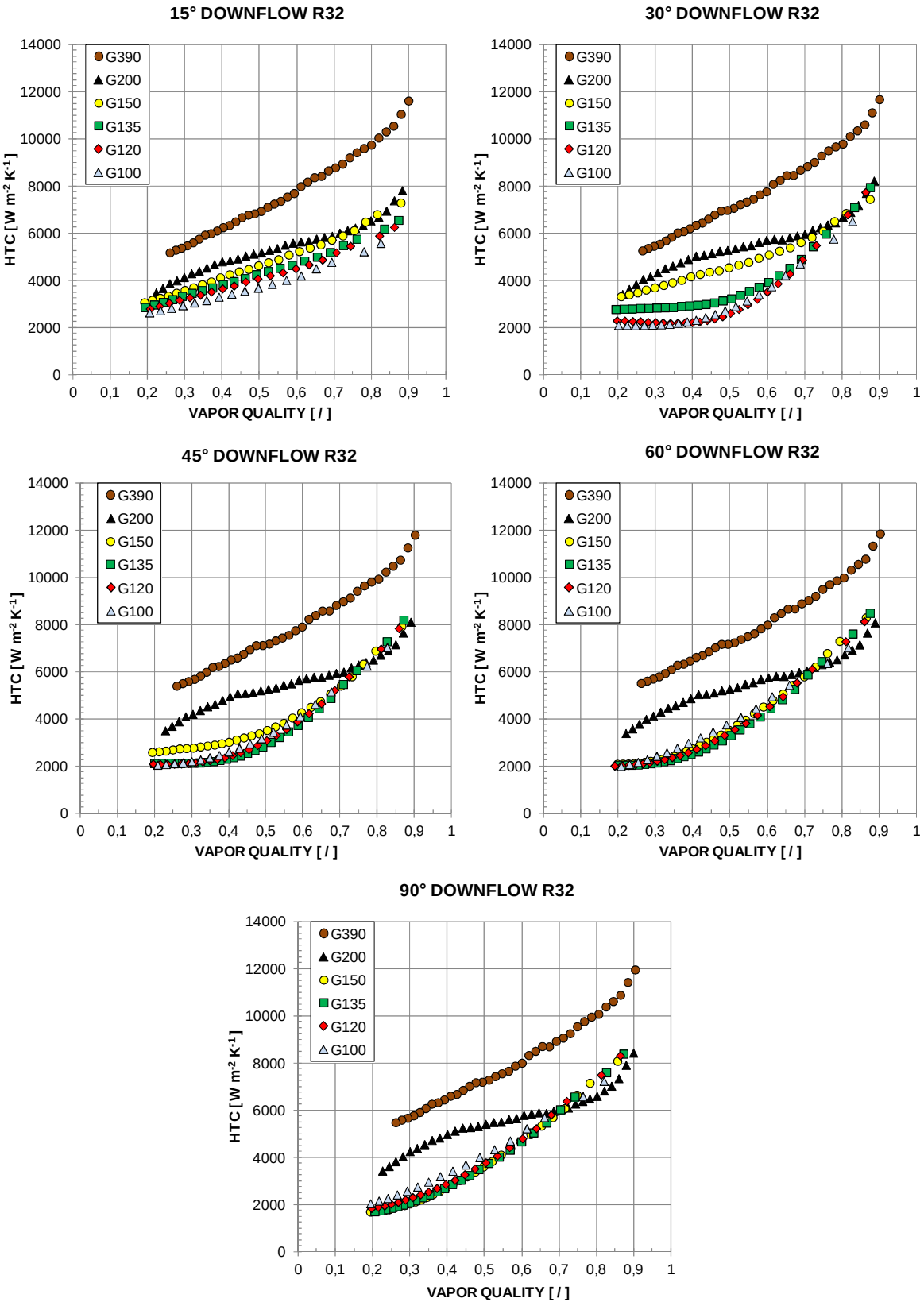

Figure 4.13. Experimental local heat transfer coefficient (HTC) during condensation of R32 inside the square cross section minichannel at different mass fluxes *G* [kg m^{-2} s^{-1}] and different configuration in downward flow.

According to the data sets at 200 kg m^{-2} s^{-1} and 390 kg m^{-2} s^{-1} for both the tested refrigerant, the heat transfer coefficients display a trend that one would expect for condensation inside a conventional tube: they increase with thermodynamic vapor quality and with mass velocity, implying that condensation must be controlled by shear stress and that the influence of surface tension and gravity may be negligible.
From the comparison between the data at 200 kg m^{-2} s^{-1} and data at lower mass velocities, whatever the fluid or the inclination, one can deduce that the shear stress may not be the dominant force any more. In fact, at high vapor qualities, the heat transfer coefficient at 200 kg m^{-2} s^{-1} is very close to those at lower mass fluxes, while the values of the heat transfer coefficients differ more and more as the condensation proceeds and the vapor quality decreases. This may be explained by considering that the distribution of the liquid film at the wall is influenced by gravity, surface tension and shear stress. As it can be seen in Figure 4.7 and in Figure 4.12, during horizontal flow, as the mass velocity decreases and the liquid film becomes thicker and thicker, the heat transfer coefficient is penalized by the lower shear stress.
In all the downflow configurations, the values of the heat transfer coefficients at 100 kg m^{-2} s^{-1} and 200 kg m^{-2} s^{-1}diverge even more, as compared to the horizontal configuration related to the investigated fluid. This may imply that, in the present square channel, gravity has still a role in the distribution of the liquid film at the wall and consequently on the condensation heat transfer process.
On the other hand, in any upward flow condition, no significant change can be observed with respect to the horizontal configuration.
With reference to the results presented in Figure 4.13 and related to the condensation of R32 in downward flow configurations, it can be easily noted that the data at 200 kg m^{-2} s^{-1} display a singular trend. Several tests have been repeated at this mass velocity for each channel orientation and they confirm the results. Furthermore, it has been observed that this trend mirrors the one of the wall temperatures along the measuring section.
The effect of orientation on the condensation heat transfer coefficient may be better discussed by comparing the experimental results at the same mass velocity and different channel configurations. In this paper, the criterion to establish if the channel orientation affects the condensation process is based on the comparison of heat transfer coefficients obtained in a certain channel configuration with respect to those measured in horizontal configuration, that is the reference case. The influence of the channel inclination on the condensation heat transfer is declared if the percentage difference between the heat transfer coefficients is clearly greater than the expanded experimental uncertainty and in any case it must not be smaller than 11% in absolute value.
First, the working conditions in which there is no effect of the channel orientation in the condensation heat transfer are presented and discussed.
Actually, no significant variation of the heat transfer coefficient is observed when performing tests in upward flow, at any channel inclination and mass velocity.
The heat transfer coefficients related to the condensation of R134a in upflow condition at 390 kg m^{-2} s^{-1}, 150 kg m^{-2} s^{-1}, 120 kg m^{-2} s^{-1} and 100 kg m^{-2} s^{-1} are reported in Figure 4.14 with the corresponding error bands against the vapor quality. The horizontal configuration is also plotted. At 390 kg m^{-2} s^{-1} and 150 kg m^{-2} s^{-1}, there is no effect of channel inclination. This observation is also confirmed for data set at 200 kg m^{-2} s^{-1}.
At 120 kg m^{-2} s^{-1} and 100 kg m^{-2} s^{-1} no variation in heat transfer coefficient are observed at vapor quality higher than 0.4. At lower vapor quality and when the channel is inclined at 60° in upward flow, a slight increase in heat transfer coefficients occurs as compared to the horizontal configuration. This increase appears also at 135 kg m^{-2} s^{-1} but it is not present at higher mass velocities. The percentage increase in heat transfer is around 11%,

so it is on the edge of the criterion here adopted to declare if the influence of channel orientation during condensation is important. Thus, in conclusion, in the present minichannel, the heat transfer coefficient during condensation in upflow is absolutely not penalized by the orientation of the channel as compared to that obtained in horizontal.

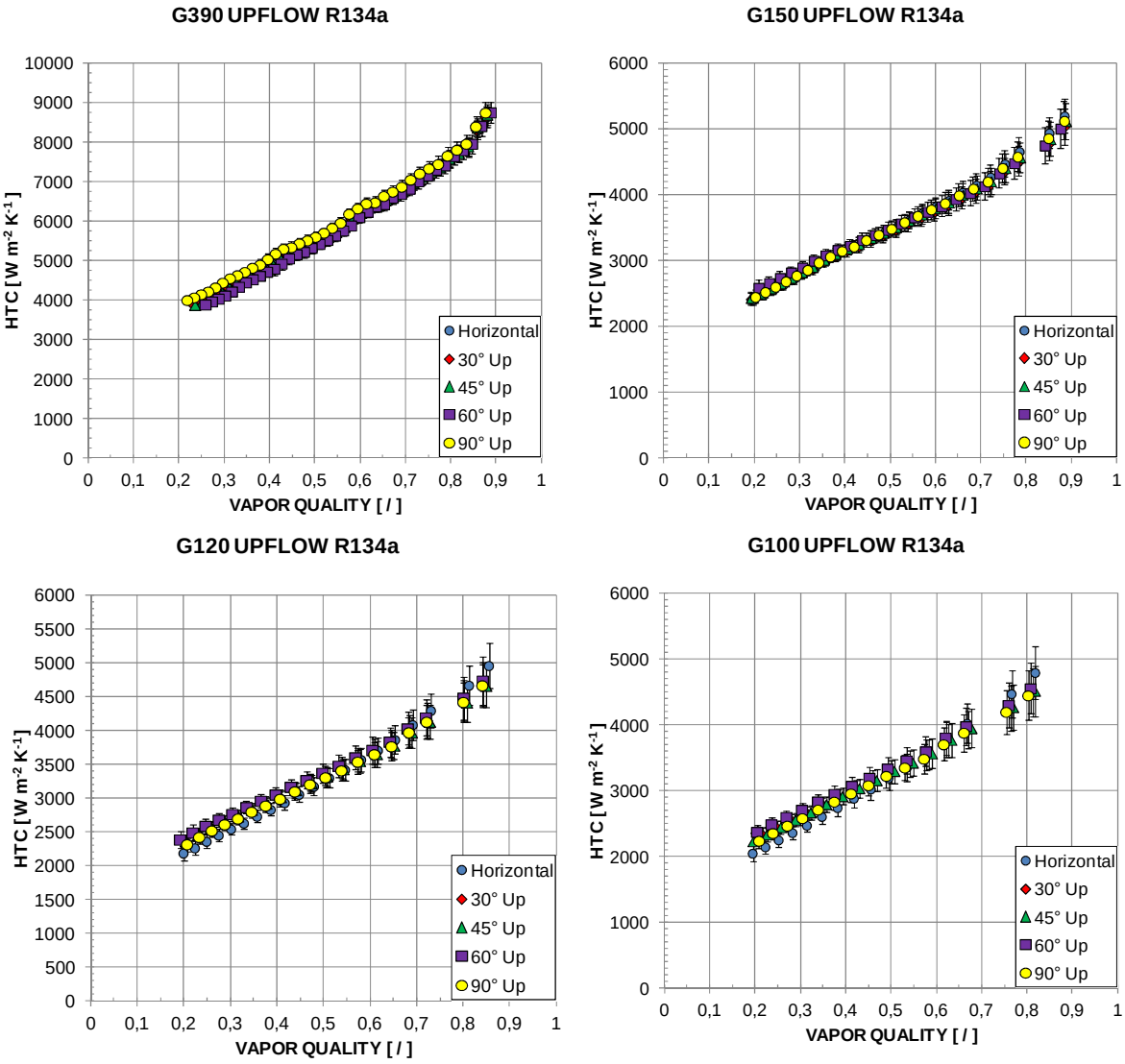

Figure 4.14. Effect of inclination on heat transfer coefficient during condensation of R134a in upward flow inside the square cross section minichannel at a constant mass flux *G* [kg m^{-2} s^{-1}]. Top: Left) *G* = 390 kg m^{-2} s^{-1}; Right) *G* = 150 kg m^{-2} s^{-1}. Bottom: Left) *G* = 120 kg m^{-2} s^{-1}; Right) *G* = 100 kg m^{-2} s^{-1}.

In downward flow configurations, the effect of the channel orientation is not important only at higher mass velocities, in a range that depends on the tested refrigerant.

When performing condensation tests in downflow with R134a, the channel inclination plays a minor role for mass velocities down to 150 kg m^{-2} s^{-1}. In Figure 4.15, the R134a heat transfer coefficients obtained at 200 kg m^{-2} s^{-1} and 150 kg m^{-2} s^{-1} are plotted against vapor quality for all the investigated orientation in downflow conditions and are compared to those obtained in horizontal configuration. The error bands of the heat transfer coefficient are also reported. At 200 kg m^{-2} s^{-1}, no effect of inclination can be observed and this is valid also for the data set at 390 kg m^{-2} s^{-1}. On the other hand, at 150 kg m^{-2} s^{-1}, negligible variation of heat transfer coefficients can be found at high vapor quality, but at vapor quality close to 0.20, in vertical downflow, a percentage decrease of

11% -13% can be observed in heat transfer coefficient as compared to that measured with horizontal test section.

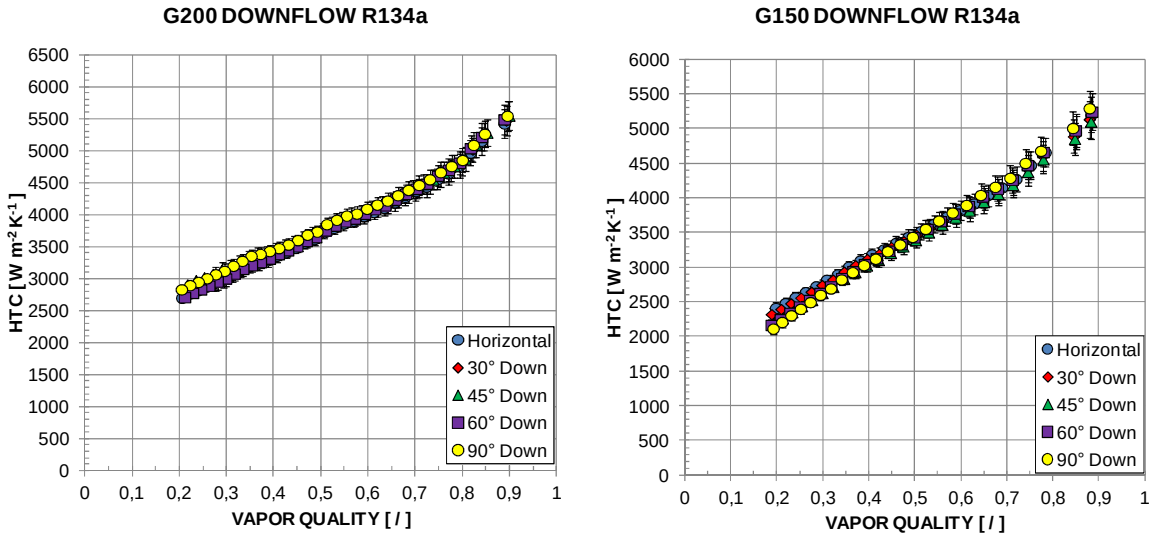

Figure 4.15. Effect of inclination on heat transfer coefficient during condensation of R134a in downward flow inside the square cross section minichannel at a constant mass flux *G* [kg m^{-2} s^{-1}]. Left) *G* = 200 kg m^{-2} s^{-1}; b) *G* = 150 kg m^{-2} s^{-1}.

The results obtained during the condensation of R32 inside the square minichannel in downward flow point out that the effect of channel orientation is negligible at mass velocities down to 200 kg m^{-2} s^{-1}. In Figure 4.16, the data set for condensation heat transfer of R32 at 400 kg m^{-2} s^{-1} and 200 kg m^{-2} s^{-1} are reported for all the investigated channel orientations in downflow as well as for the horizontal reference case. In the plots, the heat transfer coefficient is graphed with its error bands against the vapor quality. At 400 kg m^{-2} s^{-1}, no effect of inclination is found, while at 200 kg m^{-2} s^{-1}, a decrease of heat transfer coefficient can be noticed only at vapor quality lower than 0.25 when the channel is inclined at 60° and 90°.

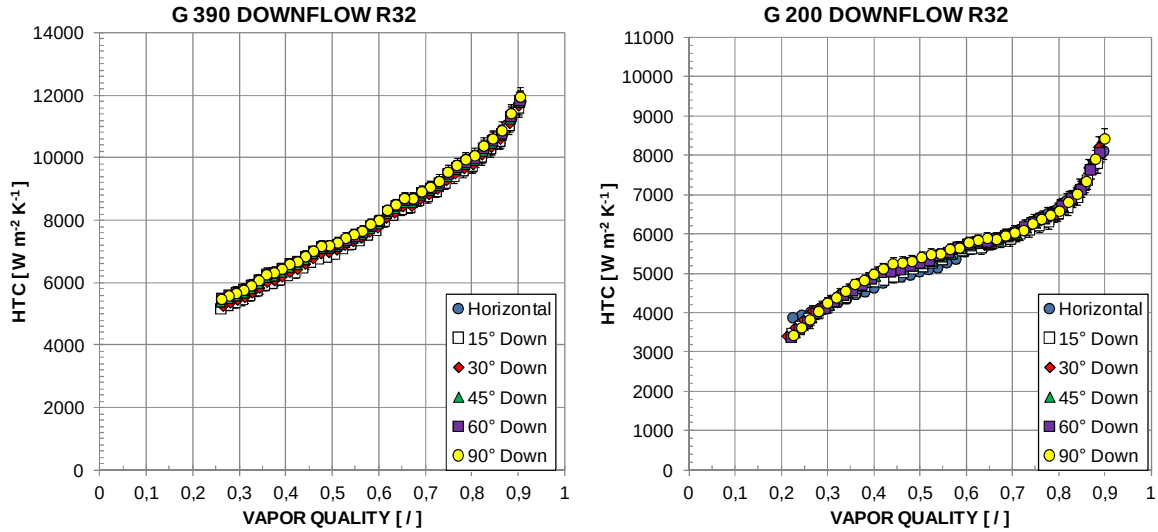

Figure 4.16. Effect of inclination on heat transfer coefficient during condensation of R32 in downward flow inside the square cross section minichannel at a constant mass flux *G* [kg m^{-2} s^{-1}]. Left) *G* = 390 kg m^{-2} s^{-1}; b) *G* = 200 kg m^{-2} s^{-1}.

According to the experimental data collected during the present tests inside the square minichannel, whatever the fluid, the effect of the channel inclination on the condensation heat transfer becomes noteworthy in downflow at mass velocities lower than a critical mass flux that is equal to 150 kg m^{-2} s^{-1} for R134a and to 200 kg m^{-2} s^{-1} for R32 (Figure 4.17 and Figure 4.18).

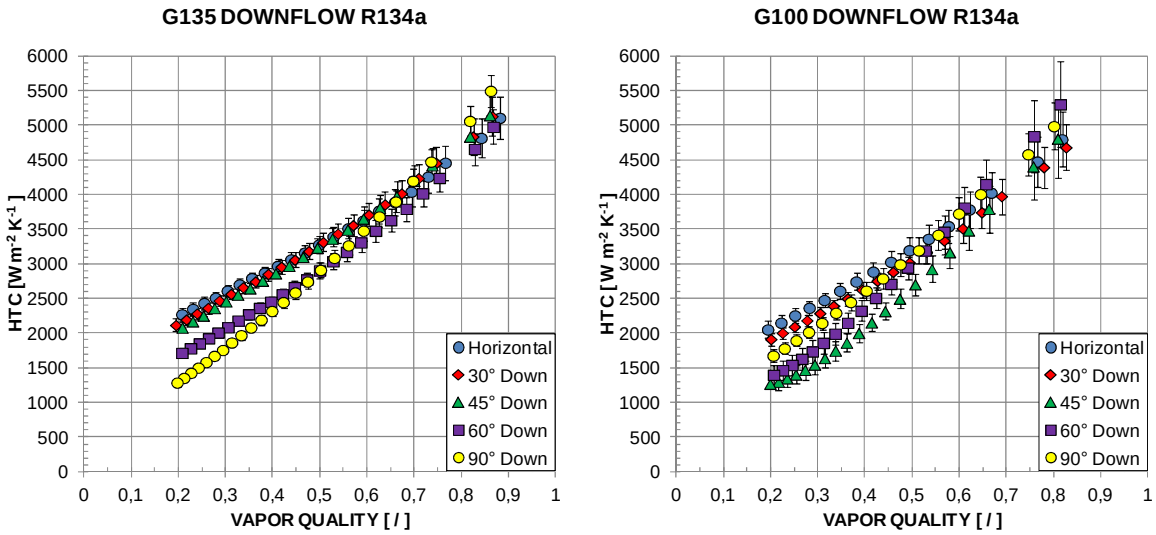

Figure 4.17. Effect of inclination on heat transfer coefficient during condensation of R134a in downward flow inside the square cross section minichannel at a constant mass flux *G* [kg m^{-2} s^{-1}]. Left) *G* = 135 kg m^{-2} s^{-1}; b) *G* = 100 kg m^{-2} s^{-1}.

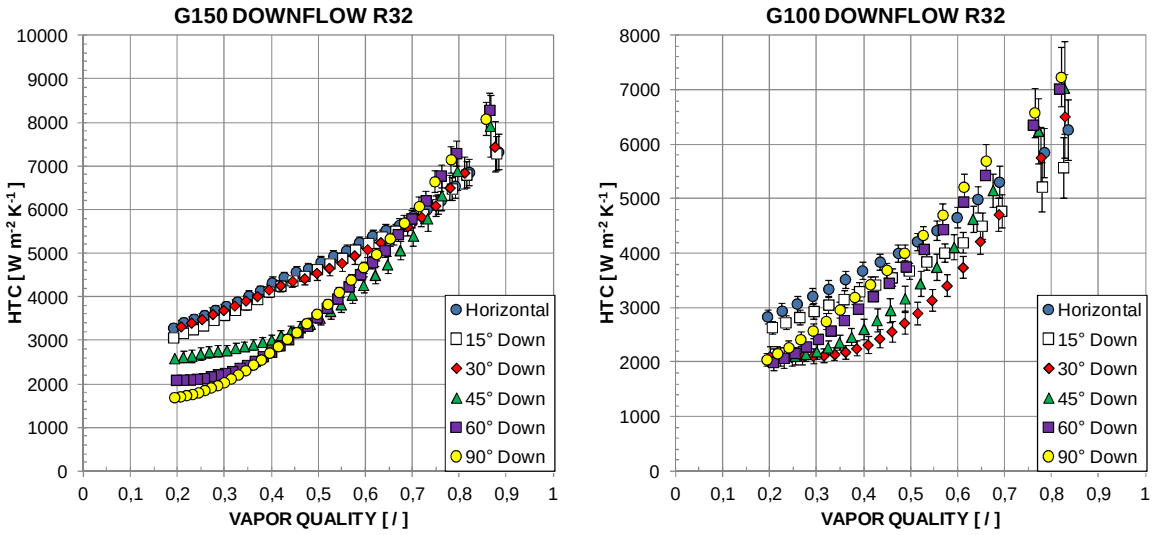

Figure 4.18. Effect of inclination on heat transfer coefficient during condensation of R32 in downward flow inside the square cross section minichannel at a constant mass flux *G* [kg m^{-2} s^{-1}]. Left) *G* = 150 kg m^{-2} s^{-1}; b) *G* = 100 kg m^{-2} s^{-1}.

In order to get a deeper insight into the matter, for each tested refrigerant, the heat transfer coefficient is plotted against the channel inclination in downflow, considering a certain vapor quality and mass velocities equal to or lower than the critical one. At the considered vapor quality, the heat transfer coefficient is evaluated by a linear interpolation between

the experimental points at the closest vapor qualities. Given the number of the experimental data, the approximation is absolutely satisfactory.
In Figure 4.19, the plots refer to a vapor quality equal to 0.75 and to R134a and R32, respectively. Even at low mass fluxes in downflow, at high vapor qualities, the effect of channel inclination is negligible. Furthermore, the increase of the R32 condensation heat transfer coefficient with a vertical configuration as compared to the reference case in horizontal is almost within the experimental expanded uncertainty, so a clear trend cannot be defined.

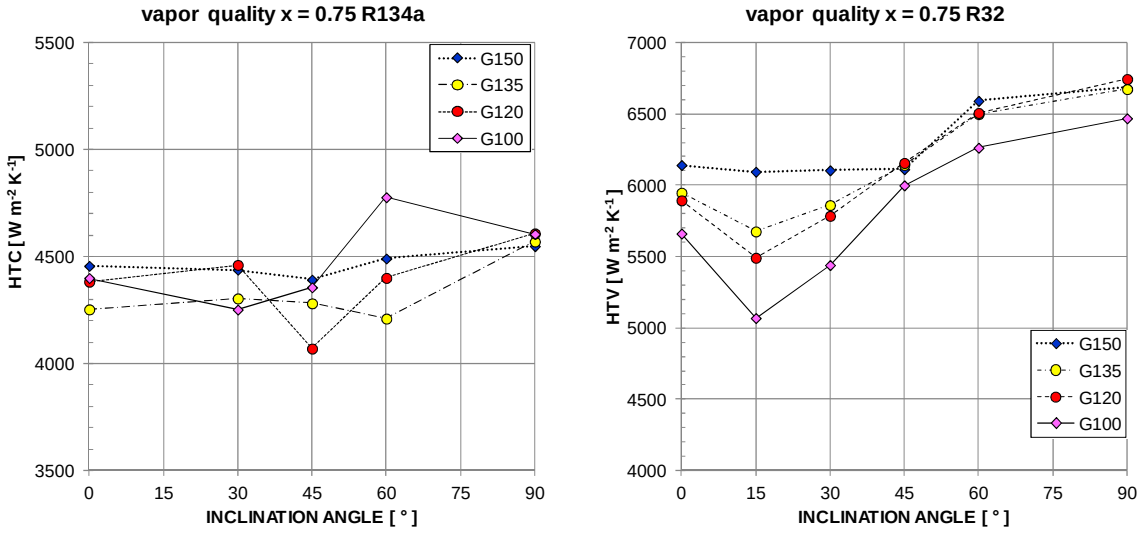

Figure 4.19. Effect of inclination on heat transfer coefficient during condensation in downflow inside the square cross section minichannel at low mass fluxes *G* [kg m^{-2} s^{-1}] and at a vapor quality *x* equal to 0.75 for the tested refrigerants. Left: Refrigerant R134a ; Right: Refrigerant R32.

In Figure 4.20, the plots are related to R134a and to vapor qualities equal to 0.50 and 0.25, respectively. In this vapor quality range, at some particular mass fluxes and channel orientations, the effect of the channel inclination causes a dramatic decrease of the heat transfer coefficient, as compared to the reference case. Moreover, observing the data at low vapor quality, the inclination affects the condensation heat transfer in a different way when changing the mass velocity. In fact, the heat transfer coefficient trend exhibits a minimum that is in correspondence of an inclination angle much closer to the horizontal as the mass velocity decreases. The maximum decrease in heat transfer coefficient as compared to the horizontal configuration is found at 100 kg m^{-2} s^{-1} and at an inclination angle of 45° and quantitatively it is around 18% at 0.50 vapor quality and 40% at 0.25 vapor quality. At 0.25 vapor quality, negligible inclination effect is found at 150 kg m^{-2} s^{-1}: at this mass velocity, the channel orientation plays a role only at vapor quality lower than or equal to 0.20 as observed from Figure 4.15.
The observations inferred from the analysis of the experimental data for R134a are confirmed even in the condensation tests performed with R32. In Figure 4.21, the heat transfer coefficient of R32 is plotted against inclination angle considering vapor quality equal to 0.50 and 0.25, respectively. In these graphs, the critical mass flux of 200 kg m^{-2} s^{-1} is not reported for the sake of clarity. As compared to the horizontal configuration, the maximum decrease in heat transfer coefficient is found at 0.25 vapor quality and 150 kg m^{-2} s^{-1} in vertical downflow and it is quantitatively equal to 48%.

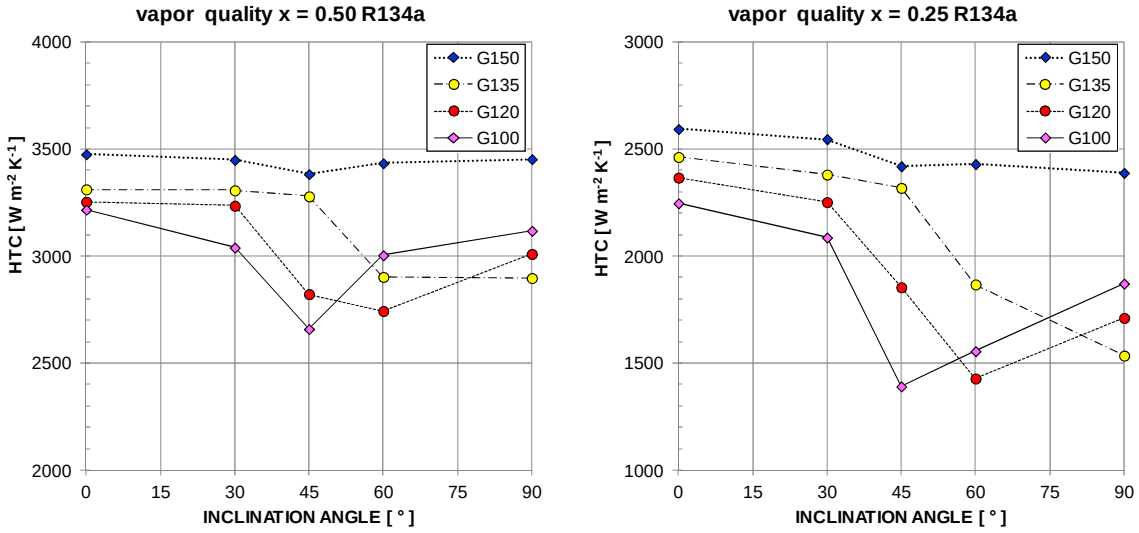

Figure 4.20. Effect of inclination on heat transfer coefficient during condensation of R134a in downflow inside the square cross section minichannel at low mass fluxes *G* [kg m^{-2} s^{-1}] Left: at 0.50 vapor quality; Right: at 0.25 vapor quality.

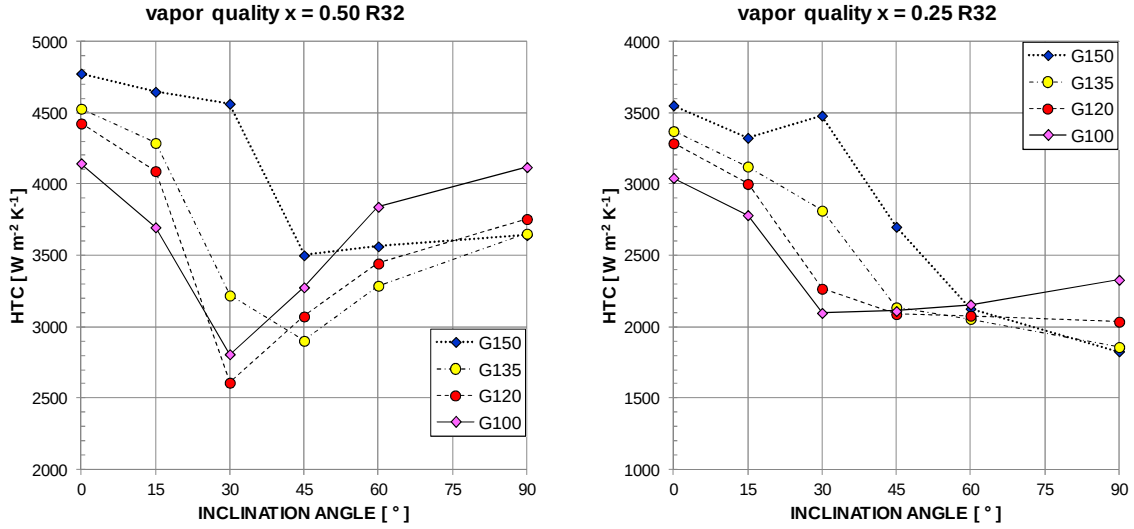

Figure 4.21. Effect of inclination on heat transfer coefficient during condensation of R32 in downflow inside the square cross section minichannel at low mass fluxes *G* [kg m^{-2} s^{-1}] Left: at 0.50 vapor quality; Right: at 0.25 vapor quality.

4.7 Dimensional analysis for the condensation inside the tilted square minichannel

The present experimental investigation has evidenced that in downward flow, for a given refrigerant, there is a critical mass velocity below which the inclination of the minichannel may play an important role in the condensation heat transfer. In fact, at mass fluxes lower than the critical one, depending on the channel inclination, the condensation heat transfer coefficient may dramatically decrease as compared to that in horizontal configuration. Given that the inclination of the minichannel potentially penalizes the condensation process in downflow, a dimensional analysis has been conducted in order to

find a predicting method that can be employed to define the conditions at which the inclination starts to affect the condensation heat transfer coefficient. The cornerstone of the dimensional analysis is the Buckingham theorem which stated that if a physical phenomenon can be completely described using a certain number of physical variables, then a number of dimensionless groups equal to the nullity of the dimensional matrix can be identified and correlated. Therefore, the first issue when performing the dimensional analysis for condensation in downflow inside the inclined minichannel is to select the most important physical variables. During condensation inside channel, the heat transfer is influenced by the gravitational acceleration g, by the shear stress of the vapor phase, by the density difference $\Delta\rho = \rho_L - \rho_V$ and by the surface tension σ, particularly in non circular minichannels. In turn, the shear stress of the vapor phase is expressed as a function of the vapor density ρ_V, the vapor dynamic viscosity μ_V, the vapor mass velocity G_V and the hydraulic diameter d_h.
According to the results of the condensation tests inside the tilted minichannel, the last parameter that should be added to the other ones is the mass velocity at which the inclination starts to affect the condensation heat transfer coefficient in vertical downflow G^*, that is to say, the goal of the present dimensional analysis.
The eight parameters listed above are composed by the fundamental physical dimensions of length [L], mass [M] and time [τ].

Table 4-c. Dimensional analysis for the physical parameters describing the in-tube condensation heat transfer.

	ρ_V	μ_V	d_h	G_V	G^*	g	$\Delta\rho$	σ
[L]	-3	-1	1	-2	-2	1	-3	0
[M]	1	1	0	1	1	0	1	1
[τ]	0	-1	0	-1	-1	-2	0	-2

Hence, the Buckingham theorem leads to the definition of five independent dimensionless groups:

$$\Pi_1 = \frac{G_V}{G^*} \quad \textbf{(4-XX)}$$

$$\Pi_2 = \frac{G_V\, d_h}{\mu_V} \quad \textbf{(4-XXI)}$$

$$\Pi_3 = \frac{\Delta\rho}{\rho_V} \quad \textbf{(4-XXII)}$$

$$\Pi_4 = \frac{\Delta\rho\, g\, {d_h}^2}{\sigma} \quad \textbf{(4-XXIII)}$$

$$\Pi_5 = \frac{\Delta\rho\, \rho_V\, g\, d_h}{{G_V}^2} \quad \textbf{(4-XXIV)}$$

When applying the theorem, dimensionless groups already defined in the open literature were sought: in fact, Π_1 is the thermodynamic vapor quality x, Π_2 is the vapor phase Reynolds number Re_V and Π_4 represents the Eötvös number Eo. It can be noted that a combination of the vapor phase Reynolds number and the dimensionless group Π_5 results in the definition of the dimensionless inclination parameter Y which is used in the work by Taitel and Duckler [83] to predict the flow regime in near horizontal two-phase flow :

$$\mathrm{Y} = \frac{\Delta\rho\ g\ \sin(\beta)}{\left(\frac{\mathrm{d}p}{\mathrm{d}z}\right)_{f,V}} \qquad \textbf{(4-XXV)}$$

where β is the inclination angle which is equal to 0° in horizontal configuration and 90° in vertical downflow and $(\mathrm{d}p/\mathrm{d}z)_{f,V}$ represents the single-phase frictional pressure gradient for the vapor phase and it is calculated from:

$$\left(\frac{\mathrm{d}p}{\mathrm{d}z}\right)_{f,V} = \frac{2\ f\ {G_V}^2}{d_h\ \rho_V} \qquad \textbf{(4-XXVI)}$$

In this work, the friction factor f is computed using the proper friction factor - Reynolds number product in the laminar region equal to 15.334, as reported in Del Col *et al.* [50] and the Churchill [18] equation in turbulent region.
The introduction of the dimensionless inclination parameter Y^* referred to the critical mass velocity G^* in vertical downflow configuration (sin β = 1) as a group of interest in the present analysis suggests a correlation in the following form:

$$\mathrm{Y}^* = F\left(x, \mathrm{Eo}, \frac{\Delta\rho}{\rho_V}\right) \qquad \textbf{(4-XXVII)}$$

Considering the mass velocities at which the inclination of the minichannel starts to affect the heat transfer coefficient during condensation as compared to the horizontal configuration for each tested refrigerant, that is to say 150 kg m^{-2} s^{-1} for R134a and 200 kg m^{-2} s^{-1} for R32, in the vapor quality range between 0.3 and 0.65, the trend of the dimensionless inclination parameter Y^* is found to be described as a function of the vapor quality x raised to a power of -1.748:

$$\mathrm{Y}^* = constant \cdot x^{-1.748} \qquad \textbf{(4-XXVIII)}$$

The constant depends on the properties of the considered refrigerant and it is supposed to be expressed as a function of Eo and $\Delta\rho/\rho_G$. The final correlation is suggested in the form of equation (4-XXIX); the coefficient and the exponents are calculated using the least square method.

$$\mathrm{Y}^* = 0.185\ \mathrm{Eo}^{0.35} \left(\frac{\Delta\rho}{\rho_V}\right)^{0.65} x^{-1.748} \qquad \textbf{(4-XXIX)}$$

In the following figures, this correlation is employed to determine a gravity dependent region when plotting the dimensionless inclination parameter against the vapor quality for all the test conditions. Since it was demonstrated by the experimental data that the inclination has negligible effect on condensation at high vapor quality even in downward flow and at low mass velocity, the gravity dependent region is limited by a vertical line corresponding to a vapor quality equal to 0.6.

Figure 4.22 refers to R134a and shows two plots of the dimensionless inclination parameter Y against the vapor quality *x*. In the graph on the left, no points are included in the gravity dependent region, indicating that at a mass velocity equal or higher than 200 kg m^{-2} s^{-1} the inclination does not affect the condensation heat transfer in downflow.
On the other hand, in the graph on the right, according to the definition of the correlation, it is shown that at 150 kg m^{-2} s^{-1}, the points related to the vertical downflow configuration lie on the gravity dependent region borderline. This means that at mass velocities equal or lower than 150 kg m^{-2} s^{-1}, the inclination of the minichannel may penalizes the heat transfer during condensation as compared to the situation with horizontal channel.
Similarly, Figure 4.23 refers to R32 and shows the dimensionless inclination parameter Y against the vapor quality *x* at 390 kg m^{-2} s^{-1} and 200 kg m^{-2} s^{-1}. In this case, the proposed method confirms that the effect of the inclination during condensation of R32 in downflow in the present test geometry is negligible at 390 kg m^{-2} s^{-1} but it becomes significant at mass velocity equal or lower than 200 kg m^{-2} s^{-1}.

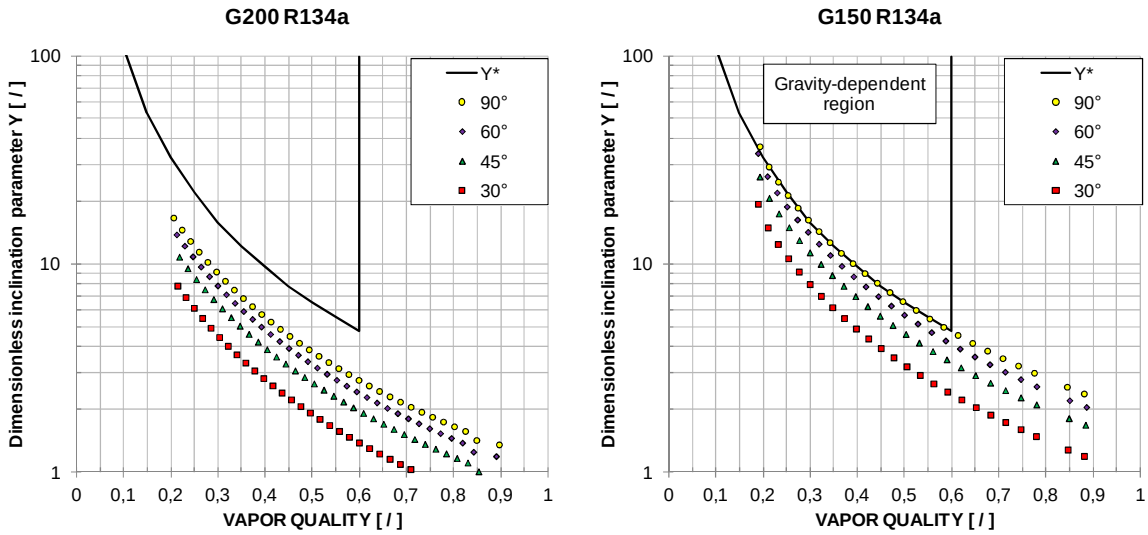

Figure 4.22. Dimensionless inclination parameter at different channel inclinations versus vapor quality. The points refer to the refrigerant R134a; each plot is related to a mass velocity *G* [kg m^{-2} s^{-1}]. Left: *G* = 200 kg m^{-2} s^{-1}. Right: *G* = 150 kg m^{-2} s^{-1}. The curve of Y* bounds the gravity-dependent region and determines at which mass velocity *G the inclination starts to affect the condensation heat transfer coefficient as compared to the horizontal configuration.**

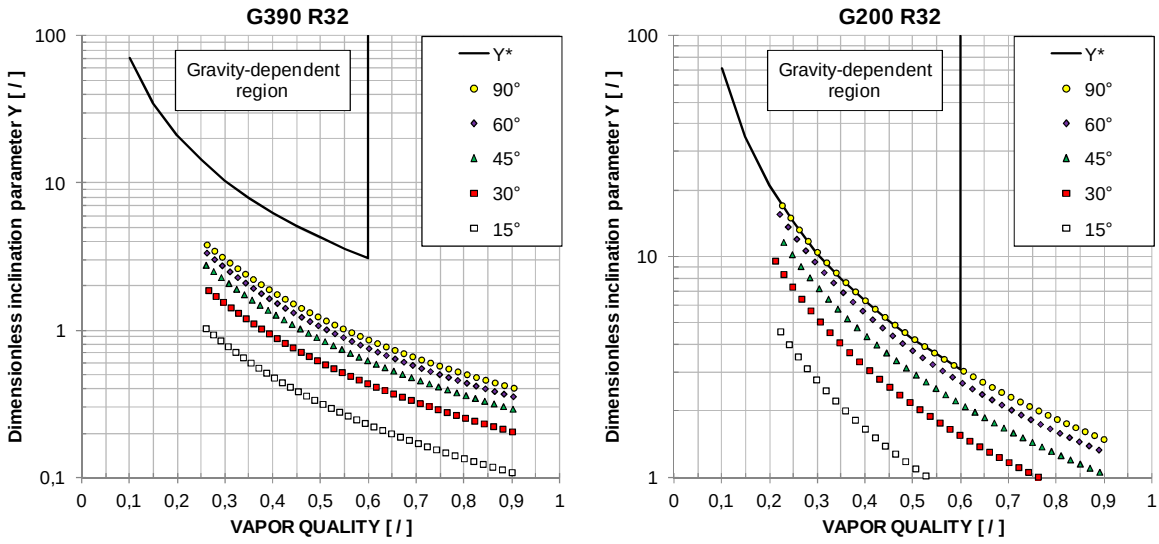

Figure 4.23. Dimensionless inclination parameter at different channel inclinations versus vapor quality. The points refer to the refrigerant R32; each plot is related to a mass velocity *G* [kg m^{-2} s^{-1}]. Left: *G* = 390 kg m^{-2} s^{-1}. Right: *G* = 200 kg m^{-2} s^{-1}. The curve of Y* bounds the gravity-dependent region and determines at which mass velocity *G the inclination starts to affect the condensation heat transfer coefficient as compared to the horizontal configuration.**

Whatever the refrigerant, when considering a mass velocity lower than the critical mass velocity *G**, for the present test section, the curve of Y* defined using the proposed correlation predicts also the minimum channel inclination from horizontal in downflow at which the condensation heat transfer coefficient may display a marked decrease as compared to the horizontal configuration.

In fact, Figure 4.24 depicts the dimensionless inclination parameter against the vapor quality for the tested mass velocities lower than 150 kg m^{-2} s^{-1}, that is the critical mass velocity for R134a. In the plots, the curve of Y* is reported as well. As an example, considering 135 kg m^{-2} s^{-1}, the gravity-dependent zone includes the points related to the channel configuration at 90° and 60° downflow. This means that, at this operative mass velocity, the inclination plays an important role during condensation when the tilt angle of the minichannel is higher than 45°.

Similarly, one can deduce that in the square minichannel, during condensation of R134a at 120 kg m^{-2} s^{-1}, the heat transfer is penalized by the inclination in a downward flow condition when the channel is tilted at an angle between 30° and 45°. Finally, when condensing R134a in downward flow in the present square minichannel, at a mass velocity equal to 100 kg m^{-2} s^{-1}, the penalization of the heat transfer coefficient is expected starting from an inclination angle slightly higher than 30°. The observations from Figure 4.24 are consistent with the experimental data reported in Figure 4.20.

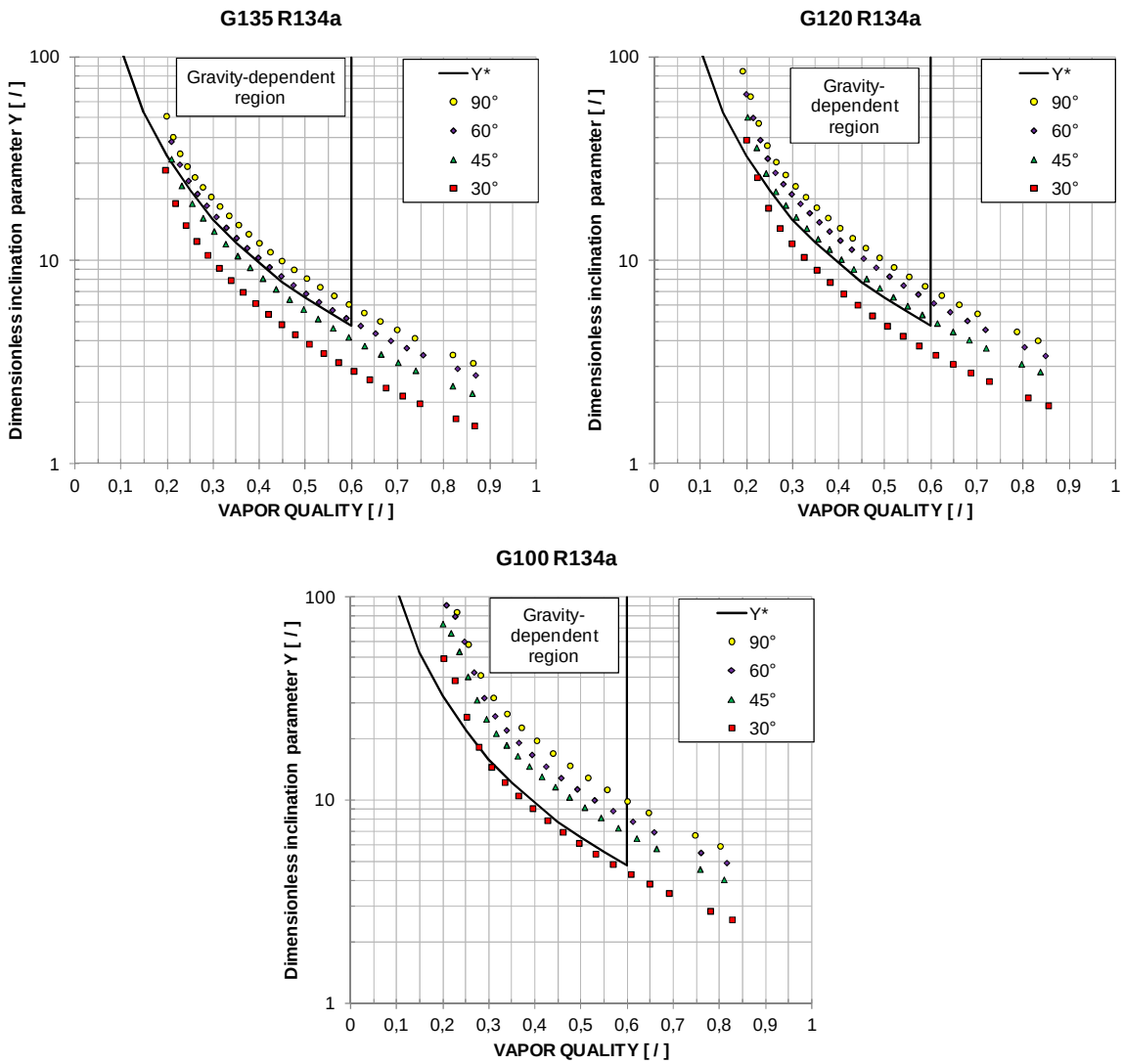

Figure 4.24. Dimensionless inclination parameter at different channel inclinations versus vapor quality. The points refer to the refrigerant R134a at mass velocities *G* [kg m^{-2} s^{-1}] lower than the critical mass velocity *G= 150 kg m^{-2} s^{-1}. Top: Left: *G* = 135 kg m^{-2} s^{-1}; Right: *G* = 120 kg m-2 s-1. Bottom: *G* = 100 kg m^{-2} s^{-1}. The curve of Y* bounds the gravity-dependent region and determines at which inclination the condensation heat transfer coefficient starts to decrease as compared to the horizontal configuration.**

Furthermore, the predicting method has been validated against the experimental data with the refrigerant R32 and for mass velocity lower than the critical one, that is equal to 200 kg m^{-2} s^{-1} in this case. By way of illustration, Figure 4.25 reports the dimensionless inclination parameter against the vapor quality and the curve of Y* for R32 at 150 kg m^{-2} s^{-1}, 135 kg m^{-2} s^{-1}, 120 kg m^{-2} s^{-1} and 100 kg m^{-2} s^{-1}. In agreement with the experimental data presented in Figure 4.21, during condensation of R32, the inclination penalizes the heat transfer in downward flow in the following conditions:

- from an inclination angle between 30 and 45° at 150 kg m^{-2} s^{-1} mass velocity;
- from an inclination angle slightly lower than 30° at 135 kg m^{-2} s^{-1} mass velocity;
- from an inclination angle between 15° and 30°at 120 kg m^{-2} s^{-1} mass velocity;
- from an inclination angle slightly higher than 15° at 100 kg m^{-2} s^{-1} mass velocity.

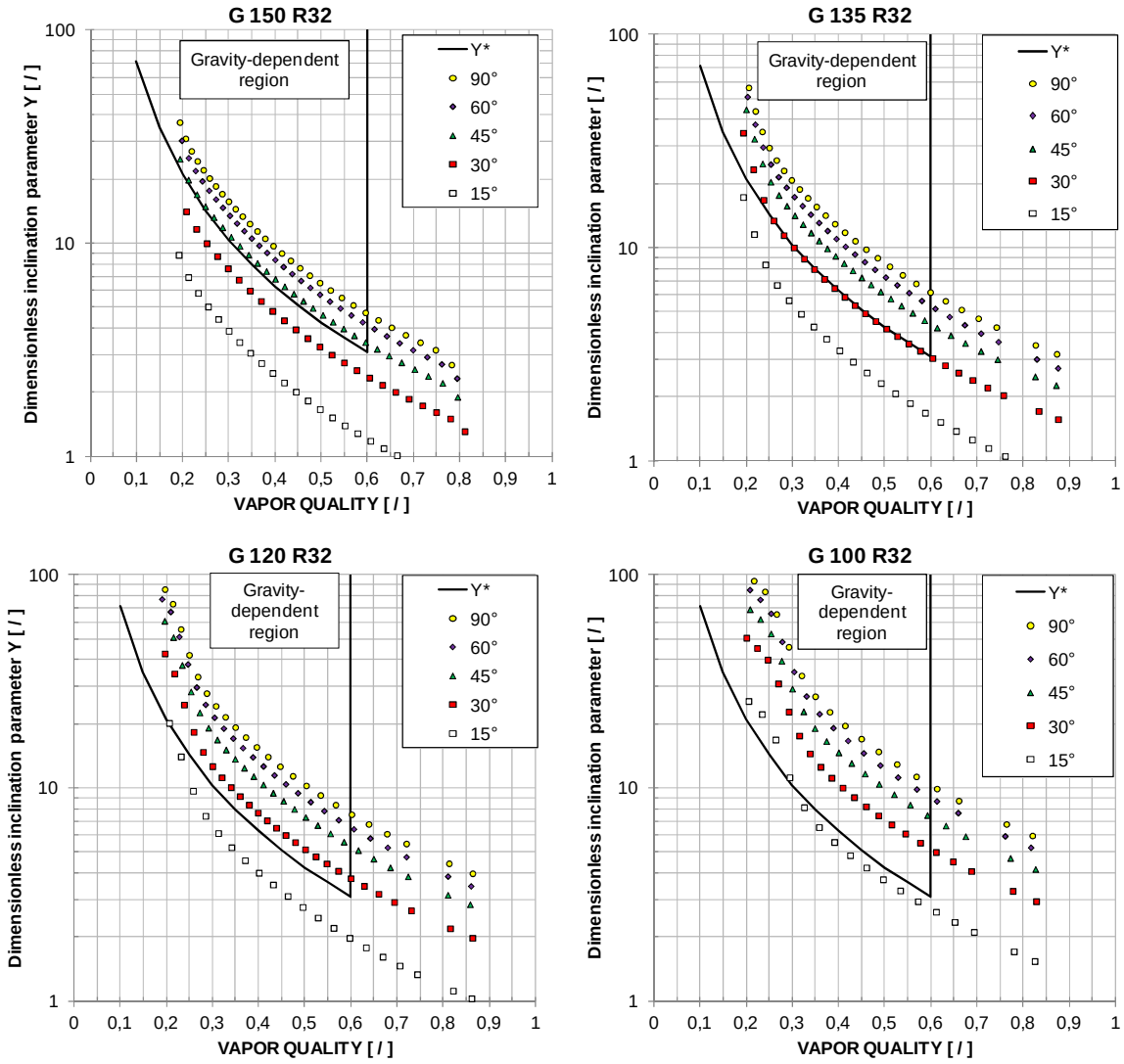

Figure 4.25. Dimensionless inclination parameter at different channel inclinations versus vapor quality. The points refer to the refrigerant R32 at mass velocities G [kg m^{-2} s^{-1}] lower than the critical mass velocity G*= 200 kg m^{-2} s^{-1}. Top: Left: G = 150 kg m^{-2} s^{-1}; Right: G = 135 kg m^{-2} s^{-1}. Bottom: Left: G = 120 kg m^{-2} s^{-1}; Right: G = 100 kg m^{-2} s^{-1}. The curve of Y* bounds the gravity-dependent region and determines at which inclination the condensation heat transfer coefficient starts to decrease as compared to the horizontal configuration.

The method for the prediction of the mass velocity G* at which the inclination starts to affect the condensation heat transfer coefficient in vertical downflow is applicable for the tested refrigerant R134a and R32. With regard to minichannels, it may be applicable only for square minichannels, because it has been developed without considering the shape of the cross section, that has proved to be important in determining the mutual influences of interfacial shear stress, gravity and surface tension that affect the condensation process..
In macrochannels, the effect of the cross section shape becomes marginal thus, in principle, the predicting method based on the curve of Y* should be applicable, because the initial assumptions take into account those parameters that influence the condensation heat transfer and are general. Hence, the method illustrated in the present work has been applied to predict the critical mass velocity G* considering the test conditions of the study by Lips and Mayer [77], who investigated the condensation of R134a at 40°C saturation

temperature in an inclined smooth circular tube with an inner diameter of 8.38 mm. In their work, the inclination effect was defined using a parameter *I* that is the ratio of the difference between the maximum and the minimum heat transfer coefficient and the heat transfer obtained in horizontal configuration. When decreasing the mass velocity starting from 600 kg m^{-2} s^{-1}, the parameter *I* was found to be higher than 20% at mass velocity equal or lower than 300 kg m^{-2} s^{-1}, so this value is assumed here as the critical experimental mass velocity *G**. The geometry of the circular macrochannel and the thermodynamic properties of the refrigerant R134a are used to calculate the Eötvös number Eo and $\Delta\rho/\rho_V$ which are implemented in the correlation expressed in equation (4-XXIX). From the obtained value of the parameter Y*, using an iterative procedure and calculating the single-phase pressure gradient for the vapor phase through the Churchill [18] model, the resulting calculated critical mass velocity is found between 282 kg m^{-2} s^{-1} and 289 kg m^{-2} s^{-1}, in satisfactory agreement with the experimental outcome. In Figure 4.26, in the mass velocity-vapor quality diagram, considering the test conditions of the work by Lips and Mayer [77], the parameter *I* and the values of critical mass velocity *G** calculated using the predicting correlation (equation (4-XXIX)) are displayed.

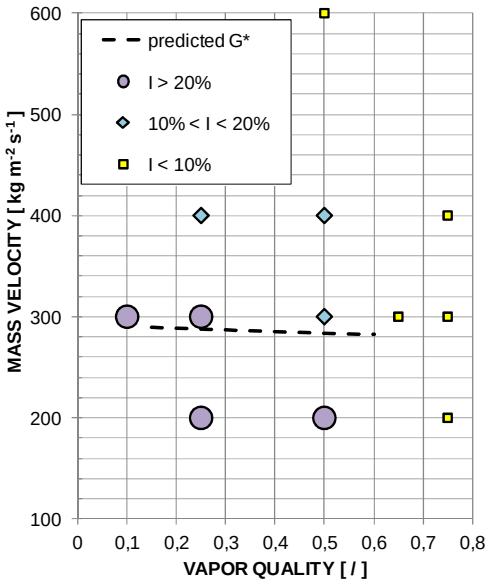

Figure 4.26. Inclination effect parameter *I* and critical mass velocity *G [kg m^{-2} s^{-1}] calculated using the predicting correlation with respect to the test conditions of the work by Lips and Mayer [77], that refers to the condensation of R134a at 40°C in a circular channel with an inner diameter of 8.34 mm.**

5 COMPARATIVE ANALYSIS OF IN-TUBE CONDENSATION HEAT TRANSFER PERFORMANCE OF REFRIGERANTS FOR REFRIGERATION APPLICATIONS

5.1 Abstract

A general methodology to evaluate the potential heat transfer performance of refrigerants during condensation inside macrochannels and minichannels is presented in this chapter. In this evaluation, not only the heat transfer coefficients but also the frictional two-phase pressure drop must be taken into account. In fact, in condensation, pressure drop affects the refrigerant temperature profile and alters the mean effective temperature difference, which is the driving potential of the heat transfer. The Performance Evaluation Criteria (PEC) named Penalty Factor for condensation (PF) and Total temperature Penalization on the refrigerant side (TTP) are here applied to rank several refrigerants with respect to their heat transfer performances in forced convective condensation starting from an experimental database collected for a single minichannel and reliable correlations predicting the pressure gradient and the heat transfer coefficient in a variety of working conditions in the considered geometry. The experimental database consists of measurements of condensation heat transfer coefficients and frictional pressure drop gradient during adiabatic flow performed with R32, R245fa, R134a, R1234yf, R1234ze(E) and propane inside a copper minichannel. The tube has an internal diameter equal to 0.96 mm and an average roughness of the inner wall of 1.3 μm. The models used to calculate the Performance Evaluation Criteria are the correlation by Del Col *et al*. [4] for the two-phase frictional pressured drop and the correlation by Cavallini *et al.* [28] for condensation heat transfer coefficients.

5.2 Definition of the Performance Evaluation Criteria (*PEC*) in condensation

In-tube condensation is widely use in refrigeration and in air conditioning systems and finds practical application in different configurations of heat exchangers, such as air-cooled condensers, tube-in-tube condensers, water-cooled shell-and-tube condensers used in larger equipments, evaporative condensers and heat pump systems of the vapor compression type. When air is used as cooling medium, the heat exchangers are provided with external finned surfaces in order to diminish the thermal resistance. The refrigerants can flow inside smooth tube, furthermore in order to enhance the condensation heat transfer efficiency, the use of tubes provided with internal extended surface (microfin tubes) or minichannels has become very common. The heat transfer during condensation is influenced by the geometrical characteristics of the tube, the operating conditions including saturation temperature, mass velocity and vapor quality and the particular refrigerant, through its thermophysical and thermodynamic properties.

The awareness of the serious environmental problems, the climate changes and the worrisome scenarios for the future have lead to the promulgations of regulations, directives, laws and recommendations aiming at replacing the commonly used refrigerants with natural fluids or new refrigerants with lower global warming potential and compatible with a sustainable development.

Hence, methodologies to evaluate the potential heat transfer performance of a refrigerant for condensation inside tubes are needed. These procedures should be simple and accurate and should enable the ranking of the refrigerants based on the potential performance in forced convective condensation and the optimization of the heat exchangers. They are

hereafter referred to as Performance Evaluation Criteria and they must account for heat transfer coefficient and pressure drop. In fact, contrary to single-phase flow, pressure drop during the condensation process plays a key role in the heat transfer because it leads to a saturation temperature drop and it is linked to the energy consumption at the interface between liquid and vapor phases (see Chapter 2). In particular, the pressure drop affects the temperature profile of the refrigerant in a condenser and thus, with respect to the ideal case, the heat transfer driving potential that is the local effective temperature difference diminishes. In fact, in a vapor compression refrigerant machine, as compared to the ideal case, an additional compression work is required to establish the necessary mean effective difference between the condensing refrigerant and the external cooling medium (usually water or air).
In order to define the Performance Evaluation Criteria, a model of a condenser with a counter-flow configuration is considered and the simplified profiles of the refrigerant and the cooling medium and the temperature of the tube wall are reported in Figure 5.1. The temperature profile of the refrigerant is valid for a pure fluid or an azeotropic mixture and includes the saturation temperature drop which results from the pressure drop. It is also assumed that the working conditions of the condenser can be expressed through bulk average parameters with reference to a condensation process from dry saturated vapor to saturated liquid, where the relevant parameters have been calculated at a mean vapor quality (e.g. x = 0.5). Moreover, the mean temperatures for refrigerant, cooling medium and heat transfer surface are taken as reference.

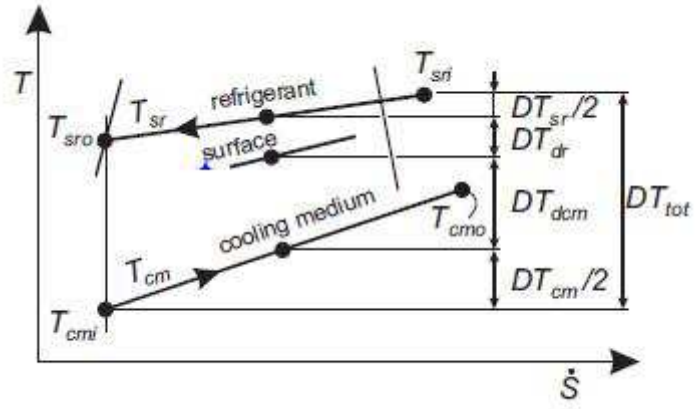

Figure 5.1. Idealized temperature profiles in a counter-flow condenser.

From the observation of Figure 5.1, one can deduce that on the refrigerant side, as compared to the ideal case, the heat transfer driving potential is reduced by one half of the saturation temperature drop. Hence, the total temperature penalization on the refrigerant side TTP can be defined as the sum of the driving temperature difference between the refrigerant saturated vapor and the channel inner surface DT_{dr} and one half of the saturation temperature drop DT_{sr}.

$$\mathrm{TTP} = DT_{dr} + \frac{DT_{sr}}{2} \qquad \textbf{(5-I)}$$

Referring to the condenser model, an energy balance and an entropy balance of the heat exchanger can be written according to

$$\dot{m}_{ref}\,(h_{in}-h_{out})_{ref}+\dot{m}_{cm}(h_{in}-h_{out})_{cm}=0 \qquad \textbf{(5-II)}$$

$$\dot{S}_{gen}=\dot{m}_{ref}\,(s_{out}-s_{in})_{ref}+\dot{m}_{cm}(s_{out}-s_{in})_{cm}\geq 0 \qquad \textbf{(5-III)}$$

In the case in point, let the condenser thermal duty, the refrigerant mass flow rate and the operating conditions of the cooling medium (inlet and outlet temperature and mass flow rate) be fixed. It follows that the enthalpy variation on the refrigerant side in equation is constant and that the flow rate of entropy generation of the cooling medium in equation is a positive and fixed quantity. On the other hand, the entropy variation of the condensing refrigerant depends on the working conditions and is a negative number.
Under these hypotheses, consider an increase of the average saturation temperature T_{sat}: from Figure 5.1, this means an increase of the total temperature penalization TTP. Second, as the average saturation temperature rises, the entropy variation of the condensing refrigerants must decrease, because the enthalpy variation on the refrigerant side remains constant and in two-phase region, the expression (5-IV) is valid:

$$\Delta h \approx T\Delta s \qquad \textbf{(5-IV)}$$

Thus, when the condensation temperature T_{sat} increases, the total flow rate of entropy generation increases. In conclusion, the two terms included in the total temperature penalization (DT_{dr} related to the heat transfer and DT_{sr} related to the pressure drop) can be linked to the exergy losses of the condensation process and can be regarded as the basic parameters to define the Performance Evaluation Criteria. Therefore, the total temperature penalization *TTP* is one of these criteria.
The concluding remarks of the previous discussion make interesting a deeper insight into the exergy losses term related to the pressure drop, which is identical to the saturation temperature drop with respect to the vapor quality and can be indicated via the chain rule as:

$$DT_{sr}=\frac{\mathrm{d}T_{sat}}{\mathrm{d}x}=\frac{\mathrm{d}T_{sat}}{\mathrm{d}p_f}\left(\frac{\mathrm{d}p}{\mathrm{d}z}\right)_f\frac{\mathrm{d}z}{\mathrm{d}x} \qquad \textbf{(5-V)}$$

Here, x is the thermodynamic vapor quality, z is the axial position along the channel and $(\mathrm{d}p\ /\ \mathrm{d}z)_f$ is the frictional pressure gradient. The first term on the right-side can be rewritten reminding the Clausius-Clapeyron equation:

$$\frac{\mathrm{d}p_{sat}}{\mathrm{d}T_{sat}}=\frac{h_{LV}}{T_{sat}\left(\frac{1}{\rho_L}-\frac{1}{\rho_V}\right)} \qquad \textbf{(5-VI)}$$

In addition, reminding the definition of the hydraulic diameter $d_h=4\,A/P$, where A is the cross section area and P is the cross section perimeter and applying the thermal balance on an elementary length of the tube dz in which an elementary variation of the vapor quality dx occurs, it follows that:

$$\frac{\mathrm{d}z}{\mathrm{d}x} = \frac{G\ h_{LV}}{\mathrm{HTC}\ DT_{dr}} \tag{5-VII}$$

Here, the mass velocity *G* is defined as the ratio of the refrigerant mass flow rate and the cross section area of the tube and HTC is the condensation heat transfer coefficient.
As a result, equation (5-V) can be rewritten as:

$$DT_{sr} = \frac{\mathrm{d}T_{sat}}{\mathrm{d}x} = \frac{G\ d_h\ T_{sat}}{4\ \mathrm{HTC}\ DT_{dr}} \left(\frac{1}{\rho_L} - \frac{1}{\rho_V}\right) \left(\frac{\mathrm{d}p}{\mathrm{d}z}\right)_f \tag{5-VIII}$$

From equation (5-VIII), the product of the two penalization terms related to the exergy losses depends on the very same parameters as the condensation heat transfer coefficient. This quantity has been dubbed Penalty Factor for condensation (PF) by Cavallini *et al.* [84] and it represent another Performance Evaluation Criterion.

$$\mathrm{PF} = (DT_{sr})(DT_{dr}) = \frac{G\ d_h\ T_{sat}}{4\ \mathrm{HTC}} \left(\frac{1}{\rho_L} - \frac{1}{\rho_V}\right) \left(\frac{\mathrm{d}p}{\mathrm{d}z}\right)_f \tag{5-IX}$$

In fact, when the Penalty Factor is computed at the same value of condensation heat transfer coefficient HTC for a given tube geometry, it can be directly used as a quantitative criterion to rank the heat transfer performance of different refrigerants: the smaller the *PF*, the better is the potential heat transfer performance of the fluid during condensation. On the other hand, for a given pipe geometry, the Penalty Factor calculated at the same condensation heat transfer coefficient and thermal duty becomes a useful tools to compare among the considered refrigerants the penalization term related to the pressure drop.
Nevertheless, the calculation of the Penalty Factor for condensation in a variety of working conditions requires the use of reliable predicting correlation both for the condensation heat transfer coefficient and for the frictional two-phase pressure drop during adiabatic flow.
Cavallini *et al.* [84] showed that when the Penalty Factor is plotted against the heat transfer coefficient in a graph that uses logarithmic scales for both the axes, the data for various refrigerants at the same hydraulic diameter, vapor quality and saturation temperature lied along nearly parallel straight lines as long as shear dominated condensation occurs. Therefore, they found that in annular flow condensation, the Penalty Factor can be represented in general form as:

$$\mathrm{PF} = C_{ref}(\mathrm{HTC})^{\hat{\varepsilon}} \tag{5-X}$$

The constant C_{ref} and the exponent $\hat{\varepsilon}$ depend on the refrigerant properties, on the vapor quality and on the channel geometry.

The Performance Evaluation Criteria named Total Temperature Penalization TTP and Penalty Factor PF can be use in design optimizations of a condenser [84] [85]. Consider the design of a condenser with the following constraints:

- constant average heat flux per unit referred to the internal heat transfer surface area;
- fixed external thermal resistance, including tube wall, external fins if present and cooling medium convective term;
- fixed working conditions for the cooling medium, including mass flow rate, inlet and outlet temperature.

Using the definition of PF and minimizing TTP, for a given fluid, one can calculate the optimal value of condensation heat transfer coefficient and consequently the optimal driving temperature difference. From a reliable correlation for the prediction of heat transfer coefficients during condensation, the optimal mass velocity can be determined and from here the optimal channel length.

As second optimization example, consider a condenser of defined geometry, fixed inlet saturation temperature of the refrigerant, given cooling medium inlet temperature and mass flow rate. For this case, the refrigerant circuitry can be optimized to obtain the maximum condenser heat duty when working with a given refrigerant.

Cavallini and coworkers [85] proved that the Penalty Factor can be use to compare the condensation heat transfer performance of a particular refrigerant in macrochannel and minichannel geometries. The results of a comparison between optimized heat exchangers show that the superiority of the minichannel geometry is more evident with decreasing cooling medium thermal resistance. Furthermore, comparing the volumes of the refrigerant in the two heat exchangers it comes out that the macrotube condenser has a refrigerant charge more than eight times that of the minitube condenser, confirming one of the major advantages of the minichannel technology.

In this chapter, the Performance Evaluation Criteria dubbed Penalty factor and Total Temperature Penalization are employed to rank the potential condensation heat transfer performance of several refrigerants starting from experimental condensation heat transfer coefficients and adiabatic frictional pressure gradient collected in a circular minichannel with inner diameter of 0.96 mm. The considered refrigerants include both commonly used fluids such as R134a and R32, a natural fluid (propane) and new halogenated olefins (R1234ze(E) and R1234yf) with less environmental impact that have been introduced to substitute R134a.

5.3 Comparative analysis between halogenated refrigerants, low GWP halogenated olefins and propane.

The experimental apparatus available at the Two-phase Heat Transfer Lab at the University of Padova includes two test sections obtained from a copper rod with an external diameter of 8 mm which underwent a drawing process to realize a 0.96 mm internal bore. The average roughness of the inner surface is Ra = 1.3 μm. The two test sections are design specifically to perform two-phase heat transfer and pressure drop experimental analysis in a single minichannel respectively. Each test section consists of two sectors: the inlet condition setter, which is used to achieve the desired thermodynamic state of the refrigerant at the intake of the actual measuring section.

The test section designed for the two-phase frictional pressure drop during adiabatic flow is illustrated in Chapter 2. During these test runs, the refrigerant enters the test section as superheated vapor to get experimental data in the vapor quality range between 0.5 and 1 while it enters as subcooled liquid to collect points at vapor quality below 0.5. The inlet

condition setter is a mini shell-and-tube heat exchanger and its purpose is to achieve the desired saturated thermodynamic state of the refrigerant at the inlet of the adiabatic measuring section. The peculiarity of the measuring section is represented by the stainless steel pressure ports carefully realized on the minichannel without perturbing the geometry, the fluid flow and thus the experimental measurements. The results obtained in this test section during the adiabatic two-phase flow of propane, R134a and R1234ze(E) are shown in Chapter 2 at different mass velocity and saturation temperature between 30°C and 50°C.

The test section for the two-phase heat transfer investigations has been described in details in Chapter 3. The two sectors act as heat exchangers and their external surfaces were machined in order to realize a tortuous path for the flow of the secondary fluid, that is distilled water. The secondary fluid flows in two different loops that serve independently the two sectors. The refrigerant enters the test section as superheated vapor, so the inlet condition setter works as desuperheater. The measuring section is provided with thirteen thermocouples embedded in the wall and fifteen thermocouples in the water flow. The local heat flux results as a variable parameter depending on the testing conditions and its accurate measurement becomes the main issue. In particular, when performing condensation tests, the local heat flux is calculated from the slope of the water temperature gradient. The local heat transfer coefficient is obtained from the ratio of the local heat flux and the wall to saturation temperature difference. In the test section for two-phase heat transfer, several fluids have been tested during condensation at 40°C saturation temperature and at different mass velocities. The saturation temperature has been chosen because it allows the investigation of many fluids, which can use the ambient air as heat sink for the condenser. Matkovic *et al.* [51] and Cavallini *et al.* [56] reported the results for the hydrofluorocarbons R134a, R32 and R245fa. Del Col *et al.* [57] investigated the condensation heat transfer for R1234yf, a new halogenated olefin which has a 100-year time horizon global warming potential equal to 4 and has emerged as the R134a replacing fluid in future mobile air conditioning systems. In Chapter 2, the experimental study during condensation of propane and R1234ze(E) has been presented. The first is a natural refrigerant, the second is another low global warming potential halogenated olefin that should replace R134a in refrigeration and electronic cooling applications.

Furthermore, in this test section some measurements of frictional two-phase pressure drop during adiabatic flow of R32, R245fa [56] and R1234yf [57] have been carried out. During these tests, no water flows inside the measuring section to realize adiabatic conditions but a correction of the measurements was required to take into account the geometrical changes in the cross section of the test section length between the pressure ports, which have been realized upstream and downstream the measuring section.

From the comparison of the collected experimental database and the models available in the open literature, it was observed that the two-phase frictional pressure drop data are well predicted by the correlation of Del Col *et al.* [4]. As regard the condensation process, it was found that the model by Cavallini *et al.* [28] provides satisfactory predictions of the condensation heat transfer coefficients for all the test range conditions and in particular when the condensation is shear stress dominated.

Figure 5.2 displays the frictional pressure gradient versus vapor quality during two-phase adiabatic flow calculated using the Del Col *et al.* [4] correlation for all the tested refrigerants in the circular minichannel with a internal diameter of 0.96 mm at 200 kg m^{-2} s^{-1} and 400 kg m^{-2} s^{-1} and at 40°C saturation temperature. In the plot, the vapor quality ranges between 0.15 and 0.85.

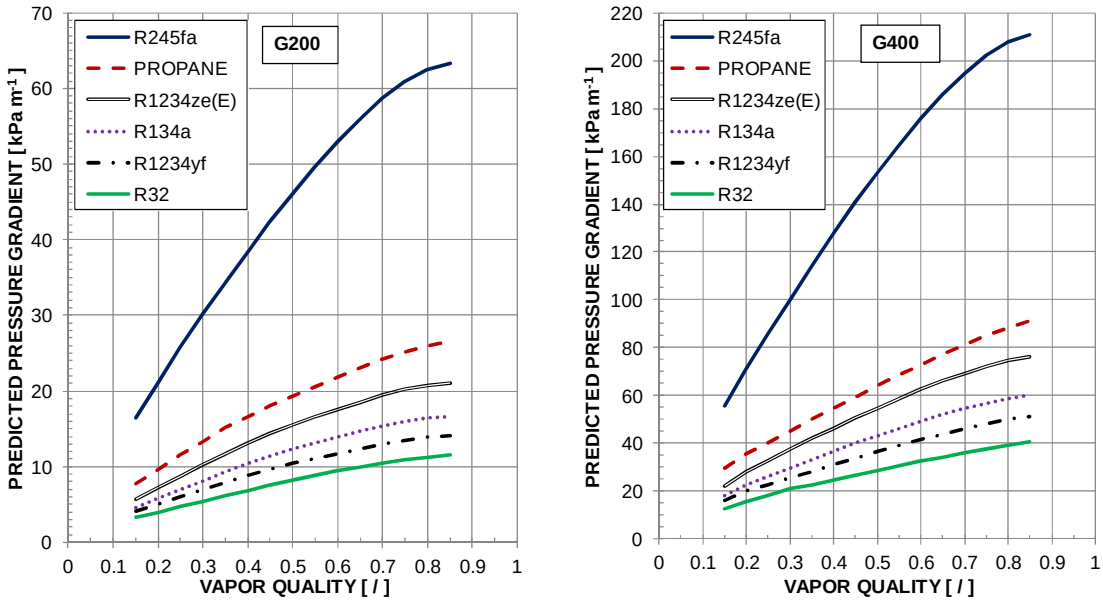

Figure 5.2. Predicted frictional pressure gradient during two-phase adiabatic flow at 40°C saturation temperature and at different mass velocities *G* [kg m^{-2} s^{-1}] inside the tested minichannel using the model by Del Col *et al.* [4] for all the considered fluids. Left: *G* = 200 kg m^{-2} s^{-1}; Right: *G* = 400 kg m^{-2} s^{-1}.

Figure 5.3 exposes the condensation heat transfer coefficients calculated through the Cavallini *et al.* [28] model at 40°C saturation temperature during the condensation of the refrigerants under examination inside the tested minichannel at different mass velocities. In the graphs, the vapor quality ranges between 0.15 and 0.85 and all the predicted points are within the ΔT-independent flow region, where the condensation process can be considered dominated by shear stress. From
Figure 5.3, one could conclude that the fluids displaying the higher heat transfer coefficients are those with the better condensation performance. This conclusion is completely wrong and misleading as explained below.

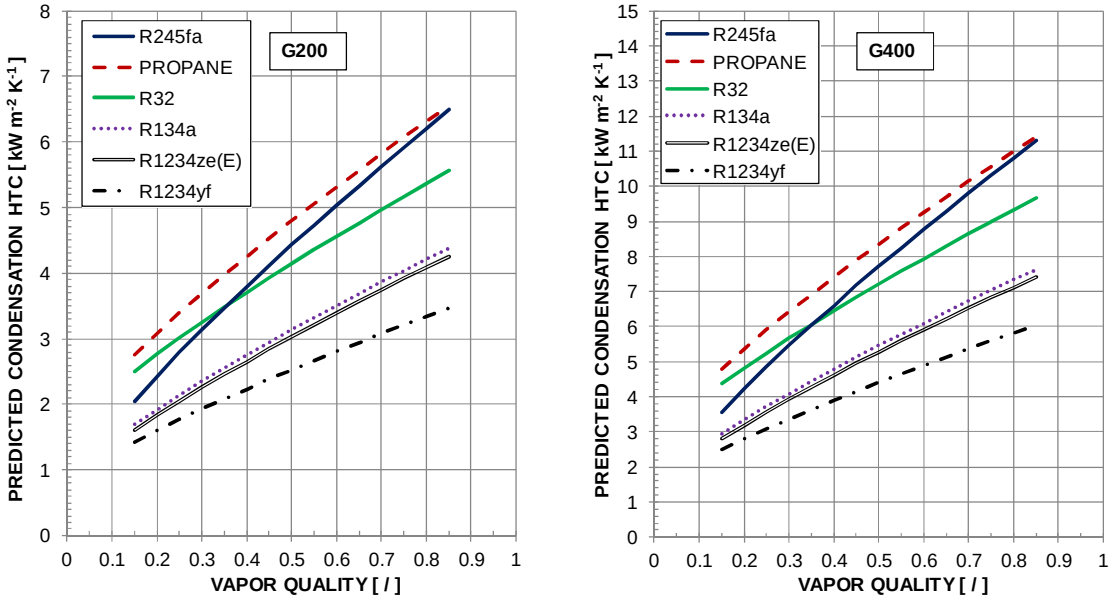

Figure 5.3. Predicted heat transfer coefficient during condensation at 40°C saturation temperature and at different mass velocities G [kg m^{-2} s^{-1}] inside the tested minichannel using the model by Cavallini *et al.* [28] for all the considered fluids. Left: G = 200 kg m^{-2} s^{-1}; Right: G = 400 kg m^{-2} s^{-1}.

Considering the collected database and the indicated reliable models for the predictions of heat transfer coefficient and two-phase pressure gradient during adiabatic flow, a comparative analysis of the potential heat transfer performance during condensation of the tested refrigerants can be properly done through the Performance Evaluation Criteria dubbed Penalty Factor (PF) and Total Temperature Penalization (TTP). In this case, the test section has a fixed geometry so the design optimization procedure with PF and TTP is not suitable for the purpose. In fact, differently from the optimization case, the comparative analysis starts considering a constant value for the Penalty Factor for condensation and this condition corresponds to maintaining a constant mass flux for a given refrigerant.
In Figure 5.4, in the DT_{dr} - DT_{sr} plot, the curves of constant PF (hyperbolas) and of constant TTP (straight lines with slope equal to -0.5) are depicted. The figure shows that, under the constraint of constant Penalty Factor, the condition of minimum Total Temperature Penalization implies:

$$\left(\frac{DT_{sr}}{DT_{dr}}\right)_{\substack{\mathrm{PF}=cost. \\ min\,\mathrm{TTP}}} = 2 \qquad \textbf{(5-XI)}$$

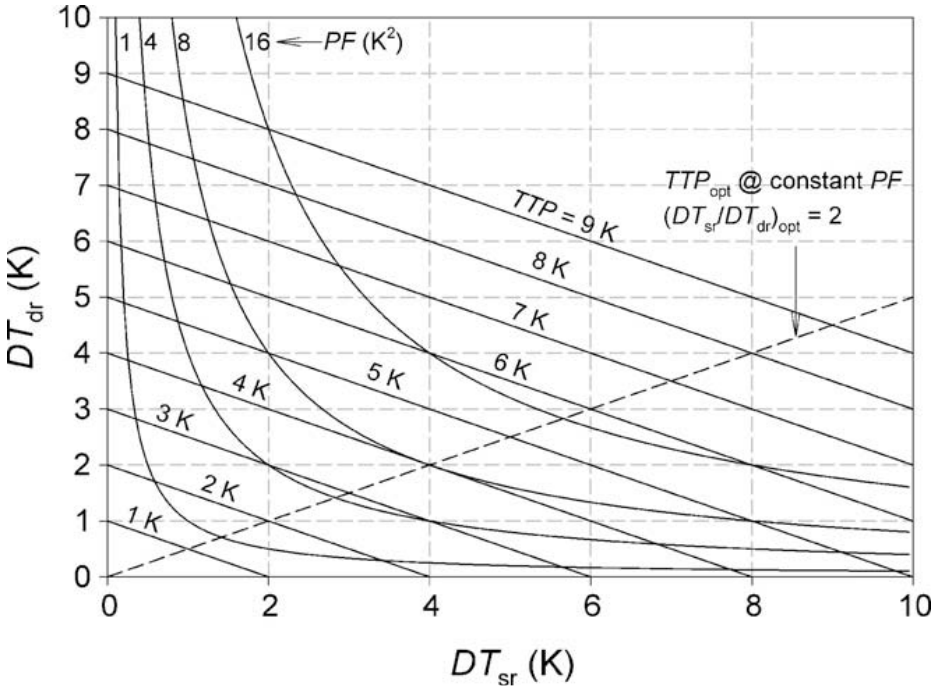

Figure 5.4. Constant Penalty Factor PF and Constant Total Temperature Penalization TTP lines on DT_{dr} - DT_{sr} coordinates.

The comparative analysis between R134a, R32, R245fa, R1234yf, R1234ze(E) and propane is performed at the following working conditions:

- hydraulic diameter equal to 0.96 mm;
- average roughness of the internal tube wall equal to 1.3 μm;
- saturation temperature of 40°C.

Furthermore, in order to calculate the mass velocity of each refrigerant, the constant value of the Penalty Factor is to be referred at a vapor quality of 0.5.The fixed value of the Penalty factor has been chosen in such a way the mass velocity resulting for each considered refrigerant is within the range of working conditions for shear stress dominated condensation. According to the model by Cavallini *et al.* [28], this means that all the working conditions defined from the fixed value of Penalty Factor have to lie in the ΔT-independent flow region. Once the mass velocities at the same PF are identified, condensation heat transfer coefficients is calculated for each refrigerant at the correspondent mass velocity within the range from 0.15 to 0.85. The comparison among the resulting heat transfer coefficients enable to rank the refrigerants in point according to their potential condensation performance.

Therefore, let the Penalty Factor for condensation PF be equal to 10 K^2 at 0,5 vapor quality and 40°C saturation temperature: the correspondent mass velocities are 1218 kg m^{-2} s^{-1} for R32, 654 kg m^{-2} $s^{-1}$for R1234yf, 594 kg m^{-2} $s^{-1}$for R134a, 484 kg m^{-2} s^{-1} for propane, 464 kg m^{-2} s^{-1} for R1234ze(E) and only 191 kg m^{-2} s^{-1} for R245fa, as demonstrated in

Figure 5.5. The heat transfer coefficient comparison considers the resulting mass velocity for each fluid arising from the previous fixed conditions and it is showed in

Figure 5.6. It clearly indicates that, at the same Penalty Factor, the refrigerant R32 outperforms all the other considered fluids. Secondly, it is clear that the better condensation performance can be achieved with the higher pressure fluids (with lower critical temperature). Furthermore, it attests that the heat transfer performance of R134a is higher than those of its low GWP alternatives. In particular, from

Figure 5.6, according to this approach, the condensation heat transfer coefficient for R134a is on average 12% higher than that for R1234yf and 21% higher than that for R1234ze(E). Finally, this proper comparative analysis completely contradicts the misleading conclusions one can get from

Figure 5.3, as the potential heat transfer performance of refrigerant R245fa is the worst.

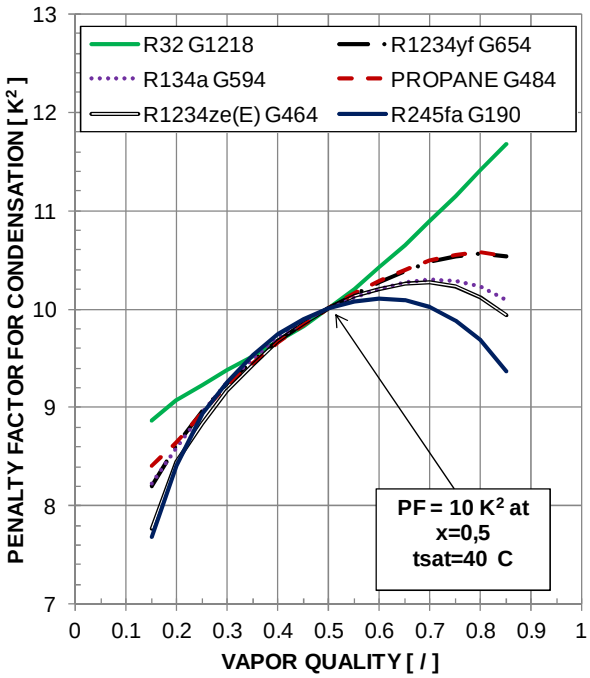

Figure 5.5. Penalty Factor versus vapor quality considering a specific mass velocity for each considered fluid in order to obtain PF = 10 K^2 at x = 0.5 and at t_{sat} = 40°C. PF has been calculated

using the Del Col *et al* [4]. correlation for the two-phase pressure drop gradient and the Cavallini *et al.* [28] model for the condensation heat transfer coefficient.

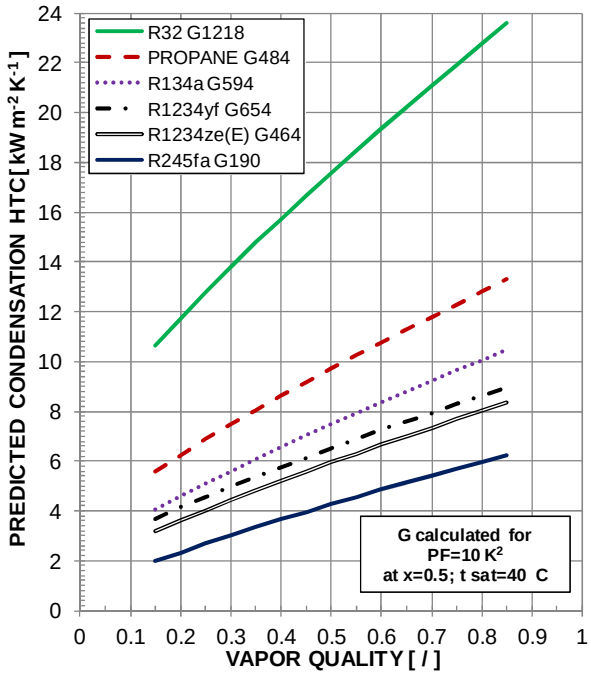

Figure 5.6. Predicted condensation heat transfer coefficient versus vapor quality at a specific mass velocity for each considered fluids giving PF = 10 K^2 at x = 0.5 and at t_{sat} = 40°C. The model by Cavallini *et al.* [28] was employed.

6 APPLICATION OF THE MINICHANNEL TECHNOLOGY IN A PARABOLIC TROUGH LINEAR SOLAR CONCENTRATOR

6.1 Abstract

In electronics, the minichannel technology has proved to be reliable and effective in removing high heat fluxes. Its application as active cooling system in solar concentrators with densely packed photovoltaic cells appears very interesting and promising, since compactness and very low thermal resistance are necessary requirements. Furthermore, it gives the possibility to cogenerate electrical energy and heat at temperature up to 100°C if triple junction solar cells are employed. In this chapter a linear solar concentrator is described and experimentally characterized testing two different receivers along the focal line. The primary optics of the concentrator consists of four mirrors that compose a half parabolic trough whose total aperture area is equal to 6.857 m^2 and whose focal length is 1.81 m. The focal line is 2.4 m long. The parabolic trough moves about two axes (azimuth and zenith motions) to have the direct normal irradiance normal to the aperture area. The first tested module is a hybrid concentrating photovoltaic thermal (CPVT) receiver provided with triple junction solar cells soldered on a ceramic substrate that is in turn in thermal contact with an aluminum roll-bond canalized plate that acts as a heat exchanger. The roll-bond channels have a hydraulic diameter of 2.1 mm. The photovoltaic cells are protected by a high transmittance glass and a secondary optics composed by two flat aluminum mirrors is used to maximize the amount of power reaching the receiver. On the back side, the CPVT module is provided with thermal insulation. In this case the geometrical concentration ratio is around 130, which is very high for a linear concentrator.

The particular geometry of the half parabolic trough concentrator has given rise to the interest in investigating the performance of a minichannel-based flat receiver for the generation of heat only in the medium temperature range (up to 150°C). The thermal receiver consist of a roll-bond plate with a selective coating. The minichannels integrated in the receiver have a hydraulic diameter of 2 mm. This receiver has been thermally insulated on the back side.

Before every experimental test, a optical modeling of the solar concentrator considering the two receivers has been developed to evaluate the optical efficiency and the concentrated flux distribution along the dimension of the receiver normal to the focal line. The analysis of the optical performance has been done using the ray-tracing codes SolTrace [86] and TracePro [87] and takes into account the sun shape and the optical errors due to the imperfections of the slope of the surfaces, the reflectance of the mirrors, the tracking system and alignment of the receiver.

Outdoor experimental tests have been carried out using water as working fluid in single-phase flow. The CPVT module has been characterized in open electrical circuit conditions and with a rheostat connected to its terminals and set in order to work close to the maximum power point. The thermal efficiency of the receivers has been defined according to the procedures described in the EN 12975-2 standard [88]. Several tests are performed with both the receiver at different values of inlet water temperature, from 20°C to 83°C.

Finally a model of the thermal receiver implemented in MATLAB [82] and Simulink [89] has been validated against experimental data and then used for a preliminary evaluation of the efficiency of the thermal module when the flow boiling of a suitable refrigerant is considered inside minichannels at saturation temperature up to 150°C.

6.2 The use of minichannels in solar systems

The effectiveness and the compactness of the heat transfer systems based on the minichannel technology promoted their application in air conditioning, refrigeration and cooling of fuel cells. The microelectronics and power electronic industries are facing the challenge of removing very high heat fluxes (up to 300 W cm^{-1}) from small devices maintaining acceptable operating temperature. From the investigation of several technologies for the cooling of microchips reported in [90], the two-phase heat transfer in minichannels has been regarded as the most promising approach as compared to the single-phase cooling in minichannels, to the use of porous media and to the jet impingement. Finally, the use of the minichannel technology in solar systems spurs growing interest.

In solar collectors, the employment of minichannels brings some geometrical features that promote the heat transfer. First, at the same area of the absorber, the number of the channels can be increased through manufacturing techniques, such as the roll-bond technology or the extrusion, that are cost-effective. In this way, the heat transfer area between the walls of the channels and the working fluid can be increased without increasing the production cost. Secondly, larger heat transfer coefficient can be achieved in minichannels as compared to those obtained in macrochannels. Furthermore, the manufactured minichannels can be easily integrated in the absorber plate and this is a clear advantage as compared to the flat solar collectors where the tube are soldered on the absorber sheet or to the evacuated tube collectors, where tube with external fins are required.

In this work, the term “minichannels” refers to small channels with hydraulic diameters lower than 3 mm. In literature there is not a rigorous distinction between minichannels and microchannels, so in this introductive section, the terms reported by the researchers in their works are observed.

Diaz [91] proposed to replace the common absorber/round tube design adopted in an evacuated tube solar collector with minichannel tubes, that has the same free flow area (Figure 6.1). This new solution leads to a much larger wetted perimeter and involves less thermal resistance as compared to the typical design. Furthermore, in the minichannel-based solar collector the amount of working refrigerant can be reduced and this is an important advantage when using high pressure fluid, such as carbon dioxide, that is considered by the author. From the computational simulation, it has been observed that the minichannel-based collector operated with an efficiency around 50% at 190°C. In consequence of this promising result, Diaz studied the combination of several innovative solar collectors with a Rankine cycle operating with carbon dioxide.

Sharma and Diaz [92] investigated numerically a novel evacuated tube solar collector whose absorber consisted of a U-shaped multiport minichannel with a selective coating on the external surface. The absorber was enclosed in an evacuated glass-tube. The performance of the novel solar collector has been compared against that of an evacuated tube solar collector with absorber/round tube configuration. The absorber area was identical for the two devices. The results showed that the increase of the area between the heat transfer absorber and the working fluid and the decrease in the total thermal resistance achieved in the minichannel-based collector gave higher efficiency specially at higher operating temperatures. When coupling the minichannel-based solar collector with a compound parabolic concentrator, a design optimization of the reflecting element was required.

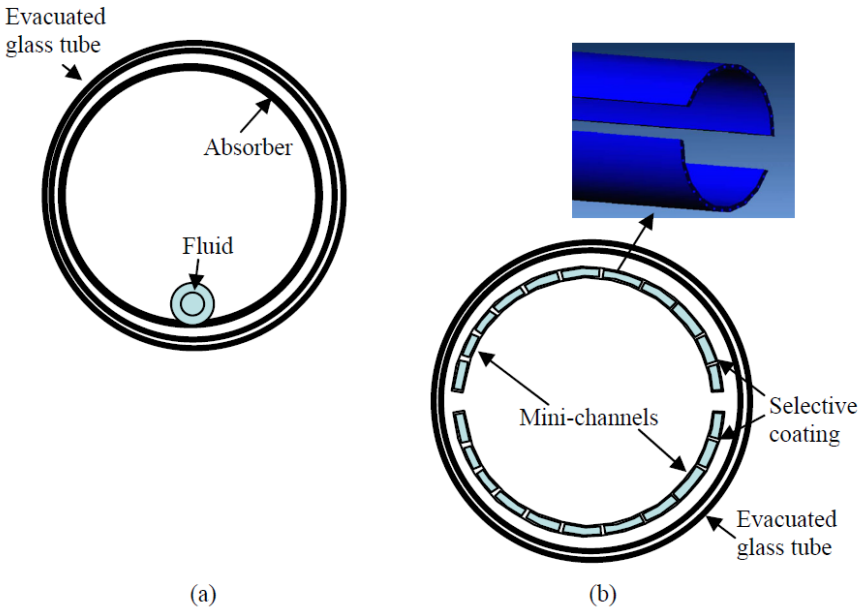

Figure 6.1. Schematics of: Left: a typical evacuated tube solar collector with absorber and round tube; Right: the minichannel-based solar collector proposed by [91].

Khamis Mansour [93] developed a numerical model to evaluate the thermal performance of a glazed flat solar collector using a square multiport minichannel absorber with a selective coating. The hydraulic diameter of each channel was equal to 2 mm and distilled water was used as working fluid. The numerical model has been validated against the experimental data collected during tests on a small-scale prototype of the minichannel solar collector. The thermal performance of the new proposed solar collector has been compared to that of a conventional glazed solar collector with the same absorber area and tubes having an hydraulic diameter of 10 mm. The results highlighted that, thanks to the higher heat transfer coefficient in small channels and to the lower thermal conduction resistance, in the minichannel design the temperature of the absorber plate was closer to that of the working fluid as compared to the conventional collector. Furthermore, in the minichannel collector, the temperature of the glass cover was very close to the ambient air temperature. Hence, the thermal efficiency of the minichannel-based solar device has found to be higher than that of the flat collector with the sheet-and-tube absorber in the entire range considered for the reduced temperature difference from 0 m^2 K W^{-1} to 0.1 m^2 K W^{-1}. The minichannel collector exhibited higher pressure drop, however the calculated power consumption was not significant. The performance comparison was finally extended to other types of collectors: the solar collector investigated by Khamis Mansour displayed higher thermal efficiency than that of an evacuated tube collector and that of an evacuated heat-pipe collector. Nevertheless, the thermal efficiency of flat minichannel collector was lower than that of the evacuated tube solar collector with a minichannel absorber presented by Sharma and Diaz [92].

In conclusion, the use of the minichannels in the mature technology of the thermal solar collector systems enables the improvement of the energy conversion efficiency and thus a lower cost of the heat generation.

The application of the minichannel technology in solar systems has mainly been studied for the purpose of cooling the photovoltaic cells. In fact, the photovoltaic cells present lower efficiency with increasing temperature, according to a penalization coefficient that is given by the manufacturer and depends on the material of the cells. For example, the silicon solar cells have a temperature penalization coefficient within 0.4% K^{-1} and 0.5%

K^{-1}, while it is within 0.05% $K^{-1}$and 0.1% K^{-1} for the triple junction solar cells. Besides, the efficiency of a photovoltaic cell depends on the uniformity of the temperature on its surface. Finally, in the case of excess temperature, photovoltaic cells may experience irreversible damages.

In flat hybrid photovoltaic thermal (PVT) modules, the heat fluxes are not very high and generally macrochannels heat exchangers are integrated in these systems. Nonetheless, the use of minichannels can provide an enhance heat transfer and so a better efficiency of the silicon photovoltaic cells generally applied in the hybrid flat solar devices.

In some mini/micro channels photovoltaic thermal modules [94] [95], the working fluid is air even if the low thermal capacity may cause a strong temperature non-uniformity along the cells. Below, studies of hybrid systems where the cells have been cooled through liquid or two-phase mixtures flow inside minichannels are reported.

Del Col *et al.* [96] experimentally characterized three hybrid prototypes provided with an active cooling system in which water is used as working fluid. The prototypes consist in a photovoltaic module and an aluminum roll-bond canalized plate applied to the back side of the module and used as an heat exchanger. The hydraulic diameter of each channel was around 2.5 mm. In the first prototype, the roll-bond panel was glued to the back side of the PV module and an insulation layer of 15 mm of polyurethane was added for reducing the heat losses from the heat exchanger to the surrounding environment in the rear part. In the second prototype, the roll-bond heat exchanger was mechanically applied to the back side the PV module by means of springs. No insulation layer was used on the roll-bond panel. Finally, the third prototype was built by a unique lamination process, in which the roll-bond sheet was added to the multilayer components of the PV module (glass, EVA, PV cells, EVA, back sheet, EVA, roll-bond). According to the experimental results, the lamination of the canalized panel with the photovoltaic module in a unique process allowed to achieve the higher thermal performance, because it ensured the lower thermal resistance between the PV cells and the aluminum plate. The collected data have been used to validate a numerical model, which enabled to predict the thermal and electrical performance of the PVT devices. Simulations of annual production of electrical energy and heat by the glued and thermally insulated PVT module have been run. It has been found that when operating in the cogeneration mode, only during summer months an appreciable production of heat available at a temperature of 40°C could be obtained. Hence the PVT devices seems to be suitable for the pre-heating of the domestic water or for the heating of the pool water.

Valeh-e-Sheyda *et al.* [97] analyzed the application of two-phase flow inside microchannels for cooling a small silicon photovoltaic module with an area of 160 x 130 mm^2.In details, a plexiglass multiport tube with 65 parallel rectangular microchannels having an hydraulic diameter of 0.667 mm has been attached to the photovoltaic module using an adhesive layer. Tests have been performed indoor under a solar simulator and considering both a single-phase flow of water and a two-phase slug flow of water and air inside the microchannels. The results pointed out that the implementation of two-phase flow could produce remarkable increase in maximum output power of photovoltaic cell as compared to the hybrid module with the single-phase active cooling system and to the reference non cooled photovoltaic module.

In solar concentrating photovoltaic systems (CPV), the cooling of the cells is one of the main issue because of the high incident energy fluxes (Royne *et al.* [98]). Generally, the geometrical concentration ratio, which is the ratio of the aperture area and the absorber area, is used to characterize a solar concentrator and is expressed in number of suns. In point-focus CPV systems, the sunlight is concentrated onto a single cell or onto very few cells. In this case, for geometrical concentration ratio up to 1000 suns, a passive cooling

system provided with finned surface for heat spreading is generally adopted and located behind cells. The geometry of the finned heat sink is more and more complex as the concentration ratio increases. The finned geometries are exposed to the ambient air, which removes the heat by natural convection.
On the other side, in linear focus concentrators or in larger point focus systems, such as dishes or heliostat fields, the receiver generally consists of many densely packed cells. The increased packaging factor necessarily requires an active cooling system, where the cooling fluid should have a high thermal capacity because cells have less area available for heat sinking as compared to the small point-focus devices. In densely packed modules, impinging jets and minichannel heat sinks are recommended because they are very compact, they can be applied in small areas behind the cells and because they are very effective and lead to a thermal resistance low enough to ensure the thermal control of the system. The jet impingement requires a high pumping power and it is difficult to model because of the disturbances between neighboring jets. Moreover, the erosion of a surface due to high-speed impinging jets has not been deeply investigated so far. The application of the minichannel technology in the densely packed modules of solar concentrators is very interesting provided that an excellent thermal contact with the photovoltaic cells is realized. In perspective, the integration of the minichannels in the ceramic substrate where the photovoltaic cells are soldered represents the best solution, but some manufacturing problems should still be faced. Differently from the impinging jets cooling system, a minichannel-based cooling system enables heat recovery making the solar device a concentrating photovoltaic thermal (CPVT) system. In a CPVT system, heat can be available at different temperatures in order to meet the needs of a variety of applications, especially if the concentrator is provided with triple junction solar cells. In fact, as reported by Perez-Higueras *et al.* [99], differently from the silicon cells, the GaInP/GaInAs/Ge triple junction cells show efficiency higher than 30% for a concentration ratio of 100 suns at least even when the working temperature approaches 100°C (Figure 6.2).

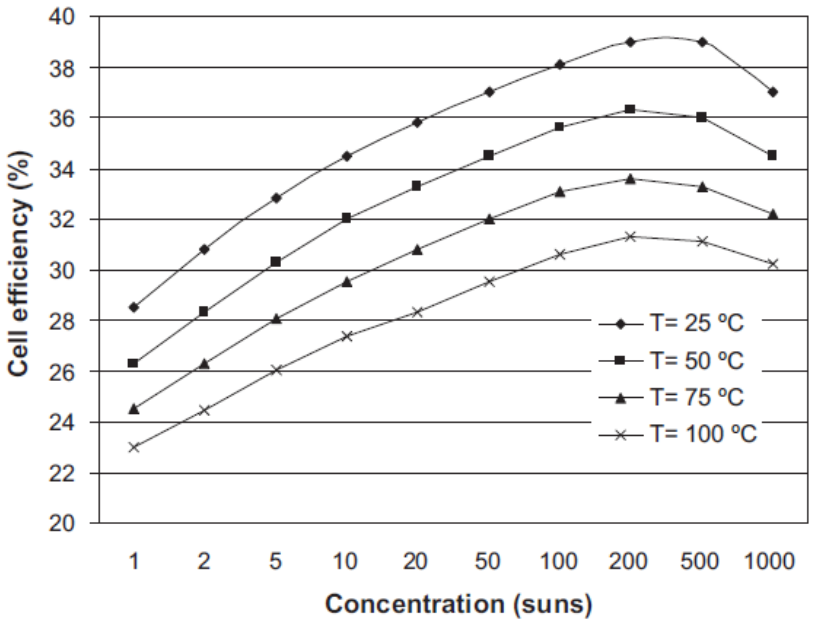

Figure 6.2. Multi-junction cell typical efficiency versus concentration ratio at different working temperatures [99].

The additional cost for an advanced active cooling system of the photovoltaic cells in a solar concentrator can be justified by the increase of the economic value of the energy output (Escher *et al.* [100]). For example, heat available at a temperature between 60°C and 90°C can be used in adsorption cooling or thermal desalinization, while heat available at 80°C-100°C can be employed in absorption systems or for district heating. A higher level of temperature cannot be considered in CPVT systems, as the maximum operating temperature of the triple junction solar cells is within 115°C-120°C.

Single-phase flow in minichannels has been established to behave similar to the macroscale flow [101] and it is widely employed in many applications for the removal of elevated heat fluxes. Nevertheless, it requires high pumping power when a limited difference between the temperatures at the inlet and at the outlet of the heat sink is desired. Several solutions have been proposed to overcome this drawback, such as the design of inlet and outlet manifolds to realize alternating flow directions and the use of fractal-like geometries similar to those of the mammalian circulatory and respiratory systems. These solutions enhance the heat transfer and reduce pressure drops as compared with parallel minichannels.

Two-phase forced convection may be a good option for the cooling of the photovoltaic cells when the heat fluxes are high. During the vaporization of the working fluid, the latent heat capacity can accommodate a significant heat flux and achieve an almost isothermal surface if the pressure drops are moderate. In this case, the limiting operating heat flux corresponds to the critical heat flux (CHF) which leads to the dryout that consists in the replacement of the liquid film wetting the internal wall of a channel with a vapor blanket. The onset of the dryout is a function of the heat flux and the vapor quality. The dryout causes a dramatic decrease of the heat transfer coefficient and thus a sudden increase of the wall temperature, which would lead to the destruction of the solar cells in a concentrator. Experimental studies on the flow boiling in microchannels and minichannels showed that the flow pattern map and models developed in macroscale geometries cannot be applied in miniscale. Nonetheless, it was found that the thermal resistance decreases with increasing heat flux (before the dryout occurs) and with decreasing hydraulic diameter. On the other side, some issue connected to the flow boiling inside small channels should be better studied such as the flow instabilities, the development of reliable models for the prediction of heat transfer coefficients and critical heat flux. The design has to be meticulously conducted to avoid maldistribution of the fluid. In conclusion, the forced convection boiling in minichannels is the most promising cooling system but it requires further research.

Ho *et al.* [102] [103]. presented a numerical analysis of a high concentrating photovoltaic system in which the densely packed silicon cells are cooled through two-phase forced convection inside a small channel. The concentration ratio was equal to 100 suns. The module was 1 m long and 10 mm wide and it was cooled by a single channel whose cross section is rectangular and has an area of 10 mm x 1 mm. For two-phase flow, the saturation temperature of the working fluid had the greatest effect on the temperature and on the efficiency of the cells. In addition the study investigated the concentration limit for eight fluids including R11, R113, R114, R123, R141b, water and ammonia. For the six organic fluids, the practical concentration limit reached about 4000 suns while for water and ammonia, which exhibit the highest latent heat, the concentration limit was estimated around 6000 suns.

In this Chapter, the new parabolic trough concentrating prototype set up at the Solar Energy Conversion Lab at the University of Padova (northern Italy), is presented and described. Two different minichannel-based receivers have been installed for

experimental investigation. In order to gain a deeper insight of the concentrator, the working fluid is water flowing in single-phase regime.
The first is a hybrid concentrating photovoltaic thermal (CPVT) module provided with an aluminum roll-bond heat exchanger for the active cooling of the cells. As compared to most existing low concentration systems with linear focus, which use silicon crystalline cells, as reported for example in the review paper by Chemisana [104], the CPVT module is composed of triple junction solar cells. The dimensions of the CPVT module give a geometrical concentrating ratio around 130. The maximum inlet temperature of the working fluid during the tests with the hybrids module is 83°C in order to prevent any damage of the cells.
The second receiver is a roll-bond plate provided with a black coating, in this case, the height of the receiver (perpendicular to the focal line) is equal to 10.5 mm. This receiver has been experimentally tested for the production of heat at temperature up to 90°C. Furthermore, a numerical model of the thermal receiver has been developed in order to investigate the production of heat a temperature up to 150°C, in order to meet also the needs of many industrial thermal process (Figure 6.3).
In literature, there are no research works focusing on the production of heat in solar concentrators at medium temperature. In fact, the great solar thermal power plants are designed for the production of electrical energy. Excellent performance even at high inlet temperature of the working fluid are expected using the thermal receiver because the minichannels assure a better heat transfer from the absorber to the working fluid and because the small surface of the receiver should reduce the heat losses to the surrounding environment.

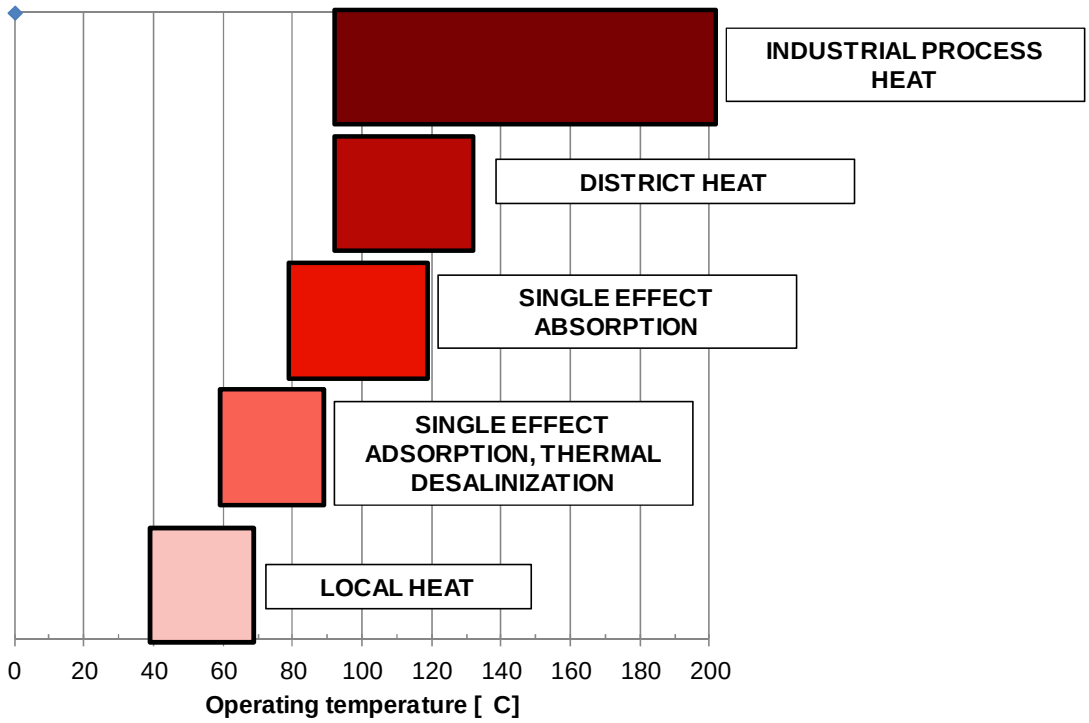

Figure 6.3. Operating temperature range of different thermal users.

6.3 Prototype of the parabolic trough linear solar concentrator and tested receivers

The primary optics of the solar concentrator installed at the Solar Energy Conversion Lab at the University of Padova is made up of four reflective panels that together produce a semi-parabolic trough with a focal length of 1810 mm and a rim angle of 78°. The reflectance of the primary mirrors measured at normal incident radiation is equal to 96.1% as reported by the manufacturer. This high value is due to the presence of a thin glass layer of 1 mm. The total aperture area of the present solar concentrator is equal to 6.857 m^2. In this prototype (Figure 6.4), the length of the focal line is 2.4 m. An aluminum bar is used to support and set the tested receivers so that the their frontal surface is as close as possible to the geometrical position of the focus line. The device has a modular arrangement and the number of the mirrors as well as the length of the focal line can be increased. The system moves about two-axis (azimuthal and zenithal motions) to have the beam radiation normal to the aperture area. The motion is governed by a solar algorithm when approaching the sun and by a sun sensor when achieving the best receiver alignment. In linear concentrators, the thermodynamic limit for the concentration ratio is around 213, as demonstrated by Rabl [105].

Figure 6.4. Prototype of the semi-parabolic trough linear concentrator installed at the University of Padova.

Two different receivers have been installed in the parabolic trough solar concentrator described above. Since the primary optics consists of a semi-parabolic cylinder, each receiver is located so that the normal to its frontal surface forms an angle of 45° with the normal to the aperture area. The first receiver has been designed for the cogeneration of electricity and heat (CPVT), while the second one has been engineered for heat production only.

The concentrating photovoltaic thermal (CPVT) module is 1.2 m long and it is equipped with GaInP/GaInAs/Ge triple junction solar cells soldered on a ceramic substrate made of alumina, which in turn is in thermal contact with an active cooling system including a canalized aluminum roll-bond heat exchanger (Figure 6.5). The photovoltaic cells have a square shape with side length equal to 10 mm and are electrically connected to form mini-modules of 22 cells. In the mini-module, there are two strings connected in parallel and each string id formed by eleven cells connected in series. Each mini-module has an efficiency of 34.5% at 25°C cell temperature, 1000 W m^{-2} direct normal irradiance (DNI), 1.5 air mass and 120 concentration ratio, as reported by the manufacturer. The photovoltaic part of the CPVT module consists of ten mini-modules connected in parallel (Figure 6.6). The triple junction cells are encapsulated using a high optical transmission silicone gel under a protective borosilicate glass. The thickness of the protective glass is equal to 3.3 mm and the index of refraction is 1,4714 at a wavelength of 587.6 nm. Furthermore, the total optical transmittance is around 93% in the wavelength range between 350 nm and 2750 nm and it is negligibly affected by the operating temperature. On the front side of the CPVT module, a secondary optics composed by two flat aluminum mirrors has been mounted to reduce optical losses. For the secondary optics mirrors, the solar specular reflectance is 85% while the solar diffuse reflectance is 5% giving a total reflectance of 90%. Each flat mirror forms an angle of 38.5° with the normal to the plane of the cells. The roll-bond heat exchanger is applied to the back side and the thermal contact with the ceramic substrate is realized through a thermal-conductive pad. On the rear of the module, an elastomeric material was applied as thermal insulation. In order to reduce the pressure drops, two loops have been integrated in the heat exchanger. The two loops are identical within the tolerance of the roll-bond manufacturing process and each loop is around 600 mm long. When using the CPVT module, the geometrical concentration ratio is 130.

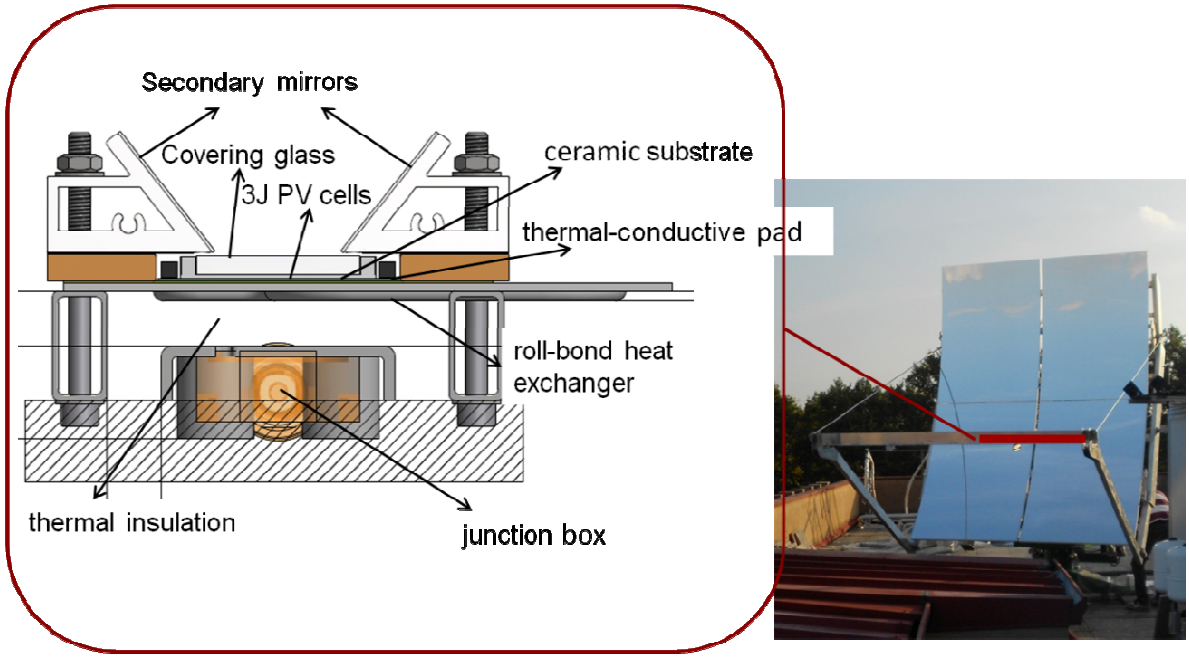

Figure 6.5. Schematic of the CPVT module.

Figure 6.6. Concentrating photovoltaic thermal (CPVT) module frontal view. Ten mini-modules connected in parallel form the photovoltaic part of the module.

The peculiar geometry configuration of the primary optics of the solar concentrator has given rise to the interest in considering a flat thermal receiver instead of the typical tube thermal absorber employed in the parabolic trough concentrating solar power systems. Therefore, the second receiver, named thermal receiver, consists in a one-side flat aluminum roll-bond canalized panel and is 1.2 m long and 105 mm high. The flat side represents the absorber and it is not glazed: in fact, the thermal receiver was built as a preliminary solution for the assessment of the potential of a concentrating system for the production of heat available a medium temperature. The absorber has a selective coating giving an absorptance equal to 87% and an emittance of 35% (Figure 6.7). The other side of the roll-bond plate exhibits four parallel channels with a hydraulic diameter of 2.0 mm and is thermally insulated. There are two inlets for the working fluid, that are located at the ends of the roll-bond plate and a unique central outlet.

Figure 6.7. Thermal receiver during a test run. The sunlight is concentrated on the absorber with selective coating.

6.4 Optical model of the parabolic trough linear concentrator using ray-tracing

The optical performance of the parabolic trough with the hybrid CPVT receiver has been evaluated by using two different Monte Carlo ray-tracing tools: SolTrace 2012.7.9 [86] and TracePro 7.3 [87]. The optical model of the concentrator with the thermal module has been developed using only SolTrace, because, in this case, the geometry of the receiver is very simple and a comparison of different ray-tracing codes is not required. SolTrace has been developed by the National Renewable Energy Laboratory (NREL) and it is suitable to model heliostat fields, parabolic trough, dish-Stirling systems and solar furnaces and to analyze their performances. TracePro is a commercial software by Lambda Research Corporation for the opto-mechanical analysis of solid models.
Two parameters are sought for the characterization of the optical performance of the parabolic trough. The first is the optical efficiency, which is the ratio of the power that reaches the surface with the absorber and the incident power on the aperture area (equation (6-I)). The second is the average flux distribution on the transversal dimension of the receiver (receiver height), that is 22 mm in the case of the CPVT module and 105 mm in the case of the thermal module.

$$\eta_{opt} = \frac{P_{absorber}}{\mathrm{DNI}\, A_{aper,LR}} \quad \textbf{(6-I)}$$

While the determination of the optical efficiency requires to take into account the entire surface of the absorber, the calculation of flux distribution requires to average the flux distributions evaluated in several positions along the receiver length.
In statistical ray-tracing methods, the path of a ray is determined from the source through the system while encountering different surfaces. In the analysis of a solar concentrator, several elements come into play: the direction of the sun, the sun shape, the optical properties of the system components and their optical defects, the tracking errors and the errors related to the position and alignment of the receiver.
In the optical model of the present parabolic trough, the rays coming from the sun are taken always normal to the aperture surface, as the system is provided with a two-axes tracking system.
The sun shape can be defined as the angular intensity distribution of the solar and circumsolar brightness across the disk of the sun, and it affects the performance of a concentrating solar system, in particular with high concentration ratio. Commonly, two ideal sun shapes based on probabilistic distributions are considered: the Gaussian distribution, which leads to inaccurate results in high concentration devices and the pillbox distribution. In the present analysis, for each ray-tracing tool, the sun shape is chosen among the implemented profiles based on studies available in the open literature and it refers to a very clear sky day. In detail, the profiles implemented in SolTrace refer to the work by Neumann *et al.* [106] in which the average solar brightness profiles with different circumsolar ratio has been defined. The sun shape CR0 describe the sun brightness on a typical clear sky and it is considered in the present investigation. On the other hand, when defining a ray source in TracePro, the setup parameters include the boundary, the dimension and the pattern of the grid and the angular profile of beam. In the present evaluation a rectangular grid big enough to include all the systems and with a random pattern has been chosen. The solar angular profile of beam defined by Allen in [107] has been taken.
When a ray encounters a surface, it can be reflected, absorbed or transmitted. The way in which the incoming light is scattered by a generic surface is named Bidirectional Scattering Distribution Function (BSDF) but in practice, a specific function, the Bidirectional Reflection Distribution Function (BRDF) is used to describe how light is reflected from a surface and another function, the Bidirectional Transmittance Distribution Function describes the scatter distribution of transmitted light. In particular, BTDF takes into account the specular reflectance, the diffuse reflectance and the optical errors of a real mirror. There are several models of BSDF such as the Harvey-Shack model, the ABg model, the asymmetric model and the elliptical model. The ABg model well matches the fit of the BRDF for many reflective surfaces but it needs the definition of the parameter A, B and g through an ad hoc optical investigation.
When the two axes in the elliptical model are imposed equal, the scatter distribution is defined as a Gaussian distribution. A elliptical BRDF model with identical axes is considered in the present analysis in order to compare the results obtained with the two ray-tracing tools. The adoption of this BRDF model brings another advantage. Neither SolTrace nor TracePro takes directly into account the tracking errors and the receiver position and alignment errors, but they can be easily included in the reflectance errors of the real mirrors composing the concentrator, as they are generally defined through Gaussian distributions. Different values of the total optical error, including tracking,

mirror slope, reflecting surfaces and receiver alignment imperfections have been considered during the evaluation of the optical performance: 2.5 mrad, 3 mrad, 3.5 mrad and 4 mrad. The selected values cover the range of typical optical errors that can be found in the open literature. Nevertheless, it should be noted that in SolTrace only the specular reflectance is taken into account.

6.4.1 Model and optical performance of the concentrator with the hybrid PVT receiver

In the model of the hybrid photovoltaic-thermal module mounted on the concentrators, the optical properties of the primary optics parabolic mirrors, the secondary optics flat aluminum mirrors and the borosilicate glass are implemented, while the absorber, that is the triple junction cells surface, is regarded as a perfect absorber with a unitary absorptance. The total optical error is applied on the BRDF of the primary parabolic mirrors.
When using SolTrace, the desired number of rays intersection is set equal to $5 \cdot 10^6$ and the flux distribution along the receiver height is computed as the average distribution of the data obtained considering 40 bins along the length of the receiver and 22 bins along the height of the receiver.
When using TracePro instead, $4 \cdot 10^6$ rays are traced during the simulation of the optical performance. Furthermore, the flux distribution is calculated with the following procedure. First, the receiver has been divided into 40 elements (25 mm x 22 mm) and for each element a irradiance map is obtained considering a Fast Fourier Transform (FFT) with a grid size of 128 x 128. The number of pixels used to control the degree of smoothing applied to the data is set at 25. The flux distribution is determined as the average of the flux distributions obtained in the middle of each element.
Table 6-a reports the values of the optical efficiency obtained using the two ray-tracing tools as a function of the total optical error. The small differences in the optical efficiency values obtained by the two codes can be explained by the different sun shape that has been implemented. Figure 6.8 depicts the distribution of the concentrated flux along the receiver height estimated with Soltrace as a function of the total optical error, while Figure 6.9 displays the flux distribution results evaluated with TracePro. At the same total optical error, the agreement between the profiles of flux along the receiver obtained with the two ray-tracing tools is satisfactory and validated the optical modeling of the entire system.

Table 6-a. Optical efficiency calculated with SolTrace and TracePro at different total optical errors. In the calculation, the receiver frontal surface is assumed as a perfect absorber.

Total Optical Error	Optical efficiency	
	SolTrace	TracePro
2.5 mrad	74.1 %	77.0 %
3 mrad	71.2 %	73.6 %
3.5 mrad	68.0 %	69.7 %
4 mrad	64.8 %	66.3 %

The parabolic trough with the hybrid CPVT receiver exhibits a geometrical concentration ratio of 130, that is quite high for a linear focus concentrating solar device, hence the total optical error affects both the optical efficiency and the concentrated flux distribution. In particular, in the central region of the receiver, the flux distribution flattens as the optical error increases. Two triple junction photovoltaic cells are located along the height of the receiver, thus according to the evaluated distribution profiles, they are subjected to a

strongly non-uniform concentrated flux. This is a negative aspect, because it plausibly penalizes the photovoltaic conversion and reduces the electrical efficiency of the system as reported in the work by Baig *et al.* [108]. Furthermore, the flat secondary optics seems to be insufficient in smoothing the distribution and maybe a different configuration should be considered and properly designed.

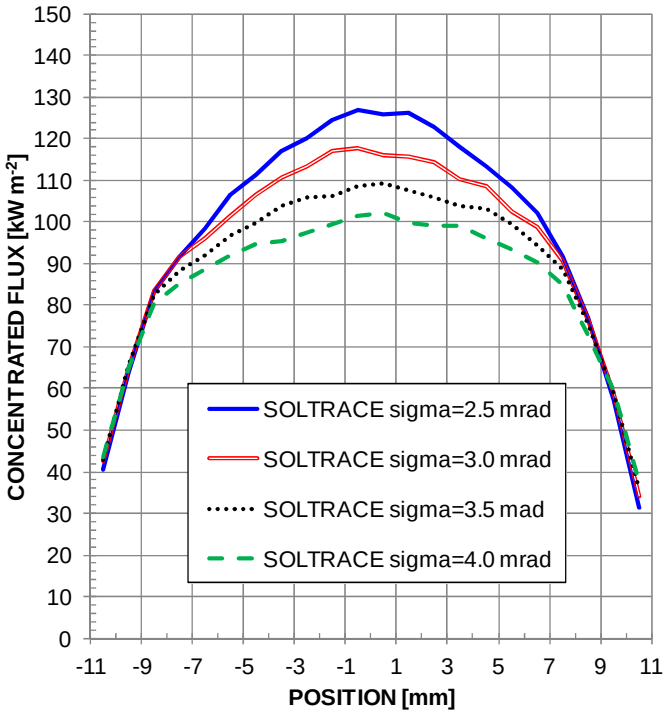

Figure 6.8. Concentrated flux distributions at different total optical errors (sigma) evaluated using SolTrace along the CPVT receiver height. The position 0 refers to the center of the receiver.

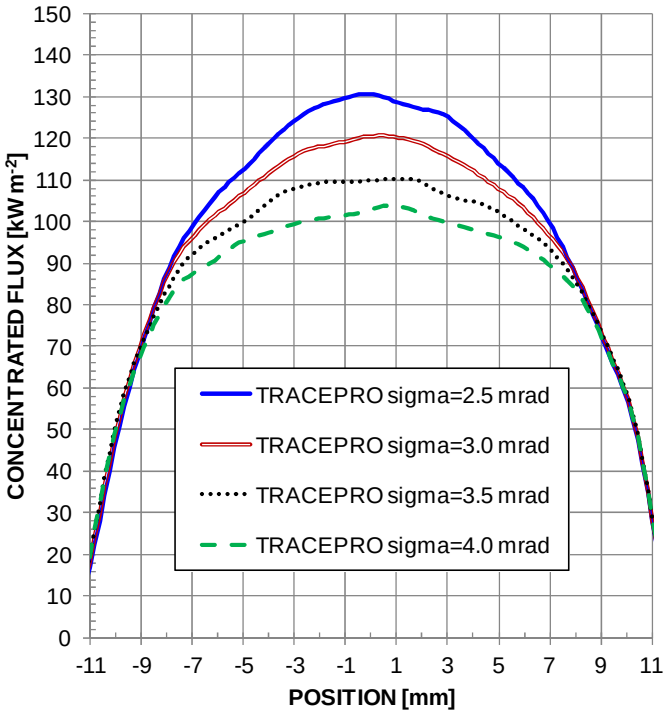

Figure 6.9. Concentrated flux distributions at different total optical errors (sigma) evaluated using TracePro along the CPVT receiver height. The position 0 refers to the center of the receiver.

6.4.2 Model and optical performance of the concentrator with the thermal receiver

The optical model of the linear focus solar concentrator with the thermal receiver is very simple and includes the reflective surfaces of the primary mirrors composing the semi-parabolic cylinder and the absorber. When considering the optical efficiency, the absorptance and the emittance of the absorber with the selective coating are not taken into account, in order to define a parameter which depends only on the flux that is actually concentrated on a surface and does not depend on the optical properties of the employed receiver. Thus the thermal module is assumed as a perfect absorber.
The total optical error is applied on the BRDF of the primary parabolic mirrors.
Since the geometry of this system is very simple, the evaluation of the optical performance is done using only SolTrace as ray-tracing tool: the desired number of rays intersections is set at $5 \cdot 10^6$ and the flux map data obtained considering 40 bins along the length and 25 bins along the height of the receiver are average to define the mean flux distribution at different total optical errors (Figure 6.10).

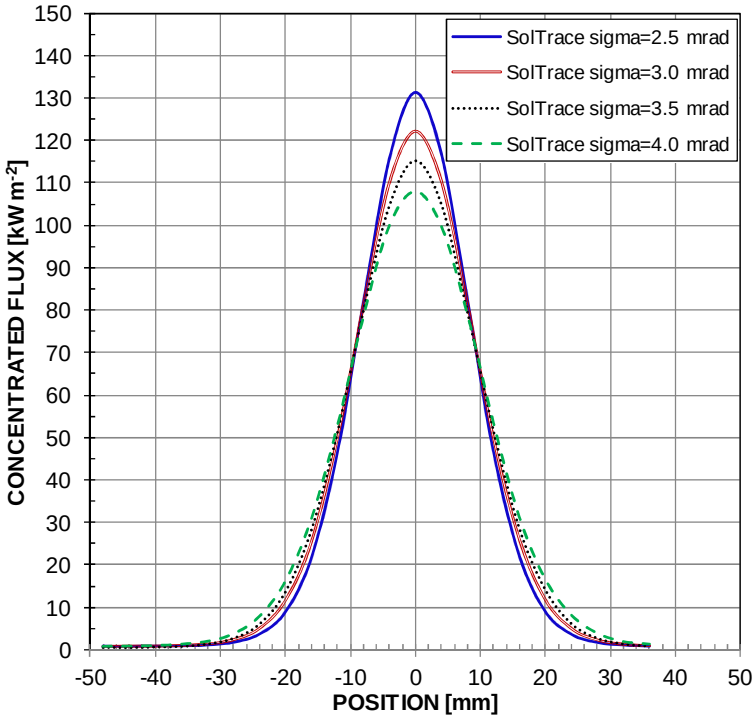

Figure 6.10. Concentrated flux distributions at different total optical errors (sigma) evaluated using SolTrace along the thermal receiver height. The position 0 refers to the center of the receiver.

In this case, the height of the receiver is 105 mm and it is higher than the sun image centered about the focal line as attested in Figure 6.7. This means that when varying the value of the total optical error, the distribution of the concentrated flux along the transversal dimension of the receiver also varies while the amount of power that reaches the absorber remains the same. Hence, with this geometry, the optical efficiency is independent on the optical error in the range between 2.5 mrad and 4 mrad and it is equal to 96 %. The thickness of the roll-bond absorber is equal to 2 mm and the central canalized part is located in a region of the thermal receiver, that is 55 mm high. The upper part and the lower part of the roll-bond absorber act as fins and contribute to the heat dissipation towards the external environment. In an optimized design, the height of the receiver should be reduced in order to improve the performance, a glazed receiver should be projected and the thickness of the thermal absorber should be defined in order to get a

heat spreading effect to level the concentrated flux distribution. Differently from the case of the CPVT receiver, the concentrated flux distribution does not affect the overall performance of the thermal receiver, but it is anyway a very useful result. During the experimental tests performed with water flowing in single-phase flow, the mass velocity inside each channel is around 1650 kg m^{-2} s^{-1}, that is quite high and the concentrated heat flux per channel is not supposed to cause the departure from nucleate boiling. When considering the vaporization of a refrigerant inside the thermal receiver to improve the efficiency of the heat transfer both on the focal line between the absorber and the fluid and in the heat exchanger where the heat is provided to the thermal user, the concentrated flux distribution is to take into account. In fact, as the latent heat of the fluid is used, the mass velocity is much lower and thus the critical heat flux should be necessarily compared to the heat flux expected for each channel. When considering the vaporization inside the thermal receiver, the critical heat flux should be not only calculated using the models available in the open literature but also determined from experimentation starting from the evaluated concentrated flux distribution to assess the reliability of the system or in case, to change and improve the design of the receiver.

6.4.3 Theory of heat flux measurement for concentrating solar devices.

The measurement of the heat flux distribution on the receiver of a solar concentrating system is very important to evaluate the radiant power incident on the aperture area of the receiver and thus its efficiency. Furthermore it allows the validation of the optical modeling of the system and it can be useful to improve the design of the receiver. Two different heat flux measurement system can be generally considered for receivers in solar concentrators, one is associated to a direct method and the other is associated to an indirect procedure (Ballestrin and Monterreal [109]).

The direct method is based in the use of heat flux microsensors (HFM) that are made up by a thin film heat flux sensor and a thin film temperature sensor deposited on aluminum nitride. The exposed face of the two sensors is generally spayed with a black coating that should exhibit a constant and high absorptance over a wide spectral range. The heat flux sensor consists of a thermopile, whose voltage signal is proportional to the magnitude of the heat flux. The temperature sensor is made by a platinum resistance that is located around the heat flux sensor. The temperature measurement is necessary to correct the heat flux reading since it enables to take into account the variation of the electrical conductivity with temperature. The heat flux microsensors can work at temperatures up to 800°C without water cooling and have a thickness of some micrometers, thus the response time is generally within 20 μs. During the measurement, several heat flux microsensors are generally integrated in a white target that moves parallel to the aperture area of the receiver. The data collected from the devices refer to discrete positions on the receiver aperture area and should be properly interpolated to determine the concentrated flux distribution. The geometry of the moving bar where the sensors are installed depends on the shape of the receiver. For example, the system described by Ballestrin and Monterreal [109] is suitable for a solar central receiver in an heliostat field.

In the indirect measuring procedure, a high resolution CCD camera records the image on a white lambertian moving target. The lambertian target can be considered an ideal diffusing reflecting surface and it is generally made of alumina, it is not equipped with a cooling system and is mounted as close as possible to the receiver aperture area. The image obtained from the camera is corrected accounting for the offset and the distortions and consists in a gray-scale map which describes the shape of the concentrating beam but it does not give any value of the physical quantity of interest. In fact, this system must be

calibrated by correlating the gray-scale value of any pixel of the image with the incident radiative flux measured by a water-cooled calorimeter (for example, a Gardon calorimeter or an absolute Kendall point radiometer) at the same position.
As proved by Ballestrin and Monterreal [109], the measurements performed with the two methods are in good agreement, so depending on the receiver geometry, one can choose the method that best suits with the studied system. The combination of the two method, named hybrid measurement method increases the confidence in the estimation of the heat flux and enables to detect changes in the calibration of the instruments.

6.5 Experimental investigation

6.5.1 Experimental test facility

The test rig, illustrated in
Figure 6.11, includes a hydraulic loop, the instrumentation for the measurement of the mass flow rate, the inlet and outlet temperature, direct solar irradiance, wind speed and ambient air temperature. Water in single-phase flow is used as working fluid in this test facility.
The water coming from the tested receiver enters in storage 1 and passes through a plate heat exchanger that acts as heat sink. In the plate heat exchanger, the heat flow rate provided by the concentrated solar radiation is taken away by a secondary fluid and then wasted in a second heat exchanger to the ground water of the building central plant. Afterward, the working fluid enters the storage 2, which is provided with four electrical heaters: three of them supply an electrical power of 5 kW while the last one, located at the bottom of the storage, has an adjustable power from 0 kW to 5 kW. Given the total mass flow rate, it is possible to set the electrical power to control the water temperature at the inlet of the receivers. A pump is used to circulate water, whose mass flow rate is measured by a Coriolis effect mass flow meter.
Depending on the tested receiver, each inlet and outlet water temperature is measured by a Pt100 platinum resistance temperature detector (RTD). Whichever the configuration of the test rig, the inlet and the outlet temperature at the mixing point are gauged, as they are used to assess the thermal performance of the receiver under examination.
The laboratory is equipped with a measuring system of solar irradiance, composed of a Kipp&Zonen secondary standard pyranometer that measures the global irradiance on the horizontal plane, a Delta Ohm LP PYRA 02 pyranometer (first class classified) shaded with a band to measure the diffuse irradiance on the horizontal plane and a Kipp&Zonen CHP 1 pyrheliometer mounted on an EKO STR-21G sun tracker for measuring the direct normal irradiance (DNI). The DNI is the power input of a concentrating solar device and it is necessary to calculate the global efficiency.
A Pt100 platinum resistance thermal detector is used to measure the ambient air temperature and an anemometer measures the air speed on the horizontal plane.
When performing tests with the CPVT module, two different testing modes are considered: in open circuit condition and with a resistive electrical load connected. In the latter case, the electrical terminals of the module are connected to a rheostat and a NORMA 4000 power analyzer that measures the current of the circuit, the voltage across the resistive load and the electrical power supplied by the triple junction photovoltaic cells. During these test runs, the sliding contact of the rheostat is set in order to make the CPVT module work very close to the maximum power point. The proper position is obtained by observing the trend of the electrical power output provided by the power analyzer and it is manually checked several times during each test run. Since, at the

maximum power point operating condition, the nominal current of the CPVT module is expected equal to 1,8 A and the nominal voltage is expected equal to 300 V, the electric resistance of the rheostat can be adjusted in the range from 50 Ω to 250 Ω.

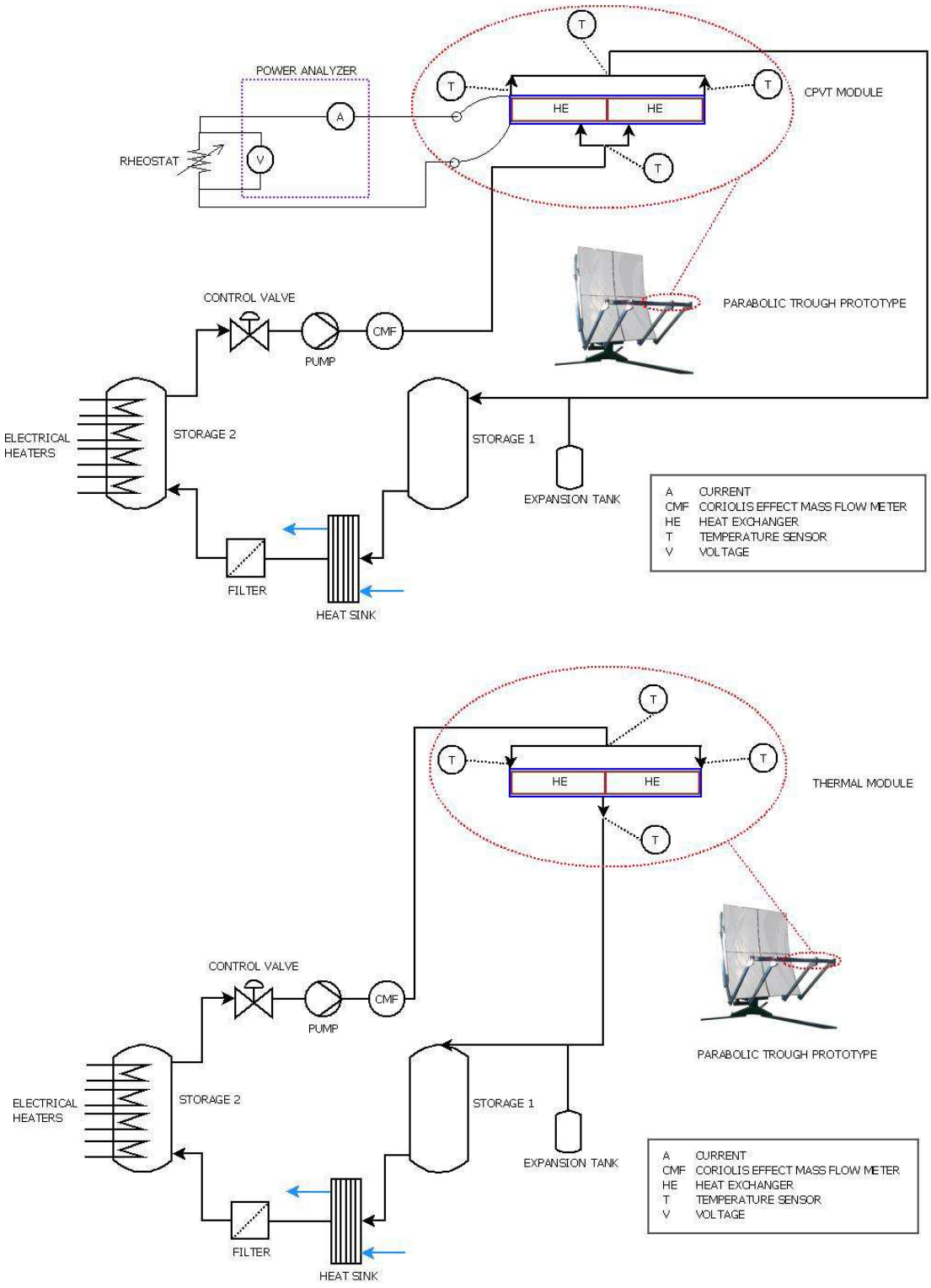

Figure 6.11. Experimental test rig. Top: Configuration with CPVT module. Bottom: Configuration with the thermal module.

6.5.2 Review on testing procedures

A concentrating solar system for heat generation is a solar thermal system and should comply with the official standards in order to guarantee functional operation and durability of the parts. These standards provide also the test method to correctly characterize the thermal performance. In particular, the quasi-dynamic test procedures illustrated in the EN 12795-2 standard [88] is applicable to a variety of collector design, from stationary-non imaging collectors, as the evacuated tube solar collectors provided with compound parabolic concentrators to high concentrating tracking systems. In case of tracking collector, a pyrheliometer is recommended to measure beam radiation. Nevertheless, no other special requirements are specified for tracking or non-tracking concentrator collectors.
On the other hand, the actively-cooled concentrating photovoltaic systems and the concentrating photovoltaic thermal systems lack specific standardizations for qualification, reliability and performance assessment. Hybrid CPVT systems are neither purely photovoltaic nor purely thermal, and the global characterization is one of the main issue for this technology.
The IEC 62108 norm [110], which is an evolution of the IEEE 1513 standard [111], is the first standard developed exclusively for concentrating photovoltaic technology and includes description of the test procedures to determine the electrical, mechanical and thermal characteristic of the CPV module. It takes in consideration five different technologies: point-focus dish concentrators, linear focus parabolic trough, point focus and linear focus Fresnel devices and heliostat CPV systems. Muñoz *et al.* [112] suggested some possible improvements of the IEC 62108 standard aiming at overcoming some technical problems encountered by organization and laboratories.
Vivar *et al*. [113] stated that the IEC 62108 standard and the EN 12975-2 standard are unsuitable and insufficient for qualifying actively cooled CPV and CPVT systems. Specifically, the IEC 62108 standard takes into account only one system, the point focus dish concentrator, that incorporates active cooling but the associated test procedures are confusing and this is a serious limit. In fact, for some tests, the result with and without active cooling can be dramatically different. Furthermore, some procedures are suitable for the passive-cooled devices and leads to unrealistic working conditions when applied to the active-cooled systems. In addition, the EN 12975-2 includes a group of tests related to high solar irradiance exposure with no liquid circulation that can lead to severe damages of the cells, the soldering points and the electric circuitry. Thus Vivar and coworkers put forward revisions of the current standards to accommodate materials and design properties of hybrid CPV and CPVT receivers, including new test procedures that aim at analyzing some failures modes of the new devices. For example, it is important to verify that the system can utilize a fail-safe mechanism when the tracking capability or the pumping of the coolant is lost and that the thermal control of the system is assured even when the related thermal storage achieves the maximum operating temperature.
The work by Dupeyrat *et al.* [114] concerns the measurement of the efficiency of flat photovoltaic thermal collectors (PVT) and concentrating photovoltaic thermal collector (CPVT), including both thermal and electrical performances. According to the authors, some tests should be performed in open electrical circuit conditions in order to compare the hybrid devices with the conventional solar thermal systems. They reported the results of an outdoor test with a CPVT system performed following the stationary approach illustrated in the EN 12975-2 standard. The results are reported in terms of efficiency curve versus the reduced temperature difference calculated considering the direct normal

irradiation as input power. Furthermore, they stated that 'electrical only' mode tests are not significant, as the electrical performance are sensitive to the thermal behavior of the receiver: hence, 'hybrid mode' tests are sufficient for the electrical characterization. Finally, it was pointed out that in the case of a concentrating solar device, the knowledge of the flux distribution at measurement conditions on the cells is very important as it greatly affects the electrical performance.
Helmers and Kramer [115] developed a performance model for both non-concentrating and concentrating photovoltaic systems. In analogy to the quasi-dynamic procedure described in the EN 12975-2 norm, the model allows to define the efficiency curve with respect to the electrical and thermal power output of the considered device. The coefficients of the efficiency curves are determined through a multi-linear regression on standard measurements data of irradiance, ambient temperature, wind speed, mean fluid temperature, thermal power output and photovoltaic power output. The model was validated for a particular CPVT collector, so further investigation of different kinds of collector is required to assess its general reliability.

6.5.3 Data reduction

As the system moves about two axes, the steady-state method described in the EN 12975-2 standard [88] is adopted here for the assessment of the thermal performance of the tested receivers. The direct normal irradiance (DNI) is considered instead of the global irradiance on the collector plane because it is the actual input energy flux of the parabolic trough concentrator. The mass flow rate is set equal to 0.02 kg s^{-1} per square meter of the aperture area, calculated considering the actual length of the receiver. Measurement are repeated at different inlet water temperature in order to produce a set of thermal efficiency data, defined as the ration of the useful heat flow rate and the input power from the sun (equation (6-II)). The useful heat flow rate depends on the water mass flow rate and on the temperature difference of the water across the receiver. The input power is the product of the direct normal irradiance and the aperture area of the concentrator (referred to the actual length of the receiver).

$$\eta_{th} = \frac{q_{th}}{\mathrm{DNI}\, A_{aper,LR}} = \frac{\dot{m}_{wat}\, c_{p,wat}\left(t_{wat,out} - t_{wat,in}\right)}{\mathrm{DNI}\, A_{aper,LR}} \qquad \textbf{(6-II)}$$

When investigating the performances of CPVT module, experimental tests both in open electric circuit conditions and with electric resistive load have been performed. In the latter case, the rheostat and the power analyzer are connected to the terminals of the module. The thermal power is defined according to the EN 12975-2 norm, considering a measurement period of 10 minutes. In the same time frame, the output electrical power is calculated as the average of the power analyzer readings thus, the electrical efficiency can be expressed as:

$$\eta_{el} = \frac{P_{el}}{\mathrm{DNI}\, A_{aper,LR}} = \frac{E_{el}\, I_{el}}{\mathrm{DNI}\, A_{aper,LR}} \qquad \textbf{(6-III)}$$

Finally, considering the useful heat flow rate and the electric power provided by the CPVT when the resistive load is connected, the global efficiency of the system can be defined as:

$$\eta = \eta_{th} + \eta_{el} = \frac{q_{th} + P_{el}}{\text{DNI}\ A_{aper,LR}} \quad \textbf{(6-IV)}$$

The experimental data are reported in a diagram plotting thermal efficiency and in case electrical efficiency and global efficiency as a function of the reduced temperature difference T_m^*:

$$T_m^* = \left[\frac{\left(T_{wat,out} + T_{wat,in}\right)}{2} - T_{amb} \over \text{DNI}\right] \quad \textbf{(6-V)}$$

6.5.4 Uncertainty analysis

The experimental uncertainty analysis of the measured data has been done in compliance with the guidelines provided by the Guide to the Expression of Uncertainty in Measurement [17]. The experimental uncertainty of a measured parameter θ, as the water mass flow rate, the water inlet and outlet temperature and the electrical current and voltage, is made up of two terms (equation (6-VI)): the Type A uncertainty and the Type B uncertainty.

$$u_C = \sqrt{u_A(\theta)^2 + u_B(\theta)^2} \quad \textbf{(6-VI)}$$

Type A uncertainty derives from the statistical analysis of the repeated measurements under steady state conditions and it is defined as the standard deviation of the mean, according to the ISO Guide to the Expression of Uncertainty in Measurement [17]:

$$u_A(\theta) = \frac{s(\theta)}{\sqrt{n}} \quad \textbf{(6-VII)}$$

where n is the number of readings and s is the standard deviation of the measured parameter.
Type B uncertainty is based on information available for the instrument, such as the manufacturers' specifications, data provided in calibration certificates and uncertainties assigned in reference book. Table 6-b reports the Type B uncertainty for the parameters measured by the different sensors installed in the experimental apparatus with a confidence level of 95.45%. The percentage values reported in the table are referred to the measured readings. The uncertainty of the Pt100 resistive temperature detectors (RTDs) depends on the working temperature.

Table 6-b. Type B uncertainties of the measured parameters.

water temperature (with RTDs)	from ± 0.04 °C at 5°C to ± 0.1 °C at 90°C
ambient air temperature (with RTD)	± 0.05 °C
water mass flow rate	± 0.1 %
direct normal irradiance (DNI)	± 2.5 % at 900 W m^{-2}
electrical current (with power analyzer)	± 0.3%
voltage (with power analyzer)	± 0.3%
wind speed	±(0.1 m s^{-1} + 1%)

When a searched parameter ξ is not directly measured but it can be expressed as a function F of uncorrelated input quantities θ_1, θ_2, …, θ_N,, its combined standard uncertainty is determined from equation (3-IX).

$$u_C(\xi) = \sqrt{\sum_{i=1}^{N} \left(\frac{\partial F}{\partial \theta_i}\right)^2 u_C(\theta_i)^2} \qquad \textbf{(6-VIII)}$$

Developing this formula, according to the definitions given in Section 6.5.3, the experimental uncertainty in the thermal efficiency (equation (6-IX), electrical efficiency (equation (6-X)) and global efficiency (equation (6-XI)) can be expressed as follows:

$$u_C(\eta_{th}) = \left(\left(\frac{c_{p,wat}\left(t_{wat,out} - t_{wat,in}\right)}{\mathrm{DNI}\, A_{aper,LR}} \right)^2 u_C(\dot{m}_{wat})^2 + \left(\frac{\dot{m}_{wat}\, c_{p,wat}}{\mathrm{DNI}\, A_{aper,LR}} \right)^2 u_C\left(t_{wat,out}\right)^2 + \left(-\frac{\dot{m}_{wat}\, c_{p,wat}}{\mathrm{DNI}\, A_{aper,LR}} \right)^2 u_C\left(t_{wat,in}\right)^2 + \left(-\frac{\dot{m}_{wat}\, c_{p,wat}\left(t_{wat,out} - t_{wat,in}\right)}{\mathrm{DNI}^2\, A_{aper,LR}} \right)^2 u_C(\mathrm{DNI})^2 \right)^{0.5} \qquad \textbf{(6-IX)}$$

$$u_C(\eta_{el}) = \left(\left(\frac{1}{\mathrm{DNI}\, A_{aper,LR}} \right)^2 u_C(P_{el})^2 + \left(-\frac{P_{el}}{\mathrm{DNI}^2\, A_{aper,LR}} \right)^2 u_C(\mathrm{DNI})^2 \right)^{0.5} \qquad \textbf{(6-X)}$$

$$u_C(\eta) = \left(u_C(\eta_{th})^2 + u_C(\eta_{el})^2\right)^{0.5} \qquad \textbf{(6-XI)}$$

Finally, the combined uncertainty of the reduced temperature difference is determined from equation (6-XII):

$$u_C(T_m^*) = \left(\left(\frac{1}{2\ \mathrm{DNI}}\right)^2 u_C\left(T_{wat,out}\right)^2 + \left(\frac{1}{2\ \mathrm{DNI}}\right)^2 u_C\left(T_{wat,in}\right)^2 + \left(-\frac{1}{\mathrm{DNI}}\right)^2 u_C(T_{amb})^2 + \left(-\frac{\frac{\left(T_{wat,out} + T_{wat,in}\right)}{2} - T_{amb}}{\mathrm{DNI}^2} \right)^2 u_C(\mathrm{DNI})^2 \right)^{0.5}$$

(6-XII)

The expanded experimental uncertainty for each parameter is obtained by multiplying the combined uncertainty by a coverage factor equal to 2 , which corresponds to a level of confidence of 95.45%.

6.5.5 Experimental results with the hybrid PVT receiver

The tests runs with the hybrid CPVT module have been performed with the direct normal irradiance (DNI) ranging between 700 W m^{-2} and 830 W m^{-2}, and the ambient temperature between 29°C and 34°C. The mass flow rate is kept equal to 0.02 kg s^{-1} per square meter of aperture area of the semi-parabolic trough mirror, which correspond to a total mass flow rate of 247 kg h^{-1}.

When performing tests runs in open electric circuit conditions, to assess only the thermal behavior of the receiver, the water inlet temperature is set at around 20°C, 53°C and 83°C. In addition, the simultaneous production of useful heat flow rate and electrical power is investigated with the electrical terminal of the CPVT receiver connected with the resistive load by sending water to the test section at inlet temperature of 28°C, 52°C and 82°C.

In order to describe the overall performance of the present linear concentrator, thermal efficiency, electrical efficiency and global efficiency, measured during test runs with electric load, have been reported in Figure 6.12 as a function of the reduced temperature difference T_m^*. In general, one can observe the declining trend of the efficiency with the reduced temperature difference. This can be explained by the following considerations: the thermal production moderately decreases because the heat losses towards the external environment increase with the fluid working temperature, moreover, the electrical efficiency diminishes due to the higher working temperature of the photovoltaic cells. Actually the decrease of the electrical performance is slight because of the peculiar properties of the triple junction photovoltaic cells employed in the CPVT receiver. On the whole, the global efficiency ranges between 0.7 and 0.6 when the reduced temperature difference T_m^* varies between 0 and 0.072 K m^2 W^{-1}. According to the optical modeling of the concentrator with the hybrid receiver, the total optical error is expected to be within 2.5 mrad and 3 mrad and the optical efficiency should be within 71.2% and 77%.

At 0.072 K m^2 W^{-1} reduced temperature difference, the thermal efficiency is around 45% while the electrical efficiency is around 15%. The electrical efficiency ranges between 18% and 15 % in the test range of T_m^* and it is appreciably lower than the expected value of 25% - 28%. This can be due to three reasons. The optical modeling of the concentrator with the CPVT receiver shows that the photovoltaic cells are probably subject to a strongly non-uniform concentrated flux condition. In the cooling system, water in single-phase flow is used: the difference between the temperature of the water at the outlet and

at the inlet is within 6°C-7°C. The temperature variation of the cooling fluids may cause a penalization of the electrical performance as the cells work in non-uniform thermal conditions. Furthermore, some parts of the hybrid receiver are not optimized from the heat transfer point of view: the cells are soldered on a alumina substrate that has a thermal conductivity around 30 W m^{-1} K^{-1}, the minichannel-based heat exchanger for the active cooling of the cells is in thermal contact with the alumina substrate by a thermal conductive pad, that has a thermal conductivity of 3 W m^{-1} K^{-1}. At high fluxes, a low thermal conductivity material could represent the dominating thermal resistance and compromise the thermal control of the entire systems. A aluminum nitride substrate should be preferred instead of the alumina one. The thermal conductive pad is definitely the weak point of the CPVT receiver as it could be easily warped during the manufacturing process, giving a non-uniform thermal contact that means non-uniform working temperature of the photovoltaic cells.
In conclusion, the tests performed with water in single-phase flow have pointed out that the performance of the concentrator with the hybrid module are promising, but several points should be considered for a redesign of the entire system, including a different secondary optics to level the concentrated flux distribution along the receiver height and a different active cooling system to realize a convective flow boiling heat transfer inside minichannels and to achieve a lower thermal resistance and a more uniform working temperature of the cells for the optimization of the global performance.

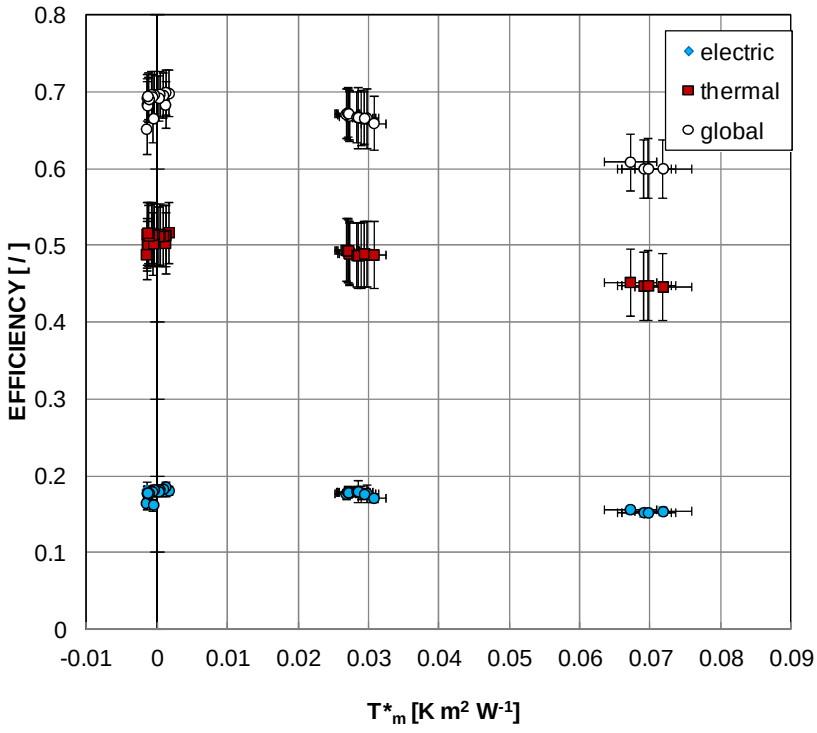

Figure 6.12. Experimental efficiency versus reduced temperature difference T_m^* obtained during the tests of the parabolic trough solar concentrator with the CPVT module connected to an adjustable resistive load. The electrical efficiency refers to the maximum power point working conditions.

The thermal behavior of the CPVT receiver has been investigated during tests with no electrical load connected to the module and the results are presented in

Figure 6.13 in terms of thermal efficiency versus reduced temperature difference. In the same graph, the thermal performance of a conventional evacuated tube solar collector provided with compound parabolic concentrators and tested in the Solar Conversion

Energy Lab are displayed. The efficiency curve for the evacuated tube solar collector refers to the steady-state procedure illustrated in the EN 12975-2 norm [88] and it is taken from the work by Zambolin and Del Col [116]. The aperture area of the conventional solar collector is equal to 3.44 m^2 and this is comparable with the aperture area referred to the CPVT module length that is 3.43 m^2. In the case of the evacuated tube collector, the reduced temperature difference and the thermal efficiency are calculated with respect to the global irradiance on the aperture area.
In the reduced temperature range within -0.01 K m^2 W^{-1} and 0.07 K m^2 W^{-1} the thermal efficiency of the CPVT module when no electrical load is connected to its terminals varies from 70% to 60%: although the hybrid receiver is not engineered for the production of heat only, its thermal performance is comparable with that of the evacuated tube collector. This result can be explain considering that the reduced surface of the absorber of the hybrid module leads to low heat losses towards the external environment.

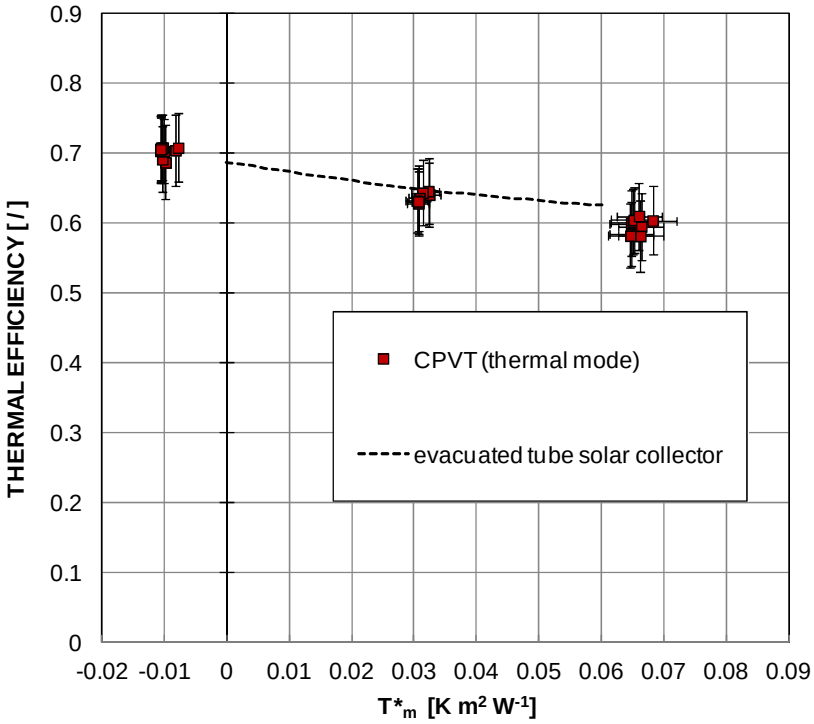

Figure 6.13. Experimental thermal efficiency versus reduced temperature difference T_m^* obtained during the tests of the parabolic trough solar concentrator with the CPVT module in open electrical circuit condition (thermal mode).

6.5.6 Experimental results with the thermal receiver

During the experimental tests with the thermal receiver, the mass flow rate of water in single-phase flow is set at 0.02 kg s^{-1} per square meter of the aperture area of the concentrator, considering the length of the test section. In this case, the total water mass flow rate is equal to 247 kg h^{-1}. Furthermore, the direct normal irradiance ranged within 615 W m^{-2} and 780 W m^{-2} and the ambient air temperature was between 21.5°C and 27.5°C. The inlet water temperature has been set at three different operating values of 50°C, 65°C and 80°C.

The experimental thermal efficiency data are plotted against the reduced temperature difference T_m^* in Figure 6.14 with the corresponding error bands. From the graph, one can observe that the thermal efficiency of the receiver only slightly decreases with increasing reduced temperature difference. In particular, the thermal efficiency is around 75% when the reduced temperature difference is 0.08 K m^2 W^{-1}, which corresponds to the production of heat available at a temperature of 87°C. This result is very promising and proves that the semi-parabolic trough with the flat thermal receiver can effectively meet the heat needs of the thermal users within the medium temperature range. The outstanding performance of the thermal receiver is due to the small area of the absorber that implies low heat losses towards the surrounding environment.

In

Figure 6.14, the experimental thermal efficiency collected with the thermal received are compared with the efficiency curve of the evacuated tube collector mentioned in Section 6.5.4 and of the CPVT module without electrical load connected. The efficiency and the reduced temperature difference of the thermal receiver and the CPVT receiver are evaluated with respect to the direct normal irradiance (DNI) while the performance of the evacuated tube solar collector is computed using the global irradiance on the plane of the device. Form the comparison, the thermal receiver mounted on the concentrator outperforms the other devices under examination. While the heat generated by the CPVT receiver can be available at a maximum temperature of 100°C because of the limit of the working temperature of the triple junction photovoltaic cells, the thermal receiver and the evacuated tube solar collector can provide heat at medium temperature in a wider range, so they can be regarded as competitor devices.

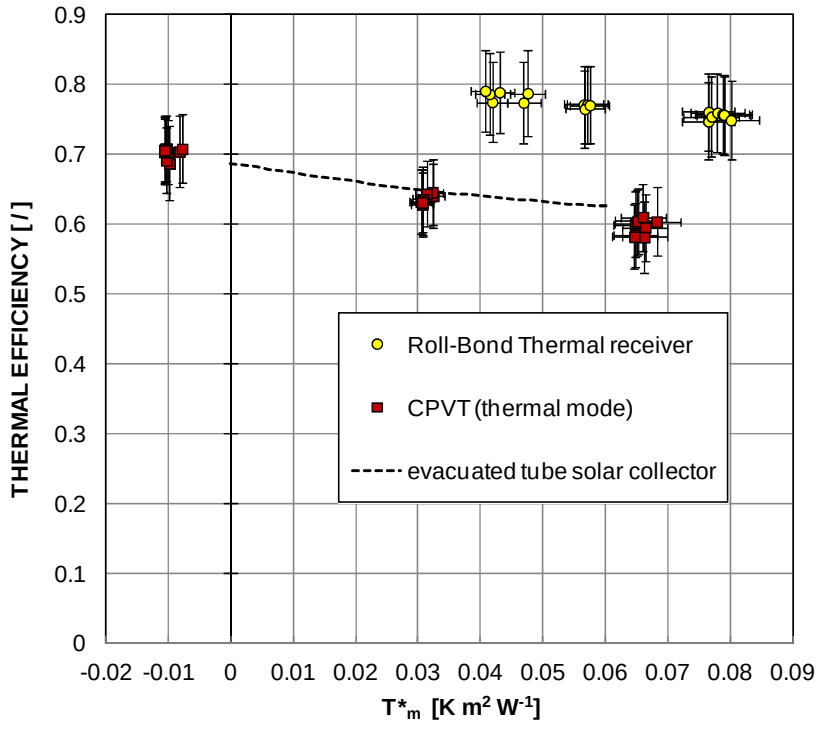

Figure 6.14. Experimental thermal efficiency versus reduced temperature difference T_m^* obtained during the tests of the parabolic trough solar concentrator with the roll-bond thermal module.

6.6 Prediction of performance of the thermal receiver at medium temperature

When discussing the present results, one can remark that the use of the minichannels in a thermal receiver is not justified by this work, as the same promising performance can be probably obtained using a multiport tube with higher hydraulic diameter. Furthermore, differently from the case of the concentrating photovoltaic module, the low thermal resistance is not a fundamental point when only the generation of heat is considered.
As stated previously, the aim of this study is to assess the potential performance of the application of the minichannel technology in solar concentrating devices, starting from tests with water in single-phase flow in order to gain a critical insight. These preliminary results should be considered as the basis to design and test a minichannel-based thermal receiver that works as a partial evaporator.
In the two-phase flow heat transfer, the latent heat of the working fluid is employed and thus the working mass flow rate is much lower than in the case of the heat transfer in single-phase flow, hence the first advantage is a decrease in the pressure drop and in the pumping power. In order to have an effective heat transfer in the thermal receiver with a low mass flow rate, channels with a small hydraulic diameter are necessarily required. Finally, when the working fluid partially vaporizes in the receiver, a condenser, that can be also realized applying the minichannel technology, should be implemented in the rig to provide heat to the thermal users. In a well-designed condenser, the heat transfer is more effective than that performed in a heat exchanger where the sensible heat of the warm fluid is employed. For these reasons, a simple model has been developed to evaluate the performance of the thermal receiver when vaporization is performed inside minichannels and when heat is generated in the medium temperature range, for different thermal applications. In the model, the thermal receiver has been divided into many elements from the water inlets to the water central outlet. Each element has a height of 105 mm, as the receiver and is modeled using a lumped capacitance scheme, where four main nodes are considered. The definition of the nodes comes from the optical modeling results and some experimental observations. For the sake of simplification, it is assumed that the concentrated flux has a pillbox distribution that covers only the central region (named ‘illuminated region’) of the thermal receiver, for a height of 45 mm across the focal line. Thus, the two central channels are included on the region of incidence of concentrated flux, while the other two channels are at the edge between the illuminated region and the peripheral regions. The peripheral regions acts as fins and contribute to the heat dissipation towards the external environment. In conclusion, the four nodes represent the central region, the peripheral regions, the fluid inside the two central channel and the fluid inside the other two channels. Equations from (6-XIII) to (6-XVI) report the thermal balances associated with each node in steady state conditions:

- central region node (subscript *C*)

$$\begin{aligned}\left(\rho\, c_p\, V\right)_C \frac{\partial t_C}{\partial \tau} = 0 \\ = q_{solar} - \frac{1}{R_{th,C-ref,C}}\left(t_C - t_{ref,C}\right) - \frac{1}{R_{th,C-P}}\left(t_C - t_P\right) \\ - \frac{1}{R_{th,C-ref,P}}\left(t_C - t_{ref,P}\right) - \frac{1}{R_{th,C,top}}\left(t_C - t_{amb}\right) \\ - \frac{1}{R_{th,C,bottom}}\left(t_C - t_{amb}\right)\end{aligned} \quad \textbf{(6-XIII)}$$

- peripheral region node (subscript *P*)

$$\left(\rho\, c_p\, V\right)_P \frac{\partial t_P}{\partial \tau} = 0 = -\frac{1}{R_{th,P-C}}\left(t_P - t_C\right) - \frac{1}{R_{th,P-ref,P}}\left(t_P - t_{ref,P}\right) - \frac{1}{R_{th,P,top}}\left(t_P - t_{amb}\right) - \frac{1}{R_{th,P,bottom}}\left(t_P - t_{amb}\right) - \frac{1}{R_{th,P,edge}}\left(t_P - t_{amb}\right) \quad \textbf{(6-XIV)}$$

- fluid in central channels node (subscript *ref,C*)

$$\left(\rho\, c_p\, V\right)_{ref,C} \frac{\partial t_{ref,C}}{\partial \tau} = 0 = -\, q_{th,ref,C} - \frac{1}{R_{th,ref,C-C}}\left(t_{ref,C} - t_C\right) \quad \textbf{(6-XV)}$$

- fluid in peripheral channels node (subscript *ref,P*)

$$\left(\rho\, c_p\, V\right)_{ref,P} \frac{\partial t_{ref,P}}{\partial \tau} = 0 = -\, q_{th,ref,P} - \frac{1}{R_{th,ref,P-C}}\left(t_{ref,P} - t_C\right) - \frac{1}{R_{th,ref,P-P}}\left(t_{ref,P} - t_P\right) \quad \textbf{(6-XVI)}$$

The water temperature at the outlet of the first element is then set equal to the temperature entering the second element and so on. The model also includes conduction heat transfer along the flow direction; this terms are omitted in the equation balances, for the sake of simplicity. The optical efficiency of the concentrating system is equal to 0.96 and as obtained from the ray-tracing modeling. The thermal resistance associated to the fluid flows required in the model above described and implemented in MatLab [82] and Simulink [89] have been calculated through a CFD analysis performed with the commercial code ANSYS FLUENT 13 [117].
In particular, the CFD simulation allowed the evaluation of the velocity distribution of the flow inside the channels of the roll-bond plate. Figure 6.15 reports the velocity distribution in a central and in an external channel: because of the configuration of the inlet manifold, the velocity in the central channels is higher than that in the external channels. This well suits to the concentrated flux distribution obtained from the optical modeling, which shows higher fluxes for the central channels. The input data of the numerical model include the inlet temperature and the mass flow rate of the working fluid, the direct normal irradiance, the ambient air temperature and the wind speed, while the expected results are the outlet water temperature, the useful thermal power and the thermal efficiency. The model has been validated against the experimental data of the thermal receiver, showing good agreement as depicted in
Figure 6.16.

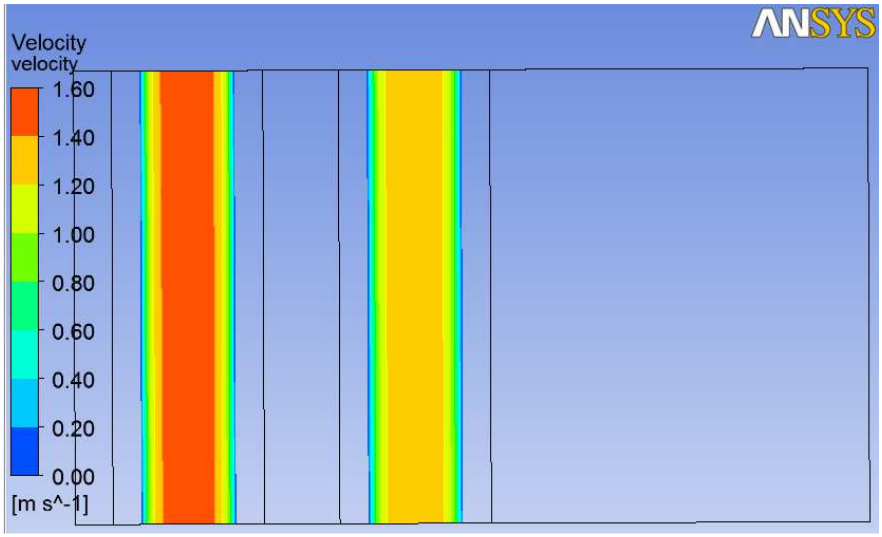

Figure 6.15. Velocity distribution in a central channel (left) and in a external channel (right) provided by the CFD simulation with ANSYS FLUENT [117]. A region of the roll-bond plate equidistant from the inlet and the outlet of the working fluid has been considered in this picture.

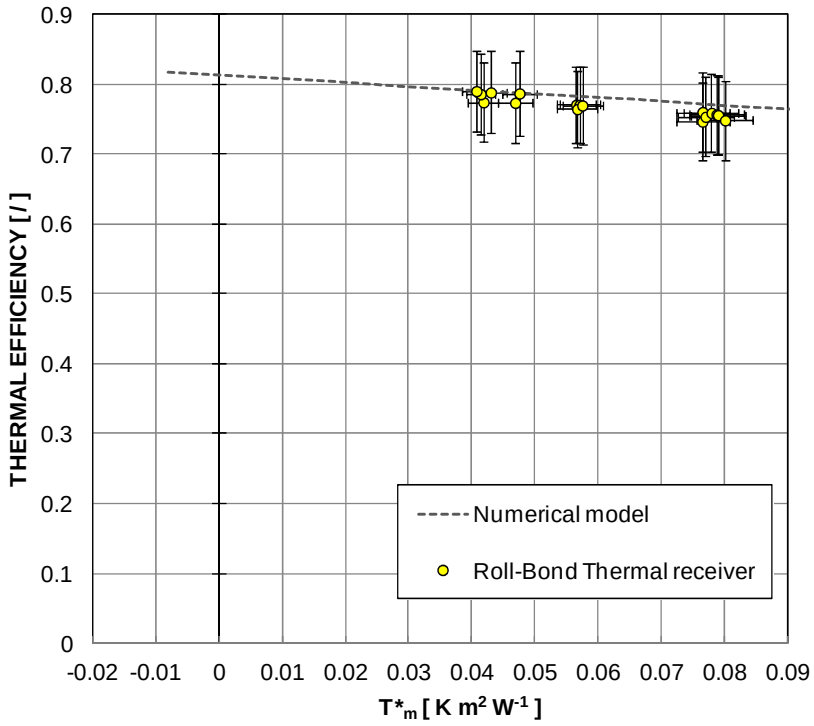

Figure 6.16. Comparison between the experimental thermal efficiency data of the thermal receiver and the efficiency calculated with the numerical model.

Once validated, the model is used to predict the performance of the thermal receiver at medium temperature up to 150°C when the working fluid is vaporizing inside the minichannels. The following assumptions have been done and they should be experimentally verified. First, the heat flux on each channel and the vapor quality of the refrigerant at the outlet of the thermal receiver are supposed low enough to avoid the departure from nucleate boiling (DNB). Second, since in literature no correlations are

reliable to predict the flow boiling heat transfer coefficient inside minichannels in the working range of the medium temperature, it is assumed an average heat transfer coefficient equal to 10 kW m^{-2} K^{-1}. The criteria for choosing the working fluids include the high latent heat of vaporization at a saturation temperature within 100°C and 150°C and a saturation pressure lower than 20 bars in order to avoid expensive components in the rig. Water and R245fa (the latter in the range from 100°C to 115°C) have emerged as possible refrigerants for this application. Table 6-c and Table 6-d report respectively the thermodynamic properties of water at saturation temperature ranging from 100°C and 150°C and those of R245fa at saturation temperature ranging from 100°C to 115°C. The thermodynamic properties have been evaluated using NIST Refprop version 9.0 [16].

Table 6-c. Properties of saturated water at saturation temperature ranging from 100°C to 150°C from NIST Refprop Version 9.0 [16].

Refrigerant	t_{sat} [°C]	p_{sat} [bar]	p_r [/]	h_{LV} [kJ kg^{-1}]	ρ_L [kg m^{-3}]	ρ_V [kg m^{-3}]	μ_L [μPa s]	λ [mW m^{-1} K^{-1}]
water	100	1.0142	0.0046	2256.4	958.35	0.59817	281.58	25.096
	110	1.4338	0.0065	2229.6	950.95	0.82693	254.61	26.245
	120	1.9867	0.0090	2202.1	943.11	1.1221	232.03	27.467
	130	2.7028	0.0122	2173.7	934.83	1.4970	212.94	28.765
	140	3.6154	0.0164	2144.3	926.13	1.9667	196.64	30.140
	150	4.7616	0.0216	2113.7	917.01	2.5481	182.61	31.595

Table 6-d. Properties of saturated R245fa at saturation temperature ranging from 100°C to 115°C from NIST Refprop Version 9.0 [16].

Refrigerant	t_{sat} [°C]	p_{sat} [bar]	p_r [/]	h_{LV} [kJ kg^{-1}]	ρ_L [kg m^{-3}]	ρ_V [kg m^{-3}]	μ_L [μPa s]	λ [mW m^{-1} K^{-1}]
R245fa	100	12.646	0.3464	134.48	1093.3	72.777	164.34	19.889
	105	14.110	0.3865	129.35	1071.8	82.319	153.97	20.586
	110	15.698	0.4300	123.90	1049.1	93.117	143.95	21.361
	115	17.417	0.4770	118.06	1025.0	105.41	134.21	22.242

When predicting the performance, the following working conditions have been contemplated:

- direct normal radiation (DNI) equal to 800 W m^{-2};
- ambient air temperature equal to 20°C;
- wind speed equal to 2 m s^{-1}.

The inlet temperature of the working fluid is set equal to the saturation temperature. Simulations at saturation temperature within 100°C and 115°C with R245fa and at saturation temperature ranging from 125°C to 150°C with water have been performed. The resulting range of the reduced temperature difference is between 0.09 and 0.17 K m^2 W^{-1}. The results of the numerical simulations are presented in
Figure 6.17, where the experimental points collected with water in single-phase flow inside minichannels are also displayed for comparison. One can realize that in the present concentrator with a thermal module, the generation of heat at temperature up to 150°C can be achieved with a thermal efficiency higher than 70%.

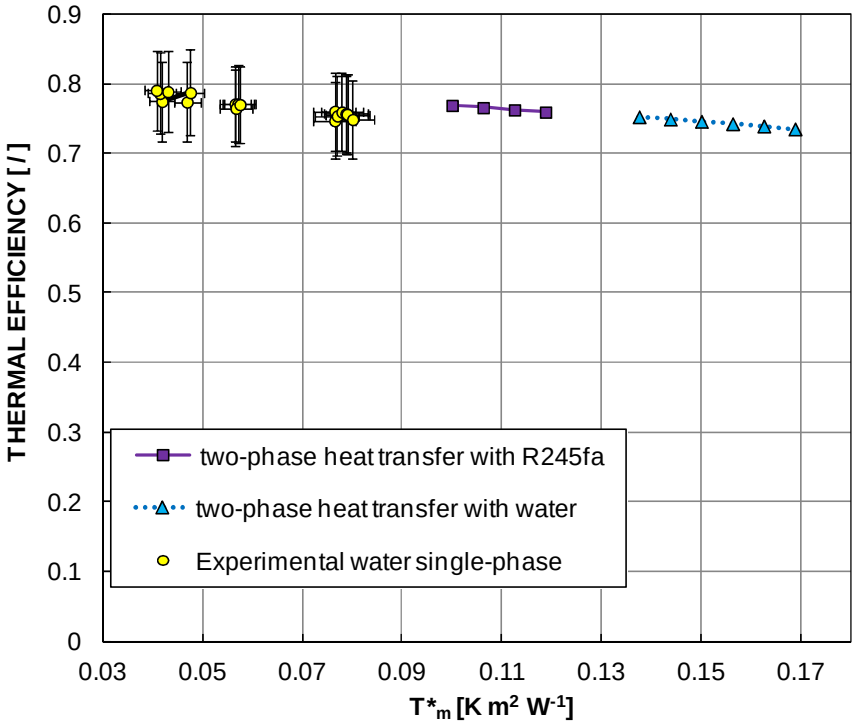

Figure 6.17. Results numerical simulations to calculate the thermal efficiency of the semi-parabolic trough concentrator with the thermal receiver when two-phase heat transfer is realized in the minichannels with R245fa at a saturation temperature ranging between 100°C and 115°C and with water with a saturation temperature ranging between 125°C and 150°C. The experimental points collected using water in single-phase flow as working fluid.

7 CONCLUSIONS

A detailed experimental investigation on the frictional pressure drops during adiabatic flow of three refrigerants inside circular minichannels has been performed in a new test section. The tested minichannels are provided with pressure ports realized in order to avoid any change in the geometry of the cross section and in the fluid flow. Results in terms of pressure gradient versus vapor quality have been presented in the following test conditions:

- for R134a, R1234ze(E) and propane (R290) inside a 0.96 mm circular minichannel at mass velocities between 800 kg m^{-2} s^{-1} and 200 kg m^{-2} s^{-1} at 40°C saturation temperature;
- for R134a inside a 0.96 mm circular minichannel at 400 kg m^{-2} s^{-1} and at 40°C and 50°C saturation temperatures;
- for R1234ze(E) inside a 0.96 mm circular minichannel at 400 kg m^{-2} s^{-1} and at 30°C and 40°C saturation temperatures;
- for R134a inside a 2.0 mm circular minichannel at mass velocity ranging from 500 kg m^{-2} $s^{-}1$ to 200 kg m^{-2} s^{-1} at 40°C saturation temperature;
- for R134 a inside a 2.0 mm circular minichannel at 400 kg m^{-2} s^{-1} and at 40°C and 50°C saturation temperatures.

At the same hydraulic diameter, mass velocity and saturation temperature, the two-phase frictional pressure drop are the lowest. In the 0.96 mm circular minichannel, propane exhibits the highest value of pressure gradient at 200 kg m^{-2} s^{-1} and 400 kg m^{-2} s^{-1} because of the low vapor density, while at 800 kg m^{-2} s^{-1} the data for propane are lower than those for R1234ze(E) up to 0.85 vapor quality because of the strong effect of liquid entrainment noticed with the hydrocarbon refrigerant. The correlation by Del Col *et al.* [4] is the only one that predicts almost all the experimental data for each tested refrigerant within ±20% band. Nevertheless, no model is able to catch the pressure gradient trend of R134a data inside the 2.0 mm minichannel or the change of slope in the propane pressure gradient trends at 600 kg m^{-2} s^{-1} and 800 kg m^{-2} s^{-1} probably due to the liquid entrainment.

The heat transfer coefficient of the natural refrigerant propane and of the low GWP refrigerant R1234ze(E) are investigated during condensation and flow boiling in a single circular cross section minichannel having a inner diameter of 0.96 mm and an average roughness of the inner tube wall of 1.3 μm. During the tests, the refrigerant exchanges heat with a secondary fluid, that is distilled water. Condensation test runs have been performed at 40°C saturation temperature and at mass velocities between 100 kg m^{-2} s^{-1} and 800 kg m^{-2} s^{-1} for R1234ze(E) and between 100 kg m^{-2} s^{-1} and 1000 kg m^{-2} s^{-1} for propane. The local heat flux is computed from the profile of the coolant temperature along the measuring section. The experimental heat transfer coefficients are well predicted using the model by Cavallini *et al.* [28] and the model by Moser *et al.* [29] implemented with the Zhang and Webb [3] correlation for the two-phase frictional pressure drop in small diameter channels. Flow boiling tests have been carried out at 31°C saturation temperature and at mass velocities within 200 kg m^{-2} s^{-1} and 500 kg m^{-2} s^{-1} for R1234ze(E) and within 100 kg m^{-2} s^{-1} and 600 kg m^{-2} s^{-1} for propane. Two different methods are considered for the computation of the local heat flux: the first is related to the temperature profile of the water along the minichannel, the second is based on the calculation of the heat transfer coefficient on the water side. The heat transfer coefficients obtained with the two procedures are in good agreement and this is an important validation of the experimental technique. For both the refrigerants, it has been found that

the flow boiling heat transfer coefficients strongly depends on the heat flux while mass velocity and vapor quality have a minor influence and no hysteresis is observed in the boiling curves. All the considered models underestimate the experimental data for both the fluid probably because they do not take into account the effect of the internal roughness or they do not consider it properly. The predictions on the propane flow boiling heat transfer coefficient by the Sun and Mishima [65] model are satisfactory, nevertheless for R1234ze(E) the predicting correlations do not reach a sufficient level of accuracy.

An accurate experimental technique has been employed in this work to assess the effect of channel orientation on heat transfer coefficients during the condensation of R134a and R32 refrigerants at 40°C saturation temperature inside a square section minichannel, with a hydraulic diameter of 1.23 mm. Local heat transfer coefficients have been reported at mass velocities between 100 kg m^{-2} s^{-1} and 390 kg m^{-2} s^{-1} in horizontal and in several upflow and downflow configurations for R134a and in horizontal and in several downflow configurations for R32. Considering the heat transfer coefficient obtained with horizontal channel as the reference case, it has been observed that the channel inclination has negligible effect on condensation both in downflow configurations at high mass velocity and in upflow configurations for the entire test range of mass velocity. On the other hand, whatever the fluid, the effect of the channel inclination on the condensation heat transfer becomes noteworthy in downflow, at vapor qualities lower than 0.6 and at mass velocities equal or lower than a critical mass flux that is equal to 150 kg m^{-2} s^{-1} for R134a and to 200 kg m^{-2} s^{-1} for R32. In these working conditions, the channel tilt generally penalizes the condensation process and may cause a dramatic decrease of the heat transfer coefficient, up to 48% with respect to that obtained in horizontal.
The Buckingham theorem has been applied to develop a correlation of dimensionless groups with the aim of predicting the critical mass velocity at which, in vertical downflow configuration, the effect of inclination begins to appear. The correlation includes the dimensionless inclination parameter Y, the Eötvös number Eo, the thermodynamic vapor quality x and the density ratio $\Delta\rho/\rho_V$. It is applicable for the tested refrigerants and for the present square minichannel but it has found to provide results consistent with the experimental investigation when employed in macrochannels.

The Performance Evaluation Criteria (PEC) dubbed Penalty Factor (PF) and Total Temperature Penalization (TTP) have been applied to rank the potential heat transfer performance in shear stress dominated condensation of R32, R245fa, R134a, R1234yf, R1234ze(E) and propane. In this case, as the comparative analysis starts from experimental data taken in a circular minichannel, the geometry is fixed and the purpose is not the design optimization of the condenser. Therefore, a constant value of the Penalty Factor is considered with respect to a vapor quality equal to 0,5 and a saturation temperature of 40°C. The condition of operating at a constant value of *PF* in a given geometry leads to the definition of a constant mass velocity for each considered refrigerant. This calculation required the use of a reliable correlation for the two-phase frictional pressure gradient and of an accurate predicting correlations for the condensation heat transfer coefficients. For this purpose, two procedure developed at the University of Padova have been employed. The mass velocity at a constant PF defined for every fluid is used to calculate the condensation heat transfer coefficients in the range of vapor quality from 0.15 to 0.85. The comparison among the coefficients establishes the ranking of the refrigerants in forced convective condensation applications. It was found that:

- R32 outperforms all the other fluid;

- the higher pressure refrigerants (R32 and propane) have the better condensation performance;
- the heat transfer performance for in-tube condensation of R134a is better than that of its low global warming potential alternatives (R1234ze(E) and R1234yf);
- even if at the same temperature saturation and mass velocity, the heat transfer coefficients for R245fa are among the highest, the condensation performance of this fluid is the worst, because of the high pressure drop during two-phase flow.

The use of two different minichannel-based receivers has been considered in a semi-parabolic trough linear solar concentrator, that moves about two axes (azimuthal and zenith motions). The first receiver is a concentrated photovoltaic thermal (CPVT) module provided with a roll-bond heat exchanger that acts as active cooling system. The second receiver is a roll-bond canalized plate sprayed with a selective coating. The optical modeling of the solar concentrators with the CPVT receiver shows that the cells are subject to a strongly non-uniform concentrated flux distribution, while, in the case of the thermal receiver, the optical efficiency is very high, about 96% because of the bigger geometrical dimensions. The experimental tests have been done using water as working fluid in single-phase flow. The performance of the concentrator with the CPVT module is assessed both in with a load with variable resistance in order to set working conditions close to the maximum power point and in open electrical circuit conditions (thermal only mode). In the former test conditions, on the whole, the global efficiency ranges between 0.7 and 0.6 when the reduced temperature difference T_m^* varies between 0 and 0.072 K m^2 W^{-1}. Thus, according to the opto-mechanic model, the optical efficiency should be within 71.2% and 77%. The electrical efficiency ranges between 18% and 15 % in the test range of T_m^* and it is appreciably lower than the expected value probably because of the non-uniform concentrated flux distribution and because of some non-optimized features of the active cooling system. When performing the tests with the CPVT receiver in thermal only mode, in the reduced temperature range within -0.01 K m^2 W^{-1} and 0.07 K m^2 W^{-1} the thermal efficiency varies from 70% to 60% and it is comparable to that of a typical evacuated tube solar collector.
With respect to the tests performed using the thermal roll-bond receiver with selective coating, the thermal efficiency is around 75% when the reduced temperature difference is 0.08 K m^2 W^{-1}, which corresponds to the production of heat available at a temperature of 87°C. A model of the thermal receiver has been developed and validated to predict the performance when heat is generated at medium temperature, up to 150°C, and when the working fluid is vaporizing inside the minichannels. In the simulations, water and R245fa are considered as working fluids because they present a high latent heat of vaporization in the saturation temperature range between 100°C and 150°C and because the working pressure does not require expensive components in the test rig. The preliminary numerical results show that, in the present concentrator and with a thermal module, the generation of heat at temperature up to 150°C can be achieved with a thermal efficiency higher than 70%.

REFERENCES

[1] L. Friedel, «Improved friction pressure drop correlations for horizontal and vertical two phase flow,» in *Proceedings of the European Two Phase Flow Group Meeting, Paper E2*, Ispra, 5-8 June 1979, 1979.

[2] H. Muller-Steinhagen e K. Heck, «A simple friction pressure drop correlation for two phase flow in pipes,» *Chemical Engineering and Processing: Process Intensification,* vol. 20, n. 6, pp. 297-308, 1986.

[3] M. Zhang e R. L. Webb, «Correlation of two-phase friction for refrigerants in small-diameter tube,» *Experimental Thermal and Fluid Science,* vol. 25, n. 3-4, pp. 131-139, 2001.

[4] D. Del Col, A. Bisetto, M. Bortolato, D. Torresin e L. Rossetto, «Experiments and updated model for two phase frictional pressure drop inside minichannels,» *International Journal of Heat and Mass Transfer,* vol. 67, pp. 326-337, 2013.

[5] S. Garimella, J. Killion e J. W. Coleman, «An experimental validated model for two phase pressure drop in the intermittent flow regime for noncircular microchannels,» *Journal of Fluids Engineering* , vol. 125, n. 5, pp. 887-894, 2003.

[6] S. Garimella, A. Agarwal e J. D. Killion, «Condensation pressure drop in circular microchannels,» *Heat Transfer Engineering,* vol. 26, n. 3, pp. 28-35, 2005.

[7] A. Cavallini, D. Del Col, L. Doretti, M. Matkovic, L. Rossetto e C. Zilio, «Two-phase frictional pressure gradient of R236fa, R134a and R410A inside multi-port mini-channels,» vol. 29, n. 7, pp. 861-870, 2005.

[8] R. Revellin e J. R. Thome, «Adiabatic two-phase frictional pressure drops in microchannels,» vol. 31, n. 7, pp. 673-685, 2007.

[9] M. Hossain, Y. Onaka e A. Miyara, «Experimental study on condensation heat transfer and pressure drop in horizontal smooth tube for R1234ze(E), R32 and R410A,» *International Journal of Refrigeration,* vol. 35, n. 4, pp. 927-938, 2012.

[10] S. Grauso, R. Mastrullo, A. W. Mauro, J. R. Thome e G. P. Vanoli, «Flow pattern map, heat transfer and pressure drops during evaporation of R-1234ze(E) and R134a in a horizontal, circular smooth tube: Experiments and assessment of predictive methods,» *International Journal of Refrigeration,* vol. 36, n. 2, pp. 478-491, 2013.

[11] B. S. Field e P. Hrnjak, «Adiabatic two-phase pressure drop of refrigerants in small channels,» *Heat Transfer Engineering,* vol. 28, n. 8-9, pp. 704-712, 2007.

[12] K. I. Choi, A. S. Pamitran, J. T. Oh e K. Saito, «Pressure drop and heat transfer during two-phase flow vaporization of propane in horizontal smooth minichannels,» *International Journal of Refrigeration,* vol. 32, pp. 837-845, 2009.

[13] M. Maqbool, B. Palm e R. Khodabandeh, «Investigation of two phase heat transfer and pressure drop of propane in a vertical circular minichannel,» *Experimental Thermal and Fluid science,* vol. 46, pp. 120-130, 2013.

[14] D. Torresin, Experimental study of two phase flow and heat transfer during vaporization, filmwise and dropwise condensation of refrigerants and steam inside small diameters channels. Ph.D. Thesis, Padova, Italy: Università degli Studi di Padova, 2012.

[15] International Standard Organization, *EN ISO 4287:1998/A1, Geometrical Product Specifications (GPS) - Surface Texture: Profile method - Terms, definitions and*

surface texture parameters, 1998.

[16] E. W. Lemmon, M. L. Huber e M. O. McLinden, *NIST Standard Reference 23: Reference Fluid Thermodynamic and Transport Properties - REFPROP, Version 9.0,* Gaithersburg: National Institue of Standard and Technology, Standard Reference Data Program, 2010.

[17] International Standard Organization, *Guide to the Expression of Incertainty in Measurements,* 1995.

[18] S. W. Churchill, «Friction factor equation spans all fluid-flow regimes,» *Chemical Engineering (New York),* vol. 45, pp. 91-92, 1977.

[19] H. Blasius, «Das Ahnlichkeitsgesetz bei Reibungsvorgangen in Flussigkeiten,» *Forsch. Arb. Ing. Wes.,* vol. 131, 1913.

[20] A. Cavallini, D. Del Col, M. Matkovic e L. Rossetto, «Frictional pressure drop during vapor-liquid flow in minichannles: modelling and experimental evaluation,» *International Journal of Heat and Fluid Flow,* vol. 30, n. 1, pp. 131-139, 2009.

[21] M. Zhang, A new equivalent Reynolds number model for vapor shear-controlled condensation inside smooth and micro-fin tubes. PhD Thesis, Pennsylvania State University, 1998.

[22] S. Jeong, E. Cho e H. Kim, «Evaporative heat transfer coefficient and pressure drop of CO2 in a microchannel tube,» in *Proceedings of the Third International Conference on Microchannels and Minichannels,* June 13-15, Toronto, ON, USA, 2005.

[23] C. Y. Park e P. Hrnjak, «CO2 flow condensation heat transfer and pressure drop in multi-port microchannels at low temperatures.,» *International Journal of Refrigeration,* vol. 32, n. 6, pp. 1129-1139, 2009.

[24] C. Y. Park e P. Hrnjak, «Flow boiling heat transfer , pressure drop and flow patterns for CO2 in a 3.5 mm horizontal smooth tube,» *Journal of Heat Transfer,* vol. 131, n. 9, p. 091501 (12 pages), 2009.

[25] Y. J. Kim, J. Jang, P. S. Hrnjak e M. S. Kim, «Adiabatic Horizontal and Vertical Pressure Drop of Carbon Dioxide Inside Smooth and Microfin Tubes at Low Temperatures,» *Journal of Heat Transfer,* vol. 130, n. 11, p. 111001 (10 pages), 2008.

[26] M. Ducoulombier, S. Colasson, J. Bonjour e P. Haberschill, «Carbon dioxide flow boiling in a single microchannel – Part I: Pressure drops,» *Experimental Thermal and Fluid Science,* vol. 35, n. 4, pp. 581-596, 2011.

[27] G. F. Hewitt e N. S. Hall-Taylor, Annular two-phase flow, Oxford: Pergamon Press, 1970.

[28] A. Cavallini, D. Del Col, L. Doretti, M. Matkovic, L. Rossetto, C. Zilio e G. Censi, «Condensation in horizontal smooth tubes: a new heat transfer model for exchanger design,» *Heat Transfer Enginnering,* vol. 27, n. 8, pp. 31-38, 2006.

[29] K. Moser, R. Webb e B. Na, «A new equivalent Reynolds number model for condensation in smooth tubes,» *Journal of Heat Transfer,* vol. 120, pp. 410-417, 1998.

[30] M. M. Shah, «An improved and extended general correlation for heat transfer during condensation in plain tubes,» *HVAC&Research,* vol. 15, n. 5, pp. 889-913, 2009.

[31] United Nations Environmental Program - Ozone Secretariat, *Montreal Protocol on*

substances that deplete the ozone layer, Montreal, 1987.

[32] United Nations, *Kyoto Protocol to the United Nations Framework Convention on Climate Change*, New York, 1997.

[33] European Parliament and Council, *Directive 2006/40/EC of the European Parliament and of the Council of 17 May 2006 relating to emissions from air conditioning systems in motor vehicles and amending Council Directive 70/156/EEC (Text with EEA relevance)*, 2006.

[34] European Parliament and Council, *Regulation (EC) No 842/2006 of the European Parliament and of the Council of 17 May 2006 on certain fluorinated greenhouse gases*, 2006.

[35] European Commission, *Proposal for a regulation of the European Parliament and the Council on flourinated greenhouse gases 2012/0305 (COD)*, Bruxelles, 2012.

[36] T. Harms, E. Groll e J. Braun, «Accurate charge inventory modeling for unitaryair conditioners,» *HVAC&R Research*, vol. 9, n. 1, pp. 55-78, 2003.

[37] J. M. Corberan e I. O. Martinez, «Charge optimization study of reversible water-to-water propane heat pump,» *International Journal of Refrigeration*, vol. 31, pp. 716-726, 2008.

[38] A. Cavallini, E. Da Riva e D. Del Col, «Performance of a large capacity propane heat pump with low charge heat exchangers,» *International Journal of Refrigeration*, vol. 33, pp. 242-250, 2010.

[39] H. Lee e C. Son, «Condensation heat transfer and pressure drop characteristics of R-290, R-600a, R-134a and R-22 in horizontal tubes,» *Heat and Mass Transfer*, vol. 46, pp. 571-584, 2010.

[40] L. Shao, L. Yang, C. Zhang e B. Gu, «Numerical modeling of serpentine microchannel condensers,» *International Journal of refrigeration*, vol. 32, pp. 1162-1172, 2009.

[41] A. Cavallini, G. Censi, D. Del Col, L. Doretti, G. Longo e L. Rossetto, «In-tube condensation of halogenated refrigerants,» *ASHRAE Transactions*, vol. 108, n. 1, pp. 146-161, 2002.

[42] P. Fernando, B. Palm, T. Ameel, P. Lundqvist e E. Granryd, «A minichannel aluminium tube heat exchanger – Part III: Condenser performance with propane,» *International Journal of Refrigeration*, vol. 31, n. 4, pp. 696-708, 2008.

[43] P. Fernando, B. Palm, T. Ameel, P. Lundqvist e E. Granryd, «A minichannel aluminium tube heat exchanger - Part II: Evaporator performance with propane,» *International Journal of refrigeration*, vol. 31, n. 4, pp. 681-695, 2008.

[44] Maqbool, B. Palm e R. Khodabandeh, «Experimental investigation of dryout of propane in uniformly heated single vertical mini-channels,» *Experimental Thermal and Fluid Science*, vol. 37, pp. 121-129, 2012.

[45] J. Park, F. Vakili-Farahani, L. Consolini e J. Thome, «Experimental study on condensation heat transfer in vertical minichannels for new refrigerant R1234ze(E) versus R134a and R236fa,» *Experimental Thermal and Fluid Science*, vol. 35, n. 3, pp. 442-454, 2011.

[46] M. Hossain, Y. Onaka, H. Afroz e A. Miyara, «Heat transfer during evaporation of R1234ze(E), R32, R410A and a mixture of R1234ze(E) and R32 inside a horizontal smooth tube,» *International Journal of Refrigeration*, vol. 36, n. 2, pp. 465-477, 2013.

[47] C. Tibiriçá, G. Ribatski e J. Thome, «Flow boiling characteristics for R1234ze(E) in 1.0 and 2.2 mm circular channels,» *Journal of Heat Transfer*, vol. 134, n. 2, p. 020806 (8 pages), 2012.

[48] F. Vakili-Farahani, B. Agostini e J. Thome, «Experimental study on flow boiling heat transfer of multiport tubes with R245fa and R1234ze(E),» *International Journal of Refrigeration*, vol. 36, n. 2, pp. 335-352, 2013.

[49] M. Matkovic, *Experimental condensation inside minichannels*, Ph.D. Thesis, University of Padova, Italy, 2006.

[50] D. Del Col, S. Bortolin, A. Cavallini e M. Matkovic, «Effect of cross sectional shaper during condensation in a single square minichannel,» *International Journal of Heat and Mass Transfer*, vol. 54, n. 17-18, pp. 3909-3920, 2011.

[51] M. Matkovic, A. Cavallini, D. Del Col e L. Rossetto, «Experimental study on condensation heat transfer inside a single circular mnichannel,» *International Journal of Heat and Mass Transfer*, vol. 52, n. 9-10, pp. 2311-2323, 2009.

[52] J. O. Rawlings, S. G. Pantula e D. A. Dickey, Applied regression analysis, New York: Springer, 1998.

[53] A. Paliwoda, «Generalized method of pressure drop calculation across pipe components containing two-phase flow of refrigerants,» *International Journal of Refrigeration*, vol. 15, n. 2, pp. 119-125, 1992.

[54] I. Idelchik, Handbook of hydraulic resistance, Begell House, 1996.

[55] W. H. Press, B. P. Flannery, S. A. Teukolsky e W. T. Vetterling, Numerical recipes, New York: Cambridge University Press, 2007, pp. 773-793.

[56] A. Cavallini, S. Bortolin, D. Del Col, M. Matkovic e L. Rossetto, «Condensation heat transfer and pressure losses of high and low pressure refrigerants flowing in a single circular minichannel,» *Heat Transfer Engineering*, vol. 32, n. 2, pp. 90-98, 2011.

[57] D. Del Col, D. Torresin e S. Bortolin, «Heat transfer and pressure drop during condensation of the low GWP refrigerant R1234yf,» *International Journal of Refrigeration*, vol. 33, n. 7, pp. 1307-1318, 2010.

[58] M. M. Shah, «Heat transfer during condensation inside small channels: applicability of general correlation for macrochannels,» in *Proceedings of the 14th International Heat Transfer Conference IHTC14*, Washington DC, USA, 2010.

[59] D. Del Col e S. Bortolin, «Investigation of dryout during flow boiling in a single microchannel under non-uniform axial heat flux,» *International Journal of Thermal Sciences*, vol. 57, pp. 25-36, 2012.

[60] Z. Rouhani e E. Axelsson, «Calculation of the void volume fraction in the subcooled and quality boiling region,» *International Journal of Heat and Mass Transfer*, vol. 13, n. 2, pp. 383-393, 1970.

[61] D. Del Col, S. Bortolin, D. Torresin e A. Cavallini, «Flow boiling of R1234yf in a 1 mm diameter channel,» *International Journal ofRefrigeration*, vol. 36, n. 2, pp. 353-362, 2013.

[62] G. M. Lazarek e S. H. Black, «Pressure drop and critical heat flux in small vertical tube with R-113.,» *International Journal of Heat and Mass Transfer*, vol. 25, n. 7, pp. 945-960, 1982.

[63] P. A. Kew e K. Cornwell, «Correlation for the prediction of boiling heat transfer in small diameter channels,» *Applied Thermal Engineering*, vol. 17, n. 8-10, pp. 705-

715, 1997.

[64] K. I. Choi, A. S. Pamitran, C. Y. Oh e J. T. Oh, «Boiling heat transfer of R-22, R-134a and CO2 in horizontal smooth minichannels,» *International Journal of Refrigeration,* vol. 30, n. 8, pp. 1336-1346, 2007.

[65] L. C. Sun e K. Mishima, «An evaluation of prediction methods for saturated flow boiling heat transfer in mini-channels,» *International Journal of Heat and Mass Transfer,* vol. 52, n. 23-24, pp. 5323-5329, 2009.

[66] S. S. Bertsch, E. A. Groll e S. V. Garimella, «A composite heat transfer correlation for saturated flow boiling in small channels,» *International Journal of Heat and Mass Transfer,* vol. 52, n. 7-8, pp. 2110-2118, 2009.

[67] J. C. Chen, «A correlation for boiling heat transfer to saturated fluids in convective flow,» *Industrial & Engineering Chemistry Process Design and Development,* vol. 5, n. 3, pp. 322-329, 1966.

[68] M. G. Cooper, «Heat flow rates in saturated nucleate pool boilng - a wide-ranging examination using reduced properties.,» *Advances in Heat Transfer,* vol. 16, pp. 157-239, 1984.

[69] S. Bortolin, D. Del Col e L. Rossetto, «Flow boiling of R245fa in a single circular microchannel,» *Heat Transfer Engineering,* vol. 32, n. 13-14, pp. 1160-1172, 2011.

[70] S. Garimella, «Condensation in minichannels and microchannels,» in *Heat transfer and fluid flow in minichannels and microchannels*, Elsevier Ltd., 2006, pp. 227-408.

[71] H. S. Wang e J. W. Rose, «Theory of heat transfer during condensation in microchannels,» *International Journal of Heat and Mass transfer,* vol. 54, n. 11-12, pp. 2525-2534, 2011.

[72] E. Da Riva, S. Bortolin e D. Del Col, «Condensation in a square minichannel: application of the VOF method.,» in *Proceedings of 3rd Micro and Nano Flows Conference*, Thessaloniki, 2011.

[73] E. Da Riva, D. Del Col, S. V. Garimella e A. Cavallini, «The importance of turbolence during condensation in a horizontal minichannel,,» *International Jorunal of Heat and Mass Transfer,* vol. 55, n. 13-14, pp. 3470-3481, 2012.

[74] J. S. Shin e M. H. Kim, «An experimental study of flow condensation heat transfer inside circular and rectangular minichannels,» *Heat Transfer Engineering,* vol. 26, n. 3, pp. 36-44, 2005.

[75] A. Agarwal, T. M. Bandhauer e S. V. Garimella, «Measurement and modeling of condensation heat transfer in non-circular microchannels.,» *International Journal of Refrigeration,* vol. 33, n. 6, pp. 1169-1179, 2010.

[76] M. Derby, H. J. Lee, Y. Peles e M. K. Jensen, «Condensation heat transfer in square, triangular and semi-circular minichannels,» *International Journal of Heat and Mass Transfer,* vol. 55, n. 1-3, pp. 187-197, 2012.

[77] S. Lips e J. P. Mayer, «Experimental study of convectiv condensation in an inclined smooth tube. Part I: Inclination effect on flow pattern and heat transfer coefficient.,» *International Journal of Heat and Mass Transfer,* vol. 55, n. 1-2, pp. 395-404, 2012.

[78] B. X. Wang e X. Z. Du, «Study on laminar film-wise condensation for vapor flow in an inclined small/mini-diameter tube.,» *International Journal of heat and Mass Transfer,* vol. 43, n. 10, pp. 1859-1868, 2000.

[79] H. Saffari e V. Naziri, «Theoretical modelling and numerical solution of stratified condensation in inclined tube.,» *Journal of Mechanical Science and Technology,* vol. 24, n. 12, pp. 2587-2596, 2010.

[80] Y. Lyulin, I. Marchuk, S. Chikov e O. Kabov, «Experimental study of laminar convective condensation of vapor inside an inclined circular tube,» *Microgravity Science adn Technology,* vol. 23, n. 4, pp. 439-445, 2011.

[81] E. Da Riva e D. Del Col, «Effect of gravity during condensation of R134a in a circular minichannel.,» *Microgravity Science and Technology,* vol. 23, n. 1 Supplement, pp. 87-97, 2011.

[82] The MathWorks Inc., *MATLAB R2009a,* Natick, Massachusetts, USA, 2009.

[83] Y. Taitel e A. E. Dukler, «A model for predicting flow regime transitions in horizontal and near horizontal gas-liquid flow,» *American Institute of Chemical Engineers (AIChE) Journal,* vol. 22, n. 1, pp. 47-55, 1976.

[84] A. Cavallini, J. S. Brown, D. Del Col e C. Zilio, «In-tube condensation performance of refrigerants considering penalization terms (exergy losses) for heat transfer and pressure drop.,» *International Journal of Heat and Mass Transfer,* vol. 53, n. 13-14, pp. 2885-2896, 2010.

[85] A. Cavallini, D. Del Col e L. Rossetto, «Heat transfer and pressure drop of natural refrigerants in minichannels (low charge equipment),» *International Journal of Refrigeration,* vol. 36, n. 2, pp. 287-300, 2013.

[86] National Renewable Energy Laboratory (NREL), *SolTrace version 2012.7.9,* <http://www.nrel.gov/csp/soltrace>, 2012.

[87] Lamda Research Corporation, *TracePro version 7.1,* <http://www.lambdares.com>, 2013.

[88] Comité Européen de Normalisation (CEN), *EN 12975-2: Thermal solar systems and components - solar colector - part 2: test methods,* Brussels, Belgium, 2006.

[89] The MathWorks Inc., *Simulink 7.3,* Natick, Massachusetts, USA, 2009.

[90] B. Agostini, M. Fabbri, J. E. Park, L. Wojtan, J. R. Thome e B. Michel, «State of art of high heat flux cooling technologies.,» *Heat Transfer Engineering,* vol. 28, n. 4, pp. 258-281, 2007.

[91] G. Diaz, «Numerical analysis of a minichannel solar collector for CO2-based Rankine cycle applications.,» *TWi Transactions on Ecology and the Environment,* vol. 121: Energy and Sustainability II, pp. 23-34, 2009.

[92] N. Sharma e G. Diaz, «Performance model of a novel evacuated-tube solar collector based on minichannels.,» *Solar Energy,* vol. 85, n. 5, pp. 881-890, 2011.

[93] M. Khamis Mansour, «Thermal analysis of a novel minichannel-based solar flat-plate collector,» *Energy,* vol. 60, pp. 333-343, 2013.

[94] S. Agrawal e G. N. Tiwari, «Energy and exergy analysis of a hybrid micro-channel photovoltaic thermal module.,» *Solar Energy,* vol. 85, n. 2, pp. 356-370, 2011.

[95] S. Agrawal e A. Tiwari, «Experimental validation of the glazed hybrid micro-channel solar thermal tile.,» *Solar Energy,* vol. 85, n. 11, pp. 3046-3056, 2011.

[96] D. Del Col, M. Dai Prè, M. Bortolato e A. Padovan, «Investigation of PV solar devices for electricity production and heat recovery.,» in *67° Congresso Nazionale ATI,* Trieste, 11-14 Settembre 2012, 2012.

[97] P. Valeh-e-Sheyda, M. Rahimi, E. Karimi e M. Asadi, «Application of two-phase flow for cooling of hybrid microchannel PV cells: A comparative study,» *Energy*

Conversion and Management, vol. 69, pp. 122-130, 2013.

[98] A. Royne, J. D. Christopher e D. R. Mills, «Cooling of photovoltaic cells under concentrated illumination: a critical review.,» *Solar Energy Materials & Solar Cells,* vol. 86, n. 4, pp. 451-483, 2005.

[99] P. Pérez-Higueras, E. Munoz, G. Almonacid e G. Vidal, «High concentrator photovoltaics efficiencies: present status and forecast.,» *Renewable and Sustaianble Energy Reviews,* vol. 15, n. 4, pp. 1810-1815, 2011.

[100] W. Escher, S. Paredes, S. Zimmermann, C. L. Ong, P. Ruch e B. Michel, «Thermal management and overall performance of a high conventration PV,» *American Institute of Physics (AIP) Conference Proceedings,* Vol. %1 di %21477: 8th International Conference on Concentrating Photovoltaic Sysyems (CPV-8), pp. 239-243, 2012.

[101] S. G. Kandlikar, S. Colin, Y. Peles, S. Garimella, R. F. Pease, J. J. Brandner e D. B. Tuckerman, «Heat transfer in microchannels - 2012 status and research needs,» *Journal of Heat Transfer,* vol. 135, n. 9, p. 091001 (18 pages), 2013.

[102] T. Ho, S. S. Mao e R. Greif, «improving efficiency of high-concentrator photovoltaics by cooling with two-phase forced convection.,» *International Journal of Energy Research,* vol. 34, n. 14, pp. 1257-1271, 2010.

[103] T. Ho, S. S. Mao e R. Greif, «The impact of cooling on cell temperature and the practical solar concentration limits for phototvoltaics.,» *International Journal of Energy Research,* vol. 35, n. 14, pp. 1250-1257, 2011.

[104] D. Chemisana, «Building integrated concentrating photovoltaics: a review.,» *Renewable and Sustainable Energy Reviews,* vol. 15, n. 1, pp. 603-611, 2011.

[105] A. Rabl, «Comparison of solar concentrators,» *Solar Energy,* vol. 18, n. 2, pp. 93-111, 1976.

[106] A. Neumann, A. Witzke, S. A. Jones e G. Schmitt, «Representative terrestrial solar brightness profiles.,» *Journal of Solar Energy Engineering,* vol. 124, n. 2, pp. 198-204, 2002.

[107] C. W. Allen, in *Astrophysical quantities (Second Edition).*, London, The Athlone Press, 1963, p. Chapter 9.

[108] H. Baig, K. C. Heasman e T. K. Mallick, «Non-uniform illumiantion in concentrating solar cells.,» *Renewable and Sustainable Energy Reviews,* vol. 16, n. 8, pp. 5890-5909, 2012.

[109] J. Ballestrin e R. Monterreal, «Hybrid heat flux measurement system for solar central receiver evaluation.,» *Energy,* vol. 29, n. 5-6, pp. 915-924, 2004.

[110] International Electrochemical Commission, *IEC 62108 standard. Concentrator photovoltaic (CPV) modules and assemblies-design qualification and type approval.,* Geneva, Switzerland, 2007.

[111] Institute of Electical and Electronics Engineers, *IEEE 1513 - IEEE recommended practica for qualification of concentrator photovoltaic (PV) receiver sections and modules.,* New York, USA, 2001.

[112] E. Muñoz, P. G. Vidal, G. Nofuentes, L. Hontoria, P. Perez-Higueras, J. Terrados, G. Almonacid e J. Aguilera, «CPV standardization: an overview,» *Renewable and Sustainable Energy Reviews,* vol. 14, n. 1, pp. 518-523, 2010.

[113] M. Vivar, M. Clarke, J. Pye e V. Everett, «A review of standards for hybrid CPV-thermal systems,» *Renewable and Sustainable Energy Reviews,* vol. 16, n. 1, pp.

443-448, 2012.

[114] P. Dupeyrat, H. Helmers, S. Fortuin e K. Kramer, «Recent advances in the development and testing of hybrid PV-thermal collectors.,» in *Proocedings of the 30th ISES Biennal Solar World Congress (SWC 20111)*, Kassel, Germany, 28 August- 2 September, 2011.

[115] H. Helmers e K. Kramer, «Multi-linear performance model for hybrid (C)PVT solar collectors,» *Solar Energy*, vol. 92, pp. 313-322, 2013.

[116] E. Zambolin e D. Del Col, «An improved procedure for the experimental characterization of the optical efficiecny in evacuated tube solar collectors,,» *Renewable Energy*, vol. 43, pp. 37-46, 2012.

[117] ANSYS Inc., *ANSYS Fluent 13 Theory Guide*, Canonsburg PA, USA, 2010.

PUBLICATIONS

In Conference Proceedings

Del Col D., Dai Prè M, Bortolato M, Padovan A (2011). Experimental characterization of thermal performance of flat plate solar collectors with roll-bond absorbers. In: Proceedings Ises Solar World Congress 2011. p. 2859-2870, Kassel, Germany- .

Del Col D., Bortolato M., Bortolin S., Cavallini A. (2012). Experimental Study of Condensation Inside a Square Minichannel: Effect of Channel Orientation . In: ECI 8th International Conference on Boiling and Condensation Heat Transfer . Lausanne, Switzerland, 3-7 June 2012

Del Col D., Bortolin S., Bortolato M., Rossetto L. (2012). Condensation heat transfer and pressure drop with propane in a minichannel. In: 14th International Refrigeration and Air Conditioning Conference at Purdue . p. 1-10, Purdue University, West Lafayette, Indiana, USA, July 16-19

Del Col D., Bortolato M., Bortolin S., Azzolin M. (2012). Minichannel condensation in downward, upward and horizontal configuration. In: Journal of Physics: Conference Series. IOP PUBLISHING LTD, ENGLAND, Poitiers, France, September 04 - 07, 2012, doi: 10.1088/1742-6596/395/1/01209

Del Col D., Dai Prè M., Bortolato M., Padovan A. (2012). Investigation of PV solar devices for electricity production and heat recovery. In: Atti del 67° Congresso Nazionale ATI. ISBN: 9788890767609, Trieste, 11-14 Settembre 2012

Del Col D., Bortolato M, Bortolin S (2013). Measurements of heat transfer coefficient during flow boiling of two HFOs inside a circular microchannel. In: 8th World Conference on Experimental Heat Transfer, Fluid Mechanics, and Thermodynamics. paper 490, Lisbona, June 16-20, 2013

Del Col D., Azzolin M., Bortolato M., Bortolin S. (2013). Condensation heat transfer and pressure drop in a single minichannel with R1234ze(E)and other refrigerants. In: 4th IIR Conference on Thermophysical Properties and Transfer Processes of Refrigerants. TP-051, Delft, The Netherlands, June 2013

Del Col D., Bortolato M., Padovan A., Quaggia M. (2013). Experimental and numerical study of a parabolic trough linear CPVT system. In: ISES Solar World Congress 2013. Cancun; Mexico, 3-7 November 2013

In International Journals

Del Col D., Padovan A., Bortolato M., Dai Prè M., Zambolin E. (2013). Thermal performance of flat plate solar collectors with sheet-and-tube and roll-bond absorbers. ENERGY, vol. 58, p. 258-269, ISSN: 0360-5442, doi: 10.1016/j.energy.2013.05.058

Del Col D., Bisetto A., Bortolato M., Torresin D., Rossetto L. (2013). Experiments and updated model for two-phase frictional pressure drop inside minichannels. International

Journal of Heat and Mass Transfer, vol. 67, p. 326-337, ISSN: 0017-9310, doi: 10.1016/j.ijheatmasstransfer.2013.07.093

Papers to be submitted to International Journals

Del Col D., Bortolato M., Azzolin M., Bortolin S. Condensation heat transfer and two-phase frictional pressure drop in a single minichannel with R1234ze(E) and other refrigerants. To be submitted to International Journal of Refrigeration.

Del Col D., Bortolato M., Azzolin M., Bortolin S. Effect of channel inclination on the condensation inside a square cross section minichannel. To be submitted to International Journal of Heat and Mass Transfer.

Del Col D., Bortolato M., Bortolin S., Rossetto L. Experimental characterization of the propane thermal performance in a single circular minichannel during two-phase heat transfer. To be submitted to Experimental Thermal and Fluid. Science

NOMENCLATURE

A	area [m^2]
a_0,..., a_M	coefficients of the water temperature fitting equation
Bo	boiling number [/]
C	covariance matrix
Co	confinement number [/]
c_p	isobaric specific heat [J kg^{-1} K^{-1}]
DNI	direct normal irradiance [W m^{-2}]
d_h	hydraulic diameter [m]
(dp/dz)	pressure drop gradient [Pa m^{-1}]
DT_{dr}	driving temperature difference [K]
DT_{sr}	saturation temperature decrease [K]
E_{el}	voltage [V]
Eo	Eötvös number [/]
e_P	percentage deviation = 100 (ψ_{CALC}-ψ_{EXP}) / ψ_{EXP} [%]
e_R	average deviation = (1/N_P) Σe_P [%]
f	friction factor [/]
g	gravitational acceleration [m s^{-2}]
G	mass velocity [kg m^{-2} s^{-1}]
G_V	mass velocity of the vapor phase [kg m^{-2} s^{-1}]
G^*	critical mass velocity in vertical downflow at which the inclination starts to affect the condensation HTC as compared to the one with horizontal channel [kg m^{-2} s^{-1}]
h	specific enthalpy [J kg^{-1}]
h_{LV}	latent heat = h_V - h_L [J kg^{-1}]
HTC	heat transfer coefficient [W m^{-2} K^{-1}]
I	parameter that describes the effect of inclination in [77] [/]
I_{el}	current [A]
L	length [m]
L_{MS}	length of the measuring section [m]
L_{PP}	distance between the pressure ports [m]
M	mass [kg]
$\dot{m}$	mass flow rate [kg s^{-1}]

n	number of observations of a measured quantity [/]
N_P	number of data points [/]
nTC	number of water thermocouples considered for data reduction [/]
Nu	Nusselt number [/]
P	power [W] or perimeter [m]
p	pressure [Pa]
p_r	reduced pressure [Pa]
PF	penalty factor for condensation [K^2]
Pr	Prandtl number [/]
q_{solar}	incident solar power [W]
q_{th}	useful heat flow rate [W]
q'	local heat flux [W m^{-2}]
R^2	R square coefficient of determination [/]
R^2_{adj}	adjusted R square coefficient of determination [/]
R_{th}	thermal resistance [K W^{-1}]
Ra	arithmetic mean deviation of the assessed profile [µm] according to EN ISO 4287:1998/A1 [15]
Re	Reynolds number [/]
s	standard deviation for a measured quantity or specific entropy [J kg^{-1} K^{-1}]
$\dot{S}_{gen}$	flow rate of entropy [W K^{-1}]
T	temperature [K]
T^*_m	reduced temperature difference [K m^2 W^{-1}]
t	temperature [°C]
TTP	total temperature penalization [K]
U	expanded uncertainty
u	uncertainty of a fitting parameter
u_A	type A uncertainty
u_B	type B uncertainty
u_C	combined experimental uncertainty
We	Weber number [/]
x	thermodynamic vapor quality [/]

y	fitting function for water temperature as a function of z
Y	dimensionless inclination parameter [/]
Y^*	dimensionless inclination parameter referred to G^*[/]
z	axial position [m]
Greek symbols	
β	inclination angle computed from the horizontal [°]
$\Delta \rho$	difference of density = $\rho_L - \rho_V$ [kg m^{-3}]
Δp	pressure drop [Pa]
Δs	difference of specific entropy [J kg^{-1} K^{-1}]
Δt	temperature difference [°C]
ΔT	temperature difference [K]
ΔT_{dr}	driving temperature difference [K]
ΔT_{sr}	saturation temperature decrease [K]
ε	absolute roughness of the channel [m]
η	global efficiency [/]
η_{opt}	optical efficiency [/]
η_{th}	thermal efficiency [/]
θ	directly measured quantity
λ	thermal conductivity [W m^{-1} K^{-1}]
μ	dynamic viscosity [Pa s]
ξ	quantity expressed as function of uncorrelated inputs
Π_1..... Π_5	dimensionless groups obtained from the application of the Buckingham theorem [/]
ρ	density [kg m^{-3}]
σ	surface tension [N m^{-1}]
σ_N	standard deviation (prediction method) = $[\Sigma (e_p - e_R)^2/(N_P - 1)]^{1/2}$ [%]
τ	time [s]
χ^2	merit figure [/]
Subscripts	
amb	ambient air
aper	aperture
C	central region

CALC	Calculated
cm	cooling medium
EXP	experimental
f	Frictional
i	corresponding to *i-th* water thermocouple
in	inlet
ICS	inlet condition setter
L	saturated liquid
LIQ	liquid phase
LO	liquid only
LR	referred to the receiver length
MS	measuring section
out	outlet
P	peripheral region
ref	refrigerant
ref C	refrigerant in the central channels
ref P	refrigerant in the peripheral channels
sat	saturation
V	saturated vapor
VAP	vapor phase
wall	wall
water	water